Autopsy of a quantum electrical current

Benjamin Roussel

N° d'ordre NNT : 2017LYSE1285

THÈSE DE DOCTORAT DE L'UNIVERSITÉ DE LYON
opérée au sein de
l'Université Claude Bernard Lyon 1

École Doctorale ED52
Physique & Astrophysique de Lyon

Spécialité de doctorat : Physique

Soutenue publiquement le 15 décembre 2017, par :
Benjamin Roussel

Autopsy of a quantum electrical current
Autopsie d'un courant électrique quantique

Devant le jury composé de :

Natalia Del Fatti, UCBL	Présidente
Daniel Estève, CEA Saclay	Rapporteur
Serge Florens, CNRS et Institut Néel	Rapporteur
Patrick Flandrin, CNRS et ENS de Lyon	Examinateur
Janine Splettstoesser, École Polytechnique de Chalmers	Examinatrice
Pascal Degiovanni, CNRS et ENS de Lyon	Directeur de thèse

Autopsie d'un courant électrique quantique

Les expériences de physique quantique ont atteint un niveau de contrôle permettant de préparer avec précision l'état quantique de nombreux systèmes physiques. Cela a mené à la naissance de l'optique quantique électronique, un sujet émergent qui vise à préparer, manipuler et caractériser l'état de courants électriques contenant quelques excitations électroniques se propageant dans un conducteur quantique ballistique. Ceci est un défi conséquent qui se heurte à la difficulté de caractériser un état quantique à N corps.

Le sujet de cette thèse sera le développement de méthodes de traitement du signal quantique permettant d'accéder à une connaissance partielle d'un tel état pour des courants électriques quantiques. Une première méthode consiste à les analyser à nombre d'excitations fixé au travers des cohérences électroniques. Pour cela, nous élaborons une analyse de la cohérence à un électron en termes d'« atomes de signaux » électroniques. En combinant cela au protocole de tomographie par interférometrie HOM, nous présentons la première autopsie, fonction d'onde par fonction d'onde, d'un courant électrique quantique.

Une autre approche consiste à examiner des indicateurs sondant directement l'état à N corps. Nous étudions le rayonnement émis par un conducteur quantique ainsi que la décohérence électronique d'une excitation à un électron. Ensuite nous analysons la distribution de probabilité de la chaleur dissipée par un système quantique mésoscopique. Dans ce cadre, nous développons une théorie de l'effet Joule en régime quantique et explorons comment celle-ci pourrait permettre de sonder l'état à N corps.

Mots clés : optique quantique électronique, traitement du signal quantique, cohérence quantique

Un, deux... ?

Je ne vais pas vous parler des courants électriques quantiques. Disons, pas tout de suite. L'histoire que j'ai à vous raconter maintenant est bien plus importante, beaucoup trop importante pour ne pas être évoquée en premier. Sans elle, les courants électriques quantiques, ils l'auraient sans doute eu dans le baba. En tout cas, ils se seraient épargnés ce manuscrit à leur sujet.

En réalité, ce n'est pas vraiment une histoire en soi. Il s'agit plutôt de remercier les gens qui d'une manière ou d'une autre, ont leur part de responsabilité dans tout ceci. De leur rendre hommage. D'évoquer peut-être, quelques souvenirs. Le lecteur doit cependant être prévenu. La notion de vérité, dans les lignes qui vont suivre, sera volontairement quelque peu élastique, ce qui rendra sans doute le texte plus amusant. Je suis également certain d'oublier des gens, qui auraient pourtant tout à fait leur place dans ces lignes. J'espère qu'ils ne m'en tiendront pas rigueur.

Les lieux sont importants. Pas tant pour leur emplacement physique que pour les gens qui les peuplent, leur ambiance, leur odeur. J'ai beaucoup apprécié le temps passé ces six dernières années à l'ENS de Lyon. Il y aurait bien des histoires à raconter, encore qu'il vaille mieux que certaines restent relativement confidentielles. Je reviendrai sur ces choses-là un peu plus tard.

Le dénouement est important. Contrairement au début, qui est toujours brouillon et qu'il est nécessaire de reconstruire, voire de réinventer, la fin est claire. Parmi les participants, se trouvent bien sûr les membres du jury. Ceux-ci ont du mérite, et pour plusieurs raisons. Tout d'abord, le manuscrit devait être compact, un objectif que je ne suis pas certain d'avoir tenu. Mais chacun en jugera à sa façon. D'autre part, ils sont tous venus pour la soutenance, pour m'entendre parler de chiens et de chats, ce à quoi ils ne s'attendaient peut-être pas. Pour tout cela, je souhaite remercier Janine, Natalia, Patrick ainsi que les rapporteurs, Daniel et

Serge avec lesquels il aura été un plaisir d'échanger avant et pendant la soutenance.

Certaines rencontres ayant initialement pour objet les histoires d'électrons uniques et de courants électriques quantiques ont été marquantes. Parfois pour moi, parfois pour les autres. Peut-être plus souvent pour les autres. Salutations à vous, Thierry, Jérôme et Thibaut. Plus au nord, à Paris, se trouve l'agence tout risque de la physique expérimentale des électrons uniques. Un grand merci à Gwendal pour son accueil toujours chaleureux, malgré ce que l'on pourra faire passer pour un choc culturel entre les parisiens et les gens des régions. Merci également au reste de l'équipe, Bernard, Jean-Marc, Erwann, Arthur, Rémi, Hugo et Manohar, ainsi qu'à Takis et à Christophe qui se sont parfois joints à nos discussions. Les passages à Paris étaient toujours un plaisir, malgré l'augmentation des actions UPSA qui en résultait généralement. Je voudrais également remercier Inès, à la fois pour sa vision originale du transport électronique et pour son partage de quelques pans de culture Soufi.

Une autre rencontre mémorable fut celle de Misha. J'ai découvert que j'aimais les discussions de physique animées. S'engueuler devant un tableau peut sembler un spectable un peu baroque, voire carrément comique. Je crois qu'en fait, à chaque fois que cela est arrivé, une idée est sortie de la discussion, de manière incroyablement rapide. J'ai également beaucoup apprécié nos échanges, plus calmes, au-delà de la physique.

Il est temps de revenir à Lyon. Le laboratoire de physique a été véritablement un endroit fantastique, notamment pour la liberté qu'il y règne. Pascal a été en partie responsable de cette liberté. Je suis certain qu'être mon directeur de thèse n'a pas dû être de tout repos. Ou, disons plutôt que cela a été riche en émotions. J'ai pu toutefois noter une certaine exagération dans les propos de Pascal, tout n'étant pas à prendre au pied de la lettre. Je l'ai souvent entendu dire que je lui aurais tout fait. Cela arrivait à chaque fois que j'inventais une solution nouvelle à un problème non existant jusqu'alors. Je pondererais cela par le fait que je n'ai jamais pu finir mon projet de réacteur fusée à base de péroxyde d'hydrogène. Le principal problème étant le manque d'équipements pour la purification de l'eau oxygénée, son bureau n'étant manifestement pas équipé pour. Cela viendra.

Pendant ces trois années de thèse, j'ai partagé un petit bureau sans prétention avec Alexandre. Je crois que nous nous accorderons pour dire que nous y avons ajouté notre touche personnelle, installé une certaine ambiance. Il faut dire qu'Alex a une capacité impressionnante à faire

bouger les choses. Cela s'est souvent traduit par l'invention de projets farfelus qu'il fallait absolument finir en des temps impossibles, mais parfois, par souci de simplicité sans doute, il faisait simplement bouger les murs de notre bureau. Je tiens d'ailleurs à remercier nos voisins de couloir, et l'ensemble de l'équipe théorie, pour son calme et sa patience.

Afin de garder un certain équilibre, il nous fallait quelqu'un de raisonnable, quelqu'un qui a les pieds sur Terre, quelqu'un de posé. Clément était parfait dans ce rôle. Je ne pense pas trop m'avancer en disant qu'il en a probablement vu de toutes les couleurs, si ce n'est l'ensemble du spectre électromagnétique, pendant le temps que nous avons passés ensemble. J'ose croire néanmoins qu'il s'est amusé autant que moi.

Parmi les gens qui sont passés au laboratoire, je ne suis pas le seul à avoir éprouvé la joie de travailler avec Pascal, joie parfois accompagnée d'un certain désarroi. Je pense notamment à Arnaud et à Charles, qui ont pu découvrir l'animation que notre petit groupe pouvait causer une fois réuni dans un même bureau. Ils n'ont cependant pas trop eu à subir les discussions de physique, contrairement à Étienne, Dario, Manu et Raphaël. Parmi ces derniers, Manu a eu le mérite de me supporter lors de son stage, ce qui a visiblement eu pour conséquence de l'éloigner durablement de la physique théorique.

Outre la liberté, l'autre élément que j'ai apprécié au laboratoire de physique a été la diversité thématique. Ainsi, si vous en avez marre des théoriciens extravagants, il est toujours possible de faire quelques mètres pour retrouver un pragmatisme relatif avec les gens qui étudient la physique des choses qui se voient. Je me suis quelque peu éternisé au café avec, entre autre, Marius, Sylvain, Éric, Stéphane, Sébastien et Caroline. Je les remercie d'avoir gardé ma productivité raisonnable, et je pense que Pascal les remercie de m'avoir gardé tout court. Je remercie également Thierry, pour ses bons mots ainsi que pour l'entrain qu'il communique au laboratoire. Par ailleurs, je serais bien mal placé pour avoir quoi que ce soit contre l'extravagance des théoriciens. Je me suis beaucoup amusé avec Michel, sans doute l'un des plus extravagants qu'il m'ait été donné de croiser. Il est en effet rare de pouvoir discuter d'idées complètement absurdes de manière extrêmement sérieuse. Je tiens également à remercier Pierre, pour sa gentillesse ainsi que Marc, pour sa gestion de la dame de l'accueil à un moment critique. J'espère également que Jean-Michel ne nous en voudra pas trop pour l'épisode de désinsectisation que nous avons déclenché.

Un temps important est celui du repas. Notre petit groupe de théoriciens les partageait en général avec Guilhem, Grimaud et plus récemment Félix. Cette diversité thématique amenait en général des discussions philosophiques de haute volée. En vérité, vous ne voulez pas connaître les détails. Toujours est-il que j'ai passé du bon temps grâce à eux également.

Il est temps que ces remerciements s'achèvent, afin de laisser place aux électrons. Je n'ai néanmoins pas encore mentionné les véritables héros. Mes parents, Irène, Jean, ont un énorme mérite. Ils m'ont supporté, à temps plein, durant de longues années, et je ne crois pas que cela aura toujours été facile. Je ne pourrai jamais les remercier assez, pour la créativité qu'ils m'ont laissé développer, ainsi que l'inspiration qu'ils m'auront donnée. Je dois aussi remercier Bryan, mais surtout Vincent, que j'aurai fait souffrir jusqu'au bout de ce manuscrit. Il y avait en effet assez peu de gens désireux de relire quelques centaines de page d'anglais durant un week-end. Fort heureusement la fin de ce manuscrit n'a pas marqué la fin des souffrances, et il nous reste, je l'espère, des tas de choses à faire.

Cette fois-ci, j'ai véritablement fini. Laissons donc place à la physique quantique, aux électrons, etc.

Contents

Introduction **13**

1 Electron quantum optics **21**
1.1 Scientific context and motivation 21
1.2 Building blocks of electron quantum optics 26
1.2.1 Transmission channels 26
1.2.2 Electronic beamsplitter 29
1.2.3 Sources 30
1.2.4 Probes 33
1.3 Quantum optics formalism 35
1.3.1 Coherences in photon quantum optics 35
1.3.2 Coherences in electron quantum optics 39
1.4 First-order electronic coherence 42
1.4.1 Definition and basic properties 42
1.4.2 Wick's theorem 45
1.4.3 Representations of the first-order coherence 45
1.4.4 Simple examples 52
1.5 Second-order electronic coherence 69
1.5.1 Definition, basic properties and physical interpretation 70
1.5.2 Intrinsic two-electron coherence 72
1.5.3 Representations of two-electron coherence 72
1.5.4 Relation to current noise 77
1.6 Measuring electronic coherences 79
1.6.1 Tomography from single-particle interferometry . . 79
1.6.2 Single-electron tomography from two-particle interferometry 82
1.6.3 Probing two-electron coherence through two-particle interferometry 91

1.7 Summary 92

2 Signal processing for electron coherence 95
2.1 Introduction 95
2.2 Arithmetics of single-electron coherence 96
2.2.1 Basic building blocks 96
2.2.2 Electron and hole trains 100
2.3 The Floquet–Bloch spectrum 103
2.3.1 Single-electron coherence as an operator 104
2.3.2 The Floquet–Bloch theorem 105
2.3.3 Eigenvalue equations 106
2.3.4 Physical interpretation 106
2.3.5 Hole excitations and electron/hole coherences . . . 107
2.4 Electronic atoms of signal 109
2.4.1 Floquet–Wannier functions 109
2.4.2 Floquet–Wannier function ambiguities 110
2.4.3 Minimal-spreading principle 112
2.4.4 Coherences between Floquet–Wannier states . . . 114
2.4.5 Relation to experimentally relevant quantities . . . 118
2.5 Electron/hole entanglement 120
2.5.1 Floquet–Bloch parametrization of the many-body state 121
2.5.2 Electron/hole entanglement entropy 126
2.6 Electron-source diagnostic 127
2.6.1 The mesoscopic capacitor 127
2.6.2 Square drive 128
2.6.3 Sinusoidal drive 133
2.6.4 Lorentzian pulse trains 141
2.7 A quantum electrical current analyzer 147
2.7.1 Quantum tomography 147
2.7.2 Signal processing of the experimental $\Delta\mathcal{G}_S^{(e)}$ 152
2.8 Summary 154

3 Electrons, plasmons and photons 157
3.1 Introduction 157
3.2 Electrons and plasmons 158
3.2.1 From electrons to plasmons 158
3.2.2 From plasmons to electrons 159
3.2.3 Single-electron states as Schrödinger cats 162
3.3 Quantum optics of current noise 163

3.3.1 Plasmons and photons 164
3.3.2 Plasmon fluctuations from current noise 167
3.3.3 Accessing $W_{\Delta S_i}$ through homodyne measurements 169
3.3.4 Single-particle states in electron and plasmon quantum optics 174
3.4 Interactions and plasmon scattering 177
3.4.1 General method 179
3.4.2 The $\nu = 1$ case 181
3.4.3 The $\nu = 2$ case 182
3.4.4 The $\nu = 2$ case with a loop 185
3.5 Electronic decoherence 186
3.5.1 General results 187
3.5.2 Computing single-electron coherences 188
3.5.3 Many-body decoherence 191
3.5.4 Experimental test 197
3.6 On-going works and perspectives 203
3.6.1 The $\nu = 1$ case 203
3.6.2 Decoherence control 204
3.6.3 The delocalized electron 205
3.6.4 Perspectives 206

4 Energy flows in quantum mesoscopic system 207
4.1 Motivation and scientific context 207
4.2 Path integral approach 210
4.2.1 Variations on Feynman path integrals 210
4.2.2 Energy flows and Feynman path integral 217
4.3 Energy flows in electronic systems 224
4.3.1 One-dimensional non-relativistic free fermions . . . 226
4.3.2 Chiral fermions: expansion near k_F 227
4.3.3 Energy current, electronic coherences and edge magnetoplasmons 228
4.4 Joule heating in quantum conductors 230
4.4.1 Scattering theory approach to the Joule heating . 232
4.4.2 Joule heating from current pulses 238
4.4.3 Joule heating from single-electron excitations . . . 244
4.4.4 And next... 247

5 Conclusion and perspectives **251**
5.1 General conclusions 251
5.2 Perspectives 252
5.2.1 Applications of electron quantum optics 253
5.2.2 Plasmon quantum optics 255
5.2.3 Signal processing in electron quantum optics . . . 255
5.2.4 Heat transport and quantum thermodynamics . . 257

A Conventions **259**
A.1 Wavepacket 259
A.2 Fermionic operators 259
A.3 Single electron coherence operator 260

B Some remarks on Levitons **261**
B.1 Classically driven two-electron excitations 261
B.1.1 $n = 2$ case 263
B.2 Wavefunction of a Leviton train 264
B.2.1 Other Wannier functions for a Leviton train 266
B.2.2 Minimally-spread Levitonoids 266

C Splitting unitary matrices **269**

D An effective long range model for $\nu = 1$ **273**

E Technical stuff for path integrals **277**
E.1 Path integral for open quantum system 277
E.2 Harmonic bath linearly coupled to the system 278
E.3 Two trajectories, single-mode environment 280
E.3.1 Classical couple of trajectories 280
E.3.2 Quantum trajectories 282

Bibliography **283**

Introduction

It is hard to imagine our world as it is today without the advent of quantum mechanics. Since its discovery, quantum mechanics has made its way into almost all everyday technologies. Lasers, computers, camera sensors and solar cells, to give a few examples, were enabled by our understanding of the quantum laws of Nature. These technologies are all children of the so-called "first quantum revolution" that followed the unraveling of quantum mechanics. However, they didn't make use of the full power of quantum physics. They are mainly based on the particle/wave duality at the single-particle level which is far narrower than the full promises of quantum physics. As we build more precise, faster devices, we hit limits in measurement precision due to quantum mechanics, the so-called standard quantum limit. At the same time, simulating quantum systems with classical computers is an extraordinary challenge when considering systems involving hundreds of particles.

All these considerations initiated a new trend at the end of the 20th century, in which we try to harness quantum mechanics at the fundamental level and to its full extent, to circumvent the limitations of first quantum revolution technologies. This marks the "second quantum revolution" [Dowling and Milburn, 2003] which combines both technological developments, the emergence of new fields such as quantum information and communication and, in my opinion, a deeper understanding of quantum mechanics. The common characteristic of these new quantum technologies is that they actively use the full realm of quantum states, especially the ones that cannot be interpreted in classical terms, such as squeezed or entangled states. This encompasses the fields of quantum simulation [Feynman, 1982] but also of quantum computation, quantum sensing and quantum metrology. A recent example of these new quantum technologies is the use of squeezed light to increase the sensitivity of the LIGO interferometers [Aasi et al., 2013].

These technologies require mastering generation, manipulation as

well as characterization of quantum states. The latter task, often called quantum tomography is indeed difficult to achieve, because information carried by quantum states is very peculiar. In a way, it is robust since it cannot be erased [Pati and Braunstein, 2000], but it is also very fragile because it cannot be cloned [Wootters and Zurek, 1982]. As a consequence, it can only be retrieved through statistics performed on a large number of realizations of the quantum state. Moreover, in many experiments, the system is not observed directly but through the imprints it leaves within its environment, which can be for example a propagating electromagnetic mode in a circuit QED experiment [Wallraff et al., 2004; Bianchetti et al., 2009] or a stream of atoms flying across a cavity in atomic physics experiments performed by Guerlin et al. [2007]. This immediately raises the question of the recovery of the information carried by quantum states from measurements.

This very broad question has been studied for a long time [Breuer and Petruccione, 2007; Wiseman, 2014; Haroche and Raimond, 2006]. But it finds a new echo in the development of multimode quantum optics and, as I will explain, quantum coherent nanoelectronics. The progress of quantum communication, and more generally of quantum information processing as well as advanced sensing technologies, brings the necessity to be able to process signals that carry quantum information instead of classical information as it was common in technological devices born from the first quantum revolution. The evolution of electronics, radar and telecommunication technologies have catalyzed the development of classical information theory [Shannon and Weaver, 1975] as well as of signal processing. In its broadest acceptance, signal processing is an enabling technology that aims at processing, transferring and retrieving information carried in various physical formats called "signals" [Moura, 2009]. Signal processing involves a huge arsenal of techniques to detect, filter, represent, transmit, and finally extract information or recognize patterns within signals.

I think that quantum technologies require the development of a new type of signal processing, that is quantum signal processing directly operating on quantum signals themselves. This thesis will indeed deal with these questions: what are quantum signals? How to access and process quantum signals to extract significant information from them?

These questions are at the heart of the field of multimode photon quantum optics. It is now possible to generate multimode quantum states, featuring entanglement, in a rather controlled way. Yet, the

characterization of photonic beams and more generally of quantum particle beams, is a hard task. Of course, in general it is not possible to perform a full reconstruction of the quantum many-body state because the Hilbert space is too large. The solution is then to study partial indicators suitable for the considered problem that will give relevant information about the quantum properties of the beam. In the same way, and this is how the general idea of this thesis emerged, the development of quantum coherent nanoelectronics gives rise to a very similar question: *how can we characterize a quantum electrical current?*

This question is indeed a very natural one to ask in electron quantum optics [Bocquillon et al., 2014], an emerging field that aims at generating, manipulating and characterizing the elementary excitations of the electronic fluid in ballistic conductors using, in particular, single- to few-electron sources. Electron quantum optics has a strong relevance for condensed-matter physics since it enables us to realize gedanken experiments such as probing the fate of a single-electron excitation in a quantum conductor under the influence of Coulomb interactions [Marguerite et al., 2016b]. There is hope that it may provide new probes for strongly-correlated phases such as fractional quantum Hall fluids or superconductors and for the edge channels of topological insulators as reviewed in [Ferraro et al., 2017].

Nevertheless, I have given this thesis a different perspective more connected to quantum information, a topic of strong interest for me. My discussion of electron quantum optics will therefore be focused on the different ways we can obtain and process knowledge about the state of the electron fluid propagating within ballistic quantum conductors, with a specific focus on quantum Hall edge channels.

There are several roads towards analyzing a quantum electrical current or a quantum light beam. Historically, the first one is to probe the beam at the level of one mode, then two, etc. This is achieved through the concept of quantum coherence introduced by Glauber [1963b]. There is a whole hierarchy of coherences, each one giving all the possible correlations between the number of particles in a given number of modes. We will follow this road in the first two chapters of this thesis, focusing on the first members of this hierarchy in electron quantum optics.

In chapter 1, I will present the domain of electron quantum optics by insisting on the comparison with optics. After introducing experimental elements, I will describe the main theoretical tools we will use throughout this manuscript, replacing them within a global perspective

common to optics. I will then focus on first-order coherences, containing single-particle physics as well as second-order coherences that contain two-particle physics and as such, Fermi statistics and two-particle entanglement. I will then introduce recent experimental results on the tomography of single-electron coherence. For this part, most of the theoretical framework was laid down by my predecessors [Grenier, 2011; Thibierge, 2015]. However, I think the presentation is quite new and original and paves the way to the work described in the next chapters. It also delivers two important messages for the quantum signal perspective discussed in this introduction and which we have elaborated in [Roussel et al., 2017].

The first message is that quantum optics coherences and their extensions (amplitude and pair amplitude) are the quantum signals of interest and can be accessed through quantum interference experiments in electron quantum optics. The second message is that quantum interferometers are nothing but on-chip analog quantum signal processors. They realize simple transforms on quantum signals (such as "linear filtering" or "overlaps"), encoding them into experimentally accessible quantities such as average current or low-frequency noise. This gives more substance to Landauer's aphorism: *The noise is the signal* [Landauer, 1998].

Quantum signals being quantum objects defined from a set of indistinguishable particles or from a quantum field, it would be highly desirable to represent them in a simple intuitive way. In chapter 2, I will introduce a new representation of first-order electron coherence in terms of elementary electronic wavefunctions [Roussel et al.], which is directly inspired by a discussion of photonic modes propagating along a transmission line in Devoret's lectures at Collège de France [Devoret, 2008]. This kind of decomposition has been done recently in [Vanević et al., 2007, 2016, 2017] in the specific case of a classical current but so far, this pioneering work was not developed within the general framework of electron quantum optics and in the perspective of quantum signal processing.

My contribution, which will be detailed in a specific paper under completion, has been to invent and implement a general signal-processing technique for analyzing any time-periodic single-electron coherence, allowing to perform an autopsy of any time-periodic quantum electrical current at the single-particle level, without any extra hypothesis. I will show how, within the framework of Floquet theory, this method can be used to assess quality of single-electron sources and to extract re-

alistic single-electron wavefunctions for decoherence studies. Finally I will present our joint work with G. Fève's team [Marguerite et al., 2017] which consists in the demonstration of a quantum current analyzer extracting from the first time single-electron wavefunctions present within a quantum electrical current, their emission probabilities and their coherence properties.

As will be clear to all experimentalists working on electron quantum optics, probing second-order electronic coherence already represents a formidable challenge. This motivates us to explore the second road for quantum signal processing of quantum electrical currents.

The idea is to look for quantities that gather information about higher-order coherences and/or multimode quantum correlations in a nutshell. The coherences properties of the electromagnetic radiation emitted by a quantum electrical current provide a first step in this direction. Another more exploratory possibility is to look at the statistical properties of the heat dissipated by a quantum electrical current due to its coupling to environmental degrees of freedom.

This is why chapter 3 will be devoted to studying the influence of the coupling of a quantum electrical current to its environment, in particular electromagnetic. This will enable us to connect electron quantum optics to photon quantum optics through the radiation emitted by a quantum electrical current, a problem that has attracted a strong attention [Zakka-Bajjani et al., 2007, 2010; Grimsmo et al., 2015; Virally et al., 2016; Thibaut et al., 2015; Gasse et al., 2013; Forgues et al., 2014; Mendes and Mora, 2015; Hofheinz et al., 2011] in the mesoscopic physics community since the prediction that a quantum conductor would radiate a non-classical radiation by Beenakker and Schomerus [2001, 2004].

In quantum Hall edge channel, the possibility to describe the state of bosonic degrees of freedom that are charge density waves at the edge of the sample (also called edge magnetoplasmons) is crucial. This description called bosonization can be used to make bridges between electron quantum optics and microwave quantum optics. It also enables us to treat Coulomb interactions in a non-perturbative way. In chapter 3, I will introduce this technique and discuss the connection between electron and photon quantum optics. I will also discuss the problem of single-electron coherence which was my entry point in the field during my physics Master. At this time, together with C. Cabart, D. Ferraro and P. Degiovanni, we have computed the decoherence of an arbitrary single-electron excitation propagating along a quantum Hall edge channel. To

obtain explicit results, I have developed a code that is able to compute the post-interaction single-electron coherence for any input single-electron wavepacket propagating in an interacting region. This description is valid for any reasonable capacitive interaction model. In [Ferraro et al., 2014b], we have compared the death of Levitov and Landau quasiparticles and shed light on the role of many-body decoherence by making an analogy with decoherence observed in cavity QED experiments by Guerlin et al. [2007]. In parallel, Wahl et al. [2014] had developed another method to compute experimentally-relevant quantities at non-zero temperature, although their method is restricted to one interaction model. This led to a comparison between both theoretical methods and the experiment in [Marguerite et al., 2016b]. In chapter 3, I will also summarize all these works and give an insight on the further explorations led by C. Cabart in a paper also under completion, in which I participate. These explorations focus on the case of ideal $\nu = 1$ edge channels in which many-body decoherence is not present, and on decoherence control by a careful sample design.

Finally, in the last chapter, I will explore the second road to quantum signal analysis by considering energy transfers in quantum mesoscopic systems. Originally, this arose from my own interest for quantum thermodynamics. I am not sure to have fully understood what quantum thermodynamics is and even if it really makes sense but energy tranfers may provide a way to look at the many-body coherence properties of a quantum electrical current. In this last chapter, I will also present a framework based on Feynman path integral suitable for exploring quantum trajectories in full generality and more precisely the ones associated with a monitoring of heat transfer with a thermal reservoir. A scattering theory approach that allows us to bypass the explicit computation of Feynman path integral, will then be used to develop a theory of Joule heating by quantum electrical current. This work is still under development.

Last but not least, during my PhD, I was also interested in foundations of quantum physics and its relations to computation and information theory. I am sure that these questions have heavily influenced my questionings that led to my research, my approach to the problems and finally the present manuscript. I won't give too many details on these questions here but I would like to mention that this work, which has been done in collaboration with P. Degiovanni, N. Portier, C. Cabart and A. Feller will lead to a book [Degiovanni et al., shed], that should

be published in 2018. The goal of this book is to shed some light on the nature of the quantum theory using the teachings of the recent developements in quantum information theory, quantum computing and in the manipulation of single quantum systems. Can quantum theory provide a description of the whole physical world? And if yes, what would be the implications?

A central point in this book is the role played by entanglement in relating quantum mechanics to information theory and computational complexity theory. Developing decoherence theory and its extensions, we also discuss how the classical reality we are accustomed to can indeed emerge from a fully quantum universe. An even more striking consequence of quantum theory is that the quantum state of the system is not objective, but rather relative to the system, as originally stated by Everett [1957b,a], or more recently by Rovelli [1996] and by Auffèves and Grangier [2015]. This is probably, in a sense, the major rupture introduced by quantum theory, a point often overlooked in textbooks. Actually, this is quite natural since quantum theory encapsulates the fact that no information is accessible without any disturbance because, as Landauer would say, information can only be processed or transmitted through a physical process [Landauer, 1991, 1996]. The relative or relational nature of the quantum theory leads us to draw a parallel between general relativity, where space and time are relative to an observer and what is called space time is usually reconstructed from a computation as we are all used to with the GPS. We conclude by discussing some of the conceptual issues behind the marriage between quantum mechanics and general relativity.

Chapter 1

Electron quantum optics

1.1 Scientific context and motivation

Quantum transport is a central topic of mesoscopic physics that deals with electronic transport in a regime where the effects of quantum mechanics cannot be neglected. The semi-classical image mixing a Drude model of electronic transport supplemented by parameters such as effective masses or collision times deduced from quantum mechanics is no longer valid. In quantum transport, the wave nature of electrons cannot be ignored: transport is influenced by electronic phase coherence. This requires that the inelastic scattering length l_φ which characterizes the distance over which an electron can propagate without experiencing an inelastic collision and thus randomization of its phase, is of the order or larger than the sample size L. Quantum conductors became experimentally accessible in the 80s: the first evidence global phase coherence over a whole conductor came with the observation of permanent currents in normal metal rings [Sharvin and Sharvin, 1981; Webb et al., 1985] and of universal conductance fluctuations [Washburn et al., 1985].

Two regimes of coherent electronic transport are considered: the most common one, in which static impurities introduce elastic scattering over distances $l_e \ll L$ is called the diffusive transport and bears a strong analogy with wave propagation in disordered media [Montambaux, 2004]. This alters the electronic transport by introducing the so-called weak localization correction and universal fluctuations of the conductance.

The other regime is the ballistic transport regime in which the elastic scattering length is significantly larger than the sample size. Electrons then propagate within the quantum conductor as waves in a waveguide.

This has inspired R. Landauer [Landauer and Büttiker, 1985; Landauer, 1989] and then later M. Büttiker [Büttiker et al., 1985; Büttiker, 1986; Büttiker, 1990] and Th. Martin [Martin and Landauer, 1992], and many others to develop a scattering approach to quantum transport in which a quantum conductor is seen as a scatterer, thus already using a strong analogy with optics. In this paradigm, a quantum conductor appears as a linear optics element for quantum electronic waves.

Dealing with electronic waves instead of a particle flow implies that the usual impedance composition laws are expected to be violated: interference effects in non-simply connected quantum conductors break the conductance addition formula whereas the impedance addition breaks down since, almost by definition, it makes no sense to split a quantum conductor into two parts.

However, this is far from being the whole story. First of all, as M. Büttiker himself remarked, the scattering theory approach to electrical transport assumed that electron interactions could be neglected, a natural idea within the line of thought of the Landau–Fermi liquid theory [Pines and Nozières, 1966]. But this approximation breaks down when considering finite-frequency transport: Coulomb interactions must be taken into account to describe electrical transport. To describe quantum transport at finite frequency, Buttiker, Prêtre and Thomas [Büttiker et al., 1993; Prêtre et al., 1996] have developped a mean field theory approach in which the time-dependent flow of electrons generates a classical electrical field within the conductor which alters its scattering properties. At the microscopic level, during its propagation within a conductor, an electron interacts with the others through Coulomb interactions. This leads to the generation of electron/hole pairs from the Fermi sea. Using an analogy with optics, Coulomb interactions turn a quantum conductor into a non-linear optics element.

This image is still not the end of the story since electrons within a quantum conductor also interact with the electromagnetic environment of the conductor itself. One would naively think of the electromagnetic field in the surrounding space but the quantum conductor is always connected to reservoirs through leads and cables: the electromagnetic environment also includes the collective modes of the surrounding circuit. In Büttiker, Prêtre and Thomas's approach to high-frequency quantum transport, it was assumed that the electrons within the conductor just felt a modified potential landscape generated by the average electronic density within the conductor.

But under certain circumstances, this simple classical mean field image is not sufficient. One has to take into account the fact that the potential seen by electrons within the conductor comes from the coupling to the external environment of the conductor and therefore exhibits quantum fluctuations. Another way to present it consists in saying that individual passing of electrons within the conductor will alter its electromagnetic environment and this could be seen on quantum transport properties. This effect is called the dynamical Coulomb blockade [Devoret et al., 1990; Girvin et al., 1990]. Moreover, electronic transport across a quantum conductor leads to quantum radiation within its environment: this is the bright side of dynamical Coulomb blockade [Hofheinz et al., 2011].

Until a decade ago, quantum electronics relied on sources such as batteries, a.c. and advanced waveform generators, that send streams of electrons in which no quasi-particle could be singularized. Therefore, with such sources, even ballistic quantum transport is a complicated many-body problem from the start. Of course this has not prevented the mesoscopic physics community from getting quite a detailed understanding for it but at the price of a rather complicated formalism (see for example [Abrikosov et al., 1963; Caroli et al., 1971; Fisher and Lee, 1981; Meir and Wingreen, 1992]) and of overlooking the analogy with optics that we have stressed.

Things changed when technological progress made it possible to access the 1 GHz to 100 GHz frequency range in quantum transport experiments [Gabelli et al., 2006]. This allowed to probe the dynamical timescales of the quantum conductor itself such as the electronic ballistic time of flight across the conductor[1]. In 2007, a source able to inject coherent single-electron excitations within a quantum Hall edge channel was demonstrated [Fève et al., 2007]. This opened a new era for quantum electronics based on the study of quantum electrical currents carrying one to few electronic excitations per period.

The hope was then to study quantum transport using these sources exactly as in quantum optics experiments with single-photon sources. In this sense, this breakthrough shed a strong light on the analogy between quantum electronics and photon quantum optics.

Quantum optics is an old field started in the 60s that has reached a maturity level where it is now possible to generate, manipulate and probe states of the quantum electromagnetic field involving one to few

1. Typically of the order of tens to hundreds of pico-seconds for a micrometer-long ballistic conductor.

photons per mode or even spread over multiple modes. The degree of control reached in photon quantum optics, both in the microwave and in the optical domain makes photon quantum optics a very promising platform for exploring quantum phenomena [Haroche and Raimond, 2006]. Potential applications range from quantum computation [Knill et al., 2001], quantum communication [Reiserer and Rempe, 2015; Braunstein and van Loock, 2005; Scarani et al., 2009] to the quantum simulation of more complicated physical systems [Le Hur et al., 2016].

Since, at least in principle, electron quantum optics aims at reaching a high degree of control on the quantum states of the electron fluid in a quantum conductor, it is based on the same experimental tools and theoretical paradigms than photon quantum optics. The main objective of this chapter is to introduce them, starting from experimental tools such as electronic sources and interferometers, and then moving forward to the theoretical concepts inspired by quantum optics now used for studying electronic states and quantum transport. We will finally close this chapter by presenting various protocols for measuring single- and two-electron coherences. But before going into this, let us explain why, although these fields of quantum transport and photon quantum optics are to some extent unified by this approach, their respective goals are not the same as of today.

Photonic systems are by nature and construction very clean because photons do not interact with each other. Actually, they are so clean that the main difficulty is to make photons interact strongly enough through a clever use of light–matter interaction. On one hand, the cleanliness of photonic systems allows to transmit quantum states over hundreds of kilometers (see [Vallone et al., 2015; Yin et al., 2017] for spectacular examples), making photons a platform of choice for quantum information and communication protocols. On the other hand, the level of control on light–matter interaction is now so good that, in some system, it is possible to generate interesting collective photonic states [Hofheinz et al., 2009].

By comparison, electronic systems are much more messy as could be expected from our presentation of quantum transport. There are two major, fundamental differences between electron and photon quantum optics. First, electrons are fermions and not bosons. This difference in statistics is, per itself, quite drastic. It first implies that, given a set of modes, there are way much less accessible fermionic states than bosonic states. In particular, there is no direct counterpart of the classical

limit that leads to classical electromagnetism. Another consequence of Fermi statistics is that the ground state in a metal, the Fermi sea, is filled with a huge number of electrons, making it much richer than the photonic vacuum. The second difference is that electrons are charged, and interact through long-ranged Coulomb interaction. Combined with the fact that even in the ground state, an electron possesses a lot of peers to interact with, Coulomb interactions lead to a collective, strongly non-linear dynamics. Electronic propagation is strongly influenced by inelastic collisions which lead to strong electronic decoherence. To summarize this last difference in a language that may be familiar to opticians:

- In photon quantum optics, ballistic propagation and linear optics components are quite common. An experimental and/or engineering challenge in quantum state manipulation and control is to induce strong non-linearities.

- In electron quantum optics, Coulomb interactions turn most ballistic quantum conductors into non-linear optics components. Understanding and controling these non-linearities is both a challenge for further applications and basic condensed matter physics (electronic decoherence).

Therefore, in my opinion, although there were proposals in this direction [Bertoni et al., 2000; Ionicioiu et al., 2001; Ionicioiu, 2006; Bertoni, 2007; Zibold and Vogl, 2007], the main objective of electron quantum optics is, in the present state of technology, not to provide a reliable powerful platform for quantum computation or communication along these lines but to probe the complex, rich, many-body dynamics induced by Coulomb interactions, using elementary excitations so that we can gain an insight into the emergence of collective quantum correlations in the electronic fluid. An electrical engineer would say that electron quantum optics is a platform for exploring high-frequency electronic transport in its ultimate regime, that is to say at the single-electron level and when quantum mechanical effects are dominant. Last but not least, one should not conclude from my statement that the difficulties mentioned in this introduction do not imply that electron quantum optics is irrelevant for quantum technologies. I am indeed convinced of the opposite: even decoherence effects could be used for sensing applications, maybe quantum metrology and electron quantum optics may also be very relevant for building new photon sources and detectors in the microwave regime. And we should not close the door to unforeseen developments of

electron quantum optics systems in which electronic coherence would be preserved over a larger distance than in AsGa/AsGaAl quantum Hall systems.

1.2 Building blocks of electron quantum optics

1.2.1 Transmission channels

Quantum optics experiments rely on the fact that, during photon propagation, interaction with matter occurs in a very controlled way, through lenses and mirrors which have been specifically manufactured and within samples where light/matter interaction is probed. In a quantum transport language, quantum optics deals with ballistic photon propagation most of the time, except in specifically engineered devices. This explains why the concepts and paradigms of quantum optics find their best incarnation within ballistic quantum conductors. Only they provide a medium for electronic propagation minimizing unwanted scattering events.

A system of choice for this are 2D electron gases, in which electrons are confined in two dimensions where they can propagate almost freely. Such gases are commonly found in high-frequency transistors, found in microwave devices such as cell phones. They possess a high electronic mobility, implying a long elastic mean free path for electrons. In transistors, as well as in experiment involving quality 2D electron gas, the gas is formed at a 2D semiconductor heterojunction between AsGa and AsGaAl. At the interface, conduction and valence bands bending create a triangular well of potential where, provided the temperature is low enough, electrons are kept in the lowest energy level of the well, keeping them maximally confined in the direction perpendicular to the interface. Electrons come from donor atoms that are located 100 nm away from the electron gas and therefore, the resulting disordered potential is smoother than in a normal metal. This leads to high mobilities and, at cryogenic temperatures, electrons can travel more than 20 µm without experiencing any elastic collisions[2]. It turns out that scattering is mostly inelastic and comes at very low temperatures from electron/electron interactions.

The next requirement for electron quantum optics is the practical

2. The elastic mean free path l_e is related to the mobility of the 2DEG and to the electronic density: the conductivity is given by $\sigma = n_e e^2 \tau_e / m^* = n_e e \mu$ where m^* is the effective mass of conduction electrons and τ_e the elastic mean free time. This leads to $l_e = v_F \tau_e = m^* \mu v_F / e$. The Fermi velocity also depends on the density. Using $\mu = 100\,\mathrm{m^2\,V^{-1}\,s^{-1}}$ and $v_F = 10^6\,\mathrm{m/s}$ and $m^* = 0.067 m_e$, we obtain $l_e \simeq 40\,\mu\mathrm{m}$.

ability to conduct electrons from one point to another inside the gas along controlled optical paths. Quantum wires could be a solution but these are notoriously difficult to manufacture. A more practical solution comes from the use of edge channels in quantum Hall systems: at cryogenic temperatures, in the presence of a strong external perpendicular magnetic field (typically few teslas), the 2DEG enters the regime of integer quantum Hall effect [von Klitzing et al., 1980]. In this regime, the bulk is insulating and conduction is only possible along the edges of the sample. Furthermore, conductivity is quantized along these edges, by integer multiples of the inverse of von Klitzing resistance

$$R_K = \frac{h}{e^2} \approx 25.8\,\mathrm{k}\Omega. \tag{1.1}$$

The integer multiple corresponds to quantized electronic conduction channels at the edge of the samples, ν being the number of channels. The origin of conduction channels can be understood through fig. 1.1. Due to strong magnetic field $\mathbf{B}$, Landau levels appear and are filled up to the Fermi level which, in the quantum Hall regime, falls between two such levels. They are separated by synchrotron energy $e\,\|\mathbf{B}\|\,/m^*$. Spin degeneracy is lifted because of the magnetic field by Zeeman splitting. In the bulk of the sample, it requires a lot of energy to go from one filled Landau level to an empty one, making the bulk an insulator. At the edge, however, the confinement potential bends the energy levels which will then cross Fermi level and excitations can be created at a vanishing energy cost in the thermodynamic limit, thus making the edge conducting. The number of channels is equal to the number of levels that cross Fermi energy which is precisely the number of filled Landau levels. This number is lowered when the magnetic field, and thus the synchrotron energy, is raised. Disorder plays an essential role in the existence of stable plateaus in the magnetic field [Ando et al., 1982; Halperin, 1982]. At even higher magnetic fields, only the first Landau level is partly filled but due to Coulomb interactions, the electron fluid may enter another bulk-insulating phase: this is the fractional quantum Hall regime discovered by Tsui et al. [1982] (see [Stormer, 1999] for a nice review), a very interesting strongly correlated phase involving collective excitations with fractional charge and spin [Laughlin, 1983]. Despite the interest of this exotic phase, we shall only focus on the integer quantum Hall regime in this thesis.

As advocated by Büttiker [1988], quantum Hall edge channels play the role of electronic waveguides. They have several interesting properties.

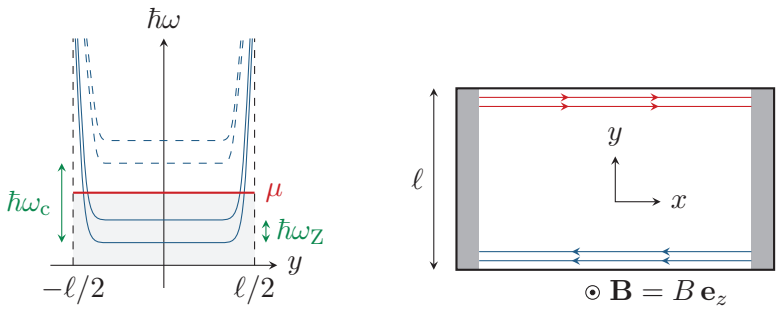

Figure 1.1: Origin of conduction channels. On the left, we can see the Landau levels. For each spin, they are separated by the cyclotron pulsation ω_c. The spin degeneracy is lifted because of the magnetic field, and initially degenerate Landau levels are separated in energy by the Zeeman energy $\hbar\omega_Z$. The levels are filled up to chemical potential μ. At the edge of the samples, the confinement potential bends the levels upwards. Whereas in the bulk, the conduction is prevented because of the energy gap, on the edge, we have a metallic behavior. On the right, we can see the edge channels inside the samples corresponding to the situation depicted on the left.

First, they are chiral which means that electronic excitations experience no backscattering. Second, the number of channels can be tuned by changing the external magnetic field, making it a platform of choice for exploring different situations. Third, for excitations nearby Fermi energy they possess linear dispersion relation, which emphasizes the analogy with photon propagation. In this thesis, we will focus on low-energy excitations, and thus always consider a linear dispersion relation. Finally, interchannel tunnelling of electrons happens only over large propagation lengths (typically several hundreds of micrometers) so that edge channels can, in a first approximation, be viewed as independent channels for electronic waves. To be more specific, since at $\nu = 2$, the two channels are spin polarized, inter-channel tunneling requires a spin flip which is a rare event by sample design. At $\nu = 3$, two channels will possess the same polarization but the Fermi velocity is not the same in these two channels [Kumada et al., 2011], preventing tunneling events from happening due to energy and momentum conservation.

The number of edge channels might seem a detail right now. But we will see in chapter 3 that it plays a crucial role in understanding Coulomb

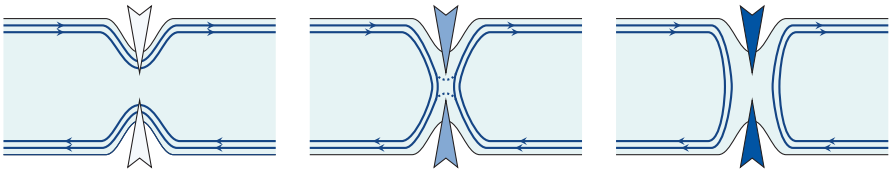

Figure 1.2: Quantum point contact. The quantum point contact is constituted of two top gates on top of the gas. By polarising the gates negatively, it is possible to go from a situation in which both channels goes across the QPC (on the left) to a situation in which both channels are reflected (on the right). By tuning the voltage, it is possible to find a regime in which the outer channel is partially reflected and partially transmitted, realising an electronic beamsplitter.

interaction effects on electrons.

1.2.2 Electronic beamsplitter

Using quantum Hall edge channels, electrons can be guided within the sample along optical paths which are defined through the engineering of the 2DEG edge. Interestingly there are two ways of doing this. The first one is by etching the sample, giving a definitive, static form to the edge by acting on the confinement potential. But it is also possible to deplete the gas without touching the sample, by adding a negatively charged top gate which will repel electrons locally. Its effect can be tuned by changing the negative d.c. voltage, allowing to shape the 2DEG at will.

This electrostatic repulsion effect is used to create a tunable electronic beamsplitter. The principle, depicted on fig. 1.2, is to partition the gas with a negatively charged top gate that will play the role of a "semi transparent mirror". Such a device is called a quantum point contact (QPC) [van Wees et al., 1988; van Houten et al., 1992; van Wees et al., 1991]. It is possible to change the potential of the gate from a situation in which edge channels follow the edge of the sample, to a situation in which they are completely reflected. In between, it is possible to tune the gate voltage so that electrons in the outer channel can either be totally reflected or transmitted by tunnelling. In this regime, it is possible to tune the transmission of the QPC by changing its potential.

The QPC is thus a crucial tool in electron quantum optics. It plays the role of an electronic beamsplitter and, as such, will be present in every electron quantum optics experiment. It is an essential element of

interferometers but also plays a key role in the source used by G. Fève at Laboratoire Pierre Aigrain.

1.2.3 Sources

To perform electron quantum optics experiments, we need sources that can emit simple and well-controlled electronic excitations. All sources used in experiments are periodic sources. The necessity to be above thermal noise imposes to go to gigahertz frequencies. A particularly interesting type of source are single-electron sources that emit exactly one electron, or exactly one electron and one hole excitation per period.

Classical driving

The simplest electronic source is, obviously, classical driving in which the electronic fluid is excited by means of a classical voltage generator. Such sources require a connection between the electron gas and the coaxial cable powered by a classical voltage generator.

A first possibility is to build an Ohmic contact directly into the sample. The Ohmic contact is a bulk of metal in contact with the edge channel. The proximity between the edge channel and the contact makes them strongly coupled, both by capacitive and tunnelling effects. An Ohmic contact will thus impose its potential to outgoing electrons and even add a d.c. part. In the absence of any a.c. excitation applied to it, the Ohmic contact generates an equilibrium distribution function at its chemical potential and temperature.

A second possibility is to connect the classical generator to a top gate, thus creating a capacitive coupling between the generator and the 2DEG [Misiorny et al., 2017]. An important difference with the Ohmic contact is that it is only possible to transfer a.c. excitations: no electron tunneling is allowed between the coaxial cable and the 2DEG. Moreover, depending on the geometry, the frequency dependence of the response of the fluid can be quite complicated [Grenier, 2011]. Nonetheless, if the generator sends a single-tone voltage, the Ohmic contact and the top gate will excite the fluid in the same way, up to a renormalization of the voltage amplitude.

Leviton source

In general, a classical drive generates a continuous stream of excitations which are electron/hole pairs and their number has fluctuations. Generi-

cally, it cannot be a good single-electron source.

However, such a source is very flexible: provided that one possesses a waveform generator, it is possible to generate a lot of different and interesting electronic states [Gabelli and Reulet, 2012]. Remarkably, among all of them, one leads to a stream of single-electron excitations on top of the Fermi sea as predicted by Levitov et al. [1996]. This is obtained by driving with a Lorentzian current pulse of duration τ_0 and total charge $q = -e$ such as the average current $V_{\rm d}(t)/R_K$ is given by

$$i(t) = \frac{q}{\pi\tau_0}\frac{1}{1+(t/\tau_0)^2}. \tag{1.2}$$

When applying a drive with $q = -ne$, one obtains an excitation called a Levitov quasiparticle of charge $-ne$, or n-Leviton. It is also possible to have a positive charge $q = ne$, and in this case, the resulting excitation is an excitation of charge ne, that we will call here a n-anti-Leviton. Remarkably, the n-Leviton is a collective excitation obtained by adding $n > 0$ electrons in a Slater determinant on top of the Fermi sea [Keeling et al., 2006; Grenier et al., 2013; Battista et al., 2014]. The n-anti-Leviton corresponds to the removal of a Slater determinant of n electrons below the Fermi level. These excitations are time localized around the center of the Lorentzian pulse. Their energy content is a decaying exponential: they are localized in energy space close to the Fermi level.

Even more interestingly, a sum of Lorentzian voltage pulses of charge e or $-e$ will always lead to a state solely composed of electrons and holes. This allows the creation of periodic sources based on Lorentzian current pulses which have been demonstrated by the group of D.C. Glattli in a 2DEG at zero magnetic field [Dubois et al., 2013b].

Landau quasi-particle source

Another source, that departs from classical current, is the one used by G. Fève at Laboratoire Pierre Aigrain [Fève et al., 2007]. Its interest is that it is able to emit excitations that are significantly away from the Fermi surface. In this respect, those excitations are called Landau quasi-particles in electron quantum optics.

To achieve this, we need a device that can raise the energy of electrons before sending them into the channel. This device is depicted in fig. 1.3. Its main component is a quantum dot, which is nothing more than an electronic cavity. Inside this dot, energy levels are discrete, separated by an energy gap Δ. On top of this dot there is a gate which is used,

by capacitive coupling, to shift the energy of the levels inside the dot. Of course, it is also necessary that the dot is somehow connected to the output channel. This connection is made through a quantum point contact with tunable transmission D.

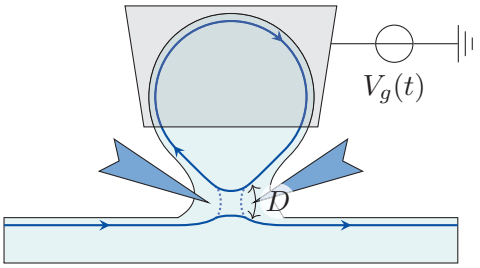

Figure 1.3: LPA source. This source is composed by an island (quantum dot) coupled to the 2DEG through a QPC. The driving is done through a gate on top of the dot.

The operating cycle is shown on fig. 1.4. The top gate, driven by a square voltage, is used to lower and raise the energy of electrons abruptly. This shifts a level initially below the Fermi surface and thus populated with an electron and brings it above the Fermi level. Then, this electron tunnels into the output channel, all other electrons being blocked by the Pauli principle. Once the electron has escaped, we can lower the dot energy levels. Then, an electron from the edge channel can fill this empty level, leading to an outgoing hole. When driven periodically, this device creates an elementary a.c. current where one electron is emitted during half a period and one hole is emitted for the next half period. Of course, this idealized vision works when the escape time $1/\gamma_e$ of the electron is shorter than the half period of the driving. This means that the dot must be open enough, so that the electron has time to fly into the channel. On the other hand, the more we open the dot, the wider the energy levels become. Since it is important to have only one energy level that goes fully above and below the Fermi surface, there is some optimal transmission coefficient and voltage amplitude at which we can do both for a given voltage. To summarize, we expect to recover this optimal regime when we have the following hierarchy for energies:

$$hf \ll \hbar\gamma_e \ll \Delta/2 \simeq eV. \tag{1.3}$$

In the case of a square driving, the current associated to a single electron decays exponentially after the beginning of the emission, because

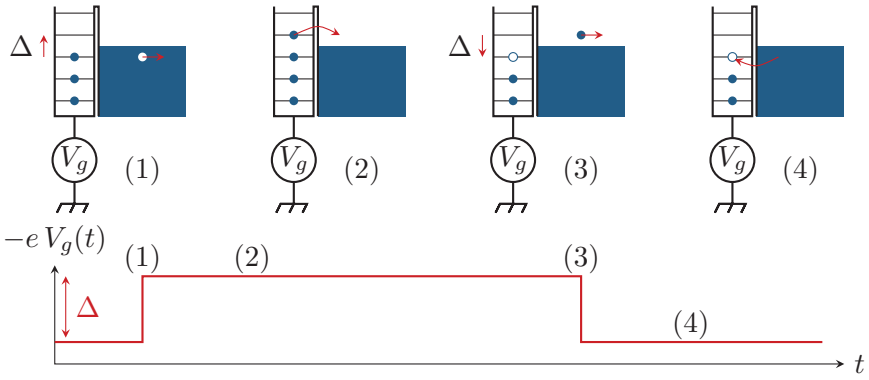

Figure 1.4: Operating cycle of the LPA source. By driving the top gate with a square signal, it is possible to achieve the following cycle. (1) The voltage is raised, promoting an electron inside the dot on top of the Fermi sea. (2) The electron escape by tunnel effect. (3) We lower the voltage, promoting a hole below the Fermi sea. (4) The hole escape by tunnel effect.

of tunnelling [Mahé et al., 2008]. Conversely, in energy, the excitation is localized around a chosen energy, with a Lorentzian distribution. By Heisenberg principle, the more energy-localized the particle is, the longer the escape time is.

This source is interesting also because it is quite flexible. It is possible to change the voltage and the transmission of the dot, depending on what is needed as we will see in chapter 2. First, it is possible to turn it into a classically driven source, by fully opening the dot. In this case, we are back to a capacitive coupling between the a.c. generator and the channel. It is also possible to go to a regime where the electron does not have enough time to escape and where we can expect strong electron/hole correlations. We can also change the shape of the driving voltage to output different wavefunctions in the single-electron regime.

1.2.4 Probes

Besides sources and optical components such as beam splitters, important components in quantum optics are detectors. In the optical domain, these are usually avalanche photodiodes which have a typical response time of a few picoseconds and which can be used to perform photocounting statistics with single-photon resolution.

In electron quantum optics, we are dealing with electrical signals in the low frequency or in the microwave range. Detectors thus belong to the field of electronics and radio-frequency technology. We thus have to explain how the relevant signals are collected from the electronic fluid into a microwave coaxial cable before they are amplified and processed.

Most frequently, to convert the electronic excitations into microwave radiations, an Ohmic contact is used. We expect it to be a perfect absorber which will probe the incoming current and convert it into voltage variations which can then be measured.

Timescales involved when considering single-electron emission (usually a few tens of picoseconds) are comparable to what is accessible with state of the art microwave equipment at the time of writing which can reach 30 ps using cryogenic amplifier with 15 GHz bandwith and a fast acquisition system. In optics, we deal with single photons arriving with repetition rates in the megahertz range which are detected with few picosecond resolutions. The real difference comes when considering the detection efficiency: whereas one-shot single-photon detections can be performed with relatively good efficiency, this is not, as of now, the case with single electrons.

Thus, the main challenge is to find low-frequency quantities that can nonetheless be used to characterize the electronic fluid. Through homodyning, one can access the average finite-frequency current. The low- and high-frequeny current-noise measurements have been performed without homodyning but using lock-in detection techniques, time averaging over long times around the measurement frequency and this is essential for getting a high sensitivity.

Noise measurements at gigahertz frequencies are far from being trivial to perform due to impedance mismatch between the quantum Hall resistance R_K and standard transmission line impedances ($50\,\Omega$) [Mahé et al., 2010]. A key point was to eliminate the noise of the amplifiers by using an interferometric system [Parmentier et al., 2011].

Tomography experiments which will be described in section 1.6 rely on low-frequency noise measurement which are performed on a high impedance to maximize the signal. These measurements are realized at megahertz frequencies thanks to a tank circuit to eliminate low-frequency parasitic noise [Freulon, 2014].

1.3 Quantum optics formalism

What we need on the theoretical side is to identify the correct quantities that characterize the many-body states of the electronic fluid. In many-body systems, it is usually impossible to access experimentally — and even to represent in simple terms — the full density operator of a many-body system, especially when interactions are present. This raises the question of finding experimentally-relevant quantities that could be accessed experimentally capturing partial physically-relevant information on the many-body state.

For the quantum electromagnetic field, apart from specific situations such as cavity QED where the full state of one to few electromagnetic modes can be characterized [Haroche and Raimond, 2006], such quantities are the quantum optics correlators introduced by Glauber, then completed by other correlators. They will be discussed in section 1.3.1.

For electronic systems, the analogous quantities are called electronic coherences. We will present their definition which is inspired from the analogous concepts of quantum optics in section 1.3.2. The rest of this chapter will be devoted to clarify what insight the electronic coherences give on the electronic many-body state and finally how they can be measured.

But in order to fully motivate the introduction of electron quantum optics concepts and before looking more precisely at single- and two-electron coherence, it is useful to make one step back and consider quantum optics as a whole, independently of the quantum statistics of the excitations considered. As we shall see, the quantum optics correlation functions provide a way to probe the physics of the system at the level of k modes. At the same time, one would like to introduce quantum information quantities in terms of elementary physical systems such as qubits or harmonic oscillators. This immediately raises the question of extracting quantum information quantities from the quantum optical description of the system. As we shall briefly explain, this relation is far from being trivial when the system involves fermionic excitations.

1.3.1 Coherences in photon quantum optics

For the quantum electromagnetic field, canonical quantization suggests to use the electric field operator $\mathbf{E}_\sigma(\mathbf{r}, t)$ that corresponds to the real amplitude of the electric field in the polarization σ. This quantum field operator can be decomposed into its positive and negative frequency

parts

$$\mathbf{E}_\sigma(\mathbf{r},t) = \mathbf{E}_\sigma^{(-)}(\mathbf{r},t) + \mathbf{E}_\sigma^{(+)}(\mathbf{r},t), \tag{1.4}$$

which respectively correspond to the creation and annihilation of a photon at position $\mathbf{r}$ and time t. From their definition, these operators are related by Hermitian conjugation:

$$\mathbf{E}_\sigma^{(-)}(\mathbf{r},t) = \mathbf{E}_\sigma^{(+)}(\mathbf{r},t)^\dagger. \tag{1.5}$$

Classical amplitude of the field

The average $\langle \mathbf{E}(\mathbf{r},t)\rangle_\rho$ represents the classical electric field associated with a given state ρ of the quantum electromagnetic field. This quantity, which is the real part of $\left\langle \mathbf{E}^{(+)}(\mathbf{r},t)\right\rangle_\rho$ is non vanishing for a large class of pure quantum states of the electromagnetic field and, in particular, for the coherent states of the quantum electromagnetic field introduced by Glauber [1963a]. These pure states are in one-to-one correspondence with the classical configurations of the quantum electromagnetic field. At a given time t, a coherent state is fully characterized by the average value of the quantum electromagnetic field $\langle \mathbf{E}(\mathbf{r})\rangle$ as a function of $\mathbf{r}$. In the presence of external classical currents, coherent states remain coherent and the corresponding $\left\langle \mathbf{E}^{(+)}(\mathbf{r},t)\right\rangle_\rho$ evolves according to Mawxell's equations in the presence of a classical current distribution.

Quantum fluctuations of the field

Contrary to what happens in classical electromagnetism, the state of the quantum electromagnetic field ρ is not fully determined by field average values. For example, Fock states have a vanishing average electric field and yet are different from the true vacuum. We thus have to account for quantum and statistical fluctuations of the electromagnetic field, the latter being present when ρ is not a projector on a pure quantum state. This suggests considering higher-order terms which are averages of products of the $\mathbf{E}_\sigma^{(+)}$ and $\mathbf{E}_\sigma^{(-)}$ fields at different positions and times. Such a description is, as we shall see, well adapted to experimental detection schemes available in the laboratory.

As a first step, we consider the fluctuations of the quantum electric field. They are described by two independent functions of two times and two positions (the other two being deduced from the hermiticity and the

commutation relations of the field):

$$\left\langle \mathbf{E}_\sigma^{(-)}(\mathbf{r}_2, t_2) \otimes \mathbf{E}_\sigma^{(+)}(\mathbf{r}_1, t_1) \right\rangle, \tag{1.6a}$$

$$\left\langle \mathbf{E}_\sigma^{(+)}(\mathbf{r}_1, t_1) \otimes \mathbf{E}_\sigma^{(+)}(\mathbf{r}_2, t_2) \right\rangle. \tag{1.6b}$$

First-order coherence The quantity eq. (1.6a) has been introduced by Glauber and is called the first-order coherence in quantum optics [Glauber, 1962, 1963b]. Denoted by $\mathcal{G}_\rho^{(1)}(\mathbf{r}_1, t_1|\mathbf{r}_2, t_2)$, it is directly related to photodetection theory. This can be understood at the intuitive level since we can rewrite

$$\mathcal{G}_\rho^{(1)}(\mathbf{r}_1, t_1|\mathbf{r}_2, t_2) = \mathrm{tr}\left(\mathbf{E}_\sigma^{(+)}(\mathbf{r}_1, t_1)\, \rho \mathbf{E}_\sigma^{(-)}(\mathbf{r}_2, t_2)\right). \tag{1.7}$$

Remembering that a density operator is a weighted sum of projection operators onto pure states, this rewriting shows that each pure state appearing in this expression of ρ has a photon destruction operator applied to it ($\mathbf{E}^{(+)}(\mathbf{r}_1, t_1)$ for the ket side and $\mathbf{E}^{(-)}(\mathbf{r}_2, t_2)$ for the bra side). This corresponds to the action of removing one photon from the quantum electromagnetic field, which is precisely what a photodetection does. A pedagogical and rather complete account for the theory of photodetection can be found in C. Cohen-Tannoudji's lectures at Collège de France [Cohen-Tannoudji] as well as in M. Fox's book [Fox, 2006], or for French readers, in É. Thibierge's thesis [Thibierge, 2015]. The main point is that the probability for a detector initialized in a stationary state to capture a single photon is, at short times, of the form

$$P_{[0,t]}^{(1\mathrm{ph})} = \int_0^t K_d(t_1 - t_2)\mathcal{G}^{(1)}(\mathbf{r}, t_1|\mathbf{r}, t_2)\, \mathrm{d}t_1 \mathrm{d}t_2, \tag{1.8}$$

where $K_d(t_1 - t_2)$ characterizes the detector: it depends on its state as well as on its physical characteristics (bandwidth, efficiency). In particular, when $K_d(\tau) \sim \delta(\tau)$, the detection is time resolved and we access the instantaneous light intensity which is proportional to $\langle \mathbf{E}^{(-)}(\mathbf{r}, t)\mathbf{E}^{(+)}(\mathbf{r}, t)\rangle$. On the other hand, when the detection is frequency resolved, $K_d(\tau) \sim \mathrm{e}^{\mathrm{i}\omega\tau}$, we directly access this quantity at a given ω: our detector measures the power spectrum of the radiation.

Pair amplitude The quantity (1.6b) is an indicator of squeezing. To keep the discussion simple, we shall consider here a single mode

of the quantum electromagnetic field, described by destruction and creation operators b and $b^\dagger$ satisfying the canonical commutation relations $[b, b^\dagger] = \mathbf{1}$. Up to constants which are not relevant to the point discussed here, $\mathbf{E}^{(+)}$ is to be assimilated to b and $\mathbf{E}^{(-)}$ to $b^\dagger$ so that the electric field $\mathbf{E}$ could, up to a constant, be identified with $X = (b + b^\dagger)/\sqrt{2}$.

We can now introduce $X_\theta = (\mathrm{e}^{\mathrm{i}\theta} b + \mathrm{e}^{-\mathrm{i}\theta} b^\dagger)/\sqrt{2}$ which is Hermitian. In the Fresnel plane defined by (X, P) where $P = \mathrm{i}(b^\dagger - b)/\sqrt{2}$, the observable X_θ corresponds to the coordinate along a rotated axis with angle θ with respect to X. Then, the quantum fluctuation of X_θ is

$$(\Delta X_\theta)^2 = \frac{1}{2}\left(\langle b\, b^\dagger + b^\dagger b\rangle\right) - |\langle b\rangle|^2 \tag{1.9a}$$

$$+ \frac{1}{2}\left(\mathrm{e}^{2\mathrm{i}\theta}\left[\langle b^2\rangle - \langle b\rangle^2\right] + \text{h.c.}\right). \tag{1.9b}$$

Around the point defined by $\langle b\rangle$ in the Fresnel plane, $\theta \mapsto (\Delta X_\theta)^2$ defines an ellipsoid describing the scale of the fluctuations of X_θ in direction θ (see fig. 1.5). The first line does not depend on θ and represent the isotropic part of these fluctuations. It is the difference between the average of the quantum energy of the mode and the classical energy which is the square modulus of the classical amplitude $\langle b\rangle$. The θ-dependence which describes the anisotropy of fluctuations is given by (1.9b). It is vanishing for coherent states since $\langle b^2\rangle = \langle b\rangle^2$ for them.

Many states exhibit anisotropic fluctuations. However, only some states with anisotropic fluctuations are truly interesting. They possess, for some values of θ, fluctuations of X_θ smaller than the vacuum fluctuations. Their potential for metrological applications had been realized very early [Walls, 1983; Caves, 1981] and they are on the point of being used in the future upgrades of interferometers for gravitational wave astronomy [Abadie et al., 2011]. These states are called squeezed states and for intuitively obvious reasons, cannot be obtained as statistical mixtures of coherent states and thus cannot be radiated by classical sources alone. In the optical domain, they have originally been produced using non linear optics processes [Xiao et al., 1987] and, in the microwave domain, they now are generated through the use of superconducting quantum amplifiers [Yurke, 1987; Castellanos-Beltran et al., 2008]. We will come back on the issue of squeezing in chapter 3 when discussing the properties of the radiation emitted by a quantum electrical current.

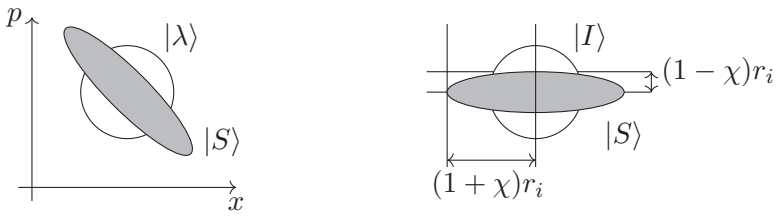

Figure 1.5: Left panel: ellipsoid of fluctuations for a squeezed state $|S\rangle$ around $\lambda = \langle b \rangle_{|S\rangle}$. In one of the directions, fluctuations are smaller than the ones of the vacuum (or of any coherent state). Right panel: definition of the anisotropy parameter from the ellipsoid of fluctuations. Starting from the ellipsoid, we build isotropic fluctuations r which span the same area in the Fresnel plane and define the anisotropy parameter χ as depicted.

1.3.2 Coherences in electron quantum optics

In electron quantum optics, the situation is quite different from the one in quantum optics. First of all, electrons are fermions. This implies that the space of possible quantum states for electrons is more limited than for bosonic particles because no more than one excitation can be present within each electronic mode. In electron quantum optics, the electronic field is described by $\psi(x,t)$ and $\psi^\dagger(x,t)$ which respectively annihilate and create an electron at position x and time t. At equal times, these operators obey canonical anticommutation relations:

$$\left\{\psi(x,t), \psi(x',t)\right\} = 0, \tag{1.10a}$$

$$\left\{\psi(x,t), \psi^\dagger(x',t)\right\} = \delta(x-x')\mathbf{1}. \tag{1.10b}$$

Note that in this thesis, we shall consider only one-dimensional chiral edge channels with a linear dispersion relation. In a region where interactions can be neglected, the time dependence of ψ and $\psi^\dagger$ is given by chiral propagation with a linear dispersion relation at the Fermi velocity v_F. In 1D systems, one usually focuses on effective long-wavelength fermionic fields, taking into account the Fermi momentum and energy dependence through a suitable prefactor (see section 4.3 for a detailed discussion).

Superselection rules

By analogy with photons, the first quantity we could think of is the "amplitude of the electronic field":

$$\langle \psi(x,t) \rangle_\rho \,. \tag{1.11}$$

This quantity is non-vanishing only in the presence of a quantum superposition between the presence and the absence of an electron. Since electrons are charged particles, it would be a quantum superposition of charge 0 and $-e$. However, such superpositions are never observed in a metallic conductor. Let us comment on this assertion starting from an empirical discussion of quantum electrical circuits.

A first idea to generate such a superposition would be to use the quantum delocalization of a single electron from one conductor to another to which it is connected via a tunnel junction. However, this would not lead to a superposition of states with different charge for the first conductor because tracing over the degrees of freedom of the other conductor would kill interferences between states of different charge. Interestingly, superconductors behave differently: when a small superconductor is connected to a large superconducting reservoir via a Josephson junction, it is possible to observe superposition of charges involving different numbers of Cooper pairs. This is due to the existence of a macroscopic BCS state which, in the thermodynamic limit, is characterized by a superconducting phase.

The general rule, common to superconductors and metal thus concerns parity: superpositions of states involving charges Q having different parities in units of e seem to be forbidden. Such a rule which restricts the physical states of a quantum system is called a superselection rule. In the present case, it is a parity superselection rule: states involving a superposition of electrons with different parities seem to be absent in the lab.

An important question is to determine whether such a superselection rule has a fundamental origin or arises dynamically. A superselection rule can emerge dynamically from decoherence through a mechanism called *einselection*, which means environmentally induced selection [Zurek, 1982]. In the case of charge degrees of freedom, superselection could arise from the electromagnetic degrees of freedom to which charge and currents are coupled: states with different charge may leave different imprints in their electromagnetic environment, thus suppressing effectively interferences between them. This example suggests that, by proper

shielding, the superselection rule could be bypassed. Nevertheless, the parity superselection rule that prevents any superposition of states with different parities for the number of electrons seems to be enforced. This suggests to look for a more fundamental origin of this superselection rule.

Historically, the term superselection rule was coined by Wick, Wight and Wigner in the old days of quantum field theory [Wick et al., 1952]. The parity superselection rule is deeply connected to the spin/statistics theorem which states that fermionic quantum fields have half-integer spin whereas bosonic fields have integer spins [Pauli, 1940]. If we require physical states to be exactly invariant under 2π rotations, then superpositions of states involving different parities for the number of excitations with respect to the vacuum are effectively forbidden. The point is that a 2π rotation would change the relative phase between odd and even number states by π. If the relative phase between the even- and odd-number components of the state could be accessed, which assumes that there exists a physical device able to probe it, then this would contradict the physical impossibility to distinguish a 2π rotation from doing nothing. Consequently, for the theory to be consistent with this fact, there must be no way to observe a quantum superposition between the even and odd sectors of the Hilbert space and thus, the parity superselection rule does apply.

This argument being based on the spin/statistics connection, it relies on Lorentz invariance and, as such, is relevant for justifying the parity superselection rules for fundamental fields. However, in condensed matter systems, we often work with effective fields that are not directly the microscopic fields describing all the electrons present in matter. A recent comment by Johansson [2016] on a paper by Friis [2016] presents an argument in favor of the parity superselection rule that appeals to no-signaling instead of Lorentz invariance.

The bottom line of this discussion is the full relevance of the parity superselection rule. An important consequence is the vanishing of the fermionic field average amplitude which is one of the reasons why one can experience difficulties when trying to define classical limits for electrons. It is not the only one: since it is not possible to put more than one electron into one mode, it is also not possible to have the counterpart of coherent states, which would be eigenvalues of $\psi(x,t)$. Thus it is not possible to build fermionic states with a large number of excitations compared to their quantum fluctuations.

The parity superselection rule does not only imply that $\langle\psi(x,t)\rangle_\rho = 0$

but also the vanishing of a whole bunch of higher-order quantities. Since in a metal, the superselection forbids any superposition between different charge sectors, even of the same parity, non-vanishing fermionic correlators must have equal numbers of creation and annihilation operators.

However, some of these correlators can still be non-zero in the presence of superconductivity since, in a macroscopic superconductor with well-defined superconducting phase, the number of Cooper pairs is not defined. In other words, the superconductor generates superpositions between charge sectors of the same parity. This way, it is possible to have a bigger phase space, allowing more superpositions. In such a situation, more correlators are needed to fully characterize the quantum state of the electromagnetic field. During my PhD, this possibility has been explored during R. Menu's M1 internship and the formalism will be developed in the forthcoming year. Instead of discussing this very interesting possibility, we shall now focus on the non-zero correlators present in a normal metal. These are the electronic version of Glauber's coherences.

1.4 First-order electronic coherence

1.4.1 Definition and basic properties

As we have seen, the superselection rules impose to look at higher-order functions in the field operators. We can form two functions that contain a balanced number of creation and annihilation operators, that are

$$\mathcal{G}^{(e)}_\rho(x_1,t_1;x_2,t_2) = \left\langle \psi^\dagger(x_2,t_2)\psi(x_1,t_1)\right\rangle_\rho , \tag{1.12}$$

$$\mathcal{G}^{(h)}_\rho(x_1,t_1;x_2,t_2) = \left\langle \psi(x_2,t_2)\psi^\dagger(x_1,t_1)\right\rangle_\rho . \tag{1.13}$$

In the following, we will call $\mathcal{G}^{(e)}$ the electron first-order coherence and $\mathcal{G}^{(h)}$ the hole first-order coherence, by analogy with Glauber denomination. When no superscript is indicated, it is usually that we can consider both electron and hole coherences.

It is easy to show that first-order coherences obey the following conjugation relation,

$$\mathcal{G}(x_1,t_1;x_2,t_2) = \mathcal{G}(x_2,t_2;x_1,t_1)^* . \tag{1.14}$$

As we will see later in this section, this relation ensures that the probability to find an electron in a particular wavefunction is real.

More interestingly, it is possible to relate electron coherence and hole coherence through anticommutation relation. Within a non interacting region,

$$\mathcal{G}^{(e)}(x_1,t_1;x_2,t_2)+\mathcal{G}^{(h)}(x_2,t_2;x_1,t_1)=\delta\left((x_1-v_Ft_1)-(x_2-v_Ft_2)\right). \tag{1.15}$$

Of course, this relation is true even in an interaction region if $t_1 = t_2$, since in this case it derives directly from canonical anticommutation relations. Usually, it is not possible to access the state of the electronic fluid in the full length of the edge channel. The detector is at a fixed, localized position in the edge channel. In this case, we have $x_1 = x_2 = x$, where x is the position of the detector. We will also assume that the detector is in a non-interacting region, enforcing the above relation between electron and hole first-order coherence. From now on, we will get rid of the position dependence and place ourself at the location of the detector.

We can now ask what kind of information is contained inside first-order coherence. Like in optics, it encodes all single-mode physics. But actually, since we have fermions here, there can only be at most one electron per mode. This is why first-order coherence contains the knowledge of every single-electron wavefunction. Before we proceed to the properties of electronic coherence and its representation, let us see with a simple example how the single-particle physics is represented through first-order coherence.

To this end, we consider N electrons in mutually orthogonal normalized wavefunctions $(\varphi_n)_{n\in\{1,\dots,N\}}$. The many-body state is then a pure state $|\Psi_N\rangle$ written in second quantization as:

$$|\Psi_N\rangle=\prod_{n=1}^{N}\psi^\dagger[\varphi_n]\,|0\rangle\,, \tag{1.16}$$

where $|0\rangle$ is the true particle vacuum and $\psi^\dagger[\varphi]$ creates an electron in the single-particle state given by φ:

$$\psi^\dagger[\varphi]=\int\varphi(t)\psi^\dagger(t)\,\mathrm{d}t. \tag{1.17}$$

Note that the electronic wavefunction is expressed in time. This is of course because of the linear dispersion relations. More formally, we define the wavefunction in time as $\varphi(t) = \phi(x - v_Ft)$, at a fixed point x,

where ϕ is the usual wavefunction expressed in position. The first-order coherence is the sum of the contribution of each electron:

$$\mathcal{G}^{(e)}_{|\Psi_N\rangle}(t_1,t_2)=\sum_{n=1}^{N}\varphi_n^*(t_2)\varphi_n(t_1). \tag{1.18}$$

Each term of the sum, $\varphi_n^*(t_2)\varphi_n(t_1)$ can be seen as the density matrix corresponding to the single-electron state in wavefunction φ_n, $\psi^\dagger[\varphi_n]\,|0\rangle$. As such, first-order coherence is sometimes called the one-body reduced density matrix. Its normalization is equal to the average number of particles in the system (which can be infinite). Of course, we might wonder if it is possible to access two-particle wavefunctions, and so on. That is exactly what is done with higher-order coherences as we shall see in section 1.5.

A natural question we can answer with first-order coherence is the probability to find an electron in a given wavefunction φ. The number of electrons in wavefunction φ is given by a

$$n[\varphi]=\psi^\dagger[\varphi]\psi[\varphi]. \tag{1.19}$$

It is naturally expressed in terms of first-order coherence (relation 1.14 ensuring the probability is real):

$$p[\varphi]=\langle n[\varphi]\rangle=\int\varphi^*(t_1)\varphi(t_2)\mathcal{G}^{(e)}(t_1,t_2)\,\mathrm{d}t_1\mathrm{d}t_2. \tag{1.20}$$

Usually, we are not looking at the absolute properties of the electronic fluid. We always probe the fluid with another one, which serves as a reference. Usually, the reference is an equilibrium state, namely a Fermi sea at a given chemical potential and temperature. What is accessed is the deviation of the probed fluid from the equilibrium one. It is thus useful to define the excess single-electron coherence[3]:

$$\Delta\mathcal{G}^{(e)}(t_1,t_2)=\mathcal{G}^{(e)}(t_1,t_2)-\mathcal{G}^{(e)}_{\mu,T_\mathrm{el}}(t_1,t_2), \tag{1.21}$$

where $\mathcal{G}^{(e)}_{\mu,T_\mathrm{el}}(t_1,t_2)$ is the first-order coherence of the Fermi sea with chemical potential μ and temperature T_el. If the system contains only one extra electron whose frequencies are well above thermal fluctuations, we have from (1.18)

$$\Delta\mathcal{G}^{(e)}(t_1,t_2)=\varphi^*(t_2)\varphi(t_1). \tag{1.22}$$

3. In [Haack et al., 2012], the excess single-electron coherence is called Glauber coherence for electrons.

Its normalization is equal to the average number of electrons added from the Fermi sea. If we denote N_e the average number of electrons above the Fermi sea and N_h the average number of holes in the Fermi sea, we have

$$v_F^2 \int \Delta\mathcal{G}^{(e)}(t_1, t_2)\, \mathrm{d}t_1 \mathrm{d}t_2 = N_e - N_h. \tag{1.23}$$

1.4.2 Wick's theorem

Before we go into the various ways to represent first-order coherence, let us have a look at cases where this quantity is sufficient to fully determine the state of the many-body system. Notably, this means that the higher-order correlation functions can be expressed in terms of single-electron coherence.

A wide class of states for which this is true are Gaussian states. Similarly to Gaussian statistics that can be described only by its first two moments, a full description of those states is given by first-order coherence, the second moment. Of course, equilibrium states are Gaussians, since they can be written as $\mathrm{e}^{-\beta H}/Z$, but they are not the only ones. In general, when considering non-interacting problems, electronic states stay Gaussians. This is notably the case when we apply Floquet theory, as well as when the electronic fluid is driven classically.

The way we can express higher-order correlation functions in terms of single-electron coherence in the Gaussian case, is through Wick's theorem. We can express every average of balanced product of ψ and $\psi^\dagger$, by summing over all the possible pairings between ψ and $\psi^\dagger$ operators, each ordered pair giving rise to a factor which contains exactly one ψ and one $\psi^\dagger$, and thus is either a single-electron or single-hole coherence. Fermionic statistics impose that a minus sign appear when the pairing requires an odd number of crossing. A reader more interested about Wick's theorem in electron quantum optics as well as its extension can read [Grenier, 2011].

1.4.3 Representations of the first-order coherence

Up to now, we have considered the expression of single-electron coherence in time domain. Here, we will discuss three different representations for the same object: the time-domain representation, the frequency-domain representation and finally a mixed time-frequency representation called the electronic Wigner distribution function [Ferraro et al., 2013]. This

is similar to the representations of a density operator, respectively in position space, in momentum space or in phase space.

Figure 1.6 presents these three representations for an electron emitted by the LPA source (see section 1.4.4, page 55). Time representation is pictured on the right, frequency representation on the left, and in the middle it is the Wigner function representation.

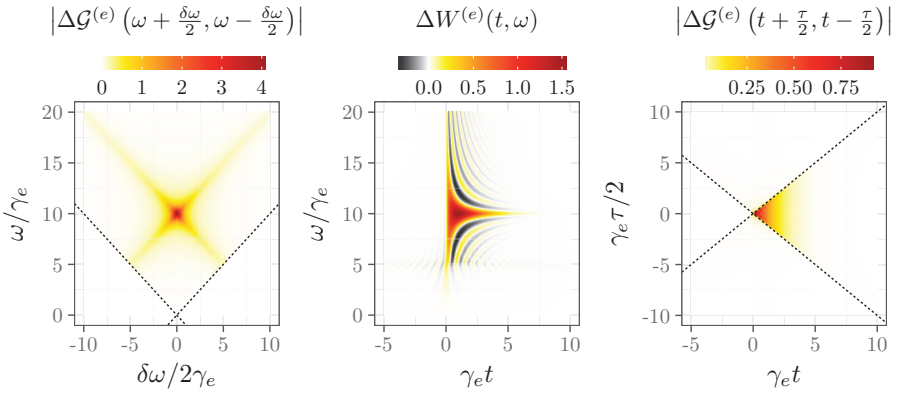

Figure 1.6: Representations of the coherence. Here is depicted a typical wavepacket emitted by the LPA single-electron source. On the left, we have the modulus of the energy representation. We can see that the excitation is only electronic since there is nothing outside $\omega_1, \omega_2 > 0$. On the right, we have the modulus of the time representation. We can see that the current is an exponential decay. On the middle, we have the Wigner representation. It is real and contains both positive and negative values. We can see both the energy dependence of the excitation (which populates only positive energies) and its time dependence (which is an exponential decay).

Time-domain representation

Let us first come back to the time-domain representation. The diagonal part defined by $t_1 = t_2$ of the single-electron coherence is proportional to the probability density of detecting an electron at a given time [Thibierge, 2015]. More directly, it is the average excess electronic density at detector's location. Within a region with chiral relativistic dispersion relation, it also gives the particle current

$$\langle i_e(t)\rangle = v_F \Delta\mathcal{G}^{(e)}(t,t). \tag{1.24}$$

However, this representation is not the most convenient for reading out the energy of particles since it is contained in the phase of the off-diagonal terms. This information is contained in the electronic occupation number and this leads us to introduce the frequency domain representation.

Frequency-domain representation

The frequency-domain representation is defined through a double Fourier transform:

$$\begin{aligned}\mathcal{G}^{(e)}(\omega_1,\omega_2) &= v_F^2 \int \mathcal{G}^{(e)}(t_1,t_2)\mathrm{e}^{\mathrm{i}(\omega_1 t_1-\omega_2 t_2)}\,\mathrm{d}t_1\mathrm{d}t_2 \\ &= \frac{2\pi}{v_F}\left\langle c^\dagger(\omega_2)c(\omega_1)\right\rangle,\end{aligned} \tag{1.25}$$

where we have introduced the annihilation operator $c(\omega)$ defined by

$$c(\omega) = \sqrt{\frac{v_F}{2\pi}}\int \psi(t)\mathrm{e}^{\mathrm{i}\omega t}\,\mathrm{d}t, \tag{1.26}$$

satisfying the anticommutation relations

$$\{c(\omega), c^\dagger(\omega')\} = \delta(\omega-\omega'). \tag{1.27}$$

The diagonal part $\mathcal{G}^{(e)}_{\rho,x}(\omega,\omega)$ gives a direct access to the electronic occupation number at position x. Besides, this representation is well adapted to discuss the nature of excitations. First of all, the notion of electron and hole are relative to a given chemical potential which fixes the position of the Fermi level at zero temperature. For the moment, let us put $\mu = 0$. We then divide the frequency plane (ω_1,ω_2) into four quadrants (see fig. 1.7). If both frequencies are positive, excitations are called electronic whereas when they are negative, we call them holes. Quadrants with ω_1 and ω_2 of opposite signs are called the electron/hole coherence quadrants.

Unfortunately this representation is not very practical if we are interested about time dependence of the excitations. It would be ideal to have a representation that allows us to easily view time and frequency dependence such as the Wigner representation.

Wigner representation

For now, we have just considered first-order coherence expressed in different bases. However, it is possible to have a mixed representation, analogous to the phase-space representation of density matrices introduced

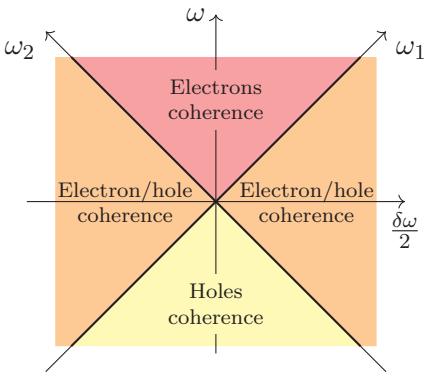

Figure 1.7: Frequency domain quadrants for single-electron coherence. The electronic quadrant defined by both ω_1 and ω_2 positive gives information about electronic excitations. The hole quadrant defined by both ω_1 and ω_2 being negative gives information about hole excitations. The two electron/hole quadrants ($\omega_1\omega_2 < 0$) contain information about electron/hole coherences.

by Wigner [1932]. Before introducing this concept in electron quantum optics, let us review the case of single-particle density matrices. The following discussion is inspired by [Ballentine, 2000; Le Bellac, 2003].

Classically, a state can be represented by a probability distribution over phase space. Namely, if we consider only a single-particle state, it is fully determined by the probability $p_{\mathrm{cl}}(x, p; t)$ to find the particle at x with momentum p, at time t. This probability distribution has the following properties:

1. It is non-negative, $p_{\mathrm{cl}}(x, p; t) \geq 0$.

2. Its marginals are the position and momentum probability distributions. We thus have $p_{\mathrm{cl}}(x; t) = \int p_{\mathrm{cl}}(x, p; t)\mathrm{d}p$ and $p_{\mathrm{cl}}(p; t) = \int p_{\mathrm{cl}}(x, p; t)\mathrm{d}x$.

3. It is normalized to unity, $\int p_{\mathrm{cl}}(x, p; t)\frac{\mathrm{d}x\mathrm{d}p}{2\pi\hbar} = 1$.

It is then natural to ask whether we can find such a probability distribution for quantum states. If we do not make other assumptions, it is possible to find an infinity of functions that satisfy those conditions [Cohen, 1986]. Which one shall we retain?

A mixed state described by a density operator ρ can always be decomposed in infinitely many ways as a statistical mixture of pure

states (which are not necessarily mutually orthogonal). Since all these decompositions can be seen as arising from projective measurements made on a purification of the density operator ρ [Haroche and Raimond, 2006], no-signaling imposes that it is not possible to distinguish among them by a measurement performed only on the system. It is thus natural to impose that the probability distribution does not depend on the way we decompose the mixed state over pure states. It turns out that if we impose this simple condition, no function can satisfy the three properties mentioned above [Wigner, 1997; Srinivas, 1982][4].

To circumvent this result, there are two possible approaches. The first one leads to the Wigner distribution. In this case, the marginals correspond to the expected probability density but the Wigner distribution can be negative, invalidating the interpretation as classical probability distribution. On the other hand, the Husimi Q function is non-negative and can be interpreted as a probability distribution in the coherent state basis. But its marginals do not correspond to the probabilities associated with a measurement of x or p [Husimi, 1940]. The Husimi Q function can be computed by smoothing out the Wigner distribution with a Gaussian filter corresponding to the Wigner function of the vacuum state. In what follows, we will concentrate on the property of Wigner distribution, since later we will define a time–frequency representation analogous to Wigner distribution.

The Wigner distribution is defined from the density operator ρ by

$$W_\rho(x,p) = \frac{1}{2\pi\hbar}\int \mathrm{e}^{-\mathrm{i}p\chi/\hbar}\rho\left(x+\chi/2, x-\chi/2\right)\mathrm{d}\chi. \tag{1.28}$$

As stated earlier, this function is real and its marginals correspond to probability distributions in x and p. More interestingly, it is possible to express the average value of an observable as the scalar product between a function that depends only on the observable and the Wigner distribution

$$\langle O\rangle_\rho = \int O(x,p)W_\rho(x,p)\,\mathrm{d}x\,\mathrm{d}p, \tag{1.29}$$

4. Quite amusingly, there is a connection between the difficulty of expressing quantum mechanics in phase space, and more fundamental questions about quantum theory. A first possibility for hidden-variable theories, would be to associate to a quantum state a distribution over phase space. However, given the previous considerations, a hidden variable theory would be quite strange, in the sense that characterizing the physical state of the system would require a lot more information than what is contained in its density operator. These considerations on foundations of quantum physics would be far away from the topic of the manuscript but will be expanded in our forthcoming book [Degiovanni et al., shed].

where $O(x,p)$ is the Wigner representation of the operator O, defined as

$$O(x,p) = \int \mathrm{e}^{-\mathrm{i}p\chi/\hbar} \langle x + \chi/2 \,|\, O \,|\, x - \chi/2 \rangle \,\mathrm{d}\chi. \tag{1.30}$$

This expression of the mean value of any operator as an "average" weighted by a real function of the state makes the Wigner function a quasiprobability distribution. This property is shared by Husimi Q function, but the expression of operators is somewhat more complicated than for Wigner distribution. As a side note, a state in Wigner representation can also be seen as a measurement operator, corresponding to the projector of the state (up to a factor h). If we consider a coherent state, it is a Gaussian filter that corresponds to the measurement of both quadratures, with symmetric, minimal uncertainty in x and p. It turns out that the projectors on all possible coherent states define a generalized measurement. Considering the probability of such detection for every possible coherent state parameter, we obtain the Husimi Q function, ensuring its probabilistic interpretation.

One might wonder whether states that possess a non-negative Wigner function have special properties. Actually, it has been shown that a pure state with positive Wigner function would necessarily have the form [Hudson, 1974]:

$$\psi(x) = \mathrm{e}^{-ax^2+bx+c}, \tag{1.31}$$

where a, b, c are complex numbers, with $\Re(a) > 0$. These include coherent states but also squeezed states which are non-classical Gaussian states. The negativity of Wigner function can thus be seen as a witness of non-classicality. A classical state will have a positive Wigner function, but the opposite is not necessarily true: there are non-classical states with positive Wigner function.

Let's go back to first-order coherence. We can introduce the Wigner representation [Ferraro et al., 2013]:

$$W^{(e)}_{\rho,x}(t,\omega) = v_F \int \mathcal{G}^{(e)}_{\rho,x}(t + \tau/2, t - \tau/2)\, \mathrm{e}^{\mathrm{i}\omega\tau} \,\mathrm{d}\tau. \tag{1.32}$$

First of all, this function is real but, as we will see later, can take positive or negative values. A second interesting feature is that both the average particle current and occupation number are obtained by integrating out

the corresponding variable:

$$\langle i_e(x,t)\rangle = \int \Delta W^{(e)}_{\rho,x}(t,\omega)\,\frac{\mathrm{d}\omega}{2\pi}, \tag{1.33}$$

$$\delta f_{e,x}(\omega) = \overline{\Delta W^{(e)}_{\rho,x}(t,\omega)}^{t}, \tag{1.34}$$

where $\delta f_{e,x}(\omega)$ is the average excess occupation number at frequency ω and position x, and $\overline{\cdots}^t$ denotes the average over time, which can either be a simple integration (in case of finite number of particles) or an average over the time period (in case of a periodic state). We warn the reader that in the first case, the quantity is a probability density, and has the dimension of a time. In the periodic case, it is a dimensionless quantity that corresponds to the number of excess particles at a given frequency.

Those properties, graphically represented on fig. 1.8 for one electron emitted by LPA single-electron source, are much alike those of Wigner distribution for density matrices. One major difference is that Wigner representation of the first-order coherence is not normalized, the normalization being the average total number of electrons present in the system (or the average excess number of electrons for excess coherence).

Classicality criterion In order to interpret Wigner function as a classical probability distribution, it is necessary that it is non negative. This fact can be used to define a notion of classicality for first-order coherence: Wigner functions for electrons and holes must be non negative. This can be summarized that a classical fermionic state satisfies the following constraint:

$$0 \leq W(t,\omega) \leq 1. \tag{1.35}$$

This notion of classicality is, as we will see later, a bit different from the one we have in optics. In optics, quasi-classical states are not the only ones to have a non-negative Wigner function, as stated earlier. However, they are the only ones that result from a classical driving under linear interactions. In electronics, the classical limit is not as well defined as in optics, because of Pauli exclusion principle. The main advantage of this definition is that it corresponds to what one would have in mind for an adiabatic driving. In this case, as we shall see in the next section, the Wigner function corresponds to a chemical potential that evolves along time.

However, it is possible to generate states that are highly non classical from this electronic point of view, just by driving classically the electronic

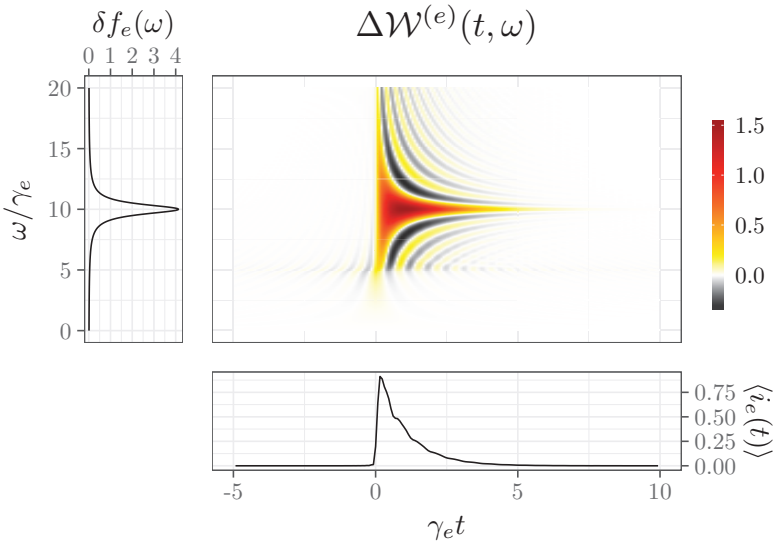

Figure 1.8: Wigner representation of the wavepacket emitted by the LPA source. The particle current is an exponential decay, and the excess energy distribution is a Lorentzian in energy. Wigner distribution possesses negativities and values above one, signature of a non-classical state in an electronic point of view.

fluid. As we will see in chapter 3, the notion of "classical driving" is a bosonic many-body notion, whereas the classicality introduced by the constraint on the Wigner function is a fermionic single-particle notion. Since the link between bosons and fermions is far from trivial, it is not shocking that there is a mismatch between those two notions of classicality. We will also see in next section cases of classical driving that lead to non-classical Wigner functions.

1.4.4 Simple examples

Let us now discuss some examples of first-order coherences for simple electronic states. We will mainly focus on the Wigner representation that will be used throughout the manuscript.

The Fermi sea

The equilibrium state of the metal is described by two parameters: chemical potential μ and temperature $T_{\rm el}$. The chemical potential represents just a global shift in energy. In the following, we will almost always use $\mu = 0$. The many-body state of the Fermi sea is usually described by $\rho = \exp(-\beta H)/Z$, Z being the partition function. It is also possible to write down a nice many-body expression by considering each independent mode at frequency ω:

$$\begin{aligned}\rho_{F,T_{\rm el}} = \bigotimes_{\omega\in\mathbb{R}} \Big(& (1 - f_{e,T_{\rm el}}(\omega)) \left|0_\omega\right\rangle \left\langle 0_\omega\right| \\ & + f_{e,T_{\rm el}}(\omega) c^\dagger(\omega) \left|0_\omega\right\rangle \left\langle 0_\omega\right| c(\omega) \Big).\end{aligned} \tag{1.36}$$

where $f_{e,T_{\rm el}}$ is the Fermi statistics at zero chemical potential and temperature $T_{\rm el}$. It corresponds to having each energy-resolved mode independently populated with a probability $f_{e,T_{\rm el}}(\omega) = 1/(\mathrm{e}^{\hbar\omega/k_B T_{\rm el}} + 1)$. It is really easy to compute first-order coherence in the energy representation.

$$\mathcal{G}^{(e)}_{F,T_{\rm el}}(\omega_1,\omega_2) = \frac{2\pi}{v_F}\delta(\omega_1-\omega_2) f_{e,T_{\rm el}}\left(\frac{\omega_1+\omega_2}{2}\right). \tag{1.37}$$

The δ distribution comes from the fact that, for any stationary single-electron coherence, there are no coherences between different energy modes. What remains is the electronic distribution function along the diagonal of the frequency plane.

In the time representation, single-electron coherence is equal to

$$\mathcal{G}^{(e)}_{F,T_{\rm el}}(t_1,t_2) = \frac{\mathrm{i}}{2\pi v_F \tau_{\rm th} \sinh\left((t_1-t_2)/\tau_{\rm th} + \mathrm{i}0^+\right)}, \tag{1.38}$$

where $\tau_{\rm th} = \hbar/\pi k_B T_{\rm el}$ is the thermal coherence time at temperature T. As expected for a stationary many-body state, single-electron coherence depends only on $t_1 - t_2$. Finally, the divergence at $t_1 = t_2$ comes from the infinite number of electrons in the Fermi sea[5]. At zero temperature, the above expression reduces to

$$\mathcal{G}^{(e)}_{F,T_{\rm el}=0}(t_1,t_2) = \frac{\mathrm{i}}{2\pi v_F}\frac{1}{t_1 - t_2 + \mathrm{i}0^+}. \tag{1.39}$$

5. Since we are considering a linear dispersion relation, we should rather speak about a Dirac sea here.

By stationarity, the Wigner representation does not depend on time and reduces to the electronic distribution function and thus shows no divergences:

$$W^{(e)}_{F,T_{\rm el}}(t,\omega) = f_{e,T_{\rm el}}(\omega). \tag{1.40}$$

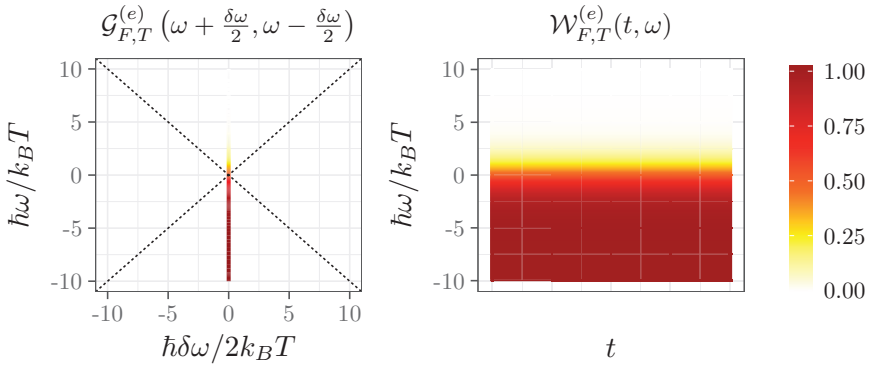

Figure 1.9: Frequency and Wigner representations of the Fermi sea first-order coherence. On the left, we have the frequency representation of the single-electron coherence for an equilibrium state at temperature T, in units of $2\pi/v_F$. Only the diagonal is non-zero, and follows a Fermi–Dirac distribution. On the right, we have the Wigner representation of the same state. This is a stationary state whose frequency content is given by the Fermi–Dirac distribution.

Single-excitation states

Now we will focus on the Wigner function generated by a single electron over the Fermi sea. We will review three families of wavefunctions that are relevant in electron quantum optics. For simplicity, all discussion will be done at zero temperature but the results remain valid as long as the wavepackets considered here are located further in energy from the Fermi sea than thermal fluctuations which deploy over $k_BT_{\rm el}$.

As we have already seen, when we emit a single electron above the Fermi sea, the excess coherence is the product $\varphi^*(t_2)\varphi(t_1)$. It is also possible to deplete the Fermi sea and create a hole excitation. The many-body state is thus given by

$$\rho = \psi[\varphi_h]\,\rho_{F,T_{\rm el}=0}\,\psi^\dagger[\varphi_h], \tag{1.41}$$

where φ_h is a hole wavefunction containing only negative frequencies. It is therefore straightforward to compute first-order coherence, since we just have to subtract the hole contribution from the Fermi sea

$$\mathcal{G}^{(e)}(t_1,t_2) = \mathcal{G}^{(e)}_{F,T_{\rm el}}(t_1,t_2) - \varphi_h^*(t_2)\varphi_h(t_1). \tag{1.42}$$

Turning a hole wavefunction from an electronic one and vice-versa is obtained by changing ω into $-\omega$. This corresponds to the following anti-unitary transformation on single-particle states:

$$\varphi_h(t) = \varphi_e^*(t) \tag{1.43}$$

or, in frequency space

$$\varphi_h(\omega) = \varphi_e^*(-\omega). \tag{1.44}$$

Before we go deeper in the examples, I must insist on one thing. In the case considered, a single electron emitted above the Fermi sea, $\Delta\mathcal{G}^{(e)}(t_1,t_2)$ is equal to the density matrix of this single electron alone, expressed in time. This equality implies that Wigner representation is the very same object as the usual Wigner distribution of quantum mechanics. *As such, it is a complete, faithful and convenient representation of the wavefunction.*

However, this correspondence is true only when there is a single particle added in the system. In other cases, when the source emits more than a single-electron excitation into the system, the single-electron coherence becomes a sum of each single-particle contribution. Retrieving the individual wavefunctions present within a given excess single-electron coherence is far from being a simple problem, as we will see in chapter 2. As stated before, compared to usual cases in optics, where the state of a single mode is manipulated, the case of electron quantum optics is a multimode problem from the very beginning due to fermionic statistics.

The Landau excitation First, let us start with the Landau excitation emitted by the LPA single-electron source (see section 1.2.3, page 31). This excitation is emitted at a given energy ω_e above the Fermi level and possesses a spectral width γ_e. The current is decaying exponentially on the timescale $\tau_e = 1/\gamma_e$. In the frequency domain, the wavefunction is given by

$$\varphi_e(\omega) = \sqrt{\frac{v_F\gamma_e}{\mathcal{N}}}\frac{\mathrm{H}(\omega)}{\omega-\omega_e+\mathrm{i}\gamma_e/2}, \tag{1.45}$$

where $\mathrm{H}(\omega)$ denotes the Heaviside function and

$$\mathcal{N} = \frac{1}{2} + \frac{1}{\pi} \arctan\left(\frac{2\omega_e}{\gamma_e}\right) \tag{1.46}$$

is the normalization factor arising from the absence of negative energies. Of course, this wavefunction is valid only in the idealized regime. Notably, this implies that the situations to which this wavefunction is physically relevant restrict to $\gamma_e \ll \omega_e$. We will however look at the general case, without this restriction, because it will give us insight about the Wigner representation of electronic excitations.

Let us look at Wigner representation of first-order coherence for different ω_e/γ_e ratios on fig. 1.10. The ratio ω_e/γ_e is nothing but a

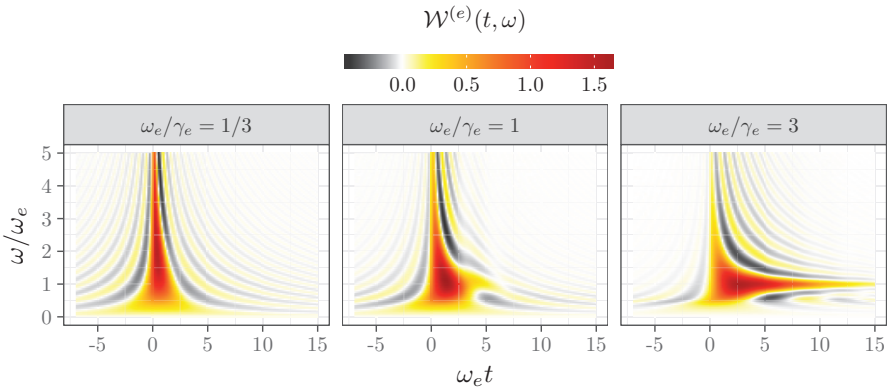

Figure 1.10: Wigner representation of Landau excitation wavepackets. From left to right, the ratio of the injection energy ω_e to the escape rate γ_e is raised. Note that only the right-most pannel corresponds to a physically relevant situation. The wavepacket is emitted at $t = 0$.

quality factor that determines the energy resolution of the excitation. At fixed injection energy, the higher the energy resolution is, the longer is the excitation duration as expected from Heisenberg's uncertainty principle. Figure 1.10 also shows the effect of the Pauli exclusion principle on the Wigner function: there is a cut at $\omega = \omega_e/2$ on the right panel of fig. 1.10. It arises from the constraint that electronic excitations only involve positive frequencies with respect to the Fermi level. In the frequency domain (see fig. 1.6, page 46), if we consider a fixed ω, the electron coherence can only take values when $\delta\omega \in [-\omega/2, \omega/2]$. Thus, a single electron will have a Wigner function spread over times of order

$1/\omega$, and thus will be more and more spread, when ω tends to zero, as seen on the right panel of fig. 1.10.

We have considered a purely electronic excitation, containing only positive frequencies. As stated earlier, it is also possible to emit hole excitation. The discussion is very similar and therefore, we will just show the corresponding Wigner function and excess Wigner function on fig. 1.11. Note that, in this case, there is a difference in interpretation between the full Wigner function, which contains contribution from the Fermi sea, and the excess Wigner function. In the first case, negativities as well as values above one cat be interpreted as non classical. In the second one, negativities naturally arise from the subtraction of one electron from the Fermi sea. However, at sufficiently low negative frequency, so that the temperature effects can be neglected, values belows -1 and above zero are signs of non classicality.

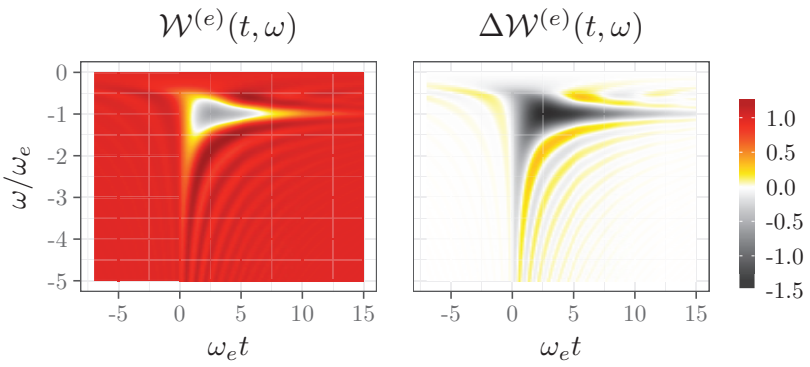

Figure 1.11: Wigner representation of holes Landau excitations. Left panel: Fermi sea included. Right panel: excess single-electron coherence (Fermi sea contribution substracted).

Before going to other kind of excitations, we might want to know how we can derive such an expression from elementary principles. A first idea would be to start from a standard edge channel, and model a dot of size L with a tunnel operator between position $x = 0$ and $x = L$:

$$T = \psi^\dagger(L)\psi(0) + \psi^\dagger(0)\psi(L). \tag{1.47}$$

Since we have a non-interacting problem, rather than solving the equations of motion, we can use a one-particle scattering approach to connect the incoming Fermi sea and the outgoing state. Developments based on

such an approach has been carried out by Moskalets et al. [2013], for adiabatic driving and square driving. It is also possible to perform numerical simulations on a discretized many-body system. Other approaches replace the quantum dot by a single level and focus on single-particle quantities. It is thus possible to derive exact equation for a linear driving [Keeling et al., 2006], or perform numerical simulation [Jonckheere et al., 2012] in the case of a square driving.

Levitons The other source of single-electron excitations is the Leviton source, introduced in section 1.2.3, page 30. This source is obtained by applying a classical, Lorentzian pulse, to an Ohmic contact.

Once we have fixed the amplitude of the pulse, so that exactly one excess electron is emitted, we only have one parameter left, which is the typical duration of the pulse, τ_e. Its wavefunction can be expressed in the energy domain as:

$$\varphi_e(\omega) = \sqrt{4\pi\tau_e v_F}\,\mathrm{H}(\omega)\,\mathrm{e}^{-\omega\tau_e}. \tag{1.48}$$

The Leviton is thus a low-energy excitation, mainly localized close to the Fermi surface, as can be seen from its Wigner representation depicted on fig. 1.12. As we will see later, this property is shared by all voltage drives: the resulting single-electron coherence shows that, contrarily to the case of the Landau excitation, the available energy levels are filled from the bottom to the top. The Landau excitation generated by the mesoscopic capacitor thus appears as far from being classical. This point will be discussed more exhaustively in chapter 3. By the way, we can ask what happens when the charge carried by Lorentzian voltage is N times the elementary charge. In this case, the electronic state is still pretty simple: the excitation is a Slater determinant built from the N mutually orthogonal electronic states

$$\varphi_n(\omega) = \sqrt{4\pi\tau_e v_F}\,\mathrm{H}(\omega)\,\mathrm{e}^{-\omega\tau_e} L_{n-1}(2\omega\tau_e), \tag{1.49}$$

with L_n the n-th Laguerre polynomial. The full many-body state is thus formed by the Slater determinant of the Fermi sea, plus the N electrons in wavefunctions φ_n.

Martin–Landauer wavepackets This electronic excitation has originally been introduced by Martin and Landauer [1992] to discuss the current noise generated by a continuous stream of electrons emitted

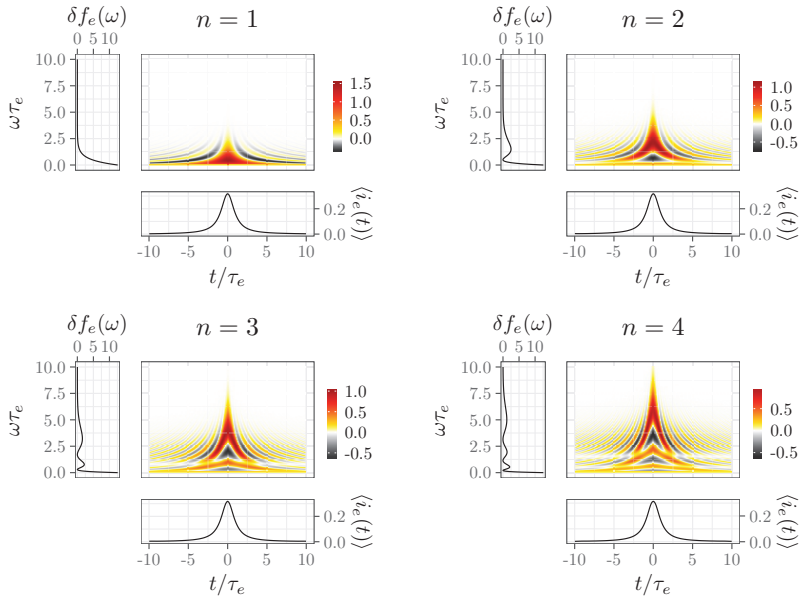

Figure 1.12: Wigner representation of the single-electron wavefunctions eq. (1.49) building the n-Leviton excitations up to $n = 4$. These wavefunctions have the same average current but have different energy distributions. Note that for $n \geq 2$, their Wigner functions exhibit negativites close to $t \simeq 0$.

by an electronic reservoir. Although there do not exist any on-demand single-electron source generating such wavepackets yet, it is an interesting example to discuss here because, as we shall see in chapter 2, it naturally appears when characterizing an arbitrary stationary source.

The Martin–Landauer wavepacket is a window in energy centered around ω_e, and of width γ_e.

$$\varphi_e(\omega) = \begin{cases} \sqrt{2\pi v_F/\gamma_e}, & \text{if } \omega \in [\omega_e - \gamma_e/2, \omega_e + \gamma_e/2]. \\ 0, & \text{otherwise.} \end{cases} \tag{1.50}$$

Its Wigner function is depicted on fig. 1.13. In the time domain, its expression is

$$\varphi_e(t) = \sqrt{\frac{\gamma_e}{2\pi v_F}} \mathrm{e}^{-\mathrm{i}\omega_e t} \operatorname{sinc}\left(\frac{\gamma_e t}{2}\right), \tag{1.51}$$

which is known in the signal processing community as the Shannon wavelet.

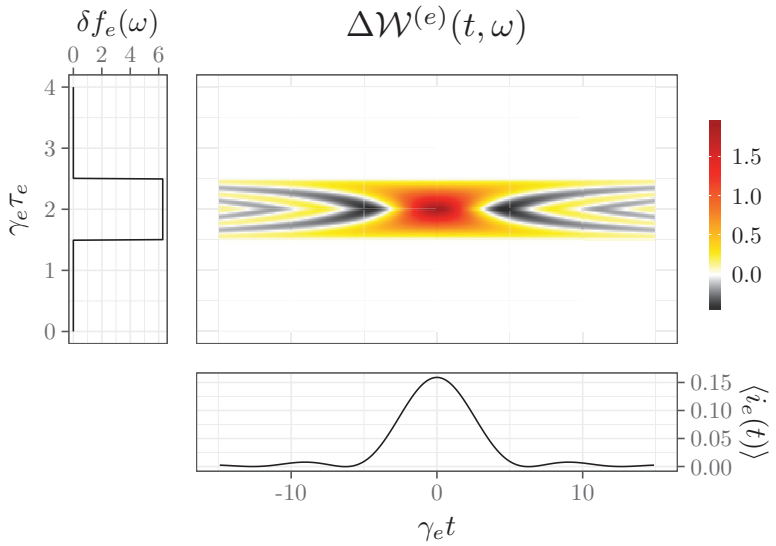

Figure 1.13: Wigner representation of a Martin–Landauer wavepacket. Note the typical sinc^2 current shape. The Wigner function spreads close to the boundaries of the energy window of width hf as a consequence of the Heisenberg time/energy uncertainty relation.

Coherent electron/hole excitation states

The excitations we have described up to now are either pure electron or pure hole excitations. As such, they exhibit vanishing electron/hole coherences. However, these are not the only excitations emitted by electronic sources. In particular, as we shall see, most sources do generate some non-zero electron/hole coherence.

In order to get an intuition of the physical meaning of non-zero electron/hole coherence, let's start a simple discussion from the true fermionic vacuum. The key point is that introducing a single electron with both positive and negative frequencies, will generate electron/hole coherences. Let us see why. First, we start from a wavefunction $\varphi(\omega)$ with non-zero values both on positive and negative frequencies and consider the many-body state

$$|\Psi\rangle = \psi^\dagger[\varphi]\,|0\rangle\,. \tag{1.52}$$

We always can decompose φ on positive and negative frequencies

$$\varphi(\omega) = v\varphi_e(\omega) + u\varphi_h(\omega), \tag{1.53}$$

where φ_e is a normalized electronic wavefunction and φ_h is a normalized hole wavefunction and $|u|^2 + |v|^2 = 1$ since, by construction, φ_e and φ_h are orthogonal and normalized. The first-order coherence is then expressed as

$$\begin{aligned} \mathcal{G}^{(e)}(\omega_1,\omega_2) &= |v|^2\,\varphi_e^*(\omega_2)\varphi_e(\omega_1) && \text{(1.54a)}\\ &+ |u|^2\,\varphi_h^*(\omega_2)\varphi_h(\omega_1) && \text{(1.54b)}\\ &+ v^*u\,\varphi_e^*(\omega_2)\varphi_h(\omega_1) \\ &+ u^*v\,\varphi_h^*(\omega_2)\varphi_e(\omega_1). && \text{(1.54c)} \end{aligned}$$

These four terms describe different types of excitations. Equation (1.54a) is a purely electronic term, since it is non zero only when ω_1 and ω_2 are positive. Equation (1.54b) describes only hole contribution for a similar reason. Finally, cross terms contained in eq. (1.54c) are non zero in the electron/hole quadrants of the frequency domain. Consequently, this shows that non zero electron/hole coherences arise from the quantum delocalization of a single-particle excitation between the electronic and hole parts of the energy spectrum.

This discussion can now be reformulated in the presence of the Fermi sea $|F\rangle$. We first start by taking out one electron in the single-particle state φ_h. Then we have the same situation as before, where the single-particle states φ_e and φ_h are empty. We just have to add one electron in the delocalized state φ. All this can be described in terms of many-body states as

$$|\Psi\rangle = \Big(v\psi^\dagger[\varphi_e] + u\psi^\dagger[\varphi_h]\Big)\,\psi[\varphi_h]\,|F\rangle\,. \tag{1.55}$$

Negative energies being populated, we have $(\psi^\dagger\psi)[\varphi_h]\,|F\rangle = |F\rangle$. Consequently

$$|\Psi\rangle = \Big(u + v\,\psi^\dagger[\varphi_e]\psi[\varphi_h]\Big)\,|F\rangle\,. \tag{1.56}$$

The resulting excess single-electron coherence is then

$$\begin{aligned} \Delta\mathcal{G}^{(e)}(t_1,t_2) &= |v|^2\varphi_e^*(t_2)\varphi_e(t_1) - |v|^2\varphi_h^*(t_2)\varphi_h(t_1) \\ &\quad + v^*u\,\varphi_e^*(\omega_2)\varphi_h(\omega_1) + u^*v\,\varphi_h^*(\omega_2)\varphi_e(\omega_1). \end{aligned} \tag{1.57}$$

Periodic sources

Up to now, we only have considered elementary excitations, composed of a single electron or a single hole. However, one shot single-electron detection on the fly has not yet been demonstrated although there are

theoretical proposals to split a Fermi gas in a time-resolved way [Klich and Levitov, 2009] or to exploit the capacitive coupling of the flying electron to a two-electron spin qubit [Thalineau et al.]. Consequently, most experiments are performed using statistical measurements on the current and therefore rely on periodic electron sources. Periodicity is particularily important for tomography protocols, as we will see in section 1.6. Because of its importance, we shall first discuss the general properties of the corresponding electronic coherence. Then, as example, we shall illustrate the specific case of a periodically driven voltage applied on an equilibrium electronic state.

General properties When a state has a period $T = 1/f$, its first-order coherence obeys the following periodicity property

$$\mathcal{G}(t_1 + T, t_2 + T) = \mathcal{G}(t_1, t_2). \tag{1.58}$$

In other words, $\mathcal{G}(t_1, t_2)$, is periodic in $t = (t_1 + t_2)/2$. Note that the periodicity is only in the "diagonal variable" and not in each variable. This is not surprising since the $\bar{t} = (t_1 + t_2)/2$ dependence encodes the time evolution whereas the $\tau = t_1 - t_2$ dependence encodes electronic coherence.

How can we translate this property within each different representations of $\mathcal{G}^{(e)}$? In the frequency representation, we only have harmonics along the diagonal. The coherence can be represented by a sequence of functions $\mathcal{G}_n(\omega)$, such as

$$\mathcal{G}(\omega_1, \omega_2) = v_F \sum_{n\in\mathbb{Z}} \delta\left(\omega_1 - \omega_2 - 2\pi n f\right) \mathcal{G}_n\left(\frac{\omega_1 + \omega_2}{2}\right). \tag{1.59}$$

In the Wigner representation, periodicity is recovered in the time variable

$$W(t + T, \omega) = W(t, \omega). \tag{1.60}$$

When we come back to marginals, periodicity also plays a role. Of course, the current being the diagonal part of the excess coherence expressed in time, it is also T-periodic. The (excess) occupation number must be computed by period, since the number of extra excitations is infinite

$$f_e(\omega) = \frac{1}{T}\int_0^T W^{(e)}(t, \omega)\,\mathrm{d}t, \tag{1.61a}$$

$$\delta f_e(\omega) = \frac{1}{T}\int_0^T \Delta W^{(e)}(t, \omega)\,\mathrm{d}t. \tag{1.61b}$$

The normalization of the first-order coherence gives the excess average number of electrons per period. If we note N_e the number of excess electrons above the Fermi sea in one period, and N_h the number of excess holes in the Fermi sea in one period, we have

$$\frac{1}{T}\int_0^T \left(\int_{\mathbb{R}} \Delta W^{(e)}(t,\omega)\,\frac{\mathrm{d}\omega}{2\pi}\right)\mathrm{d}t = \int \delta f_e(\omega)\,\frac{\mathrm{d}\omega}{2\pi} = \frac{N_e - N_h}{T}. \quad (1.62)$$

It is now time to discuss examples starting with periodic classical drive. We will see in chapter 3 the more general case of a periodic source treated in the non interacting electron approximation.

Classical drives Classical drives are interesting for several reasons. First, they are straightforward to implement experimentally. Among them are a.c. drives, which are historically the first time-dependent sources considered within the mesoscopic physics community. More importantly, under rather general circumstances, a.c. drives are also rather immune to the effect of Coulomb interactions. This property makes them a tool of choice for probing an unknown source.

A periodic drive adds up a $\mathbb{R}$-number term to the single-particle Hamiltonian, which is $-eV(t)$. The dynamics is then easily obtained by replacing free field operators by

$$\psi_V(t) = \exp\left(\frac{\mathrm{i}e}{\hbar}\int_{-\infty}^{t} V(\tau)\,\mathrm{d}\tau\right)\psi(t). \quad (1.63)$$

From this, the first-order coherence can be obtained in the time domain as

$$\mathcal{G}(t_1,t_2) = \exp\left(\frac{\mathrm{i}e}{\hbar}\int_{t_2}^{t_1} V(t)\,\mathrm{d}t\right)\mathcal{G}_{F,T_{\mathrm{el}}}(t_1,t_2). \quad (1.64)$$

If the voltage drive is periodic, the first-order coherence obeys the property given by eq. (1.58). Let us now turn to the other representations of $\mathcal{G}^{(e)}$.

To obtain them, it is convenient to introduce the photo-assisted transition amplitudes. As we have seen, the fermionic creation operator is modulated by a time-dependent phase $\alpha(t) = \exp\left(\mathrm{i}e/\hbar\int_{-\infty}^{t} V(\tau)\mathrm{d}\tau\right)$, when expressed in time. In the frequency domain, this leads to

$$c_V(\omega) = \int \alpha(\omega')c(\omega-\omega')\frac{\mathrm{d}\omega}{2\pi}. \quad (1.65)$$

When the driving is periodic in time, α only contains discrete frequencies. The corresponding creation operators in the presence of the drive are then expressed in terms of the equilibrium ones as

$$c_V(\omega) = \sum_{n\in\mathbb{Z}} \alpha_n c(\omega - 2\pi n f). \tag{1.66}$$

Applying a classical drive can thus be interpreted as a scattering process in which the incoming unperturbed electronic states are scattered into the outgoing states shifted in energy due to photon absorptions from the classical drive. The transition amplitudes are given by

$$\begin{aligned}\mathcal{A}(\omega \to \omega') &= {}_{\text{out}}\langle \omega'|\omega\rangle_{\text{in}} = \langle 0|c_V(\omega')c^\dagger(\omega)|0\rangle \\ &= \sum_{n\in\mathbb{Z}} \alpha_n \delta(\omega' - \omega - 2\pi n f).\end{aligned} \tag{1.67}$$

That explains why the α_n for $n \in \mathbb{Z}$ are called the photo-assisted transition amplitudes. For $n > 0$, α_n is the amplitude for absorption of n photons of energy hf whereas for $n < 0$ it corresponds to the emission of n photons of energy hf. The α_0 amplitude is the amplitude for elastic scattering of an electron at energy $\hbar\omega$.

Coming back to first-order coherence, these amplitudes are useful to express it in the frequency domain:

$$\mathcal{G}_n^{(e)}(\omega) = \sum_p \alpha_p \alpha_{p-n}^* f_{e,T_{\text{el}}}\left(\omega + (n-2p)\pi f\right). \tag{1.68}$$

At zero temperature, it is possible to see the quantized exchanges between the drive and the electronic fluid directly on the coherence in energy (see fig. 1.14). In this case, the coherence takes values only for integer harmonics of the frequency in the variable $\delta\omega$, because of the periodicity. The fact that the exchanges are quantized makes that each harmonic is a staircase function, steps occuring every $2\pi f$. When increasing temperature, those steps are smoothed over a frequency width $k_B T_{\text{el}}/\hbar$.

We can also look at the outgoing occupation number per period

$$f_e(\omega) = \sum_{n\in\mathbb{Z}} |\alpha_n|^2 f_{e,T_{\text{el}}}\left(\omega - 2\pi n f\right). \tag{1.69}$$

We immediately interpret $|\alpha_n|^2$ as the probability for shifting the energy of an electron by nhf.

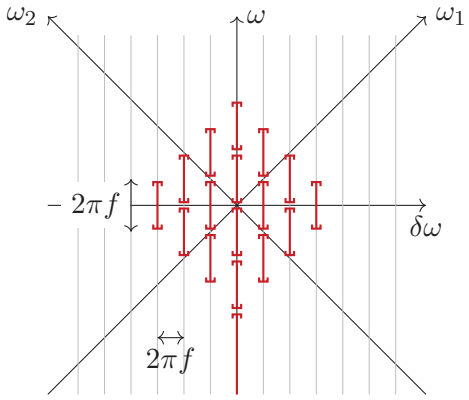

Figure 1.14: Representation of the coherence in energy for a classical a.c. voltage at zero temperature, as given by eq. (1.68). Here we consider that α_n is non zero when $-2 \leq n \leq 2$. On each bracketed red segment, the energy coherence takes a non-zero constant value, and it is zero everywhere else. Due to periodicity, only $\delta\omega$ that are integer multiple of $2\pi f$ (light grey lines) possess a non-zero coherence. Since the exchanges between the drive and the fluid are quantized, at a fixed $\delta\omega$, the coherence is a staircase function, whose steps have width $2\pi f$. At non-zero temperature, the steps are smeared over the frequency associated with the temperature.

We now have all ingredients to express the Wigner function, in terms of photo-assisted transition amplitudes:

$$W^{(e)}(t,\omega) = \sum_{n_+,n_-} \alpha_{n_+}\alpha^*_{n_-} \mathrm{e}^{2\mathrm{i}\pi(n_- - n_+)ft} f_{e,T_{\mathrm{el}}}(\omega - \pi(n_+ + n_-)f). \quad (1.70)$$

Let us look at the simplest case of a sinusoidal a.c. voltage $V(t) = V_0\cos(2\pi f(t+T/2))$, where we chose the phase πfT so that the current of electron is maximum at $T = 0$. In this case, photo-assisted transition amplitudes are given by Bessel functions $\alpha_n = J_n(eV_0/hf)$. The Wigner function is thus given by

$$W^{(e)}(t,\omega) = \sum_{n=-\infty}^{+\infty} J_n\left(\frac{2eV_0}{hf}\cos\left(2\pi f(t+T/2)\right)\right) \times f_{e,T_{\mathrm{el}}}(\omega + \pi nf). \quad (1.71)$$

We now have three energy scales, associated with this problem. The first one is the energy of photonic excitations, hf. The second one is the voltage amplitude eV_0. Since the sinusoidal drive only carries photons of energy hf, the ratio eV_0/hf will give us an idea of the number of photons exchanged between the drive and the electronic fluid. Finally, the temperature gives us the scale of thermal fluctuations k_BT_{el} which smooth out quantum fluctuations.

There are two interesting regimes to discuss. The first one is the semi-classical regime. In this case we naturally expect that the Wigner function describes an equilibrium Fermi–Dirac distribution whose chemical potential varies along time. As we will see, we need to have $hf \lesssim k_BT_{\mathrm{el}}, eV_0$ in order to recover this regime. The second regime is the fully quantum regime, where less than a photon is exchanged between the drive and the electronic fluid during each period. In this case, we must have $k_BT_{\mathrm{el}} \lesssim eV_0 \lesssim hf$.

The semi-classical regime is the one realized in everyday life. Power sockets provide a voltage around 220 V at 50 Hz and temperature is around 300 K. This is typically a case where temperature and voltage energy scales are several orders of magnitude above frequency energy scale since, roughly, $eV_0/hf \approx 10^{15}$ and $k_BT/hf \approx 10^{11}$.

At a first glance, it might seem quite surprising that a non-zero temperature is necessary in order to talk about a fully classical regime. However, it is quite clear while looking at the coherence that temperature plays a key role here. As can be seen on fig. 1.15, at zero temperature,

there are a lot of riddles leading to non-classical values of the Wigner function. Temperature will act on these riddles by blurring them and then smoothing them out[6]. The right panel of fig. 1.15 shows that the Wigner function obeys our classicality criterion (its values are between zero and one) when $k_B T_{\mathrm{el}} \gtrsim hf$. In this case, the Wigner function is well described by the adiabatic evolution of the Fermi distribution by the voltage potential

$$W^{(e)}(t,\omega) = f_e\left(\omega + \frac{eV(t)}{\hbar}\right). \tag{1.72}$$

At lower temperature (see the middle and left panels of fig. 1.15),

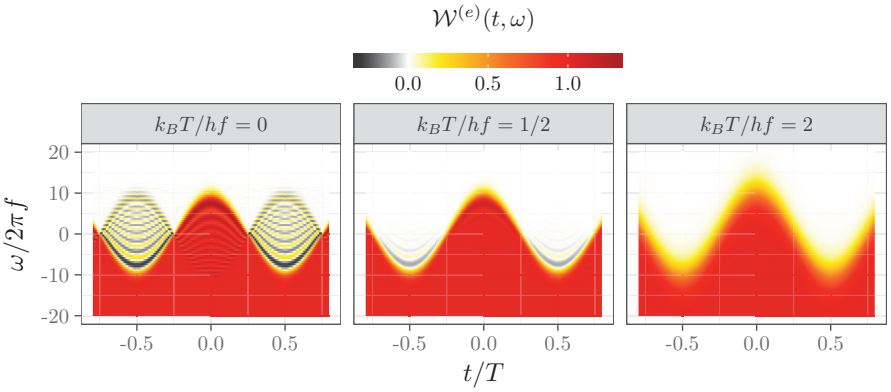

Figure 1.15: Wigner representation of a sinusoidal voltage at large amplitude ($eV_0/hf = 10$) and for increasing temperatures: for $k_B T_{\mathrm{el}} = 2hf$, the Wigner distribution corresponds to an agitated Fermi sea at temperature T_{el} and chemical potential $\mu(t) = eV_0 \cos(2\pi f t)$. When the temperature is decreased, we see quantum interference effects leading to non-classical values of the Wigner distribution function.

quantum effects manifest themselves as interference fringes. These arise because, at low temperatures, the electronic thermal coherence time $\tau_{\mathrm{th}} = \hbar/k_B T_{\mathrm{el}}$ diverges and therefore, the time dependence of the a.c. voltage is felt over such an integral. This leads to Airy function oscillations

6. Of course, one might ask whether these riddles may disappear from other phenomena, for example interactions. In the case of a single-tone classical voltage drive as we will see in chapter 3, interactions only affect the amplitude of the drive. As such, the negativities observed at zero temperature won't vanish due to interactions, provided interactions are linear in terms of current.

as discussed in [Ferraro et al., 2013] and thus to negative and larger than one values for $W^{(e)}(t,\omega)$. The Wigner function is no longer classical in this case.

In the fully quantum regime, we consider a voltage amplitude that is both smaller than the frequency and bigger than the temperature. In this case, let us expand the Wigner function in powers of the ratio eV_0/hf

$$W^{(e)}(t,\omega) = W^{(e)}_{F,T_{\mathrm{el}}}(t,\omega) \tag{1.73a}$$

$$- F_{T_{\mathrm{el}}}(\omega)\cos(2\pi f t)\left(\frac{eV_0}{hf}\right) \tag{1.73b}$$

$$+ g_{T_{\mathrm{el}}}(\omega)\cos^2(2\pi f t)\left(\frac{eV_0}{hf}\right)^2 + \mathcal{O}\left(\left(\frac{eV_0}{hf}\right)^3\right), \tag{1.73c}$$

where the auxiliary functions

$$F_{T_{\mathrm{el}}}(\omega) = f_{e,T_{\mathrm{el}}}(\omega+\pi f) - f_{e,T_{\mathrm{el}}}(\omega-\pi f), \tag{1.74a}$$

$$g_{T_{\mathrm{el}}}(\omega) = f_{e,T_{\mathrm{el}}}(\omega+2\pi f) + f_{e,T_{\mathrm{el}}}(\omega-2\pi f) - 2f_{e,T_{\mathrm{el}}}(\omega) \tag{1.74b}$$

are respectively equal at zero temperature, to -1 if $\omega \in [-\pi f, \pi f]$ and zero otherwise for $F_{T_{\mathrm{el}}}(\omega)$ and to 1 if $\omega \in]0, 2\pi f]$, -1 if $\omega \in]-2\pi f, 0]$ and 0 elsewhere for $g_{T_{\mathrm{el}}}(\omega)$.

Equation (1.73) tells us that, at low voltage, the Wigner function is a slight perturbation of the Fermi sea. The first order is, at zero temperature, a cosine in time, whose width is given by the frequency of the drive. If only terms (1.73a) and (1.73b) are non negligible, the occupation number is not affected by the driving. In this case, no photon is absorbed nor emitted by the electronic fluid, similarly to what happens with non-resonant interactions in optics. This form of the Wigner function is of particular interest because, as we will see in section 1.6, it allows us to perform an analog Fourier transform on an unknown quantum coherence signal. When the drive is high enough so that eq. (1.73c) is non-negligible anymore, the occupation number departs from the Fermi step thus showing that some electrons of the Fermi sea are promoted above the Fermi sea. Single-photon emission and absorption processes generate electron/hole pairs within the electronic fluid. At increasing voltage, multiphotonic processes take place, leading to higher frequency electron/hole pairs generation. This development in terms of eV_0/hf can be seen on fig. 1.16.

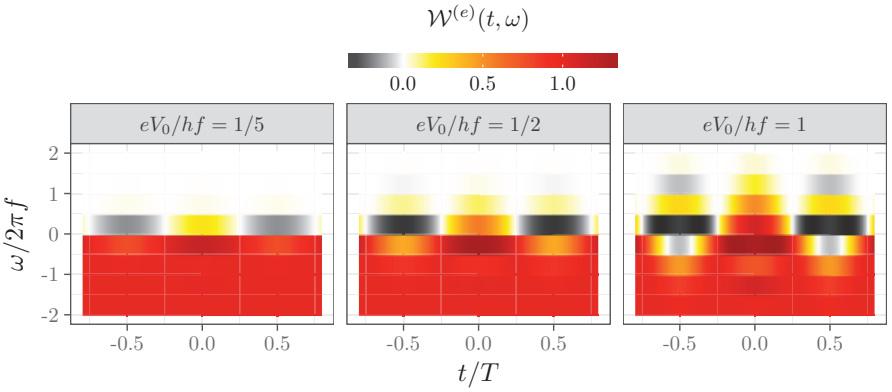

Figure 1.16: Wigner representation of a sinusoidal voltage at low amplitude ($|eV_0| \lesssim hf$) and zero temperature. At low voltage (right panel), the coherence is dominated by the term (1.73b) which contributes to the average electrical current but not to the excess occcupation number. At increasing voltages (middle panel), the quadratic contribution in eV_0/hf appears (term (1.73c)) which corresponds to real single-photon transitions. Then at higher voltages, the contribution of two-photon transitions becomes visible, progressively leading to the appearance of a sine-shaped Wigner function. Note that non-classical values are visible on all the panels.

1.5 Second-order electronic coherence

First-order coherence is a great tool for studying single-electron physics. But there are good reasons to go beyond this physics. A first example would be the study correlations of two-electron detection events which indeed are directly probed by current noise measurements. In particular, probing two-electron physics is a first step towards understanding entanglement in quantum conductors. This motivates the search for a unifying concept able to characterize two-electron physics in all possible experiments. This concept is nothing but the second-order electronic coherence, also called two-electron coherence.

In this section, we thus explore two-electron coherence along the lines used to discuss single-electron coherence. We also discuss how Fermi statistics manifest itself on its properties. Finally, we clarify its relation to current noise in great details, an important step towards understanding the connection between electronic and photonic coherences as we will see

in chapter 3.

1.5.1 Definition, basic properties and physical interpretation

The natural container of two-particle physics here is the second-order electron coherence. This quite complicated object which depends on four times contains all the two-electron wavefunctions present in the system. Originally studied by [Moskalets, 2014b], it is defined by direct analogy with Glauber's second-order photonic coherence:

$$\mathcal{G}^{(2e)}(t_1,t_2;t_1',t_2') = \langle \psi^\dagger(t_1')\psi^\dagger(t_2')\psi(t_2)\psi(t_1)\rangle_\rho. \tag{1.75}$$

In order to get a better understanding of two-electron coherence, we start by considering the simple case where the system contains two electrons on top of the true vacuum in two mutually orthogonal electronic states[7]. The second-order coherence is then given by the product of the two-electron wavefunctions:

$$\mathcal{G}^{(2e)}(t_1,t_2;t_1',t_2') = \varphi_{12}^*(t_1',t_2')\varphi_{12}(t_1,t_2), \tag{1.76}$$

φ_{12} being the two-electron wavefunctions built by the Slater determinant over φ_1 and φ_2

$$\varphi_{12}(t_1,t_2) = \begin{vmatrix} \varphi_1(t_1) & \varphi_1(t_2) \\ \varphi_2(t_1) & \varphi_2(t_2) \end{vmatrix}. \tag{1.77}$$

In the case of a Slater determinant $|\Psi_N\rangle$ of N electrons built from mutually orthogonal wavefunctions $(\varphi_k)_{k=1,\dots,N}$, the above expression generalizes to a sum over all possible two-electron wavefunctions that can be constructed from the N single-electron states:

$$\mathcal{G}^{(2e)}_{|\Psi_N\rangle}(x_1,x_2|x_1',x_2') = \sum_{k<l} \varphi_{k,l}(x_1,x_2)\,\varphi_{k,l}(x_1',x_2'). \tag{1.78}$$

Because all $\varphi_{k,l}$ are antisymmetric, $\mathcal{G}^{(2e)}$ also verifies:

$$\begin{aligned} \mathcal{G}^{(2e)}(t_1,t_2;t_1',t_2') &= -\mathcal{G}^{(2e)}(t_1,t_2;t_2',t_1') \\ &= -\mathcal{G}^{(2e)}(t_2,t_1;t_1',t_2') \\ &= \mathcal{G}^{(2e)}(t_2,t_1;t_2',t_1'). \end{aligned} \tag{1.79}$$

7. This is the first non-trivial case since $\mathcal{G}^{(2e)}$ is zero when there is only one electron in the system.

Importantly, these symmetries do not depend on the peculiar state we have chosen: they are always valid and arise from the anticommutation relations and thus reflect fermionic statistics of the electrons. A thorough review of symmetries and their implication for two-electron coherence can be found in [Thibierge, 2015; Thibierge et al., 2016].

An interesting subspace of the four dimensional parameters space for second-order coherence is the diagonal plane defined by $(t_1, t_2) = (t_1', t_2')$. Along this diagonal, $\mathcal{G}^{(2e)}(t_1, t_2; t_1, t_2)$ gives the joint probability to have an electron at t_1 and another one at t_2. The Pauli exclusion principle imposes that the probability for having two electrons at the same time is zero, which follows directly from symmetries described by eq. (1.79). More generally, it is possible to compute any joint probabilities to have an electron in a wavefunction φ_1 and another one in a wavefunction φ_2. This is given by

$$\begin{aligned} p[\varphi_1, \varphi_2] &= \langle \psi^\dagger[\varphi_1]\psi^\dagger[\varphi_2]\psi[\varphi_2]\psi[\varphi_1]\rangle_\rho \\ &= v_F^4 \int \varphi_1^*(t_1')\varphi_2^*(t_2')\varphi_1(t_1)\varphi_2(t_2) \\ &\qquad \mathcal{G}^{(2e)}(t_1, t_2; t_1', t_2')\, \mathrm{d}t_1 \mathrm{d}t_2 \mathrm{d}t_1'\, \mathrm{d}t_2'. \end{aligned} \tag{1.80}$$

It is also possible to access electron number correlations. These quantities contain four fermionic operators and can be related to the probability of joint detection for two electrons defined by (we recall that $n[\varphi]$ is defined by eq. (1.19))

$$p[\varphi_1, \varphi_2] = \langle n[\varphi_1] n[\varphi_2]\rangle - \langle \varphi_1 | \varphi_2 \rangle \, \langle \psi^\dagger[\varphi_1]\psi[\varphi_2]\rangle, \tag{1.81}$$

where we have introduced the scalar product of single-particle states

$$\langle \varphi_1 | \varphi_2 \rangle = v_F \int \varphi_1^*(t)\varphi_2(t)\, \mathrm{d}t. \tag{1.82}$$

Let us now consider the extreme cases of equal and orthogonal wavepackets. For orthogonal wavepackets, the probability of joint detection events is exactly equal to occupation number correlations. But for identical wavepackets, the probability of joint detection is zero, because of Pauli's exclusion principle. Consequently

$$\langle n^2[\varphi]\rangle = \langle n[\varphi]\rangle. \tag{1.83}$$

This reflects fermionic statistics: $n[\varphi]$ eigenvalues are either 0 or 1 and thus that all moments of n are equals.

Let us clarify the concept of two-electron coherence in the presence of the Fermi sea. This is an important point which implies defining the intrinsic contribution of an electronic source to the total second-order electronic coherence.

1.5.2 Intrinsic two-electron coherence

The intrinsic two-electron coherence emitted by a source can be defined from the second-order electronic coherence by subtracting not only the Fermi sea contribution but also all processes contributing to two-electron detection and involving the excess single-electron coherence of the source. These involve classical contributions as well as quantum exchange contributions [Thibierge et al., 2016]:

$$\mathcal{G}_\rho^{(2e)}(1,2|1',2') = \mathcal{G}_F^{(2e)}(1,2|1',2') \tag{1.84a}$$
$$+ \mathcal{G}_F^{(e)}(1|1')\,\Delta\mathcal{G}_\rho^{(e)}(2|2') + \mathcal{G}_F^{(e)}(2|2')\,\Delta\mathcal{G}_\rho^{(e)}(1|1') \tag{1.84b}$$
$$- \mathcal{G}_F^{(e)}(1|2')\,\Delta\mathcal{G}_\rho^{(e)}(2|1') - \mathcal{G}_F^{(e)}(2|1')\,\Delta\mathcal{G}_\rho^{(e)}(1|2') \tag{1.84c}$$
$$+ \Delta\mathcal{G}_\rho^{(2e)}(1,2|1',2'). \tag{1.84d}$$

Equation (1.84) can schematically be represented by fig. 1.17. It should be seen as a definition of the intrinsic two-electron coherence $\Delta\mathcal{G}_\rho^{(2e)}$ from the total two-electron coherence, the Fermi sea two-electron coherence and lower-order electronic coherences. The second term (1.84b) is present for classical particles and represents classical correlations in which the origin of the two detected particles can be traced back either to the Fermi sea or the source. Such back-tracking is not possible for the exchange terms (1.84c) whose minus sign comes from the fermionic statistics. Note that eq. (1.84) is fully compatible with eq. (1.78). Finally, for a state obtained by adding a single-electron or hole excitation to the Fermi sea, the intrinsic two-electron coherence vanishes as physically expected for a source emitting only one excitation.

1.5.3 Representations of two-electron coherence

Exactly as for the first-order electronic coherence, $\mathcal{G}^{(2e)}$ as well as $\Delta\mathcal{G}^{(2e)}$ can be represented in various ways which we will review here. In particular, we will see how the fermionic statistics of electrons lead to a non-classical two-electron coherence in all cases, thus stressing the true quantum nature of two-electron coherence compared with single-electron coherence.

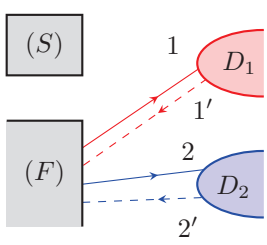

(a) Fermi sea: (1.84a).

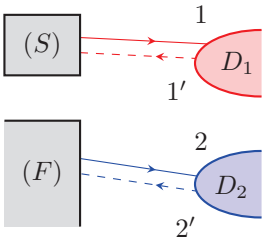

(b) Classical correlations: (1.84b).

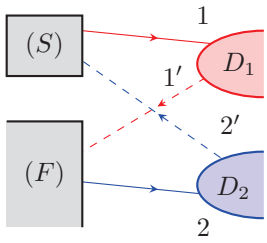

(c) Quantum exchange: (1.84c).

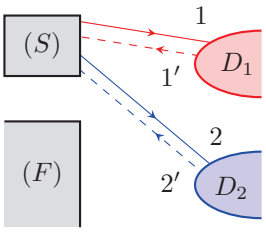

(d) Source intrinsic: (1.84d).

Figure 1.17: Contributions to the two-electron detection probability by detectors D_1 and D_2. Full lines represent direct probability amplitudes whereas dashed lines represent complex conjugated ones. The electronic system is decomposed into the Fermi sea (F) and a source (S) emitting electron and/or hole excitations. The two-electron detection probability contains four types of contributions.

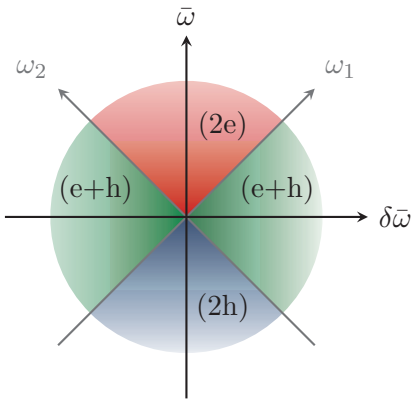

Figure 1.18: Nature of two-particle excitations: partitioning the diagonal plane $(\omega_1, \omega_2) = (\bar{\omega} + \delta\bar{\omega}/2, \bar{\omega} - \delta\bar{\omega}/2)$ in two sectors associated with pairs of electrons (2e) and pairs of holes (2h) and two sectors associated with electron/hole pairs (e+h).

The frequency domain representation of two-electron coherence

Exactly as in the case of single-electron coherence, the nature of excitations can be obtained by going to the frequency domain:

$$\widetilde{\mathcal{G}}^{(2e)}_{\rho,x}(\boldsymbol{\omega}_+|\boldsymbol{\omega}_-) = \int_{\mathbb{R}^4} \mathcal{G}^{(2e)}_{\rho,x}(\mathbf{t}_+|\mathbf{t}_-)\, \mathrm{e}^{\mathrm{i}(\boldsymbol{\omega}_+\cdot\mathbf{t}_+ - \boldsymbol{\omega}_-\cdot\mathbf{t}_-)}\, \mathrm{d}^2\mathbf{t}_+ \mathrm{d}^2\mathbf{t}_-, \qquad (1.85)$$

where $\mathbf{t}_+ = (t_1, t_2)$ and $\mathbf{t}_- = (t'_1, t'_2)$ are respectively conjugated to $\boldsymbol{\omega}_+ = (\omega_1, \omega_2)$ and $\boldsymbol{\omega}_- = (\omega'_1, \omega'_2)$. Note that antisymmetry properties (1.79) are also true in the frequency domain.

The diagonal of the frequency domain ($\boldsymbol{\omega}_- = \boldsymbol{\omega}_+ = (\omega_1, \omega_2)$) can be divided into quadrants depicted on fig. 1.18 that describe the elementary two-particle excitations. When ω_1 and ω_2 are both positive, we have an electronic pair whereas we have a pair of holes when they are both negative. In the case one is positive and the other negative, we have an electron/hole pair. Note that this classification is compatible with the permutation $\omega_1 \leftrightarrow \omega_2$.

The whole frequency domain $(\boldsymbol{\omega}_+, \boldsymbol{\omega}_-)$ can then be decomposed into 4D simplexes based on these quadrants for the diagonal. This will naturally be compatible with the antisymmetry properties of the two-electron coherence. Diagonal simplexes are based on $\boldsymbol{\omega}_+$ and $\boldsymbol{\omega}_-$

that both describe the same type of excitation. This leads to a two-electron simplex, a two-hole simplex and two electron/hole pair simplexes respectively containing the contributions of two-electron, two-hole and electron/hole pair excitations. The off-diagonal simplexes where $\boldsymbol{\omega}_+$ and $\boldsymbol{\omega}_-$ do not belong to the same quadrant describe coherences between these four different two-particle excitations.

Wigner representation of two-electron coherence

Definition Wigner representation of two-electron coherence is defined in the same way as for single-electron coherence, as a Fourier transform with respect to the time differences $\tau_j = t_j - t'_j$. When considering an intra-channel two-electron coherence, this leads to a real function

$$W^{(2e)}_{\rho,x}(t_1,\omega_1;t_2,\omega_2) = \int_{\mathbb{R}^2} v_F^2 \mathcal{G}^{(2e)}_{\rho,x}\left(\boldsymbol{t}+\frac{\boldsymbol{\tau}}{2}\middle|\boldsymbol{t}-\frac{\boldsymbol{\tau}}{2}\right) \mathrm{e}^{\mathrm{i}\boldsymbol{\omega}\cdot\boldsymbol{\tau}}\,\mathrm{d}^2\boldsymbol{\tau}. \qquad (1.86)$$

Wigner representation of the excess two-electron coherence $\Delta W^{(2e)}_{\rho,x}$ is defined by eq. (1.86) from the excess two-electron coherence. Whenever Wick's theorem applies, the total two-electron coherence can be computed in terms of the single-electron one:

$$\mathcal{G}^{(2e)}_{\rho,x}(1,2|1',2') = \mathcal{G}^{(e)}_{\rho,x}(1|1')\,\mathcal{G}^{(e)}_{\rho,x}(2|2') - \mathcal{G}^{(e)}_{\rho,x}(1|2')\,\mathcal{G}^{(e)}_{\rho,x}(2|1') \qquad (1.87)$$

and, using eq. (1.84), the same equation also describes the intrinsic two-electron coherence in terms of the excess single-electron coherence. The first term contributes to the two-electron Wigner distribution through the product $W^{(e)}_{\rho,x}(t_1,\omega_1)\,W^{(e)}_{\rho,x}(t_2,\omega_2)$ which corresponds to independent classical particles. The second term comes from quantum exchange and, as we shall see now, is responsible for non-classical features of the two-electron Wigner distribution function.

Non classicality of two-electron coherences In the case of single-electron coherence, we gave a definition of classicality based on the non negativity of Wigner function. It is natural to extend this definition to the two-particle case: $W^{(2e)}_{\rho,x}(t_1,\omega_1;t_2,\omega_2)$ would be called classical if it takes values between 0 and 1. Of course, if we consider the inter-channel two-electron Wigner distribution associated with the inter-channel two-electron coherence $\mathcal{G}^{(2e)}_{\rho,x}(1,t_1;2,t_2|1,t'_1;2,t'_2)$, then when the two channels are not correlated, we have $W^{(2e)}_{\rho,x}(1,t_1,\omega_1;2,t_2,\omega_2) =$

$W_1^{(e)}(t_1,\omega_1)\,W_2^{(e)}(t_2,\omega_2)$ as expected for uncorrelated classical objects[8]. Consequently, if the two-electron Wigner distribution in channels 1 and 2 is classical, the inter-channel two-electron Wigner distribution is also classical. But as we shall see now, because of its antisymmetry properties, the two-electron Wigner distribution in a single channel exhibits non-classical features.

To illustrate this point, let us consider mutually orthogonal time-shifted wave-packets: $\varphi_1(t) = \varphi_e(t-\tau/2)$ and $\varphi_2(t) = \varphi_e(t+\tau/2)$. The intrinsic two-electron Wigner distribution function associated with the state $|\Psi_2\rangle = \psi^\dagger[\varphi_1]\psi^\dagger[\varphi_2]|F\rangle$ is then

$$\begin{aligned}\Delta W^{(2e)}_{|\Psi_2\rangle}(t_1,\omega_1;t_2,\omega_2) = {} & W_{\varphi_1}(t_1,\omega_1)\,W_{\varphi_2}(t_2,\omega_2)\\ & + W_{\varphi_2}(t_1,\omega_1)\,W_{\varphi_1}(t_2,\omega_2)\\ & - 2\cos\left((\omega_1-\omega_2)\tau\right) W_{\varphi_e}(t_1,\omega_1)W_{\varphi_e}(t_2,\omega_2).\end{aligned} \tag{1.88}$$

When considering a quasi-classical electronic wavepacket, such that $W_{\varphi_e}(t,\omega)$ is almost everywhere positive, we see that the last term contains interference fringes due to the $\cos\left((\omega_1-\omega_2)\tau\right)$ factor. When φ_1 and φ_2 are well separated, negativities appear which reflect the non-classical nature of two-electron wavefunctions within a single edge channel. Note that the dependence in $\omega_1-\omega_2$ comes from the fact that, in the above example, φ_1 and φ_2 are time-shifted wavepackets. Energy-shifted wavepackets would lead to oscillations in t_1-t_2. In full generality, the quantum exchange interference terms present both a time and an energy dependence and this prevents $W^{(2e)}$ to be interpreted as a time-dependent two-electron distribution function.

Similarly, the two-electron Wigner distribution function of the equilibrium state at electronic temperature $T_{\rm el}$ and vanishing chemical potential is given by

$$W^{(2e)}_{\mu=0,T_{\rm el}}(t_1,\omega_1;t_2,\omega_2) = f_{T_{\rm el}}(\omega_1)\,f_{T_{\rm el}}(\omega_2) \tag{1.89a}$$

$$- 4\pi k_B T_{\rm el}\delta(\omega_1-\omega_2) f_{B,T_{\rm el}}(\omega_{\rm tot})\,\frac{\sin\left(\omega_{\rm tot}t_{12}\right)}{\sinh\left(t_{12}/\tau\right)}, \tag{1.89b}$$

where $\omega_{\rm tot} = \omega_1+\omega_2$, $t_{12} = t_1-t_2$ and $\tau = \hbar/k_BT_{\rm el}$ denotes the thermal coherence time. Here $f_{T_{\rm el}}$ is the Fermi–Dirac distribution at temperature $T_{\rm el}$ and $\mu = 0$ whereas $f_{B,T_{\rm el}}(\omega) = 1/(\mathrm{e}^{\hbar\omega/k_BT_{\rm el}}-1)$ denotes the Bose–Einstein distribution at temperature $T_{\rm el}$. The singular second term (1.89b)

8. Here the channel index breaks the indistinguishability between electrons within the two different channels.

expresses the Pauli exclusion principle and presents strong oscillations in t_{12}. Therefore $W^{(2e)}_{\mu=0,T_{\rm el}}$ cannot be interpreted as a time-dependent electronic distribution.

1.5.4 Relation to current noise

Due to the importance of current-noise measurements in nanoelectronics, let us now describe the precise relation between two-electron coherence and the excess current noise. Let's start by recalling that the excess current correlation $\Delta S_i(t,t')$ is defined as the excess of

$$S_i(t,t') = \langle i(t')\, i(t)\rangle - \langle i(t)\rangle\langle i(t')\rangle \tag{1.90}$$

when the sources are switched on with respect to the situation where they are switched off.

Since sub-nanosecond time-resolved measurements are not available in electronics yet, $S_i(t,t')$ is not directly accessible in the time domain. However, finite-frequency current-noise measurements [Parmentier et al., 2011] give access to the noise spectrum, which is a time-averaged quantity. The time-dependent power spectrum, which contains the same information as $\Delta S_i(t,t')$, is defined as the Wigner–Ville transform [Ville, 1948] of excess current correlations:

$$W_{\Delta S_i}(t,\omega) = \int_{\mathbb{R}} \Delta S_i\left(t-\frac{\tau}{2}\middle| t+\frac{\tau}{2}\right) \mathrm{e}^{\mathrm{i}\omega\tau}\,\mathrm{d}\tau. \tag{1.91}$$

Accessing this quantity is still experimentally challenging but an important step towards this goal is the recently developed homodyne measurement technique [Gasse et al., 2013] which has been used to probe the squeezing of the radiation emitted by a tunnel junction.

The canonical anticommutation relations and definition (1.84) imply that the quantity defined by eq. (1.91) is directly related to the intrinsic two-electron coherence by

$$\begin{aligned}
W_{\Delta S_i}(t,\omega) + W_{\langle i\rangle}(t,\omega) = & && \text{(1.92a)}\\
& - e\langle i(t)\rangle && \text{(1.92b)}\\
& - e^2 \int_{\mathbb{R}} h_\mu(\omega,\omega')\, \Delta W^{(e)}_\rho(t,\omega')\, \frac{\mathrm{d}\omega'}{2\pi} && \text{(1.92c)}\\
& + e^2 \int_{\mathbb{R}} v_F^2 \Delta\mathcal{G}^{(2e)}_\rho\left(t+\frac{\tau}{2}, t-\frac{\tau}{2}\middle| t+\frac{\tau}{2}, t-\frac{\tau}{2}\right) \mathrm{e}^{\mathrm{i}\omega\tau}\mathrm{d}\tau, && \text{(1.92d)}
\end{aligned}$$

where $h_\mu(\omega,\omega') = f_\mu(\omega-\omega') + f_\mu(\omega+\omega')$ and $W_{\langle i\rangle}(t,\omega)$ denotes the Wigner–Ville transform of the average time-dependent current. The first term (1.92b) is a Poissonian contribution associated with the granular nature of charge carriers. The second term (1.92c) arises from two-particle interferences between excitations generated by the source and electrons within the Fermi sea. These contributions are called the Hanbury Brown–Twiss (HBT) contributions since these two-particle interferences are precisely what is measured in an HBT experiment (we will come back to these experiments in section 1.6.2). This term comes from the presence of the Fermi sea. Finally, the last term (1.92d) corresponds to the intrinsic two-electron coherence contribution to the current noise.

Equation (1.92) is indeed the electron quantum optics version of the famous relation on fluctuations of particle number in an ideal Bose gas [Einstein, 1925] also discussed in [Aspect et al., 2008]. It mixes a Poissonian contribution to number fluctuations that reflects the particle nature of the quanta considered here with a quadratic term already identified by Einstein as coming from interferences. The latter term, which corresponds to (1.92d) minus $W_{\langle i\rangle}(t,\omega)$ in electron quantum optics, directly appears when discussing intensity correlation of classical radiation emitted by fluctuating sources as mentioned before.

Anticipating over chapter 3, this equation also relates electronic coherences to quantum optical properties of edge magnetoplasmons within the edge channel and, as we shall see, of the photons radiated into a transmission line capacitively coupled to the edge channel as in [Degiovanni et al., 2009]. It therefore establishes a bridge between electron quantum optics and the recently studied quantum optics of noise [Grimsmo et al., 2015].

Finally, let us stress that eq. (1.92), which is also valid in the presence of interactions, shows that accessing single-electron coherence as well as the current noise gives access to the diagonal part of two-electron coherence, as expected since the latter contains all the information on time-resolved two-electron detection.

Directly accessing the intrinsic two-electron coherence without any HBT contribution can be achieved by partitioning the electronic beam onto a beam splitter in an HBT setup (as we shall see on fig. 1.20). These current correlations are directly related to the inter-channel two-electron coherence right after the beam splitter since fermionic fields within different channels anticommute:

$$\langle i_{1\mathrm{out}}(t_1) i_{2\mathrm{out}}(t_2)\rangle = e^2 v_F^2 \Delta\mathcal{G}^{(2e)}_{\mathrm{out}}(1,t_1;2,t_2|1,t_1';2,t_2'). \tag{1.93}$$

Remarkably, this outgoing two-electron coherence is proportional to the incoming two-electron coherence [Thibierge et al., 2016]:

$$\Delta\mathcal{G}^{(2e)}_{\text{out}}(1,t_1;2,t_2|1,t_1';2,t_2') = RT\,\Delta\mathcal{G}^{(2e)}_{S}(t_1,t_2|t_1',t_2'). \tag{1.94}$$

Measuring outgoing inter-channel current correlations in the HBT setup thus directly probes the intrinsic excess coherence of the source, as in photon quantum optics.

1.6 Measuring electronic coherences

In this chapter, we have introduced the components of electron quantum optics, as well as the relevant theoretical quantities. As of now, we did not get interested in how we can measure those quantities in an experiment. The goal of this section is to provide a review of the different reconstruction methods for electronic coherences.

As in optics, the general way to reconstruct coherences is by making the unknown signal interfere, either with itself, or with a known probe signal. The first case is typical of amplitude interferometry experiments, that allows to probe the full coherence through time-resolved current measurement. The latest case is more typical of intensity interferometers, and allows to explore the full coherence through current noise measurements.

As we will see, the most reasonable tomography protocol to reconstruct the first-order coherence is based on intensity interferometers, which are somewhat immune to Coulomb interaction.

1.6.1 Tomography from single-particle interferometry

Introduction

In classical signal processing, linear filters transform time-dependent input signals into output signals under the constraint of linearity. Well known examples include linear circuit elements in classical electronics and linear optics elements such as lenses, beam splitters and other various optical devices. These components act as linear filters on the electromagnetic field classical coherence introduced in the 30s [Zernicke, 1938]. This statement also extends to quantum optics by considering quantum optical coherences introduced by Glauber [1963b].

In this section, we show that the same statement is true in electron quantum optics provided we use quantum conductors in which interaction effects can be neglected. As an example, we explain how the ideal Mach–Zenhder interferometer [Haack et al., 2011] or the measurement of the electronic distribution function using a quantum dot as an energy filter [Altimiras et al., 2010a] realize linear filtering of the excess single-electron coherence $\Delta\mathcal{G}^{(e)}_{\rho,x}(t,t')$, which should therefore be seen as a "quantum signal" depending on two times.

We will then briefly discuss why Coulomb interactions partly invalidate this linear optics picture and this will lead us to the discussion of two-electron interference-based tomography.

Mach–Zehnder interferometry

An ideal electronic Mach–Zehnder interferometer, such as the one depicted on fig. 1.19, is characterized by the times of flights $\tau_{1,2}$ along its two arms and the magnetic flux threading it $\Phi_B = \phi_B \times (h/e)$. When an electronic source S is placed on the incoming edge channel 1, the time-dependent outgoing electric current in channel 1 is directly proportional to the excess electronic coherence of the source [Haack et al., 2011; Ferraro et al., 2013]:

$$\langle i_{1\mathrm{out}}(t)\rangle = \sum_{j=1,2} \mathcal{M}_{j,j}\langle i_S(t-\tau_j)\rangle \tag{1.95a}$$

$$- 2e|\mathcal{M}_{1,2}| \int_{\mathbb{R}} \cos\left(\omega\tau_{12}+\phi\right) \Delta W_S^{(e)}(t-\bar{\tau},\omega)\,\frac{\mathrm{d}\omega}{2\pi}, \tag{1.95b}$$

where $\mathcal{M}_{i,j}$ denotes the product $\mathcal{A}_i\mathcal{A}_j^*$, $\mathcal{A}_j$ being the transmission amplitude of the beam splitters along path j of the interferometer. We have introduced $\tau_{12} = \tau_1 - \tau_2$, $\bar{\tau} = (\tau_1+\tau_2)/2$ and $\phi = \arg(\mathcal{M}_{1,2}) + 2\pi\phi_B$, which is the phase associated with both beam splitters and the magnetic flux. The first line (eq. (1.95a)) does not depend on the magnetic flux and therefore corresponds to classical propagation within each of the two arms of the MZI, whereas the second line (eq. (1.95b)) corresponds to quantum interferences between propagations within both arms. Because the average electric current is also proportional to the excess single-electron coherence of the source, the outgoing average current is obtained from the excess incoming coherence $\Delta\mathcal{G}_S^{(e)}$ in channel 1 by a linear filter which we write symbolically $\langle i_{\mathrm{out,dc}}\rangle = \mathcal{L}_{\mathrm{MZI}}[\Delta\mathcal{G}_S^{(e)}]$. Measurements of the Φ_B dependent part of the average d.c. current for various $\tau_1 - \tau_2$

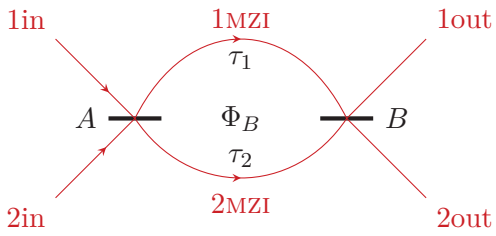

Figure 1.19: Schematic view of the Mach–Zehnder interferometer: the incoming channels are partitioned at the electronic beam splitter A and then recombined by the beam splitter B. Here τ_1 and τ_2 denote the times of flight across the two branches of the MZI and Φ_B the magnetic flux enclosed by the interferometer.

could then be used to reconstruct single-electron coherence [Haack et al., 2011].

Limits to single-particle interference tomography schemes

The key ingredient in this derivation is the absence of electronic interactions. Whenever one replaces the Mach–Zehnder interferometer by an ideal ballistic quantum conductor in which interactions are neglected, the outgoing current in the measurement lead would also be proportional to $\Delta\mathcal{G}_S^{(e)}$. Denoting by $\mathcal{S}(t_f, t_i)$ the scattering amplitude for an electron arriving into the conductor at time t_i and going out towards the measurement lead at time t_f, then the outgoing average time-dependent current is given by

$$\langle i_{\rm out}(t)\rangle = \int_{\mathbb{R}^2} \mathcal{S}(t,t_+)\,\mathcal{S}^*(t,t_-)\Delta\mathcal{G}_S^{(e)}(t_+,t_-)\,{\rm d}t_+{\rm d}t_-, \qquad (1.96)$$

which describes a linear filtering of the incoming single-electron coherence $\Delta\mathcal{G}_S^{(e)}$ associated with time-dependent scattering. In particular, this expression is valid within the framework of Floquet scattering theory [Moskalets, 2011].

A criterion for the validity of the electronic scattering theory approach to quantum transport at finite frequencies is that the frequency dependence of the electronic scattering matrix of a quantum conductor can be neglected [Blanter and Buttiker, 2000]. Single- to few-electron

excitations emitted by electron quantum optics sources such as the mesoscopic capacitor [Fève et al., 2007] or the Leviton source [Dubois et al., 2013a], as well as periodic electric currents generated using an advanced waveform generator, usually define a frequency scale in the range of one to few tens of gigahertz. On the other hand, an extended conductor such as a MZI has a scattering matrix varying over frequency scales of the order of the inverse of the time of flight of the conductor. For a 10 µm interferometer, it is of the order of 10 GHz or less for larger devices. These roughly equivalent energy scales fail to satisfy the criterion mentionned above.

The important stream of theoretical works on interaction-induced decoherence [Chalker et al., 2007; Neder et al., 2007; Levkivskyi and Sukhorukov, 2008; Neuenhahn and Marquardt, 2008; Kovrizhin and Chalker, 2009] in MZI interferometers illustrates the whole complexity of understanding interaction effects in such extended quantum conductors. More recent works [Tewari et al., 2016; Slobodeniuk et al., 2016] dealing with the propagation of individualized energy-resolved single-electron excitations in a MZI are directly relevant for electron quantum optics but also show that this problem is not yet fully understood even at the single-electron level. We will come back on the problem of Coulomb interaction induced decoherence in chapter 3 of this thesis.

By contrast, Coulomb interaction effects can be neglected over a much broader frequency range in the QPC which is an almost point-like electronic beam-splitter. As we shall see now, this plays a very important role for the intensity-based interferometry experiments.

1.6.2 Single-electron tomography from two-particle interferometry

Although amplitude interferometry relies on the measurement of average currents, it does not seem well suited to perform single-electron tomography. First of all, as in optics, it would require a perfect control on electronic optical paths down to the Fermi wavelength. More importantly, as briefly mentioned in the previous section, Coulomb interactions prevent reconstructing the incoming single-electron coherence from the experimental signals. In a simplified single-particle view, inelastic collisions can be viewed as random dephasing of each electronic wavefunctions that blurs single-particle interferences patterns.

Lessons from History

This situation is very similar to what happened in astronomy in the 30s and 40s: attempts at directly measuring the diameter of normal stars using amplitude interferometry were plagued by the random dephasing induced by atmospheric turbulences and by the technological challenge of building a large optical interferometer, which involves controlling optical paths tens of meters long with subwavelength precision.

A way to circumvent this bottleneck was found by Hanbury Brown and Twiss (HBT) in the 50s [Hanbury Brown and Twiss, 1956b]: their idea was to measure intensity correlations [Hanbury Brown and Twiss, 1956a] which contain interferences between waves emitted by pairs of atoms on the star. The whole point of their method is twofold: first of all, light intensity is immune to dephasing and therefore the problem of atmospheric dephasing is avoided. Next, intensity correlations can be done using electronics and do not require optical path control at subwavelength level.

It was however quite a surprise that interference patterns would be present in intensity correlations. Historically, Hanbury Brown and Twiss discussed intensity correlations in their stellar interferometer [Hanbury Brown and Twiss, 1956b] as well as in their table-top experiment [Hanbury Brown and Twiss, 1956a] in classical terms [Hanbury Brown and Twiss, 1957, 1958], a point that came as a surprise for some people. The interpretation in terms of two-particle interferences emerged a few years later [Fano, 1961]. The explanation for this effect came in the early 60s when Fano showed that the HBT effect ultimately relies on two-photon interferences. In the 80s, the Hong–Ou–Mandel (HOM) experiment [Hong et al., 1987] also demonstrated two-particle interferences for identical particles (photons). Since then, two-particle interference effects have been observed in many different contexts, from stellar interferometry to nuclear and particle physics [Baym, 1998] and more recently with bosonic as well as fermionic cold atoms [Jeltes et al., 2007]. Recent experiments demonstrate a higher degree of control by using independent single-photon [Beugnon et al., 2006] and single-atom sources [Lopes et al., 2015].

In this section, we review how the HOM experiment can be used to measure the overlap of the excess single-particle coherences arriving at a beam splitter. Remarkably, this result is true not only for electrons but for any fermionic or bosonic excitation. In photon quantum optics, it forms the basis of homodyne tomography [Smithey et al., 1993; Lvovsky

and Raymer, 2009] recently used to characterize few-photon states in the optical domain [Ourjoumtsev et al., 2006]. In the microwave domain, the HOM scheme has been used to access photon quantum optical correlations from electrical measurements [Bozyigit et al., 2011; Lang et al., 2013] and forms the basis of a tomography scheme for itinerant microwave photons [da Silva et al., 2010; Eichler et al., 2011].

As we shall see, exactly as in the days of Hanbury Brown and Twiss, HOM interferometry based tomography has the advantage of avoiding both the effects of Coulomb interactions within the detector and the need for optical-path control at sub-Fermi wavelength scale.

The noise is the signal

In electron quantum optics, the HBT and HOM experiments are demonstrated by sending electronic excitations generated by one or two electronic sources on an ideal electronic beam splitter, as depicted on fig. 1.20.

In order to make a precise analogy with photon quantum optics, keeping in mind that in electron quantum optics the vacuum is the reference Fermi sea and not a true vacuum, we consider that the electronic counterpart of the table-top HBT experiment (fig. 1.20a) is realized when one of the incoming channels is fed with the reference Fermi sea (S_1 or S_2 being off). By the same analogy, the electronic HOM experiment (fig. 1.20b) corresponds to situations with both electronic sources in the incoming channels switched on. Finally, contrary to photon quantum optics where the arrival of individual photons can be recorded, the quantities of interest in electronics are the current correlations at zero frequency in the two outgoing branches. An example of theoretical study of the HOM experiment with two mesoscopic capacitors can be found in [Ol'khovskaya et al., 2008].

Let us focus on the outgoing current noise in channel 1. A first important point is that the low-frequency current noise does not depend on the distance to the QPC: as will be discussed extensively in chapter 3, Coulomb interaction effects lead to edge-magnetoplasmon scattering among the various outgoing edge channels close to the one considered but the total power remains the same. This is why HBT/HOM interferometry is immune to interaction effects in the measurement stage (beyond the QPC). In the same way, the intensity correlations measured in an optical stellar HBT interferometer are not blurred by atmospheric turbulences.

Consequently, what we need is the excess low-frequency current noise just after the QPC when both sources S_1 and S_2 are switched on. It is

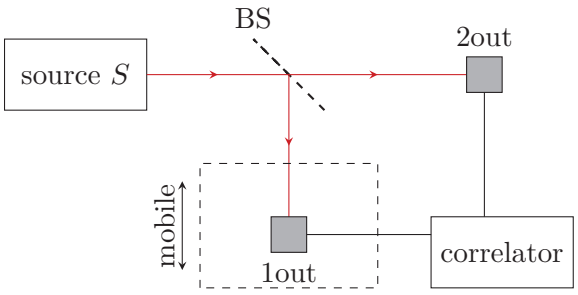

(a) The Hanbury Brown–Twiss experiment

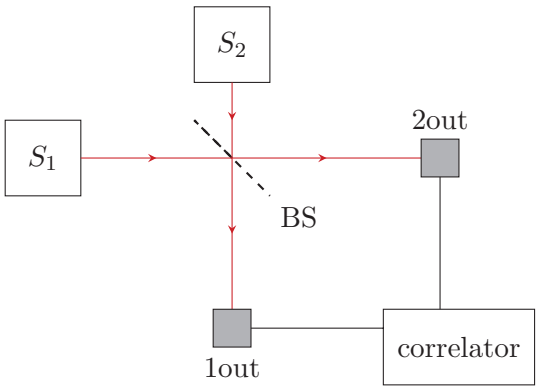

(b) The Hong–Ou–Mandel experiment

Figure 1.20: Principle of the HBT and HOM experiments: in the optical HBT experiment (a), excitations emitted by a single source S are partitioned at the beamsplitter BS whereas in the HOM experiment (b), excitations emitted by two sources S_1 and S_2 are sent onto BS. In optics, one performs a time-resolved detection of photons. In the electronic case, the beamsplitter is a QPC, and one measures current correlations between 1out and 2out or current noise in the 1out channel. In the case of the HBT experiment, vacuum is replaced by the reference Fermi sea.

the sum of three contributions [Ferraro et al., 2013]:

$$\Delta S_{11}^{(S_1\&S_2)} = \Delta S_{11}^{(S_1)} + \Delta S_{11}^{(S_2)} + \Delta S_{11}^{(\mathrm{HOM})}, \tag{1.97}$$

where $\Delta S_{11}^{(S_1)}$ and $\Delta S_{11}^{(S_2)}$ are the excess current noise when only the source S_j $(j = 1,\ 2)$ is switched on. These terms are given by:

$$\Delta S_{11}^{(S_1)} = e^2 T^2 \int_{\mathbb{R}} \overline{\Delta W_{S_1}^{(e)}(t,\omega)}^{t} \left(1 - 2f_{\mathrm{eq}}\right)(\omega) \frac{\mathrm{d}\omega}{2\pi}. \tag{1.98a}$$

$$\Delta S_{11}^{(S_2)} = e^2 R^2 \int_{\mathbb{R}} \overline{\Delta W_{S_2}^{(e)}(t,\omega)}^{t} \left(1 - 2f_{\mathrm{eq}}\right)(\omega) \frac{\mathrm{d}\omega}{2\pi}. \tag{1.98b}$$

where R and T denote the reflection and transmission probabilities of the QPC. They correspond to the excess noise in HBT experiments performed on each of the sources. Since $1 - 2f_{\mathrm{eq}}(\omega) = \tanh\left(\hbar\omega/2k_B T_{\mathrm{el}}\right)$ this expression counts the total number of excitations (electrons and hole) whose energy are above $k_B T_{\mathrm{el}}$ injected by the source S_j. When the other channel (called the probe) is at zero temperature, it is exactly the total number of excitations injected by S_j. This quantity has been measured for a single-electron source in quantum Hall edge channel in [Bocquillon et al., 2012].

The last term, called the HOM contribution since it requires both sources to be switched on, is given by

$$\Delta S_{11}^{(\mathrm{HOM})} = -2e^2 RT \int_{\mathbb{R}^2} \overline{\Delta W_{1\mathrm{in}}^{(e)}(t,\omega) \Delta W_{2\mathrm{in}}^{(e)}(t,\omega)}^{t} \frac{\mathrm{d}\omega}{2\pi}, \tag{1.99}$$

where $\overline{\cdots}^{t}$ denotes the average over time t. The HOM signal thus directly represents the overlap of the excess single-electron coherences arriving at the QPC [Ferraro et al., 2013]. Equation (1.99) encodes the effect of two-particle interferences between the excitations emitted by these sources. Note that the time delay of the two sources can be controlled and, therefore, a single experimental run gives access to the time-shifted overlaps of the excess electronic Wigner functions of the two sources. Finally, the minus sign comes from the fermionic statistics of electrons.

Our point here is to emphasize that the electronic HOM experiment automatically encodes into the experimental signal what the signal processing community would call the sliding inner product of the quantum signals formed by the incoming excess single-electron coherences in channels 1 and 2. This is why the HOM experiment is so important: it can be used to test for unknown excess electronic Wigner functions by looking

at their overlaps with themselves or with the ones generated by controlled and calibrated sources. This idea has been expanded to describe a generic tomography protocol for reconstructing an unknown excess single-electron coherence from its overlaps with coherences generated by suitable a.c. + d.c. drives, which we shall now describe.

Single-electron tomography protocol

Figure 1.21 presents the principle of the generic tomography protocol proposed in [Grenier et al., 2011a]: the source generating the unknown state, labeled by the subscript S, sends it on input 1 whereas input 2 is fed with a set of reference states called probe states and labeled $\{P_n\}, n \in \mathbb{N}$. The chirality of quantum Hall channels enables the spatial separation of the source and probe states at two distinct inputs of the splitter. The low-frequency current noise at the output of the splitter is the experimental signal. It probes the degree of indistinguishability between the source and probe states. To isolate the contribution of the source, the total excess noise ΔS at splitter output 3 between the on and off states of the source has been measured:

$$\Delta S = 2e^2 RT \int \frac{\mathrm{d}\omega}{2\pi} \left[\overline{\Delta W_S^{(e)}}^t (1 - 2f_{\mathrm{eq}}) - 2\overline{\Delta W_S^{(e)} \Delta W_{P_n}^{(e)}}^t \right], \quad (1.100)$$

where $\Delta W_{S/P_n}^{(e)}$ are respectively the source and probe excess Wigner distribution. As discussed before, the first term in eq. (1.100) represents the classical random partition noise of the source. It is reduced by the second term which represents two-particle interferences between source and probe related to the overlap between $\Delta W_S^{(e)}$ and $\Delta W_{P_n}^{(e)}$. By properly choosing the probe states, eq. (1.100) allows for the reconstruction of any unknown Wigner distribution.

The key point lies within the choice of the probes P_n, which has to satisfy the following requirements:

- By varying the experimental parameters on which the P_n depends, it is possible to reconstruct the unknown single-electron coherence, or equivalently $\Delta W_S(t, \omega)$.

- The probes must be chosen so that we can be sure of the single-electron coherence at the beam splitter despite possible interaction effects between the source generating P_n and the QPC.

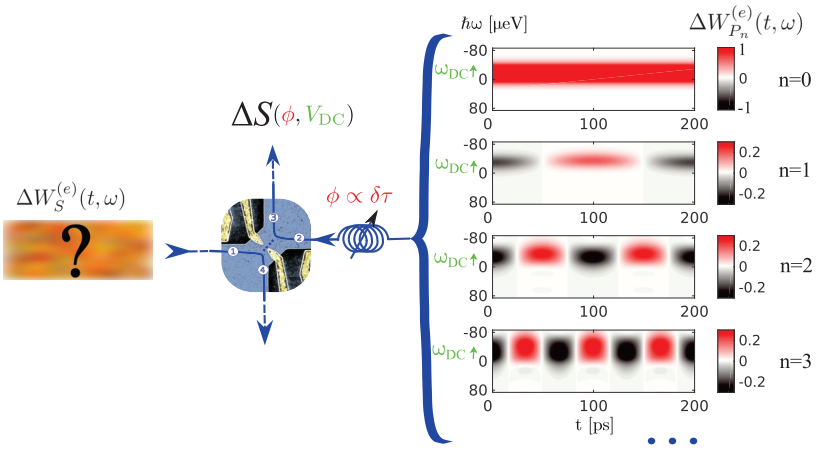

Figure 1.21: The unknown Wigner distribution $\Delta W_S^{(e)}(t,\omega)$ is sent into input 1. The probe signals $\Delta W_{P_n}^{(e)}(\omega)$ sent into input 2 are plotted for $n = 0$ to $n = 3$ (the frequency $f = 5\,\text{GHz}$ and the electronic temperature is $T_{\rm el} = 80\,\text{mK}$). The excess noise ΔS is measured in output 3 as a function of the d.c. bias $\omega_{\rm DC}$ and the phase difference ϕ between the source and probe signals.

It turns out, as shown in [Grenier et al., 2011a], that there exists a natural choice satisfying both requirements.

Accessing the stationary part of $\Delta W_S^{(e)}$ has been known for a long time. This was the idea of shot noise spectroscopy [Shytov, 2005; Kozhevnikov, 2001]: by varying the probe's chemical potential, we can probe which states are filled or empty in the source channel. This suggests to use an equilibrium reservoir whose chemical potential $\mu_P = -eV_{\rm DC}$ is experimentally controlled by a d.c. bias voltage. Using eq. (1.100), the excess electronic distribution function $\Delta W_{S,n=0}^{(e)}(\omega)$ can be obtained via the derivative of ΔS with respect to the d.c. bias $\omega_{\rm DC} = -eV_{\rm DC}/\hbar$ applied on the probe port. More explicitly, we define the experimental data

$$\Delta\widetilde{W}_{S,0}^{(e)} = -\frac{\pi}{2e^2RT}\frac{\partial\Delta S}{\partial\omega_{\rm DC}}, \tag{1.101}$$

which does not provide directly $\Delta W_{S,0}^{(e)}$ but its convolution with the

thermally-broadened function $\left(-\frac{\partial f_{\rm eq}}{\partial \omega}\right)$:

$$\Delta\widetilde{W}^{(e)}_{S,0} = \int_{\mathbb{R}} \Delta W^{(e)}_{S,0}\left(\omega\right)\left(-\frac{\partial f_{\rm eq}}{\partial \omega}\right)\left(\omega-\omega_{\rm DC}\right)\,{\rm d}\omega. \tag{1.102}$$

During his PhD, Arthur Marguerite has introduced a deconvolution technique based on Wiener filtering [Marguerite, 2017] to reconstruct $\Delta W^{(e)}_{S,0}(\omega)$ from the measurement of $\Delta\widetilde{W}^{(e)}_{S,0}$.

Accessing the time dependence of $W^{(e)}(t,\omega)$ requires measuring non-zero harmonics $\Delta W^{(e)}_{S,n\neq 0}$. Following eq. (1.100), accessing the n-th harmonic requires a probe P_n whose Wigner distribution evolves periodically in time at frequency nf. At low amplitude of the drive, the Wigner distribution of the probe depends linearly on the probe voltage $V_{P_n}(t)$, such that $V_{P_n}(t) = V_{P_n}\cos(2\pi nft+\phi)$ allows one to extract $\Delta W^{(e)}_{S,n}$. Indeed, in this linear regime, the excess Wigner distribution of the probe are given by eq. (1.73). In the present case, taking into account frequency nf and dephasing ϕ, we have

$$\Delta W^{(e)}_{P_n}(t,\omega) = \frac{eV_{P_n}}{\hbar}\cos\left(2\pi nft+\phi\right)F_n\left(\omega-\omega_{\rm DC}\right), \tag{1.103}$$

with $F_n(\omega) = \Big(f_{\rm eq}(\omega+n\pi f) - f_{\rm eq}(\omega-n\pi f)\Big)/(2\pi nf)$. The corresponding $\Delta W^{(e)}_{P_n}$ for $n=1$ to $n=3$ are plotted on fig. 1.21. Changing the phase ϕ allows us to access both the real and imaginary parts of the harmonics $\Delta W^{(e)}_{S,n}(\omega)$ at a given ω whereas the width of $\Delta W^{(e)}_{P_n}$ along the energy axis is fixed by the width of F_n, given by the maximum of k_BT and nhf. As in the $n=0$ case, varying a d.c. bias $V_{\rm DC}$ on top of the a.c. probe excitation enables scanning the energy axis. More explicitely, the noise signal enables us to reconstruct the experimental data set

$$\Re\left(\Delta\widetilde{W}^{(e)}_{S,n}\right) = \frac{h}{8e^3V_{P_n}RT}\left(\Delta S_{\phi=\pi}-\Delta S_{\phi=0}\right), \tag{1.104a}$$

$$\Im\left(\Delta\widetilde{W}^{(e)}_{S,n}\right) = \frac{h}{8e^3V_{P_n}RT}\left(\Delta S_{\phi=\frac{3\pi}{2}}-\Delta S_{\phi=\frac{\pi}{2}}\right), \tag{1.104b}$$

which is related to the harmonics we are looking for by a convolution with a thermal broadening:

$$\Re\left(\Delta\widetilde{W}^{(e)}_{S,n}\right) = \int_{\mathbb{R}}\Re\left(\Delta W^{(e)}_{S,n}\left(\omega\right)\right)\,g_n(\omega-\omega_{\rm DC})\,{\rm d}\omega, \tag{1.105a}$$

$$\Im\left(\Delta\widetilde{W}^{(e)}_{S,n}\right) = \int_{\mathbb{R}}\Im\Big(\Delta W^{(e)}_{S,n}\left(\omega\right)\Big)\,g_n(\omega-\omega_{\rm DC})\,{\rm d}\omega. \tag{1.105b}$$

The real and imaginary parts of $\Delta W_{S,n}^{(e)}$ are thus reconstructed using the Wiener filtering deconvolution technique as discussed in [Marguerite, 2017].

Experimental state of the art

The electronic HBT experiment has been demonstrated in the late 90s using d.c. sources [Oliver et al., 1999; Henny et al., 1999] and more recently using single-electron sources [Bocquillon et al., 2012] which were then used to perform the electronic HOM experiment [Bocquillon et al., 2013a]. These experiments have paved the way to measurements and studies of electron decoherence down to the single-electron level through HOM interferometry.

As reviewed in [Marguerite et al., 2016a], the HOM experiment has recently been used to probe interaction effects within quantum Hall edge channels. In these experiments, performed at filling factor $\nu = 2$, two single-electron sources are located at some distance of the QPC and interaction effects are strong enough to lead to quasi-particle destruction, as suggested by energy relaxation experiments [Le Sueur et al., 2010]. First, the HOM effect was used to probe how interactions lead to fractionalization of classical current pulses [Freulon et al., 2015] in qualitative agreement with the neutral/charge edge-magnetoplasmon mode model [Levkivskyi and Sukhorukov, 2008] which had been already probed through energy relaxation experiments [Degiovanni et al., 2010] and high-frequency admittance measurements [Bocquillon et al., 2013b]. But the real strength of HOM experiment comes from its ability to probe electronic coherence in a time- and energy-resolved way. It was thus recently used to study quantitatively the effect of Coulomb interactions on energy-resolved single-electron excitations (Landau excitations) [Marguerite et al., 2016b]. The experimental data confirm theoretical predictions and validate the decoherence scenario based on edge-magnetoplasmon scattering [Wahl et al., 2014; Ferraro et al., 2014b] which will be discussed extensively in chapter 3 of this thesis.

The idea of the tomography protocol has been recently demonstrated by D.C. Glattli's group [Jullien et al., 2014]: in this experiment, a stream of Lorentzian pulses is sent onto a beam splitter whose other incoming channel is fed with a small a.c. drive on top of a d.c. bias. Measurement of the low-frequency noise then enables reconstructing the photo-assisted transition amplitudes which, in this case, contain all the information on single-electron and higher-order electronic coherences [Dubois et al.,

2013a]. This experiment being performed in a 2DEG at zero magnetic field, interaction effects can be neglected and the experiment leads to the reconstruction of the Leviton single-electron coherence [Jullien et al., 2014]. Although this work provides a proof of principle that single-electron tomography is possible, this is not a full fledged implementation of the generic tomography protocol presented here since it relies on the knowledge that the single-electron coherence is determined by photoassisted tunneling amplitudes and on the hypothesis that the incoming electronic state is the finite-temperature version of a state obtained by adding exactly one single-electron excitation on top of the Fermi sea. However, this work beautifully demonstrates that the required levels of sensitivity in current-noise measurements for single-electron tomography have been reached.

A full implementation of the generic tomography protocol that assumes nothing on the state generated by the source S has been performed by G. Fève's group during A. Marguerite's PhD. It forms the first stage of a quantum electrical current analyzer able to extract all information on single-particle wavefunctions present within a given quantum electrical current. This will be the central topic of the next chapter of this thesis.

1.6.3 Probing two-electron coherence through two-particle interferometry

Let us finally discuss how to probe and access the intrinsic second-order coherence of an electronic source. Although much less advanced on the experimental side, this line of research is important in order to be able to quantify entanglement in electronic systems.

On the theory side, the analysis is not as advanced as for single-electron tomography. In particular, we shall only discuss protocols that are based on direct two-particle interferences and which shall thus be seen as counterparts of MZI at the two-electron level.

Even if current correlations in the HBT geometry only give access to the diagonal part of the intrinsic two-electron coherence in the time domain, eq. (1.93) naturally leads to a general idea for accessing the off-diagonal part $\Delta\mathcal{G}_S^{(2e)}(t_1,t_2|t_1',t_2')$ for $(t_1,t_2)\neq(t_1',t_2')$. The idea is to use linear filters of single-electron coherence as depicted on fig. 1.22. Let us assume that the outgoing current is obtained from a linear filtering of the incoming single-electron coherence $\langle i_A\rangle = \mathcal{L}_A\left[\Delta\mathcal{G}_{1\text{in}}^{(e)}\right]$ with a similar relation for detector B. Then, the outgoing current correlations $\langle i_A\, i_B\rangle$

are obtained by applying a linear filter to the incoming two-electron coherence:

$$\langle i_A\, i_B \rangle = RT \left(\mathcal{L}_A^{(1)} \otimes \mathcal{L}_B^{(2)} \right) \left[\Delta \mathcal{G}_S^{(2e)} \right] \tag{1.106}$$

in which eq. (1.94) has been used to obtain eq. (1.106).

Despite its compacity, eq. (1.106) unifies many different experiments under a simple physical interpretation: the intrinsic two-electron coherence $\Delta \mathcal{G}_S^{(2e)}$, describing two-particle excitations emitted by the source, is encoded into current correlations $\langle i_A\, i_B \rangle$ via an HBT interferometer and two linear filters for single-electron coherence.

In the absence of these filters, the measurement of current correlations gives information on the diagonal part of $\Delta \mathcal{G}_S^{(2e)}$ as seen in section 1.5.4. When A and B are electronic energy filters, and assuming that no electronic relaxation process takes place between the QPC and the filters (see the discussion in section 1.6.1), we access the diagonal part of $\Delta \mathcal{G}_S^{(2e)}$ in the frequency domain.

It also naturally leads to the idea of the Franson interferometer [Franson, 1989] originally invented to test photon entanglement [Brendel et al., 1999; Marcikic et al., 2002] and later considered for testing two-particle Aharonov-Bohm effect and electronic entanglement generation [Splettstoesser et al., 2009]. It is a natural way to probe the off-diagonal part of $\Delta \mathcal{G}_S^{(2e)}$ in the time domain since, as explained in section 1.6.1, a MZI converts single-electron coherences in the time domain into electrical currents. This example is detailed in [Thibierge et al., 2016] and with great details in É. Thibierge's thesis [Thibierge, 2015].

1.7 Summary

In this chapter, we have presented the electron quantum optics formalism based on the study of electronic coherences. Combined with the Landauer–Büttiker scattering formalism for electronic quantum transport and the importance of Coulomb interactions viewed as a source of electron quantum optics non-linear effects, a clear analogy between photon and electron quantum optics emerges, as well as a good insight of their differences.

In the last section of this chapter, we have presented various protocols for measuring or probing single- and two-electron coherence, stressing the importance of two-particle interferences for single-electron tomography. Beyond this point, our presentation emphasizes that all these experiments

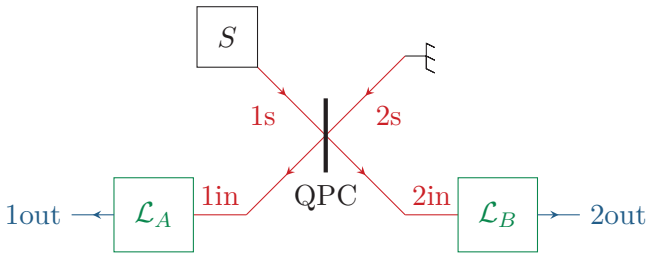

Figure 1.22: A generalized Franson interferometry experiment: the electron flow emitted by the source S is partitioned at the QPC and sent into two linear filtering components A and B. Current correlations between outgoing currents give access to second-order electronic coherence. Franson interferometry corresponds to use two Mach–Zehnder interferometers for A and B.

can be interpreted in the signal processing language as performing analog operations such as linear filtering or overlaps on quantum signals (the intrinsic single- or two-electron coherences) and encode the results into experimentally accessible quantities such as average currents and current correlations. This vision is summarized on fig. 1.23.

As a consequence of this vision, which I have developed in [Roussel et al., 2017], the electronic coherences appear as a quantum signal by themselves. After all, this is a natural step from the point of view described in section 1.3 of the present chapter: the amplitude of a classical electromagnetic field is an historical example (among many others) of a classical signal for which signal-processing techniques have been developed. But characterizing the quantum states of the electromagnetic fields requires knowing much more, and photonic coherences contain the information on fluctuations (quantum and classical) of the quantum electromagnetic field. In electron quantum optics, there is no classical amplitude of the electronic field because of superselection rules, so we have to deal with electronic coherences as the quantum signals characterizing the quantum state of the electronic fluid.

Considering electronic coherences, starting with single-electron coherence, as quantum signals raises the question of representing those signals in the simplest way. As stressed in the introduction of this thesis, the main problems in signal processing are to find techniques for detecting, filtering, representing, transmitting, and finally extracting information or recognize patterns within signals. This naturally brings us to the

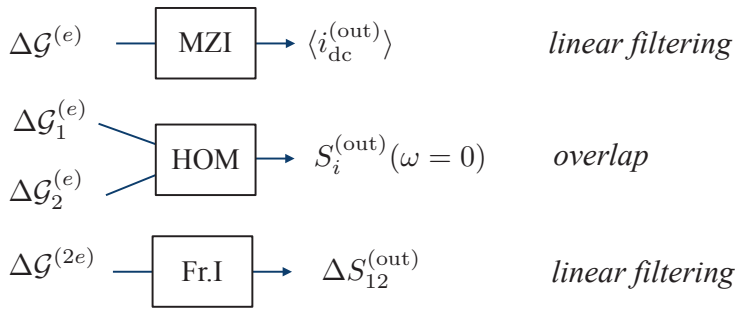

Figure 1.23: Representation of single- and two-electron quantum tomography protocol as analog operations performed in the excess single- and two-electron coherences. Mach–Zehnder interferometry (MZI) is a linear filtering operation on $\Delta\mathcal{G}^{(e)}$. Single-electron tomography based on two-particle inteferences (HOM) performs the overlap of an unknown excess single-electron coherence with a known one. Finally, Franson interferometry (Fr.I) is similar to MZI as it performs a linear filtering operation on $\Delta\mathcal{G}^{(2e)}$.

next chapter of my thesis where I precisely show how to represent in the simplest possible way single-electron coherence and what information can be extracted from such a representation.

Chapter 2

Signal processing for electron coherence

2.1 Introduction

The goal of this chapter is to present a signal-processing technique which can answer the following general question: what are the elementary single-particle excitations present in a quantum electrical current?

Single-electron coherence introduced in section 1.4 is the container of all single-particle physics within a quantum electrical current. What we will present here is an algorithm that extracts from this quantum signal a possible representation of it in terms of single-electron wavefunctions, their emission probabilities and their coherences. Because of electrons indiscernability, such a representation is not unique, but we shall see that some representations are physically more appealing than others.

For the sake of pedagogy, we will start by showing how specific builds of few-particle excitations on top of the Fermi sea manifest themselves on single-electron coherence and more specifically on its Wigner function representation. This will invite us to search for a specific representation of the single-electron coherence in terms of a notion of electronic atoms of signals, which I have introduced inspired by a similar notion described in Michel Devoret's lecture for describing photons propagating within a transmission line.

Then, in sections 2.3 and 2.4, I will present the algorithm for finding representations of single-electron coherence in terms of electronic atoms of signal for a time-periodic source. This procedure is based on the transposition of Bloch theory for bands in solids to the context of electron

quantum optics.

In section 2.5, I will discuss a specific class of many-body electronic states which are the ones obtained by perturbing in a unitary way a Fermi sea. These are known in the mathematical litterature as the infinite Grassmanian [Kac, 1990]. In this case, we will show how our algorithm does indeed find a simple parametrization of these states and how the data extracted from it can be used to quantify entanglement between the electron and hole part of the many-body state of the system. Applications to the diagnosis of single-electron sources will be presented in section 2.6.

Finally, in section 2.7, I will present an application of this algorithm to experimental data. This indeed realizes the demonstration of an on-chip quantum electrical current analyzer combining two-particle interferometry with signal-processing techniques to find the single-particle content of a quantum electrical current without any assumption on the many-body electronic state beyond time periodicity.

2.2 Arithmetics of single-electron coherence

Before we dig deeper into the subject of the recognition of elementary wavefunctions contained in first-order coherence, we will see how we can add up elementary excitations to create any generic coherence. It will provide some intuition about interference pattern that can be seen onto Wigner function.

2.2.1 Basic building blocks

Single electron, single hole

We have already discussed the contribution to coherence of a single electron in section 1.4.4. We will discuss here a bit more evolved wavepackets that we can form from a superposition of two wavepackets.

Let us consider a wavefunction $\varphi(t)$ that is a superposition of two other orthogonal wavepackets $\varphi_1(t)$ and $\varphi_2(t)$. We have

$$\varphi(t) = \sqrt{p}\,\varphi_1(t) + \sqrt{1-p}\,\mathrm{e}^{\mathrm{i}\theta}\varphi_2(t). \tag{2.1}$$

In this case, excess first-order coherence is the coherence given by each wavefunction, plus another term which is, as we will see, an interference

term:

$$\begin{aligned}\Delta\mathcal{G}^{(e)}_{\varphi}(t_1,t_2) = p\,\mathcal{G}^{(e)}_{\varphi_1}(t_1,t_2) + (1-p)\,\mathcal{G}^{(e)}_{\varphi_2}(t_1,t_2)\\ + 2\Re\left(\sqrt{p(1-p)}\mathrm{e}^{\mathrm{i}\theta}\varphi_1^*(t_2)\varphi_2(t_1)\right).\end{aligned} \tag{2.2}$$

For electrons localized at times t_1 and t_2, the last term will contribute to Wigner functions by adding an interference fringe at the average of t_1 and t_2, whose frequency is the inverse of time difference. In a more general way, if we consider two wavepackets centered around (t_1,ω_1) and (t_2,ω_2), interference fringes will be at the middle of those two points.

Such a general superposition is, indeed, very difficult to obtain experimentally, with sources that exist. However, provided we can neglect interaction, it is quite easy to use Mach–Zehnder interferometer with disbalanced paths to generate a superposition between one wavepacket and itself that is time shifted. The phase φ can be tuned through the Aharonov phase of the interferometer. To obey orthogonality condition, the disbalance of times of flight τ must be greater than the typical scale of the wavepacket. In this case, it is also easy to give an expression for the Wigner function of such a state. If we suppose that $\varphi_1(t) = \varphi_0(t-\tau/2)$ and $\varphi_2(t) = \varphi_0(t+\tau/2)$ we have:

$$\Delta\mathcal{W}^{(e)}_{\varphi}(t,\omega) = p\,\Delta\mathcal{W}^{(e)}_{\varphi_0}(t-\tau/2,\omega) \tag{2.3a}$$

$$+ (1-p)\,\Delta\mathcal{W}^{(e)}_{\varphi_0}(t+\tau/2,\omega) \tag{2.3b}$$

$$+ 2\sqrt{p(1-p)}\,\cos(\omega\tau-\theta)\Delta\mathcal{W}^{(e)}_{\varphi_0}(t,\omega). \tag{2.3c}$$

We recover contributions of φ_1 and φ_2 from eqs. (2.3a) and (2.3b). Interferences are clearly shown by term (2.3c). To illustrate this discussion, we will start on fig. 2.1 by considering this realistic case for LPA wavefunctions given by eq. (1.45) page 55.

We can consider a more generic case, where the wavepacket is made by a superposition of the same wavefunctions shifted both in time and in energy. Thus, $\varphi_1(t) = \exp(-\mathrm{i}\delta\omega\tau/2)\varphi_0(t-\tau/2)$ and $\varphi_2(t) = \exp(\mathrm{i}\delta\omega\tau/2)\varphi_0(t+\tau/2)$. We can therefore extend eq. (2.3):

$$\Delta\mathcal{W}^{(e)}_{\varphi}(t,\omega) = p\,\Delta\mathcal{W}^{(e)}_{\varphi_0}(t-\tau/2,\omega-\delta\omega/2) \tag{2.4a}$$

$$+ (1-p)\,\Delta\mathcal{W}^{(e)}_{\varphi_0}(t+\tau/2,\omega+\delta\omega/2) \tag{2.4b}$$

$$+ 2\sqrt{p(1-p)}\,\cos(\omega\tau-\delta\omega t-\theta)\,\Delta\mathcal{W}^{(e)}_{\varphi_0}(t,\omega). \tag{2.4c}$$

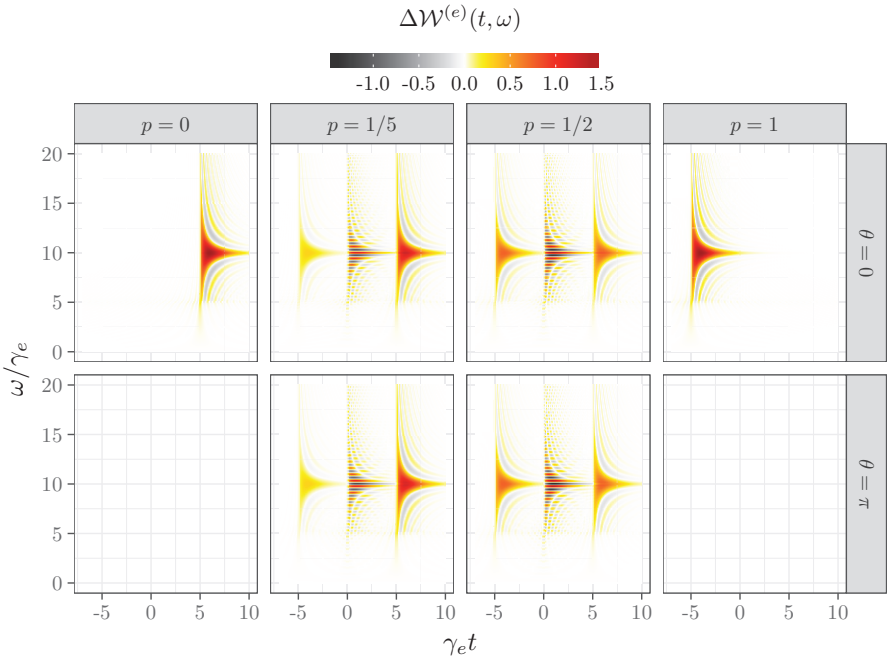

Figure 2.1: Wigner function of a time-shifted superposition of Lorentzian wavepackets. Wigner function is depicted for $\theta = 0, \pi$ and $p = 0, 1/2, 4/5, 1$. We have chosen a splitting time $\gamma_e \tau = 10$.

We can see an example of this case for orthogonal Martin–Landauer wavepackets on fig. 2.2. We distinguish clearly the two initial Martin–Landauer wavepackets and interference fringes between them. Isophase lines for fringes are parallel to the line that connects the center of each wavepacket.

It is straightforward to transpose this discussion for single-electron excitations to single-hole excitations. Basically, everything is similar, except that we are not building coherences by filling up the vacuum above the Fermi surface, but by depleting the Fermi sea. This does not change interference patterns and their behavior.

Coherent electron/hole excitation

The last single-particle excitation we have seen in the last chapter was the coherent electron/hole excitation. Since it is an excitation that is delocalized between positive and negative energies, we can expect to

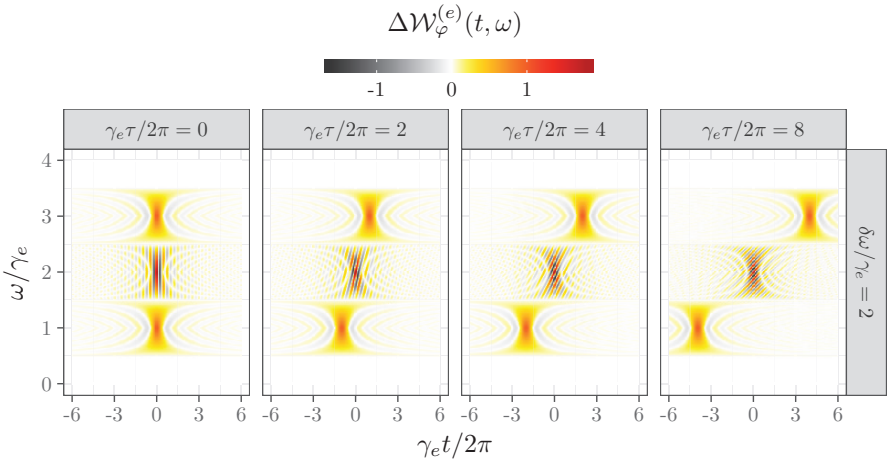

Figure 2.2: Wigner function of a time and frequency shifted superposition of Martin–Landauer wavepacket. The splitting frequency is $\delta\omega = 2\gamma_e$, and the splitting times are $\gamma_e\tau/2\pi = 0, 2, 4, 8$.

observe interference fringes around the Fermi surface, between blobs located above and below the Fermi surface (provided the two wavefunctions composing the electron/hole pair are located away of Fermi energy). This can be viewed on fig. 2.3.

Combining simple blocks

We have shown the elementary blocks that can be formed by a single-electron excitation. Those blocks are what we will need to build a general coherence. Of course, provided that wavefunctions forming the basic excitations are orthogonal, it is possible to sum up their excess coherences to the Fermi sea contribution. The object we form is then still a first-order coherence. But it is also possible to add a statistical weight to each of these contributions. This would be the case for a non-pure state, for example, or a state that exhibits higher-order coherences, such as entangled two-electron states.

Actually, if we allow not only wavefunctions but also (non-normalized) modes, and we start from $T = 0\,\mathrm{K}$ Fermi sea, we can reach any first-order coherence, from a collection of orthogonal modes, with associated probabilities. The goal of the next section is to show the reverse process, how we can extract the relevant modes from an arbitrary given single-electron coherence in a time-periodic context. Then, we define a relevant

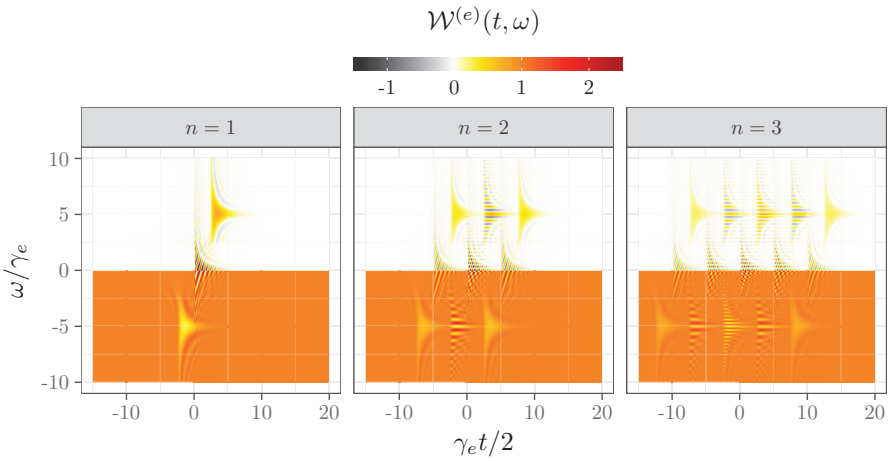

Figure 2.3: Wigner function of a balanced electron/hole excitation. n is the number of superpositions for the hole and electron wavefunctions. We thus have n electronic and n hole wavefunctions present in the superposition.

notion of wavefunctions.

2.2.2 Electron and hole trains

An ideal periodic single-electron source is a periodically operated device that emits exactly one single-electron excitation on top of the Fermi sea during each period. The corresponding many-body state is an electron train of the form

$$|\Psi_{\mathrm{SES}}\rangle = \prod_{l\in\mathbb{Z}} \psi^\dagger[\varphi_{e,l}]|F_{\mu=0}\rangle, \tag{2.5}$$

where the electronic wavefunction $\varphi_{e,l}$ differs from $\varphi_{e,l=0}$ by translation by lT in the time domain. Ideally, one would like each of these electronic excitations to be perfectly distinguishable from the others which means that $\varphi_{e,l}$ and $\varphi_{e,l'}$ are orthogonal as soon as $l \neq l'$. In this case, the excess single-electron coherence is

$$\Delta\mathcal{G}^{(e)}_{\mathrm{SES}}(t,t') = \sum_{l=-\infty}^{+\infty} \varphi_{e,l}(t)\,\varphi^*_{e,l}(t'). \tag{2.6}$$

Ideally, at its optimal operating point the mesoscopic capacitor [Fève et al., 2007; Mahé et al., 2008] generates one electronic excitation and

one hole excitation per period

$$|\Psi_{\rm LPA}\rangle = \prod_{l=-\infty}^{+\infty} \psi^\dagger[\varphi_{e,l}]\psi[\varphi_{h,l}]\,|F_{\mu=0}\rangle, \tag{2.7}$$

where $\varphi_{e,l}$ and $\varphi_{h,l}$ are time-translated by lT from the electronic wavefunction $\varphi_{e,0}$ and the hole wavefunction $\varphi_{h,0}$. These single-particle states form an orthonormal family and consequently, the excess single-electron coherence is then given by

$$\Delta\mathcal{G}^{(e)}_{\rm LPA}(t,t') = \sum_{l=-\infty}^{+\infty} \varphi_{e,l}(t)\,\varphi^*_{e,l}(t') - \sum_{l=-\infty}^{+\infty} \varphi_{h,l}(t)\,\varphi^*_{h,l}(t'), \tag{2.8}$$

where the hole contribution naturally comes with a minus sign. When closing the dot too much, it was argued [Grenier et al., 2011a] that, during each period, the mesoscopic capacitor emits a quantum superposition of no excitation and an elementary electron/hole pair. Such a state would be parametrized as

$$|\Psi_{\rm e/h}(u,v)\rangle = \prod_{l=-\infty}^{+\infty} \Big(u + v\psi^\dagger[\varphi_{e,l}]\psi[\varphi_{h,l}]\Big)\,|F_{\mu=0}\rangle, \tag{2.9}$$

where $|u|^2 + |v|^2 = 1$. The resulting single-electron coherence is then

$$\Delta\mathcal{G}^{(e)}_{\rm e/h}(t,t') = \sum_{l=-\infty}^{+\infty} \big[|v|^2\varphi_{e,l}(t)\varphi^*_{e,l}(t') - |v|^2\varphi_{h,l}(t)\varphi^*_{h,l}(t')\big] \tag{2.10a}$$

$$+ \sum_{l=-\infty}^{+\infty} \big[u\,v^*\varphi_{e,l}(t)\varphi^*_{h,l}(t') + v\,u^*\varphi_{h,l}(t)\varphi^*_{e,l}(t')\big], \tag{2.10b}$$

in which the right-hand side of eq. (2.10a) lives in the quadrants of electronic and hole excitations whereas eq. (2.10b) represents the electron/hole pair coherence arising from $|\Psi_{\rm e/h}(u,v)\rangle$ whenever $uv \neq 0$. Equation (2.8) is recovered for $(u,v) = (0,1)$ which should therefore correspond to $D \simeq D_{\rm opt}$ whereas for $(u,v) = (1,0)$ one recovers the Fermi sea, the result expected when the dot is totally closed ($D = 0$). The case where $|u|^2 = |v|^2 \simeq 1/2$ could thus be viewed as an idealized description of the electronic coherence emitted by the mesoscopic capacitor at some intermediate value of D between zero and $D_{\rm opt}$. It corresponds to maximal electron/hole entanglement [Roussel et al., 2017]. We will see in section 2.6 why this proposed description fails at low D.

Equations (2.6), (2.8) and (2.10) correspond to ideal sources and have a simple expression in terms of a family of single-electron wavefunctions called *electronic atoms of signal*. This notion introduced in [Roussel et al., 2017] is directly inspired from M. Devoret's analogous notion for photon propagating within a coaxial cable [Devoret, 2008]. It consists in a family of normalized mutually orthogonal single-electron wavefunctions $\varphi_{a,l}$ which are translated by multiples of T:

$$\varphi_{a,l}(t) = \varphi_{a,0}(t - lT) \tag{2.11a}$$

$$\langle \varphi_{a,l} | \varphi_{a',l'} \rangle = \delta_{l,l'} \delta_{a,a'}. \tag{2.11b}$$

An important question is thus to determine whether or not there are generalizations of expressions (2.6), (2.8) and (2.10) for generic periodic electronic sources.

The answer is known to be positive in the case of the periodic train of Leviton source and the corresponding wavefunctions have been identified analytically by Moskalets [2015]. This work shows that the appropriate atoms of signal depend on the ratio of the pulse widths to the period, $\tau_0/T = f\tau_0$, as could be expected since we are imposing orthogonality for two different periods. When the pulses are well separated ($f\tau_0 \ll 1$) one expects the overlap between the Moskalets electronic atoms of signal and the isolated Leviton wavefunction introduced in section 1.4.4, page 58

$$\varphi_{1,0}(t) = \sqrt{\frac{\tau_0}{\pi v_F}} \frac{1}{t + \mathrm{i}\tau_0} \tag{2.12}$$

to go to unity. However, what happens for different values of the charge per pulse q? When $q = -ne$ with n positive integer, it is expected that the emitted single-electron coherence can be written in terms of atoms of signal under a form similar to eq. (2.6) except that there would be n mutually orthogonal electronic single-electron states. But as of now, these wavepackets are not known except for $n = 1$. Moreover, when n is not an integer, the Lorentzian pulse train contains many electron/hole pairs. In this case, can we find a simple decomposition of $\Delta\mathcal{G}^{(e)}$ involving electronic as well as hole atoms of signal?

For the mesoscopic capacitor driven by a square voltage and operated optimally [Fève et al., 2007], the atoms of signal are expected to be close to Lorentzian wavefunctions in energy, truncated to a half period $[0, T/2]$, projected on the space of electronic wavefunctions and finally normalized. Such an heuristic choice of electronic wavefunctions has recently been introduced [Roussel et al., 2017] to test for the form given by eq. (2.8) or

(2.10) depending on the operation point. This study already gave a strong indication that more atoms of signals were needed to fully reproduce the electronic coherence computed from Floquet scattering theory.

The truth is that realistic sources are, in general, not ideal: first of all, at non-zero temperature, spurious electron/hole pairs may be generated from thermal fluctuations. Moreover, even at zero temperature, decompositions of the form discussed in this section appear to correspond to ideal operating regimes that are only asymptotic with respect to the experimental parameters. Last but not least, when electronic coherence is measured at some distance from such a source, Coulomb interactions alter the electronic coherence in a drastic way [Marguerite et al., 2016b].

This raises the question of finding a way to express an arbitrary periodic single-electron coherence in terms of suitable electronic atoms of signals. We will now present a systematic procedure for obtaining such an expression together with the appropriate electronic atoms of signals from single-electron coherence. Let us stress once again that our procedure can be applied to data obtained from a numerical computation as well as to experimental data obtained from an electronic tomography protocol such as the one described in section 1.6.2.

2.3 The Floquet–Bloch spectrum

In this section and the next one, we will describe how we can find electronic wavefunctions contained in a quantum signal. As stated earlier, this procedure is similar to Bloch theory. In Bloch theory, people are interested in the energies taken by a single stationary electron. Those energies take the form of energy bands, and those bands arise from the structure of the Hamiltonian, which possesses the space periodicity of the crystal. Essentially, the procedure to obtain energy bands is to diagonalize the Hamiltonian.

In this section, we will explain how we can translate this approach to obtain what we will call the Floquet–Bloch spectrum, which will contain the probabilities for the eigenmodes contained in the system. For this, we will introduce another mathematical representation of the coherence, as an operator. This way, the analogy with Bloch theory will be more obvious.

2.3.1 Single-electron coherence as an operator

We will here introduce the main object that we will use throughout this chapter. For now, we have worked with first-order coherence in different representations, but we have always considered it as a two-variable function. Here we will adopt a new point of view, that is to consider the first-order coherence as an operator. A big advantage of this point of view, is that it unifies the different representations we have seen, by regrouping them into a single, basis-independent object.

To define the single-electron coherence operator, we will use its time representation. Introducing localized single-particle states $|t\rangle$ such that $\langle t|t'\rangle = v_F^{-1}\delta(t-t')$, we introduce the dimensionless Hermitian operator $\mathbf{G}^{(e)}_{\rho,x}$ by

$$\langle t|\mathbf{G}^{(e)}_{\rho,x}|t'\rangle = \mathcal{G}^{(e)}_{\rho,x}(t,t'). \tag{2.13}$$

It is of course possible to obtain the frequency representation, by introducing frequency-localized orthogonal single-particle states $|\omega\rangle$ (see appendix A.3). In this case, we have

$$\mathcal{G}^{(e)}_{\rho,x}(\omega,\omega') = \langle\omega|\mathbf{G}^{(e)}_{\rho,x}|\omega'\rangle. \tag{2.14}$$

Before we concentrate on time-periodic systems, let's see how we can translate the properties given in section 1.4 for the operatorial point of view.

We have seen on eq. (1.14) that we have a conjugation relation for first-order coherence. This ensures, notably, that the probability to find an electron in a given state is real. In terms of operators, it means that $\mathbf{G}^{(e)}_{\rho,x}$ is Hermitian. Furthermore, if we introduce the single-particle state $|\varphi\rangle$ corresponding to an excitation described by wavefunction φ

$$|\varphi\rangle = v_F \int \varphi(t)\,|t\rangle\,\mathrm{d}t, \tag{2.15}$$

we can obtain the probability to have this wavefunction by sandwiching the single-electron coherence with $|\varphi\rangle$

$$p[\varphi] = \left\langle \varphi \middle| \mathbf{G}^{(e)}_{\rho,x} \middle| \varphi \right\rangle. \tag{2.16}$$

If we consider a normalized state $|\varphi\rangle$, this probability must be a real number comprised between 0 and 1. This ensures that $\mathbf{G}^{(e)}_{\rho,x}$ is a positive operator, bounded by 1.

Our strategy is to exploit time periodicity of single-electron coherence to gain understanding on the elementary single-particle excitations that are present in the electronic fluid. Periodicity then means that $\mathbf{G}^{(e)}_{\rho,x}$ commutes with the time-translation operator $\mathbf{T}_T$ defined by $\mathbf{T}_T|t\rangle = |t+T\rangle$.

Information on the electronic (resp. hole) excitations with respect to the Fermi level which we take here at $\mu = 0$ is obtained by projecting single-electron coherence using the projectors $\mathbf{\Pi}_\pm$ on the space of positive (resp. negative) energy single-particle states, thus leading to $\mathbf{G}^{(e)}_\pm = \mathbf{\Pi}_\pm \, \mathbf{G}^{(e)} \, \mathbf{\Pi}_\pm$. The $\mathbf{G}^{(e)}_+$ operator then contains the information on the electronic excitations present in the system whereas $\mathbf{G}^{(e)}_-$ contains the information on the purely hole excitations.

At zero temperature, we have $\mathbf{G}^{(e)}_+ = \Delta\mathbf{G}^{(e)}_+$, the electronic part of the coherence being only populated by the source. Similarly, we have $\mathbf{G}^{(e)}_- = \mathbf{\Pi}_- + \Delta\mathbf{G}^{(e)}_-$. However, when the temperature is non-zero, this is not true anymore, since temperature will populate positive frequencies with electrons, and negative frequencies with holes.

It's worth noting that the full electronic coherence $\mathbf{G}^{(e)}$ also contains the information on electron/hole coherences, which also commutes with $\mathbf{T}_T$. In order to be able to characterize electron/hole entanglement one therefore has to study both $\mathbf{G}^{(e)}$ and $\mathbf{G}^{(e)}_\pm$. Let us now describe the details of this approach to single-electron coherence.

2.3.2 The Floquet–Bloch theorem

For simplicity, let us first focus on the electronic part $\mathbf{G}^{(e)}_+$. We are led to introduce eigenstates $|\psi_{a,\omega}\rangle$ living in the positive-energy Hilbert space $\mathcal{H}_+$, indexed by a band-index a and a quasi-energy $\omega \in \mathbb{R}/2\pi f\mathbb{Z}$ which are the temporal counterparts of Bloch's functions in band theory. They are eigenvectors of the time-translation operator $\mathbf{T}_T$, which means

$$\mathbf{T}_T|\psi_{a,\omega}\rangle = \mathrm{e}^{-\mathrm{i}\omega T}|\psi_{a,\omega}\rangle. \tag{2.17}$$

Single-electron coherence is then diagonalized as

$$\mathbf{G}^{(e)}_+ = \sum_a \int_0^{2\pi f} p_a(\omega)\, |\psi_{a,\omega}\rangle\langle\psi_{a,\omega}| \, \frac{\mathrm{d}\omega}{2\pi}, \tag{2.18}$$

where the Floquet–Bloch eigenfunctions $|\psi_{a,\omega}\rangle$ satisfy the normalization condition

$$\langle\psi_{a,\omega}|\psi_{a',\omega'}\rangle = 2\pi\delta_{a,a'}\delta_{\mathbb{R}/2\pi f\mathbb{Z}}(\omega-\omega'). \tag{2.19}$$

where $\delta_{\mathbb{R}/2\pi f\mathbb{Z}}$ is a Dirac comb of period $2\pi f$. The $\mathbf{G}_+^{(e)}$ operator being dimensionless, note that the eigenvalues $p_a(\omega)$ are dimensionless too. The positivity of the operator $\mathbf{G}_+^{(e)}$ and its boundedness leads to $0 \leq p_a(\omega) \leq 1$ for all (a, ω).

2.3.3 Eigenvalue equations

The diagonalization problem that leads to the spectrum $(p_a(\omega))_{a,\omega}$ and to the Floquet–Bloch eigenfunctions is best expressed in the frequency domain [Grenier et al., 2011a; Ferraro et al., 2013]. Exactly as in Bloch's theory, we introduce T-periodic dimensionless functions $u_{a,\omega}$ such that $\psi_{a,\omega}(t) = \mathrm{e}^{-\mathrm{i}\omega t} v_F^{-1/2} u_{a,\omega}(t)$, and we decompose them in Fourier series

$$u_{a,\omega}(t) = \sum_{n=-\infty}^{+\infty} u_{a,\omega}^{(n)} \, \mathrm{e}^{-2\mathrm{i}\pi n f t}. \tag{2.20}$$

The eigenvalue equation $\mathbf{G}_+^{(e)} |\psi_{a,\omega}\rangle = p_a(\omega) |\psi_{a,\omega}\rangle$ can then be rewritten in terms of the harmonics $\mathcal{G}_{+,n}^{(e)}(\omega)$. Picking a representative $\omega \in [0, 2\pi f[$ for the quasi-energy, the eigenvector equation for $p_a(\omega)$ is

$$\sum_{p\in\mathbb{Z}} v_F \mathcal{G}_{+,n-p}^{(e)}(\omega + \pi f(n+p)) \, u_{a,\omega}^{(p)} = p_a(\omega) \, u_{a,\omega}^{(n)}. \tag{2.21}$$

This is precisely the equation that will be solved numerically to determine the spectrum of the single-electron coherence restricted to the electronic quadrant. We can also see it as the diagonalization of the matrix $M(\omega)$, defined for each $\omega \in [0, 2\pi f[$ as

$$M_{np}(\omega) = v_F \mathcal{G}_{+,n-p}^{(e)}(\omega + \pi f(n+p)). \tag{2.22}$$

The way this matrix is obtained from energy representation of the first-order coherence is graphically pictured on fig. 2.4.

2.3.4 Physical interpretation

The normalization condition (2.19) for the eigenstates $|\psi_{a,\omega}\rangle$ is the same as the one of plane waves except for the fact that, in the present case, ω is a quasi-momentum living in $\mathbb{R}/2\pi f\mathbb{Z}$. The destruction operator associated with such an excitation is thus defined by direct analogy with the operator $c(\omega)$:

$$c[\psi_{a,\omega}] = \frac{v_F}{\sqrt{2\pi}} \int_{-\infty}^{+\infty} \psi_{a,\omega}^*(t) \psi(t) \, \mathrm{d}t, \tag{2.23}$$

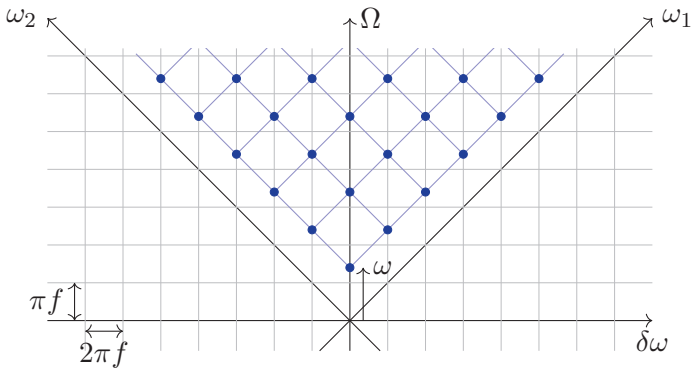

Figure 2.4: Graphical representation of the matrix M. The first-order coherence in energy representation takes values for $\delta\omega$ being an integer multiple of $2\pi f$. The matrix we extract at a given frequency ω is the one given by the value of the blue dots, that are spaced by $2\pi f$ in both vertical and horizontal direction. Shifting the frequency ω comes to shifting vertically the blue dots.

where the normalization factor ensures the canonical anticommutation relation

$$\{c[\psi_{a,\omega}], c[\psi^\dagger_{a',\omega'}]\} = \delta_{a,a'}\delta(\omega - \omega'). \tag{2.24}$$

It then follows that

$$\langle c^\dagger[\psi_{a',\omega'}]c[\psi_{a,\omega}]\rangle = \delta_{a,a'}\delta(\omega - \omega')\, p_a(\omega). \tag{2.25}$$

The eigenvalues $p_a(\omega)$ thus appear as the occupation numbers of the single-particle states $|\psi_{a,\omega}\rangle$. We can therefore interpret the spectrum of $\mathbf{G}^{(e)}_+$ as occupation number bands for the Floquet–Bloch states $|\psi_{a,\omega}\rangle$ characterized by their band index a and their quasi-energy $\omega \in \mathbb{R}/2\pi f\mathbb{Z}$.

2.3.5 Hole excitations and electron/hole coherences

Having discussed the electronic part of the single-electron coherence, let us discuss the hole part as well as the electron/hole part.

Floquet–Bloch theory for hole excitations

We can also introduce a hole operator $\mathbf{G}^{(h)}$ defined by replacing $\mathcal{G}^{(e)}(t,t')$ in eq. (2.13) by

$$\mathcal{G}^{(h)}_{\rho,x}(t,t') = \mathrm{tr}\left(\psi^\dagger(x,t)\rho\psi(x,t')\right). \tag{2.26}$$

This operator satisfies the same mathematical properties as $\mathbf{G}^{(e)}$. This can be easily shown by using the anticommutation relations of fermionic operators to relate electron and hole coherence operators

$$\mathbf{G}^{(h)} = \mathbf{1} - \mathbf{C}\mathbf{G}^{(e)}\mathbf{C}^\dagger, \tag{2.27}$$

where $\mathbf{C}$ is the anti-unitary involution that transforms electrons in holes and vice-versa, that we have seen in section 1.4.4, page 54. In time basis, it corresponds to a complex conjugation.

At zero temperature we have $\mathbf{G}^{(h)} = \mathbf{\Pi}_- - \mathbf{C}\Delta\mathbf{G}^{(e)}\mathbf{C}^\dagger$. Rather than concentrating on $\mathbf{G}^{(h)}_+$, because it will make the eigenfunctions of holes with a positive-frequency spectrum due to the conjugation operation, we will be interested in $\Delta\mathbf{G}^{(e)}_-$, which contains eigenfunctions of holes at negative frequencies, and with eigenvalues that are the opposite of the probability of occupation. Of course, this is only valid at zero temperature, and this is why we introduce $\Delta_0\mathbf{G}^{(e)} = \mathbf{G}^{(e)} - \mathbf{\Pi}_-$, where the difference is always taken with a Fermi sea at zero temperature. This is important notably to ensure that probabilities stay positive.

Exactly as $\mathbf{G}^{(e)}_+$, $\mathbf{G}^{(e)}_-$ can be diagonalized simultaneously with $\mathbf{T}_T$ and we shall introduce a basis of hole single-particle states $|\psi^{(h)}_{b,\omega}\rangle$ such that

$$\Delta_0\mathbf{G}^{(e)}_- = -\sum_b \int_0^{2\pi f} p^{(h)}_b(\omega)\, |\psi^{(h)}_{b,\omega}\rangle\, \langle\psi^{(h)}_{b,\omega}|\, \frac{\mathrm{d}\omega}{2\pi}. \tag{2.28}$$

This choice of convention for the hole Floquet–Bloch spectrum is such that $\mathbf{G}^{(h)}_+$ is diagonalized by the eigenvectors $\mathbf{C}|\psi^{(h)}_{b,\omega}\rangle$ with respective eigenvalue $p^{(h)}_b(\omega)$. Note that the full hole part $\mathbf{G}^{(e)}_-$ is diagonal in the $|\psi^{(h)}_{b,\omega}\rangle$ basis with respective eigenvalues $1 - p^{(h)}_b(\omega)$.

Electron/hole coherences

As mentioned before, the full electronic coherence $\mathbf{G}^{(e)}$ also contains the information on electron/hole coherences which also commutes with $\mathbf{T}_T$. Assuming that we have diagonalized the purely electronic and purely hole part of the single-electron coherence according to eqs. (2.18) and (2.28), the electron/hole part can then be expressed using the electronic and hole Floquet–Bloch eigenbases. Since $\mathbf{G}^{(e)}_{+-}$ as well as $\mathbf{G}^{(e)}_{-+}$ commute

with $\mathbf{T}_T$, the electron/hole coherence part are of the following form

$$\mathbf{G}^{(e)}_{+-} = \sum_{a,b} \int_0^{2\pi f} g^{(eh)}_{ab}(\omega)\, |\psi^{(e)}_{a,\omega}\rangle\langle\psi^{(h)}_{b,\omega}|\, \frac{\mathrm{d}\omega}{2\pi}, \tag{2.29a}$$

$$\mathbf{G}^{(e)}_{-+} = \sum_{a,b} \int_0^{2\pi f} g^{(he)}_{ba}(\omega)\, |\psi^{(e)}_{a,\omega}\rangle\langle\psi^{(h)}_{b,\omega}|\, \frac{\mathrm{d}\omega}{2\pi}, \tag{2.29b}$$

where $g^{(eh)}_{ab}(\omega) = g^{(he)}_{ba}(\omega)^*$ in order to ensure hermiticity of $\mathbf{G}^{(e)}$. Generically, the electron/hole coherence part cannot be inferred from the electronic and hole parts of the single-electron coherence.

2.4 Electronic atoms of signal

For a T-periodic source, an important question raised in [Roussel et al., 2016] is to determine the simplest representation of single-electron coherence in terms of electronic atoms of signals. As we shall see now, Bloch decomposition introduced in the previous subsection precisely provides such a simple decomposition.

2.4.1 Floquet–Wannier functions

The Floquet–Bloch states being quasi T-periodic, it is convenient to introduce the counterpart of Wannier functions which are the localized orbitals in solid-state band theory [Wannier, 1937]. They are defined for $l \in \mathbb{Z}$ as

$$|\varphi_{a,l}\rangle = \frac{1}{\sqrt{f}} \int_0^{2\pi f} \mathrm{e}^{-\mathrm{i}\omega l t}\, |\psi_{a,\omega}\rangle\, \frac{\mathrm{d}\omega}{2\pi}, \tag{2.30}$$

whose inverse reads

$$|\psi_{a,\omega}\rangle = \frac{1}{\sqrt{f}} \sum_{l=-\infty}^{+\infty} \mathrm{e}^{\mathrm{i}\omega l T} |\varphi_{a,l}\rangle. \tag{2.31}$$

The normalization condition (2.19) shows that they form an orthonormal family. Moreover, for a given band, all the states $(|\varphi_{a,l}\rangle)_{l\in\mathbb{Z}}$ are related by time translation since eq. (2.30) implies that:

$$\mathbf{T}_T |\varphi_{a,l}\rangle = |\varphi_{a,l+1}\rangle. \tag{2.32}$$

These functions are nothing but the electronic atoms of signals introduced in [Roussel et al., 2017].

2.4.2 Floquet–Wannier function ambiguities

Exactly as in solid-state band theory [Marzari et al., 2012], there are ambiguities in the determination of electronic atoms of signals. These ambiguities can always be traced back to degenerate common eigenspaces for $\mathbf{G}_+^{(e)}$ and $\mathbf{T}_T$. Let us introduce a unitary tranformation $\mathbf{U}$ that keeps $\mathbf{G}_+^{(e)}$ eigenspaces stable: $[\mathbf{U}, \mathbf{G}_+^{(e)}] = 0$, then using the $\mathbf{U}|\psi_{a,\omega}\rangle$ states in (2.30), we obtain a new orthonormal family of Wannier functions which we denote by $\left|\varphi_{a,l}^{[U]}\right\rangle$. Equation (2.32) becomes

$$\mathbf{T}_T \left|\varphi_{a,l}^{[\mathbf{U}]}\right\rangle = \left|\varphi_{a,l+1}^{[\mathbf{T}_T \mathbf{U} \mathbf{T}_T^\dagger]}\right\rangle. \tag{2.33}$$

In order to satisfy the time-translation property of Wannier wavefunctions (2.32), we require that $\mathbf{U}$ preserves each eigenspace of $\mathbf{T}_T$ and we will then discuss what happens depending on the structure of the common eigenspaces of $\mathbf{T}_T$ and $\mathbf{G}_+^{(e)}$.

Preserving the eigenspaces of $\mathbf{T}_T$ immediately implies that $\mathbf{U}$ preserves quasi-energy eigenspaces. Assuming that it leaves each of them invariant, this means that it reduces to a unitary transformation operating on the space generated by all the Floquet–Bloch states at a given quasi-energy. Let us now analyze what happens depending on the eigenspaces of $\mathbf{G}_+^{(e)}$ at fixed quasi-energy.

In the case where the Floquet–Bloch bands are non-degenerate, injective ($p_a(\omega) \neq p_a(\omega')$ for $\omega \neq \omega'$) and do not cross, each common eigenspace is one dimensional and the only possibility for redefining the Floquet–Bloch eigenstates is to introduce quasi-energy dependent phases:

$$|\psi_{a,\omega}\rangle \mapsto \mathrm{e}^{\mathrm{i}\theta_a(\omega)} |\psi_{a,\omega}\rangle. \tag{2.34}$$

Such quasi-energy dependent phases $\theta(\omega)$ fall into different topological sectors which are labeled by the winding number

$$n_{\mathrm{w}} = \frac{1}{2\pi} \int_0^{2\pi f} \frac{\mathrm{d}\theta(\omega)}{\mathrm{d}\omega}\, \mathrm{d}\omega. \tag{2.35}$$

For example $\theta_n(\omega) = nT\omega$ has winding number $n \in \mathbb{Z}$ and eq. (2.30) implies that

$$\left|\varphi_{a,l}^{[\mathrm{e}^{\mathrm{i}\theta_n}]}\right\rangle = |\varphi_{a,l+n}\rangle. \tag{2.36}$$

Consequently, a topologically non-trivial phase has the same effect as combining a translation by an integer number of periods with a topologically trivial energy-dependent phase.

In the case of n degenerate Floquet–Bloch bands over the whole quasi-energy interval, the above phases are replaced by a quasi-energy dependent unitary transformation $U(\omega) \in \mathcal{U}(n)$ for $0 \leq \omega < 2\pi f$ so that, considering A_α the set of n band indices, the new Wannier functions are defined by:

$$\left|\varphi_{a,l}^{[U]}\right\rangle = \frac{1}{\sqrt{f}} \int_0^{2\pi f} \sum_{b \in A_\alpha} U_{a,b}(\omega) \left|\psi_{b,\omega}\right\rangle \frac{\mathrm{d}\omega}{2\pi}. \tag{2.37}$$

Such transformations are directly relevant when a source emits n single-electron excitations on top of the Fermi sea. In this case $p_a(\omega) = 1$ for several values of a. The topological sectors of such quasi-energy dependent unitaries are classified by the topological sectors of the overall phase since all groups $\mathcal{SU}(n \geq 2)$ are simply connected.

The nature of bands we obtain is quite different from the ones we observe in Bloch theory. In particular, the mathematical structure is not the same, since the Hamiltonian operator contains spatial derivative, which is not the case here. As such, the properties we observe are different from condensed matter ones. A first observation is that bands can have discontinuities. From our observations for classical voltages and LPA source driven with a sinusoidal and square voltage, it seems that such discontinuities appear when temperature is non-zero, for purely a.c. sources.

We might also wonder about the existence of band crossings. On one hand, it is quite easy to have degenerate bands, especially for flat bands at $p_a(\omega) = 0, 1$. On the other hand, we have been only able to observe quadratic degeneracy points, in highly symmetric situations. For now, we do not have exhibited a model of source, or a set of parameters in which we observe a linear band crossing. Further numerical exploration with more possible sources as well as the unravelling of analytical properties hidden inside Floquet scattering theory will be needed to address the general questions about band structure.

Finally, since physical states are defined up to a phase, a different possibility appears in the case of flat bands. For example, one could replace eq. (2.32) by its projective version, that is introducing a phase in front of $|\varphi_{a,l+1}\rangle$. Combining this with eq. (2.33) leads to

$$U_\Omega |\psi_{a,\omega}\rangle = |\psi_{a,\omega+\Omega}\rangle, \tag{2.38}$$

where the addition is considered modulo $2\pi f$ ($\Omega \in \mathbb{R}/2\pi f\mathbb{Z}$). Substitut-

ing this into eq. (2.30) leads to

$$\left|\varphi_{a,l}^{[U_\Omega]}\right\rangle = \mathrm{e}^{\mathrm{i}\Omega T}\,|\varphi_{a,l+1}\rangle\,. \tag{2.39}$$

The time translation property (2.32) is satisfied up to a phase.

2.4.3 Minimal-spreading principle

Let us now discuss the general method used to determine suitable electronic atoms of signals. Exactly as in solid-state physics, a natural idea is to look for maximally-localized Wannier functions [Marzari et al., 2012]. Let us consider φ_a such a wave-function, the spreading $\langle(\Delta t)^2\rangle_{\varphi_a}$ is defined as

$$\begin{aligned}\langle(\Delta t)^2\rangle_{\varphi_a} = v_F \int_{\mathbb{R}} t^2 |\varphi_{a,0}(t)|^2\,\mathrm{d}t \\ - \left(v_F \int_{\mathbb{R}} t\,|\varphi_{a,0}(t)|^2 \mathrm{d}t\right)^2 .\end{aligned} \tag{2.40}$$

Let us consider directly the case of n degenerated bands $p_a(\omega) = p_\alpha(\omega)$ for all $0 \leq \omega < 2\pi f$ and $a \in A_\alpha$. We then have a quasi-energy dependent unitary transformation ambiguity described by eq. (2.37). Maximally localized Wannier wavefunctions are now found by minimizing the quadratic functional

$$\mathcal{S}[U] = \sum_{a\in A_\alpha} \left\langle(\Delta t)^2\right\rangle_{|\varphi_a^{[U]}\rangle} \tag{2.41}$$

over $U(\omega) \in \mathcal{U}(n)$ for $0 \leq \omega < 2\pi f$. Note that the right-hand side of eq. (2.40) may be divergent due to the large time behavior of $|\varphi_{a,0}(t)|^2$ as, for example, in the case of a Leviton train. In such a case, we should therefore regularize it by subtracting the same quantity for a reference choice of the unitary operator such as $U(\omega) = \mathbf{1}$.

Numerically, the implementation of the minimization process is straightforward in the case of a non-degenerate band. Since there is a natural cut-off for the length of the wavepacket, in this case it is easy to compute the functional (2.40) from an arbitrary phase (2.34). More importantly, it is also easy to compute the gradient, giving access to all efficient gradient-based minimization algorithms. In our case, we rely on the GSL implementation of the Fletcher–Reeves algorithm [Fletcher and Reeves, 1964]. It consists in a succession of line minimizations. We begin at a given point (which can either be random phase or a null phase),

and the first direction of minimization is given by the gradient. Then, at each iteration, a new direction is chosen, depending on the previous search direction, the gradient of current iteration and the norm of the gradient of previous iteration. The iteration ends when the gradient is orthogonal to the line of search.

For the degenerate case (2.37), there are several difficulties. First, we need to parametrize the unitary matrices $U(\omega)$. For this, we introduce $\Theta(\omega)$, Hermitian matrices such that

$$U(\omega) = \exp(\mathrm{i}\Theta(\omega)). \tag{2.42}$$

The main difficulty here is that, since $\mathcal{U}(n \leq 2)$ is a non-commutative group, it becomes hard to compute the gradients of the functional $\mathcal{S}[U]$. However, it is still easy to compute them if we consider a starting point at $U = \mathbb{1}$. In the following, we will denote $|\psi_{A,\omega}\rangle$ the vector containing every wavefunctions $|\psi_{a,\omega}\rangle$ with $a \in A$, A being the degenerate set of bands we want to minimize on. the matrix $U(\omega)$ acts on this vector space, mixing wavefunctions. At each iteration $n > 1$ of the algorithm, we now replace the wavefunctions $|\psi^{(n-1)}_{A,\omega}\rangle$ by the wavefunctions

$$\left|\psi^{(n)}_{A,\omega}\right\rangle = \mathrm{e}^{\mathrm{i}x_n H_n(\omega)} \left|\psi^{(n-1)}_{A,\omega}\right\rangle, \tag{2.43}$$

H_n being the search direction and x_n the real parameter that minimize this search direction. This allows us to always start the line minimization process from $U = \mathbb{1}$. To determine the minimum, we check whether our search direction is orthogonal to the local gradient computed by shifting $\mathrm{e}^{\mathrm{i}x_n H_n(\omega)}$ to identity. What makes everything work is that all quantities needed to compute the new direction of minimization are either invariant on the point of the $\mathcal{U}(n)$ group we consider them (norm of the previous gradient), computed locally (the new gradient) or trivially transported (previous search direction, which is parallel to the transport). After N iterations, we end up with

$$\left|\psi^{(N)}_{A,\omega}\right\rangle = \mathrm{e}^{\mathrm{i}\Theta_N(\omega)} \cdots \mathrm{e}^{\mathrm{i}\Theta_1(\omega)} \left|\psi^{(0)}_{A,\omega}\right\rangle. \tag{2.44}$$

emphasing the non-commutative character of the group we are minimizing on.

2.4.4 Coherences between Floquet–Wannier states

The single-electron coherence restricted to the electronic quadrant can then be rewritten as

$$\mathbf{G}_{+}^{(e)} = \sum_{a} \sum_{l_+,l_-} g_a^{(e)}(l_+ - l_-)|\varphi_{k,l_+}\rangle\langle\varphi_{k,l_-}|, \tag{2.45}$$

where

$$g_a^{(e)}(\Delta l) = \int_0^{2\pi f} p_a(\omega)\, \mathrm{e}^{\mathrm{i}\omega T \Delta l} \frac{\mathrm{d}\omega}{2\pi f}. \tag{2.46}$$

Consequently there is no coherence between electronic atoms of signals associated with different bands but electronic coherence may extend over more than one period. Indeed, $g_a^{(e)}(l_+ - l_-)$ defined by eq. (2.46) encodes the inter-period coherence through its $l_+ - l_-$ dependence: whereas a flat band won't lead to coherences between the atom of signals of type a associated with different periods, a non-flat band will. The typical scale over which $p_a(\omega)$ varies is nothing but the inverse timescale over which inter-period coherence exists.

In the same way, considering the hole part of single-electron coherence $\Delta_0\mathbf{G}^{(e)}$ and the corresponding Floquet–Wannier single-particle states, quantum coherence between these states can be described by a coefficient $g_b^{(h)}(l_+ - l_-)$ which is obtained by using $p_b^{(h)}(\omega)$ in eq. (2.46). This describes inter-period hole-excitation coherence in the Floquet–Wannier basis.

Similarly, knowing the Floquet–Wannier states describing the electronic and hole part of single-electron coherence, the electron/hole coherence can be expressed in this basis through

$$\mathbf{G}_{+-}^{(e)} = \sum_{a,b} \sum_{l_+,l_-} g_{ab}^{(eh)}(l_+ - l_-)|\varphi_{a,l_+}^{(e)}\rangle\langle\varphi_{b,l_-}^{(h)}|, \tag{2.47}$$

where

$$g_{ab}^{(eh)}(\Delta l) = \int_0^{2\pi f} g_{ab}^{(eh)}(\omega)\, \mathrm{e}^{\mathrm{i}\Delta l \omega T} \frac{\mathrm{d}\omega}{2\pi f}. \tag{2.48}$$

Note that because electron/hole coherence couples different bands, different choices of electronic atoms of signal lead to different values for $g_{ab}^{(eh)}(\Delta l)$. This is not the case for the coherence between purely electronic or purely hole wavepackets given by eq. (2.46).

The Cauchy–Schwarz inequality then implies some constraints on single-electron coherence which have been discussed in the energy eigenbasis [Ferraro et al., 2013]. Let us express them in terms of the electronic atoms of signals. Within the electron and hole quadrants, this leads to

$$\left|g_a^{(e)}(l_+ - l_-)\right| \leq \bar{p}_a^{(e)}, \tag{2.49a}$$

$$\left|1 - g_a^{(h)}(l_+ - l_-)\right| \leq 1 - \bar{p}_b^{(h)}, \tag{2.49b}$$

where $\bar{p}_a^{(e)}$ (resp. $\bar{p}_b^{(h)}$ denotes the average of the eigenvalue $p_a^{(e)}(\omega)$ (resp. $p_b^{(h)}(\omega)$) over $0 \leq \omega \leq 2\pi f$. Finally, considering the electron/hole quadrants, the Cauchy–Schwarz inequality bounds the electron/hole coherences

$$\left|g_{ab}^{(eh)}(l_+ - l_-)\right|^2 \leq \bar{p}_a^{(e)} \left(1 - \bar{p}_b^{(h)}\right). \tag{2.50}$$

This inequality immediately recovers the result saying that when there are no electronic excitations ($p_a^{(e)}(\omega) = 0$ for all ω and a) or hole excitations ($p_b^{(h)}(\omega) = 0$), then there are no electron/hole coherences ($g_{ab}^{(eh)}(l_+ - l_-) = 0$) as well as no coherence between the missing excitations [Ferraro et al., 2013].

The Martin–Landauer electronic atoms of signal

Let us now consider a stationary electronic state. In this case, the single-electron coherence only depends on $t - t'$ and the $n = 0$ harmonic is the only non-vanishing one: $v_F \mathcal{G}_n^{(e)}(\omega) = \delta_{n,0}\, f_e(\omega)$ where $f_e(\omega)$ denotes the electronic distribution function. The eigenvalue equation (2.21) then implies that for $p \in \mathbb{Z}$ and $0 < \omega < 2\pi f$ we have $f_e(\omega + 2\pi n f) u_{a,\omega}^{(n)} = p_a(\omega) u_{a,\omega}^{(n)}$. The bands are therefore indexed by $m \in \mathbb{N}$ and the corresponding eigenvectors and eigenvalues are given by:

$$p_m(\omega) = f_e(\omega + 2\pi m f), \tag{2.51}$$

$$u_{m,\omega}^{(p)} = \delta_{m,p}. \tag{2.52}$$

The Floquet–Bloch waves are plane waves $\psi_{m,\omega}(t) = v_F^{-1/2} \mathrm{e}^{-\mathrm{i}(\omega + 2\pi m f)t}$ and the corresponding Wannier wavefunctions are

$$\varphi_{m,0}(t) = \frac{1}{\sqrt{v_F T}} \frac{\sin(\pi f t)}{\pi f t}\, \mathrm{e}^{-2\mathrm{i}\pi(m+1/2)ft}. \tag{2.53}$$

The electronic atoms of signal well suited to describe a stationary electronic coherence are therefore the Martin–Landauer wavepackets [Martin and Landauer, 1992] of energy width hf centered at energies $(m+1/2)hf$ with m integer. These atoms of signals are known in the signal-processing community as the Shannon wavelets.

The spectrum is then given by the bands $p_m(\omega) = f_e(\omega + 2\pi f)$ which are generically not flat. The coherence between two periods separated by Δl is related to the electronic distribution function in the energy band $[mhf, (m+1)hf]$:

$$g_m^{(e)}(\Delta l) = \int_0^{2\pi f} \mathrm{e}^{\mathrm{i}\Delta l \omega T} f_e(\omega + 2\pi m f) \, \frac{\mathrm{d}\omega}{2\pi f}. \tag{2.54}$$

At zero temperature, in the presence of a d.c. biased voltage $V_{\mathrm{dc}} < 0$, the electronic distribution function is a step function of width $eV_{\mathrm{dc}}/\hbar$. Assuming that $f_e(\omega) = 1$ for $\omega < 0$ and $f_e(\omega) = 0$ for $\omega > -eV_{\mathrm{dc}} > 0$, the excess electronic coherence is then naturally described in terms of Martin–Landauer wavepackets of bandwidth $e|V_{\mathrm{dc}}|/\hbar$ which are a natural timescale $h/e|V_{\mathrm{dc}}|$. There is no coherence between Martin–Landauer wavepackets centered on different $\omega_n = -(n+1/2)eV_{\mathrm{dc}}/\hbar$ with $n \in \mathbb{N}$ as well as between Martin–Landauer wavepackets associated with different time periods of duration $h/e|V_{\mathrm{dc}}|$.

By contrast, at finite temperature T_{el}, the electronic distribution function has a smearing over a scale $k_B T_{\mathrm{el}}/\hbar$, thus leading to a non-flat band spectrum. Therefore, there are always inter-period coherences over the thermal coherence time $h/k_B T_{\mathrm{el}}$. It might seem surprising that when $T_{\mathrm{el}} = 0\,\mathrm{K}$, the inter-period coherences goes to zero, whereas the thermal coherence time goes to infinity. This comes from the fact that when decreasing the temperature, as the off-diagonal coherences spread over more and more period, their modulus decreases, and vanishes at zero temperature.

Case of a voltage drive at low temperature

We have seen in section 1.4.4 that classical drives possess a typical structure, especially at low temperature, depicted on fig. 1.14. We will see now how this structure translates into the Floquet–Bloch formalism.

At zero temperature, the energy coherence is piecewise constant, and the width of each step is $2\pi f$. If we consider a purely a.c. drive, we see that the discontinuities does not appear when we extract the matrix $M(\omega)$ for $\omega \in [0, 2\pi f[$ (see fig. 2.5, left). As such, the eigenvalues will be

independent on the quasi-energy, and the eigenvectors of different quasi-energy can be deduced by a frequency translation. It implies notably that it is possible to find a set of Wannier functions that are piecewise constant in energy, with discontinuities happening every $2\pi f$.

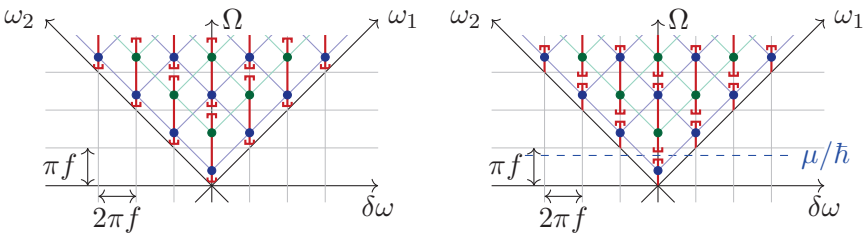

Figure 2.5: Matrices for a voltage drive at zero temperature. On the left, the case of an a.c. voltage drive. In this case, the coherence is constant for all $\omega \in [0, 2\pi f[$. The eigenvalue problem does not depend anymore on the quasi-energy. On the right, we consider that there is a d.c. part on top of the a.c. voltage. In this case, the matrix $M(\omega)$ will be piecewise constant, with a step at $\omega = \mu/\hbar \pmod{2\pi f}$.

If we add a d.c. part to the voltage, then it will shift the whole energy coherence by $\mu/\hbar$ (see fig. 2.5, right). In this case, there are two possibilities:

- If μ/hf is an integer, we are back to the a.c. case, since the discontinuity will not happen for $\omega \in [0, 2\pi f[$.

- If μ/hf is not an integer, then the matrix M will be piecewise constant, with a step at $\omega_s = \mu/\hbar \ [2\pi f]$. Similarly, the eigenvectors for $\omega \in [0, \omega_s[$ can be deduced by translating the eigenvectors at $\omega = 0$ in energy. The eigenvectors for $\omega \in [\omega_s, 2\pi f[$ can be deduced by translating the eigenvectors at ω_s. In this case, we can find a set of Wannier functions that are piecewise constant in energy, with steps happening at $2\pi nf$ and $2\pi nf + \omega_s$.

If we consider a small, non-zero temperature, such that $k_B T \ll hf$, the steps will be smoothed out over a scale $k_B T/\hbar$. We can thus expect that the property mentioned above remains true, except at the neighborhood of discontinuities.

2.4.5 Relation to experimentally relevant quantities

Let us now explain how experimental signals are related to these spectral quantities. We shall first discuss a simple repeated detection scheme of a given electronic excitation and then discuss the signal of an HOM experiment.

Repeated detections

Because electronic atoms of signals are localized in time, they are suitable single-particle states to discuss repeated detection protocols [Roussel et al., 2017]. Let us discuss this point in the light of HOM interferometry.

We consider a T-periodic source S such that the electronic part of the excess single-electron coherence is given by eq. (2.8) in terms of the electronic atoms of signal $|\varphi_{a,l}\rangle$. When performing an HOM interferometry experiment against an ideal electronic source S_a whose excess single-electron coherence is of the form

$$\Delta\mathcal{G}^{(e)}_{S_a}(t,t') = \sum_{l=0}^{N} \varphi_{a,l}(t)\,\varphi^*_{a,l}(t'), \tag{2.55}$$

the resulting current noise would be proportional to the overlap between $\Delta\mathcal{G}^{(e)}_{S}$ and $\Delta\mathcal{G}^{(e)}_{S_a}$. Using the T periodicity of $\Delta\mathcal{G}^{(e)}_{S}$, we find that

$$\int_{\mathbb{R}^2} \Delta\mathcal{G}^{(e)}_{S_a}(t,t')^*\Delta\mathcal{G}^{(e)}_{S}(t,t')\,\mathrm{d}t\,\mathrm{d}t' = N\,\bar{p}_a. \tag{2.56}$$

This overlap precisely counts the number of times an electron in the single-particle state $|\varphi_{a,l}\rangle$ is scattered against an electronic excitation in the same single-particle state for $l = 1$ to N. Since S_a is an ideal source sending a train of N identical excitations shifted by multiples of T, $\bar{p}_a$ should be interpreted as the average number of electronic excitations in the single-particle state φ_a emitted per period.

Although for the moment, these is no counterpart of HOM interferometry for second-order coherence, the same argument can be extended to two-particle quantities by considering the overlap between the intrinsic excess second-order electronic coherence $\Delta\mathcal{G}^{(2e)}_{S}$ of the source S with the second-order coherence of an ideal train of N electron pairs built from $|\varphi_a\rangle$ and $|\varphi_b\rangle$ time shifted by T [Thibierge et al., 2016]:

$$\mathcal{G}^{(2e)}_{S_{a,b}}(t_1,t_2|t_1',t_2') = \sum_{l=1}^{N} \varphi_{a,b;l}(t_1,t_2)\,\varphi_{a,b;l}(t_1',t_2'), \tag{2.57}$$

where $\varphi_{a,b;l}(t,t')$ denotes the two-particle Slater determinant

$$\varphi_{a,b;l}(t,t') = \begin{vmatrix} \varphi_{a,l}(t_1) & \varphi_a(t_2) \\ \varphi_{b,l}(t_1) & \varphi_{b,l}(t_2) \end{vmatrix}. \tag{2.58}$$

The overlap between a train of N electron pairs prepared in the two-electron states $\varphi_{a,b;l}$ for $l = 1, \ldots, N$ and the unknown two-electron coherence $\Delta\mathcal{G}_S^{(2e)}$ is then proportional to N due to T-periodicity. It is given by

$$\int_{\mathbb{R}^4} \Delta\mathcal{G}_S^{(2e)}(\mathbf{t}|\mathbf{t}')\, \mathcal{G}_{S_{a,b}}^{(2e)}(\mathbf{t}|\mathbf{t}')^*\, \mathrm{d}^2t\, \mathrm{d}^2t' = N\, \bar{n}_S[\varphi_{a,0}, \varphi_{b,0}], \tag{2.59}$$

where $\bar{n}_S[\varphi_{a,0}, \varphi_{b,0}]$ can be interpreted as the number of electron pairs prepared in $\varphi_{a,b;0}$ emitted per period.

The Hong–Ou–Mandel dip

Let us now consider an HOM experiment where excitations injected into two incoming channels collide at an ideal electronic beam splitter characterized by its energy independent transmission $\mathcal{T}$ ($\mathcal{R} = 1 - \mathcal{T}$ denoting the reflexion probability). The depth of the HOM dip can then be related to the Floquet–Bloch spectral properties of single-electron coherence. Let us recall that the two-particle interference contribution to low-frequency noise in an HOM experiment is equal to [Grenier et al., 2011a]:

$$\mathcal{Q} = -e^2 v_F^2 \mathcal{R}\mathcal{T} \int \Big(\mathcal{G}_1^{(e)}(t,t')\mathcal{G}_2^{(h)}(t,t') + [1 \leftrightarrow 2] \Big)\, \mathrm{d}t\, \mathrm{d}t'. \tag{2.60}$$

Exactly as in the previous paragraph, this noise signal being integrated over an infinite time range in the variable $\bar{t} = (t + t')/2$, a regularization is required in the case of a time-periodic system. In the present case, the right-hand side of eq. (2.60) can be expressed in terms of the electronic and hole Wannier functions which form an orthonormal family of single-particle states. A double sum on discrete time-period indexes subsist which can then be regularized by considering that these sums are truncated to $N \gg 1$ values. The T-periodicity leads to the appearance of a factor N which is the dominant term in the infrared divergence. The contribution to the finite-frequency noise is then obtained by taking the time average over $[-NT/2, NT/2]$. Only the dominant term linear in N leads to a non-vanishing contribution to the excess noise.

We then expand both contributions in terms of $\Delta_0 \mathbf{G}^{(e)}$ and this leads to three distinct contributions. Two of them involve only one of the incoming excess single-electron coherences. They correspond to the partitioning of single-particle excitations from one of the two incoming channels at the QPC. These are called the HBT contributions. At zero temperature, the HBT contribution for one source is

$$\mathcal{Q}_{\mathrm{HBT}} = e^2 \int_0^{2\pi f} \left(\sum_a p_a^{(e)}(\omega) + \sum_b p_b^{(h)}(\omega) \right) \frac{\mathrm{d}\omega}{2\pi}. \tag{2.61a}$$

and two such contributions must be added and multiplied by $\mathcal{RT}$ to obtain the contribution to the excess current noise. The third contribution corresponds to two-particle interferences between the excess excitations emitted into both incoming channels. When the two incoming channels are identical and not time shifted, we get:

$$\mathcal{Q}_{\mathrm{HOM}}^{(\mathrm{dip})} = 2e^2 \int_0^{2\pi f} \sum_a p_a^{(e)}(\omega) \left(1 - p_a^{(e)}(\omega)\right) \frac{\mathrm{d}\omega}{2\pi} \tag{2.62a}$$

$$+ 2e^2 \sum_b p_b^{(h)}(\omega) \left(1 - p_b^{(h)}(\omega)\right) \frac{\mathrm{d}\omega}{2\pi} \tag{2.62b}$$

$$- 4e^2 \int_0^{2\pi f} \left| g_{ab}^{(eh)}(\omega) \right|^2 \frac{\mathrm{d}\omega}{2\pi}. \tag{2.62c}$$

2.5 Electron/hole entanglement

For the source description we will propose, we will use Floquet scattering theory. Since Floquet theory does not take into account interactions, the many-body state is completely defined by its single-electron coherence, as discussed in section 1.4.2. The goal of this section is to propose a way to see how a source described by the Floquet formalism affects the incoming equilibrium state at the many-body level. To this end, we will introduce a many-body operator corresponding to the scattering. This will then allow us to discuss electron/hole entanglement.

Let me stress that this description as well as the result in this section are only valid when interactions can be neglected and that the incoming state that is transformed by the source is Gaussian (like the Fermi sea, thermal states or classical voltage states). In this case, Wick's theorem apply and we can determine the full many-body state from first-order coherence. Of course, this is an unrealistic hypothesis in the general case,

as we will see in chapter 3. It seems however that this hypothesis is quite relevant when one tries to describe a source like a driven quantum dot, since the length scales involved are smaller, and the screening of Coulomb interactions more important due to the gates. It is also consistent with our Floquet modelization which does not take into account interactions between electrons.

2.5.1 Floquet–Bloch parametrization of the many-body state

The most striking feature of Floquet scattering theory is that many-body dynamics can be described at the single-body level, the output ladder operators being expressed as a linear combination of the input ones. If we denote $\mathcal{S}$ the many-body scattering operator, this can be written as

$$\psi_{\text{out}}(t) = \mathcal{S}\psi_{\text{in}}(t)\mathcal{S}^\dagger = \int S(t,t')\psi_{\text{in}}(t')\,\mathrm{d}t. \tag{2.63}$$

Finding an expression for $\mathcal{S}$ is an interesting challenge, since it will give insights on the action of Floquet sources on the incoming equilibrium state, at the many-body level. To this end, we will use the Floquet–Bloch basis, we have introduced in this chapter.

Two-mode model

Before getting interested in the whole, complicated, many-body problem, let us start with simple case, where we consider only two modes, one single-electron mode described by φ_e, and one single-hole mode described by φ_h. When considering the periodic many-mode Floquet case, these modes will be Floquet–Bloch waves, as we will see next. At zero temperature, the incoming hole mode φ_h is filled and contains exactly one electron, whereas the incoming electron mode φ_e is empty. The Floquet source will scatter the mode φ_h into a linear combination of φ_e and φ_h. Note that we consider a purely a.c. source here. As such, we expect that

$$\mathcal{S}c^\dagger[\varphi_h]\mathcal{S}^\dagger = uc^\dagger[\varphi_h] + vc^\dagger[\varphi_e], \tag{2.64}$$

where u and v are complex constants such that $|u|^2 + |v|^2 = 1$. Since $\mathcal{S}$ must be unitary, eq. (2.64) defines almost the whole dynamics, up to a phase that appears in the scattering of electron mode

$$\mathcal{S}c^\dagger[\varphi_e]\mathcal{S}^\dagger = \mathrm{e}^{\mathrm{i}\theta}(u^*c^\dagger[\varphi_e] - v^*c^\dagger[\varphi_h]). \tag{2.65}$$

Before we get interested in this general case, we will look into a simpler case, where $u \in \mathbb{R}$ and $\theta = 0$. As we will see later on, this contains an important part of the physics, and the general case can easily be recovered.

We will show here that $\mathcal{S}$ can be described as a displacement-like operator defined as

$$\mathcal{S} = \exp\left(\lambda c^\dagger[\varphi_e]c[\varphi_h] - \lambda^* c^\dagger[\varphi_h]c[\varphi_e]\right), \tag{2.66}$$

where λ is a complex parameter. Note that we can also consider a real parameter, since the phase of λ can be reabsorbed by changing the phase difference between φ_e and φ_h. To develop this exponential, we will use the following identity

$$-\left(c^\dagger[\varphi_e]c[\varphi_h] - c^\dagger[\varphi_h]c[\varphi_e]\right)^2 = n_e(1-n_h)+n_h(1-n_e) = \Pi_{\text{odd}}, \tag{2.67}$$

where $n_{e/h} = (c^\dagger c)[\varphi_{e/h}]$ is the number operator for the corresponding $\varphi_{e/h}$ mode and Π_{odd} is the projector on the sector containing one particle in the two modes considered. If we also introduce the orthogonal projector Π_{even} that projects on the sector containing either zero or two particles and $\lambda = |\lambda|e^{i\phi}$, we find a simple expression for the many-body scattering operator,

$$\mathcal{S} = \Pi_{\text{even}} + \Pi_{\text{odd}}\left(\cos|\lambda| + \sin|\lambda|\left(e^{i\varphi}c^\dagger[\varphi_e]c[\varphi_h] + e^{-i\varphi}c^\dagger[\varphi_h]c[\varphi_e]\right)\right). \tag{2.68}$$

It is trivial from this expression to show that the action of the $\mathcal{S}$ gives back eqs. (2.64) and (2.64), under the previous assumption of u being real and $\theta = 0$.

Let us now look at the general two-mode case. In fact, we can decompose the general scattering operator into a product of two operators

$$\mathcal{S}_{\text{g}} = \mathcal{S}\mathcal{S}_{\text{d}}, \tag{2.69}$$

where $\mathcal{S}_{\text{d}}$ is a dephasing operator that dephases each electron and hole modes differently. In our two-mode picture, we can write this operator as

$$\mathcal{S}_{\text{d}} = \exp\left(i\left(\theta_e(c^\dagger c)[\varphi_e] + \theta_h(c^\dagger c)[\varphi_h]\right)\right). \tag{2.70}$$

The two phases θ_e, θ_h are the degrees of freedom we missed for the general case shown described by eqs. (2.64) and (2.65).

Many-body scattering operator

To understand the many-body case, we first need to understand how we can map our description in terms of Floquet–Bloch waves into the action of the scattering operator. For this, we split the scattering operator into two parts. First, we will consider a scattering that rearranges electrons and holes independently. This operator will be described by a unitary matrix $\mathrm{e}^{\mathrm{i}(\Theta^{(h)}+\Theta^{(e)})}$, where $\Theta^{(h)}$ and $\Theta^{(e)}$ are Hermitian matrices acting on the hole and electron subspaces respectively. These operators generalize the phases θ_h and θ_e we have considered for the two-mode scattering process. Their action on the Fermi sea is, as we shall see in next section, to add a global phase to the state. Then, we will consider a two-mode scattering process, where each pair of modes is scattered according to eqs. (2.64) and (2.65), with $u \in \mathbb{R}_+$ and $\theta = 0$. The mathematical details for such a decomposition of general unitary operators can be found in appendix C.

We can now use the Floquet–Bloch basis to rewrite the full many-body scattering operator as a product of uncoupled elementary two-mode operator, with a prefactor that scatters electron and hole subspaces independently.

$$\mathcal{S}_{\mathrm{g}} = \exp\left(\sum_{a\in\mathbb{N}}\int_0^{2\pi f} \lambda_a(\omega)\Big(c^\dagger[\psi^{(e)}_{a,\omega}]c[\psi^{(h)}_{a,\omega}] - c^\dagger[\psi^{(h)}_{a,\omega}]c[\psi^{(e)}_{a,\omega}]\Big)\frac{\mathrm{d}\omega}{2\pi}\right) \tag{2.71a}$$

$$\times \exp\left(\mathrm{i}\sum_{a,b\in\mathbb{N}}\int_0^{2\pi f}\Big(\Theta^{(e)}_{ab}(\omega)c^\dagger[\psi^{(e)}_{a,\omega}]c[\psi^{(e)}_{b,\omega}] + \Theta^{(h)}_{ab}(\omega)c^\dagger[\psi^{(h)}_{a,\omega}]c[\psi^{(h)}_{b,\omega}]\Big)\frac{\mathrm{d}\omega}{2\pi}\right). \tag{2.71b}$$

The many-body state at zero temperature

We can use this many-body scattering matrix to compute the outgoing many-body state, in case of a zero-temperature input state $|F\rangle$. In this case, the incoming modes below the Fermi surface are filled, and the ones above are empty. This implies several things. First, factor (2.71b) of the many-body scattering operator turns into a global phase, since it is an independent rearrangement of hole and electron modes. We will put

this irrelevant phase to one, in what follows. Second, if we develop the remaining exponential, we have a tensor product of factors having the form (2.68), one for each Floquet–Bloch wave. The contribution arising from the sector containing an even number of particle vanishes in each of these factors. What finally remains when we fully parametrize using Floquet–Bloch waves is

$$\prod_{\substack{\omega\in[0,2\pi f[\\ a\in\mathbb{N}}} \left(\sqrt{1-p_a^{(e)}(\omega)}+\sqrt{p_a^{(e)}(\omega)}c^\dagger\left[\psi_{a,\omega}^{(e)}\right]c\left[\psi_{a,\omega}^{(h)}\right]\right)|F\rangle\,. \tag{2.72}$$

There are several important things to remark here. First, there is a one-to-one correspondence between electronic bands and hole ones, with $p_a^{(e)}(\omega)=p_a^{(h)}(\omega)$. This feature is not obvious when electron/hole symmetry is not present in the system, and we will do more extensive numerical exploration in near future to check that this feature is preserved by our algorithm. Furthermore, electron/hole coherences only appear for these corresponding bands.

Flat bands at zero temperature

We will end this section by making a connection with previous work of Vanević et al. [2007, 2008, 2016]. In their work, they discuss the case of a classical a.c. voltage at zero temperature, and find a simplified expression for the many-body state, similar to eq. (2.72), as well as similar properties of the output coherence. Notably, from a smart use of the properties of first-order coherence at zero temperature, they can deduce the absence of inter-band correlations in the electron/hole coherence.

To make this connection, we will consider the case of an excitation described by flat bands, from zero temperature. We will also, as previously, consider that there are no d.c. contributions. As stated earlier, an a.c. voltage drive at zero temperature is just a specialization of this case. Note that we have $\cos(\lambda_a(\omega))=\sqrt{1-p_a(\omega)}$ and $\sin(\lambda_a(\omega))=\sqrt{p_a(\omega)}$. Since we are considering flat bands, $\lambda_a(\omega)$ is constant in ω.

This allows us to reorganize a combination of Bloch modes as a combination of Wannier wavefunctions directly at the many-body level. Of course the choice of Wannier functions in the electron quadrant will constrain the choice of Wannier functions in the hole quadrant. Namely, we have

$$\int_0^{2\pi f} c^\dagger\left[\psi_{a,\omega}^{(e)}\right]c\left[\psi_{a,\omega}^{(h)}\right]\frac{\mathrm{d}\omega}{2\pi}=\sum_{l\in\mathbb{Z}}c^\dagger\left[\varphi_{a,l}^{(e)}\right]c\left[\varphi_{a,l}^{(h)}\right]. \tag{2.73}$$

Using the same development as above, we finally obtain

$$|\Psi\rangle = \prod_{a\in\mathbb{N}} \prod_{l\in\mathbb{Z}} \left(\sqrt{1-p_a} + \sqrt{p_a} c^\dagger \left[\varphi_{a,l}^{(e)}\right] c \left[\varphi_{a,l}^{(h)}\right] \right) |F\rangle \,, \tag{2.74}$$

which is the formula for a classical voltage drive found in [Vanević et al., 2016], that we extended for the more general case of flat bands. Note that, once we choose a determination for the electronic Floquet–Wannier wavefunctions, it determines also the Floquet–Wannier wavefunctions for holes, up to a global phase. As such, we do not expect the Floquet–Wannier wavefunctions to be minimally spread for both electrons and holes.

Non-zero temperature

At non-zero temperature, all terms of eq. (2.68) will play a role. The contribution eq. (2.71b), arising from the separate rearrangement of electron and hole modes will have a non-trivial contribution to the total state. This contribution may scatter electrons deep into the Fermi sea compared to the thermal scale into the thermal fluctuations, as well scatter holes from the thermal fluctuations deeper into the Fermi sea. It is also possible to rearrange wavefunctions inside the thermal band. Similar processes appear in the electron subspace. Notably, this term will correlate explicitly different bands. The contribution eq. (2.71a) will also act differently, since sectors of even parities are expected if one of the Floquet–Bloch waves possesses thermal fluctuations at this point. We expect that the atoms of signal, as well as their respective coherences to be modified by this term. Remarkably, we note however that the description in terms of Floquet–Bloch waves at zero temperature allows us to give a many-body description up to the two Hermitian operators $\Theta^{(e)}$ and $\Theta^{(h)}$. This is interesting since it gives a way to see what processes will occur when "heating" an ideal single-electron source.

Let me stress once again that the many-body states we have considered are not valid for every situation. Especially, we expect a break down as soon as interactions will enter into the game. In this case, we can see this decomposition as the simplest guess for the many-body state from single-particle coherence. An interesting perspective would be to have a general procedure that can refine this guess as we get access to higher and higher order coherences, providing a clear insight of the electronic coherences in terms of many-body state. This question will lead to further investigations in near future.

2.5.2 Electron/hole entanglement entropy

Now that we have discussed the many-body state for the whole system, containing positive and negative frequencies, we will show how we can describe the many-body state associated only to electronic quadrant. Of course, a natural way to do this is to consider the full many-body expression and trace out the negative frequencies. This can easily be done at zero temperature since we obtained a simple expression for the whole many-body state in this case, but we want an approach that can work as long as the state obeys Wick's theorem.

A first remark is that, if the whole state obeys Wick's theorem, the reduced state will, since the associated correlation functions expressed in frequency basis are just correlation functions of the whole state taken in the simplex of positive frequencies. Thus, a Floquet state will possess density matrices for electronic part that can be fully deduced from first-order coherence.

A very natural guess for the many-body state associated to the electronic quadrant corresponds to filling non-coherently each Floquet–Bloch mode with its probability. This corresponds to the following state

$$\rho_+ = \bigotimes_{\substack{\omega\in[0,2\pi f[\\ a\in\mathbb{N}}} \left(\left(1-p_a^{(e)}(\omega)\right)|0\rangle\langle 0| + p_a^{(e)}(\omega)c^\dagger[\psi_{a,\omega}^{(e)}]\,|0\rangle\langle 0|\,c[\psi_{a,\omega}^{(e)}]\right). \tag{2.75}$$

What we obtained here is quite similar to the thermal state, as can be seen by comparing this expression to eq. (1.36). This state also obeys Wick's theorem and since it gives us the same first-order coherence for electron quadrant, it is the many-body state associated to this quadrant. It is very easy to show this from the zero-temperature many-body expression also.

One property of a perfect n-electron source is that there are no correlations between electrons and holes. Namely, the many-body state associated to positive and negative frequencies factorizes, which gives

$$\rho_{\mathrm{nES}} = \rho_+ \otimes \rho_-. \tag{2.76}$$

We can measure quantitatively how our description departs from this, in full generality, by looking at the mutual information between positive and negative frequencies. If we denote $S_{\mathrm{vN}}^{(e/h)}$ the von Neumann entropies associated respectively to electrons and holes, and $S_{\mathrm{vN}}^{(\mathrm{tot})}$ the entropy

associated to the whole system, the mutual information is defined by

$$I(e:h) = S_{\mathrm{vN}}^{(e)} + S_{\mathrm{vN}}^{(h)} - S_{\mathrm{vN}}^{(\mathrm{tot})}. \tag{2.77}$$

In what follows, we will concentrate on the zero-temperature case. In this case, the global state is pure, and its von Neumann entropy vanishes. It also imposes that the von Neumann entropy of the electronic part equals the von Neumann entropy of the hole part. As such, the mutual information is two times the von Neumann entropy of the electron part. In the case where we only emit uncorrelated electrons and holes, the von Neumann entropy will vanish, giving us an information-theoretic criterion characterizing the purity of the source.

The last piece we miss is how we can compute the von Neumann entropy from the Floquet–Bloch decomposition. Starting from the expression for the many-body state, it is easy to show that

$$\begin{aligned} S_{\mathrm{vN}}^{(e)} = -\sum_{a\in\mathbb{N}} \int \Big(& p_a^{(e)}(\omega) \log_2(p_a^{(e)}(\omega)) \\ & + (1-p_a^{(e)}(\omega)) \log_2(1-p_a^{(e)}(\omega)) \Big) \frac{\mathrm{d}\omega}{2\pi f}. \end{aligned} \tag{2.78}$$

2.6 Electron-source diagnostic

In this section, we apply our signal-processing technique to numerical data coming from a Floquet modelization of periodic electron sources. Our goal is to use the Floquet–Bloch spectrum to assess quality of the source as a single-electron source, along the lines discussed in the previous section. Because of their experimental importance, the LPA and the Leviton sources will be discussed.

2.6.1 The mesoscopic capacitor

Let us apply our method to the mesoscopic capacitor case (see section 1.2.3, page 31) operated by a time-dependent voltage $V_g(t)$ as depicted on fig. 2.6. In the present section, the mesoscopic capacitor will be modeled using Floquet scattering theory since, in most experimentally relevant regimes, interaction effects within the capacitor itself can be neglected. Motivated by experiments [Fève et al., 2007; Marguerite et al., 2016a], we will consider the case of a square drive as well as of a sinusoidal drive.

Exactly as in [Grenier et al., 2011a], the mesoscopic capacitor is characterized in the Floquet scattering theory by the level spacing of the dot Δ, the transparency D of the QPC (see fig. 2.6) as well as by the voltage drive $V_g(t)$. The Floquet scattering matrix is then expressed as

$$S(t,t') = \exp\left(\frac{\mathrm{i}e}{\hbar}\int_{t'}^{t} V_g(\tau)\,\mathrm{d}\tau\right)\mathcal{S}_0(t-t'), \tag{2.79}$$

where $\mathcal{S}_0$ denotes the scattering matrix of the dot which, in the frequency domain, is given by

$$\mathcal{S}_0(\omega) = \frac{\sqrt{1-D} - \mathrm{e}^{2\mathrm{i}\pi\hbar(\omega-\omega_0)/\Delta}}{1-\sqrt{1-D}\,\mathrm{e}^{2\mathrm{i}\pi\hbar(\omega-\omega_0)/\Delta}}, \tag{2.80}$$

where ω_0 notes a bias. Choosing $\omega_0 = 0$ ensures that a peak in the density of states of the dot is located at the Fermi level in the absence of external drive.

We will now discuss the operating regimes of the mesoscopic capacitor by computing the electron/hole entanglement from the Floquet–Bloch spectrum for the electronic excitations at fixed Δ and driving frequency f in terms of the experimentally controlled parameters D and V_0, the latter being the amplitude of the drive applied to the mesoscopic capacitor.

2.6.2 Square drive

In the case of a square drive used to demonstrate single-electron emission by the mesoscopic capacitor [Fève et al., 2007], the T-periodic voltage drive is defined by $V_g(t) = -V/2$ for $-T/2 \leq t < 0$ and $V_g(t) = V/2$ for $0 < t < T/2$.

Electron/hole entanglement

Figure 2.7 presents a density plot of the entropy defined by eq. (2.78) as a function of D and eV/Δ at fixed $\Delta/hf = 20$. There are shallow zones with minima in each square $eV/\Delta \in]n, n+1]$ ($n \in \mathbb{N}$) and $0 < D \leq 1$. In the single-electron sector, a global minimum can be found at $eV_{\mathrm{opt}}/\Delta \approx 0.37$ and $D_{\mathrm{opt}} \approx 0.47$ and the corresponding entropy is 0.20 bit. As we shall see, this is the regime where the mesoscopic capacitor behaves almost ideally, emitting exactly one electronic and one hole excitation per period.

There is also a minimum in the second square where $1 < eV/\Delta \leq 2$ but the zone is further from zero. In this zone, three electrons are emitted during the first half period and three holes during the other one, due to

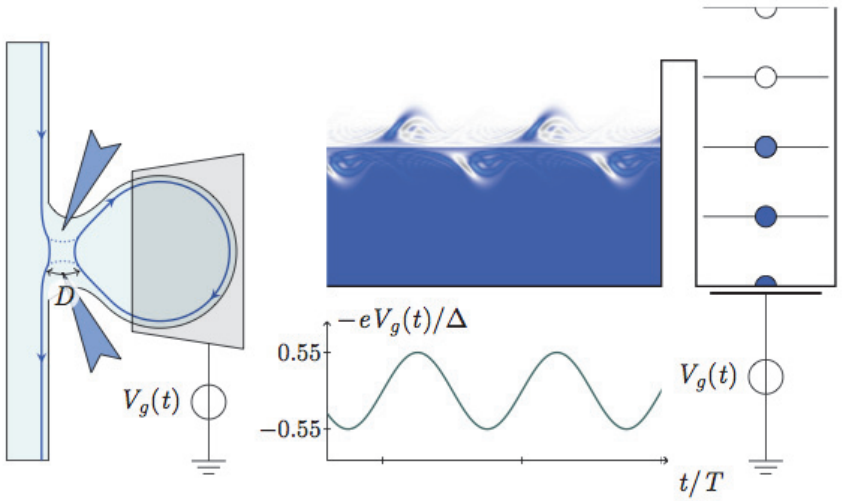

Figure 2.6: Left panel: The mesoscopic capacitor is a ballistic quantum conductor formed by connecting a quantum dot to a chiral edge channel via a quantum point contact of transparency D. Right panel: Modelization as a driven quantum dot with level spacing Δ connected to an electronic reservoir. The mesoscopic capacitor is driven by an a.c. voltage drive $V_g(t)$ applied to the top gate. Applying a d.c. voltage bias to the top gate shifts the energy levels of the dot. The mesoscopic capacitor emits a stream of electron and hole excitations whose Wigner distribution function $W_S^{(e)}(t,\omega)$ is depicted as a density plot on the right panel.

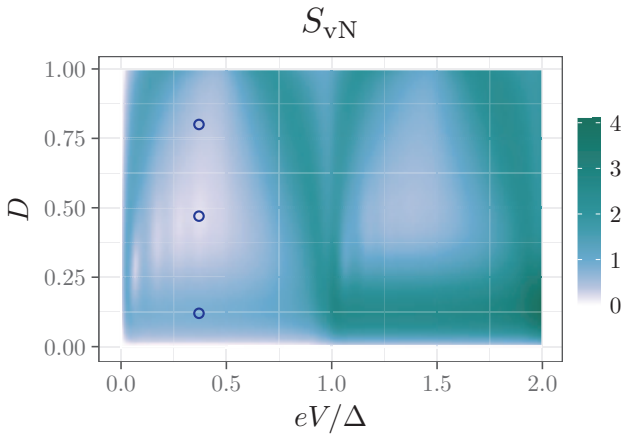

Figure 2.7: Density plot of the electron/hole entanglement entropy at zero temperature for the mesoscopic capacitor operated with a square drive of frequency f such that $\Delta/hf = 20$ as a function of eV/Δ and D.

the fact that at zero voltage, there is a level at the Fermi energy. It is not surprising that in this zone the deviation from the ideal regime is greater than in the previous case, since we expect a generation of more electron/hole pairs.

A surprising feature are the substructures that appear within each shallow zone. At the time of this writing, we do not yet understand this fact. Further numerical exploration will be necessary, especially to see if the ratio Δ/hf plays a role in these substructures.

In order to understand more precisely the electron/hole entanglement properties described by this plot, we have chosen specific points for which we will push the analysis further. The corresponding electronic Wigner distribution functions are plotted on fig. 2.9.

The Floquet–Bloch spectrum

Let us review the Floquet–Bloch spectrum for the three points that are marked in fig. 2.7. This figure presents the corresponding bands as functions of the adimensionned quasi-energy $\omega/2\pi f$ and orders them according to their averages, the $a = 0$ band being one with the highest average.

The middle panel corresponds to the absolute minimum of the entropy and therefore to the best operating point as a single-electron source.

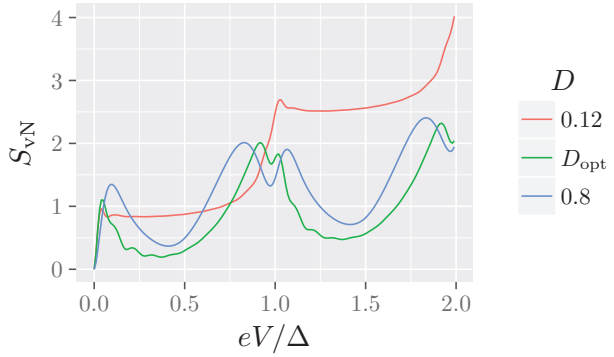

Figure 2.8: Cuts of the entropy S_{vN} for a square voltage drive depicted on fig. 2.7 as functions of eV/Δ for $D = 0.12$, $D = D_{\mathrm{opt}}$ and $D = 0.8$.

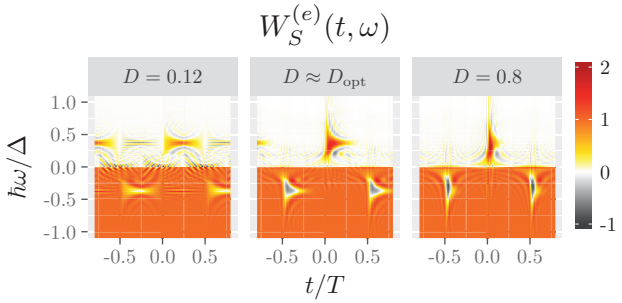

Figure 2.9: Density plot of the full Wigner distribution function $W_S^{(e)}(t,\omega)$ for the square-voltage driven LPA source as a function of t/T and $\hbar\omega/\Delta$ for the three selected points appearing on fig. 2.7.

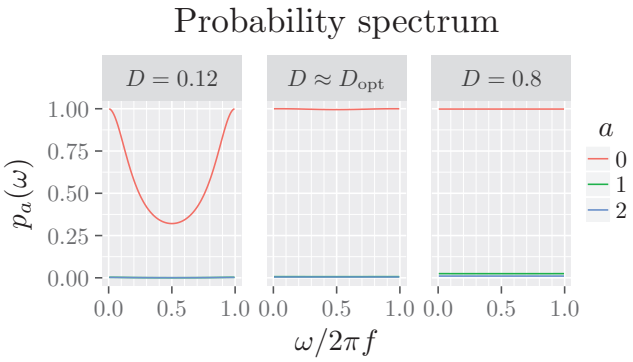

Figure 2.10: Floquet–Bloch spectrum for the three selected points appearing on fig. 2.7, in the case of a square-voltage driven LPA source. Only the first three bands are represented, all the other ones being even closer to zero.

Only one band gives eigenvalues close to one and it is flat. All the other bands are really close to zero as expected.

Opening the dot ($D = 0.8$, right panel) leads to flat bands as expected since at $D = 1$ it is really what is expected but we note that the eigenvalues are almost unity and that the $a = 1$ band has value 0.02, thus showing that we are departing from the ideal single-electron regime.

Closing the dot ($D = 0.12$, left panel) mostly changes the shape of the $a = 0$ band which shows some curvature. Its average is equal to 0.57 which shows that strong electron/hole coherences are expected. This point corresponds to the local maximum of the entropy between $D = 0$ and $D = D_{\text{opt}}$ along $eV = eV_{\text{opt}}$. At this point, the entropy is equal to 0.85 bit. Starting from the optimal point, decreasing D increases the escape time of the electron and hole excitations. In our previous publications, [Grenier et al., 2011a; Roussel et al., 2017], we have argued that at some point, the mesoscopic capacitor emits a quantum superposition of nothing and of an elementary electron/hole pair on top of the Fermi sea. Decreasing D would increase the amplitude of the emission of the electron/hole pair from modulus very close to one to modulus zero and this explains the behavior of the entropy with decreasing D at fixed eV/Δ. However, when D is decreased, inter-period coherences appear due to the band curvature. This imply that this picture is only approximative.

Electronic atoms of signals and coherences

In order to get a clearer view of the electronic state emitted by the source, let us now extract the corresponding electronic atoms of signal. Figure 2.11 presents the electronic atoms of signal associated with the $a = 0$ Floquet–Bloch band for the three operating points considered before.

As expected, the duration of each wavepacket increases with decreasing D reflecting the fact that the escaping time from the dot is longer at low QPC transparency. At the optimal value $D_{\rm opt}$, we expect the source to emit a wavepacket of the form

$$\widetilde{\varphi}_e(\omega) = \frac{\mathcal{N}_{\rm e}\ {\rm H}(\omega)}{\omega - \omega_{\rm e} - i\gamma_{\rm e}/2}, \tag{2.81}$$

where $\mathcal{N}_{\rm e}$ ensures normalization and $\gamma_{\rm e}$ denotes the electron escape rate from the quantum dot which is given by $\gamma_{\rm e} = D\Delta/h(1-D/2)$ [Mahé et al., 2008; Nigg and Büttiker, 2008]. We will plot the overlap of the extracted electronic atom of sign to such a truncated Lorentzian in energy as a function of D in our forthcoming paper [Roussel et al.]. This will show when the simplified description of the ideal single-electron source, where we consider a resonant level coupled to a truncated continuum [Grenier et al., 2011a], is correct. Nonetheless, we note that for $D = 0.12$, the electronic wavepacket remains limited to the firsf half period $0 \lesssim t \lesssim T/2$. At very low D, we expect this wavepacket to be the projection on the space of single-particle states with positive energy of the dual of the Martin–Landauer wavepacket, that is of an electronic wavefunction constant on a time interval.

Since the bands are flat for $D = D_{\rm opt}$ and $D = 0.8$, no inter-period coherence is expected as can be seen from the middle and right panels of fig. 2.12. However, when closing the dot ($D \approx 0.12$, left panel), inter-period coherences for the electronic excitations start to unfold, an expected consequence of the delocalization of the emitted electronic excitations over more than a half period. This shows that the electronic coherence time is given by the electronic escape time which, in this case, exceeds the duration of an electronic atom of signal.

2.6.3 Sinusoidal drive

Let us now consider a sinusoidal drive is of the form $V_g(t) = V \sin(2\pi f t)$ at frequency f with amplitude V. In the present case, we will work

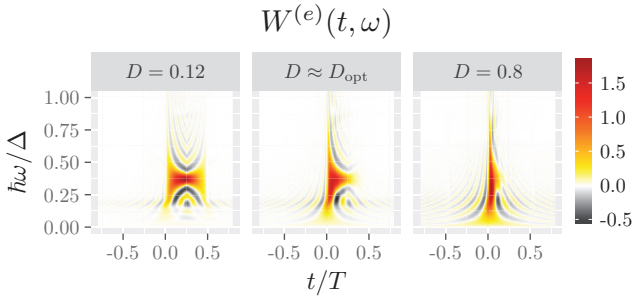

Figure 2.11: Wigner distribution functions for the Floquet–Wannier electronic atoms of signal corresponding to the $a = 0$ Floquet–Bloch band represented as a function of t/T and $\hbar\omega/\Delta$ for the three operating points of fig. 2.7 in the case of a square voltage drive.

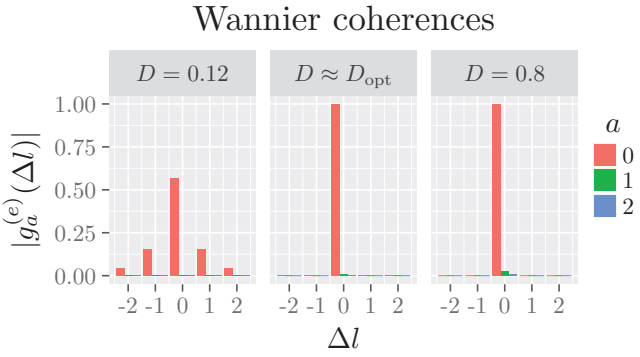

Figure 2.12: Temporal coherences $p_n(\Delta l)$ between the electronic atoms of signal of the $a = 0$, 1 and 2 Floquet–Bloch bands given by eq. (2.46) as a function of Δl for the three operating points of fig. 2.7 in the case of a square drive.

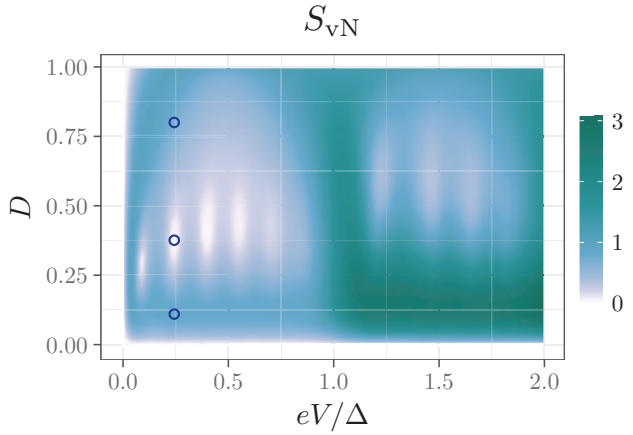

Figure 2.13: Density plot of the electron/hole entanglement entropy at zero temperature for the mesoscopic capacitor operated with a sine drive at frequency f such that $\Delta/hf = 20$ as a function of eV/Δ and D.

at fixed drive frequency and dot geometry so that $\Delta/hf \simeq 20$, which corresponds to experimentally realistic conditions.

Electron/hole entanglement

Figure 2.13 presents a density plot of the entropy defined by eq. (2.78) as a function of D and eV/Δ at fixed $\Delta/hf = 20$. There are shallow zones with minima in each square $eV/\Delta \in]n, n+1]$ ($n \in \mathbb{N}$) and $0 < D \leq 1$. A global minimum can be found at eV_{opt}/Δ slightly less than 0.24 and $D_{\mathrm{opt}} \approx 0.38$ and the corresponding entropy is very low: 0.06 bit. As we shall see, this is a regime where the mesoscopic capacitor behaves almost ideally, emitting exactly one electronic and one hole excitation per period. Decreasing D from this value leads to an increase of the entropy while decreasing leads to a local maximum ($D \simeq 0.11$) before a decrease. For the three points located at the same value of eV/Δ and corresponding to $D = 0.8$, $D = D_{\mathrm{opt}}$ and $D \simeq 0.11$, the corresponding electronic Wigner functions are depicted on fig. 2.14. As for the square drive case, interference fringes, characteristic from inter-period electronic coherence as well as for electron/hole coherences, are visible for $D \simeq 0.11$ and to a lesser extent for $D = 0.8$ whereas they are much more discrete for $D = D_{\mathrm{opt}}$.

The novelty compared to the case of a square drive discussed in the

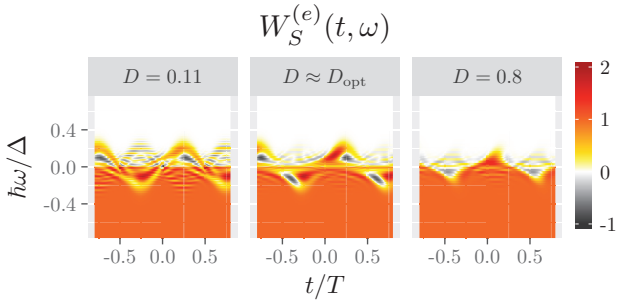

Figure 2.14: Density plots of the full Wigner distribution function $W_S^{(e)}(t,\omega)$ for the sine-drive case as a function of t/T and $\hbar\omega/\Delta$ for the three selected points appearing on fig. 2.13.

previous section comes from the more pronounced local minima in the first square $0 < D < 1$ and $0 < eV/\Delta < 1$.

These minima correspond to quite low values of the electron/hole entanglement entropy. They can also be seen on fig. 2.15 presenting cuts for fixed value of D of S_{vN} as functions of eV/Δ. By running a simplex minimization algorithm, we can find position and entropy value at each minimum as summarized on table 2.1.

	D	eV/Δ	S_{vN} (bit)
1	0.29	0.09	0.10
2	0.38	0.24	0.06
3	0.41	0.40	0.06
4	0.43	0.55	0.10
5	0.42	0.70	0.18

Table 2.1: Positions and values of different entropy minima for the sine-drive case, when one about one electron is emitted ($eV/\Delta \leq 1$).

We suspect that those minima come from an interference effect between the rising time of the drive and the energy of the cavity. Testing this hypothesis will require more numerical exploration, varying Δ/hf. Of course, though not particularly involved numerically, since we need to explore three dimensions (Δ/hf, eV/Δ and D), such an exploration will be delayed for our upcoming paper.

Figure 2.16 depicts the electronic Wigner function emitted by the

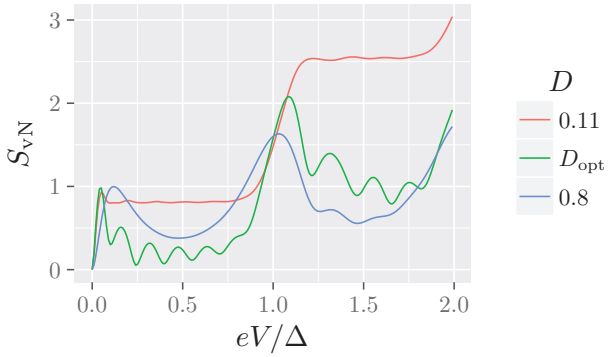

Figure 2.15: Cuts of the entropy S_{vN} in the sine-drive case depicted on fig. 2.13 as functions of eV/Δ for $D = 0.11$, $D = D_{\mathrm{opt}}$ and $D = 0.8$.

source for these local minima. As expected, higher energy regions are explored when increasing the amplitude of the drive eV/Δ but for each of these local minima, we are quite close to the ideal single-electron source regime.

There are also local minima in the second square where $1 < eV_D/\Delta \leq 2$ but the corresponding entropy values are higher (above 0.3 bit). As in the square case, in this zone we send three electrons and three holes per period. As such, it is not surprising that the purity of the source is lower, since we expect to excite more electron/hole pairs.

The Floquet–Bloch spectrum

Let us review the Floquet–Bloch spectrum for the three points that are marked in fig. 2.13. The results are qualitatively similar to what is observed in the case of a square drive: the middle and right panels depict flat bands and the middle panel corresponds to the absolute minimum of the entropy, shows one band with average very close to one. This corresponds to the best operating point as a single-electron source. Opening the dot ($D = 0.8$, right panel) also leads to flat bands as expected but we note that the eigenvalues for the first band (which is the only one that is non negligible) is only 0.83.

Exactly as in the square band case, going to a closed dot ($D = 0.11$, left panel) leads to a curved $a = 0$ band with average 0.5 and the same comments as for the square drive apply.

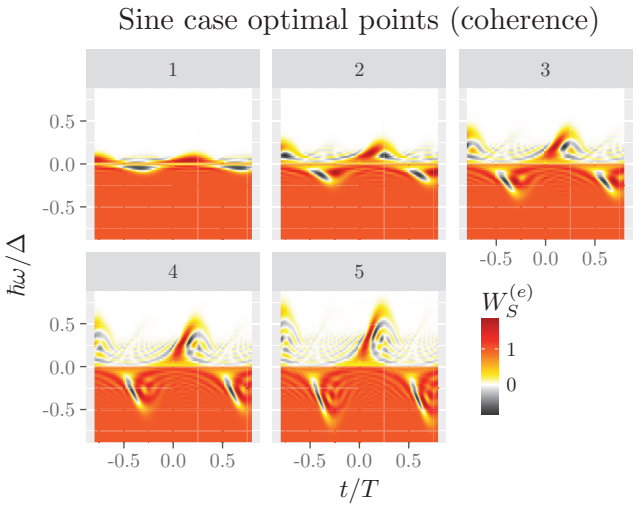

Figure 2.16: Electronic Wigner function emitted by the mesoscopic capacitor for the local minima of S_{vn} appearing on fig. 2.13 in the domain $0 < D < 1$ and $0 < eV/\Delta < 1$.

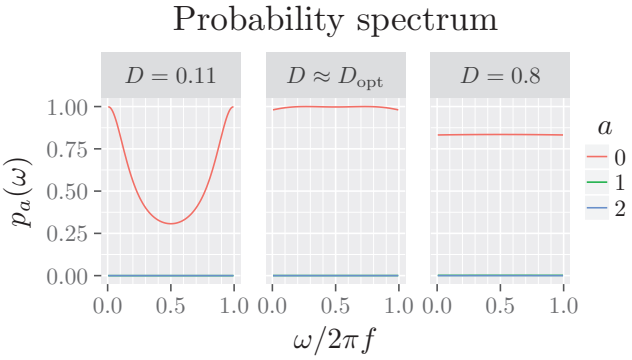

Figure 2.17: Floquet–Bloch spectrum for the three selected points in the sine-drive case appearing on fig. 2.13. Only the first three bands are represented, all the other ones being even closer to zero.

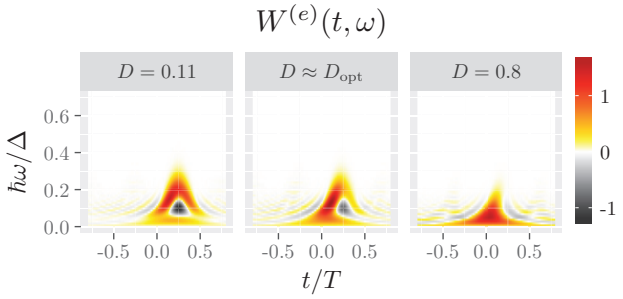

Figure 2.18: Wigner distribution functions for the Floquet–Wannier electronic atoms of signal corresponding to the $a = 0$ Floquet–Bloch band represented as a function of t/T and $\hbar\omega/\Delta$ for the three operating points of fig. 2.13. This is the sine-drive case.

Electronic atoms of signals and coherences

Let us now discuss the electronic atoms of signal in this case as well as their coherence properties. The spectra being very similar, the electronic coherence properties are also quite similar as can be seen from fig. 2.19. However, for a widely open dot, there is still one type of electronic atom of signal with no inter-period correlations that is emitted per half period, although it is emitted with a probability less than one. When closing the dot, we first encounter an optimal point where only one is emitted almost certainly: the mesoscopic capacitor behaves like an almost ideal single-electron source and there are no inter-period electronic coherences. Finally when closing the dot, the electronic excitation emitted by the capacitor tends to delocalize over more than one period and we encounter a point with a local maximum of electron/hole entanglement. In the limit $D \to 0$, the luminosity of the source decreases: the spectrum collapses to zero and nothing is emitted.

In the end, the real influence of the drive lies into the form of the electronic atoms of signals which, for the sinusoidal drive are depicted on fig. 2.18. As expected, closing the dot leads to longer Wannier wavepackets.

Figure 2.20 presents the dominant electronic atoms of signal for the local optimal points in the quadrant $0 < D < 1$ and $0 < eV/\Delta < 1$. As we raise the drive amplitude, the Wannier wavefunctions explore higher energies. For each minimum, their is a corresponding number of negative bumps in the Wigner function.

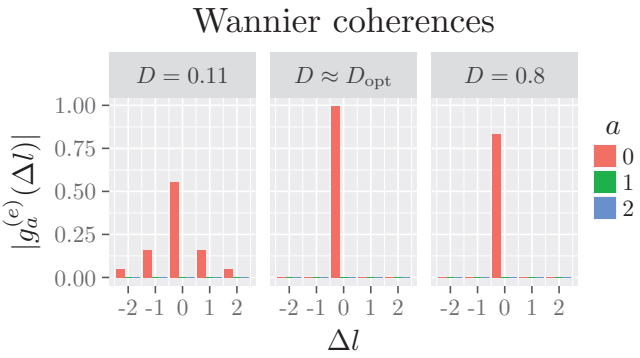

Figure 2.19: Temporal coherences $p_n(\Delta l)$ between the electronic atoms of signal of the $a = 0$, 1 and 2 Floquet–Bloch bands given by eq. (2.46) as a function of Δl for the three operating points of fig. 2.13. This is the sine-drive case.

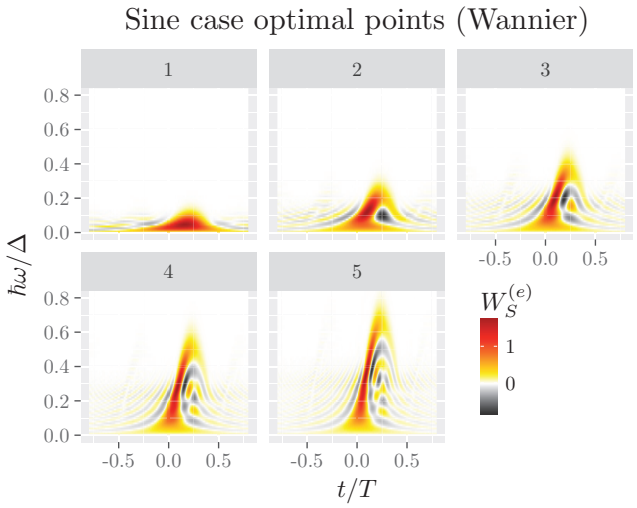

Figure 2.20: Dominant electronic atoms of signals emitted by the mesoscopic capacitor for the local minima of S_{vn} appearing on fig. 2.13 in the domain $0 < D < 1$ and $0 < eV/\Delta < 1$.

2.6.4 Lorentzian pulse trains

In this section, we consider an Ohmic contact driven by time dependent voltage which is a T-periodic train of Lorentzian pulses of width τ_0, each of them carrying an electric charge α. The resulting time-dependent voltage

$$V(t) = \frac{\alpha h f}{e} \frac{\sinh(2\pi f \tau_0)}{\sinh(\pi f \tau_0) + \sin^2(\pi f t)} \tag{2.82}$$

has a d.c. component $V_{\rm dc} = \alpha h f/e$ and an a.c. part $V_{\rm ac}(t) = V(t) - V_{\rm dc}$ [Dubois et al., 2013a]. In this section, we shall present preliminary results on how this picture is modified[1]. Unfortunately, due to lack of time, we have not completed all the numerical implementations that would enable us to treat any value of α and we shall thus only discuss integer values of α.

When α is an integer, at zero temperature, we expect the spectrum to be completely flat, since it is the classical drive case. Furthermore, since, per period, there is an emission of α electrons, there will be α bands that are constant to unity and, other bands will be zero. When α is non-integer, we expect a richer spectrum. Notably, the bands will be piecewise flat, with a step at $\alpha \pmod 1$.

For a single Lorentzian voltage pulse of duration τ_0, whenever α is a positive integer n, we have seen on section 1.4.4, page 58 that the resulting many-body state is a Slater determinant built by adding on the Fermi sea n mutually orthogonal electronic single-electron excitations whose wavefunctions are given in the frequency domain by:

$$\varphi_n(\omega) = \sqrt{4\pi v_F \tau_0}\ \mathrm{H}(\omega)\, L_{n-1}(2\omega\tau_0)\, \mathrm{e}^{-\omega\tau_0}, \tag{2.83}$$

where L_n denotes the nth Laguerre polynomial. In the limit where Lorentzian pulses are well separated $f\tau_0 \ll 1$, we expect the electronic atoms of signal to have a strong overlap with these mutually orthogonal wavefunction. Of course, the question is to find these Levitonic atoms of signals or Levitonoids.

Levitonic atoms of signals at $\alpha = 1$

Let us first present the case $\alpha = 1$. Figure 2.21 shows the Wigner function of the train for different values of $f\tau_0$. We see that we can go from a

1. The case of negative α can be studied along the same lines provided one exchanges the role of electrons and holes.

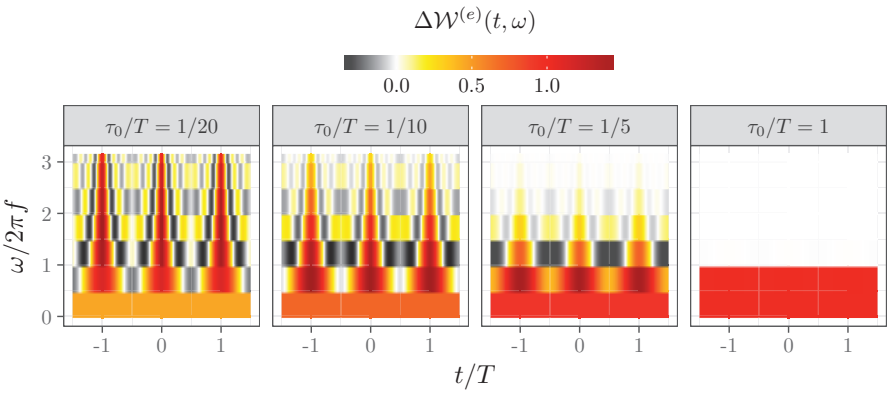

Figure 2.21: Wigner function of a Leviton train for different ratio τ_0/T. As we raise τ_0/T, the duration of each Leviton becomes longer and longer. Once it is comparable to the period, what we see is an almost stationary situation due to the raise of chemical potential.

situation from which each Leviton is quite separated to each other, to a stationary situation, where the Levitons are so spread over multiple periods that we only see the variation of the chemical potential due to the d.c. part.

In the case $\alpha = 1$, Moskalets has obtained explicit expression for electronic atoms of signal associated with a Leviton train [Moskalets, 2015]. The corresponding wavepackets are not time-reversal invariant, and lead to a Lorentzian current pulse of width τ_0. This is manifestly incompatible with the electronic atoms of signal obtained from our numerical computations. The reason of this apparent discrepancy comes from the ambiguity in the Wannier wavefunctions arising from the fact that one can multiply each electronic Floquet–Bloch eigenvector $|\psi_{a,\omega}\rangle$ by a phase that depends on the quasi-energy $0 \leq \omega < 2\pi f$. The numerical algorithms tends to produce wavepackets that have the smallest spreading in time whereas the analytical expressions obtained by Moskalets possess a Lorentzian current pulse. It is however possible to work out this analytical expression to obtain a minimally spread, time-reversal invariant wavepacket, that should be the same our algorithm finds:

$$\varphi(\omega) = \frac{1}{\sqrt{\mathcal{N}}}\,\mathrm{H}(\omega)\mathrm{e}^{-\omega_n \tau_0}, \tag{2.84}$$

where $\mathcal{N}$ is a normalisation factor, and $\omega_n = 2\pi f \lfloor \omega/2\pi f \rfloor$ is the frequency counted in multiple of $2\pi f$. We will call this new wavepacket a minimal

Levitonoid. The details of this derivation can be found in appendix B.2. We can see on fig. 2.22 that this analytical form and the one found by the algorithm match perfectly.

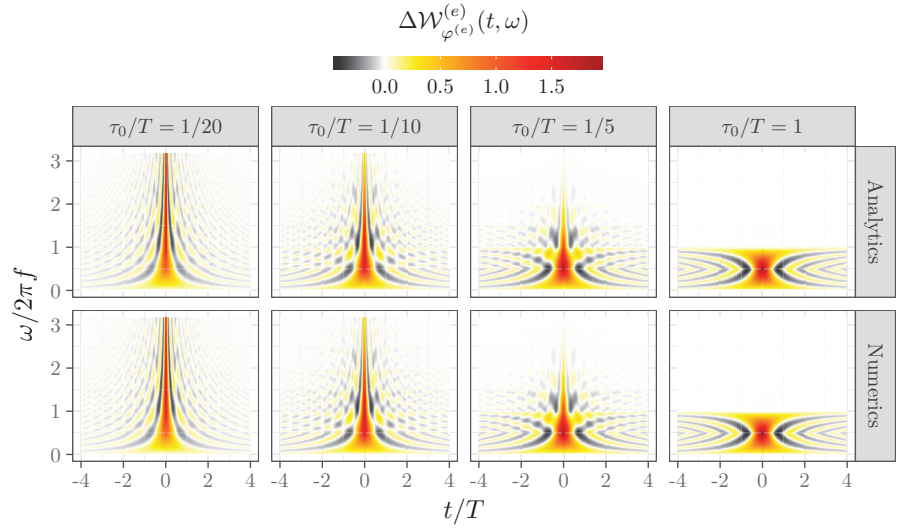

Figure 2.22: The electronic atoms of signal of a train of charge α Lorentzian pulses for $\alpha = 1$ and different values of $f\tau_0$. When $f\tau_0 \ll 1$, the wavepacket we obtain is very similar to a Leviton. When $f\tau_0 \simeq 1$, we have a Martin–Landauer wavepacket. The atoms of signal found by our algorithm (lower pane) fits perfectly the one predicted analytically (upper pane).

When $f\tau_0 \ll 1$, the minimal Levitonoid should approach the Leviton introduced by eq. (2.83). It is quite straightforward to see on the formula, since when we lower $f\tau_0$, the steps of width $2\pi f$ will become smaller, doing a better staircase approximation of the decaying exponential. We might wonder how we depart from this regime. For this, we can compute the overlap between the Levitonoid φ_{train} and a single Leviton of the same duration φ_{unique}

$$|\langle\varphi_{\text{train}} \,|\, \varphi_{\text{unique}}\rangle|^2 = \frac{1}{\pi f\tau_0}\frac{1-\mathrm{e}^{-2\pi f\tau_0}}{1+\mathrm{e}^{-2\pi f\tau_0}}. \tag{2.85}$$

In the limit $f\tau_0 \ll 1$, the overlap departs quadratically from unity.

In the case where $f\tau_0 \simeq 1$, the overlap between the minimal Levitonoid and the single Leviton tends to zero as $1/\pi f\tau_0$. We see on the left of

fig. 2.21 that the drive induces almost solely a d.c. shift, without much a.c. contribution. In this case, it seems natural to compare our Levitonoids to the Martin–Landauer wavepacket, centered around $\omega_e = \pi f$ and of width $\gamma_e = 2\pi f$. We see that this overlap goes exponentially to one as $f\tau_0$ goes to infinity

$$|\langle \varphi_{\text{train}} \,|\, \varphi_{\text{ML}} \rangle|^2 = 1 - \mathrm{e}^{-4\pi f \tau_0}. \tag{2.86}$$

Due to the 4π factor, the Levitonoid approaches extremely rapidly the Martin–Landauer wavepacket. For the examples discussed above, when $f\tau_0 = 1/5$, the overlap is around $92\,\%$. At $f\tau_0 = 1$, the overlap is unity up to the sixth significative digit, making the differentiation between a Levitonoid and a Martin–Landauer impossible in practice.

Finally, we can use those behaviors to see the difference in terms of typical duration between the minimal Levitonoids, and the wavepackets introduced by Moskalets. For Moskalets' wavepackets, the typical duration is always τ_0. In our case, the typical duration is τ_0 when τ_0 is shorter than the period. However, when τ_0 is increased above the time period, our wavepacket will tend to a Martin–Landauer, and its typical duration will be the time period.

Integer values of α

We have used the case $\alpha = 1$ to check the validity of our algorithm. We can now focus on integer values of $\alpha > 1$. In these cases, the bands will be degenerate, forcing us to search a set α Wannier wavefunctions. We will concentrate here on $\alpha = 2$ and $\alpha = 3$. Figure 2.23 presents the Wigner function of the electronic atoms of signals found by the algorithm for the same values of $f\tau_0$ as before.

Exactly as before, the electronic atoms of signal have a typical width that goes from τ_0 to T, as $f\tau_0$ increases. The wavepackets are however not time-reversal invariant. They rather come by symmetrical pairs, that, altogether, restore the time-reversal symmetry (except for the central pair when α is odd, which is time-reversal invariant).

We can compare the Wigner functions given by the algorithm to the Wigner functions of the different Levitons shown in fig. 1.12. A first striking difference is that Leviton wavepackets are invariant by time-reversal symmetry, which is not the case for our wavepackets. Another difference is that the average current of Leviton wavepackets is a Lorentzian of duration τ_0 and charge $-e$. Here, the average current is split into smaller pieces, as can be seen on fig. 2.24. This explains why our atoms of signal

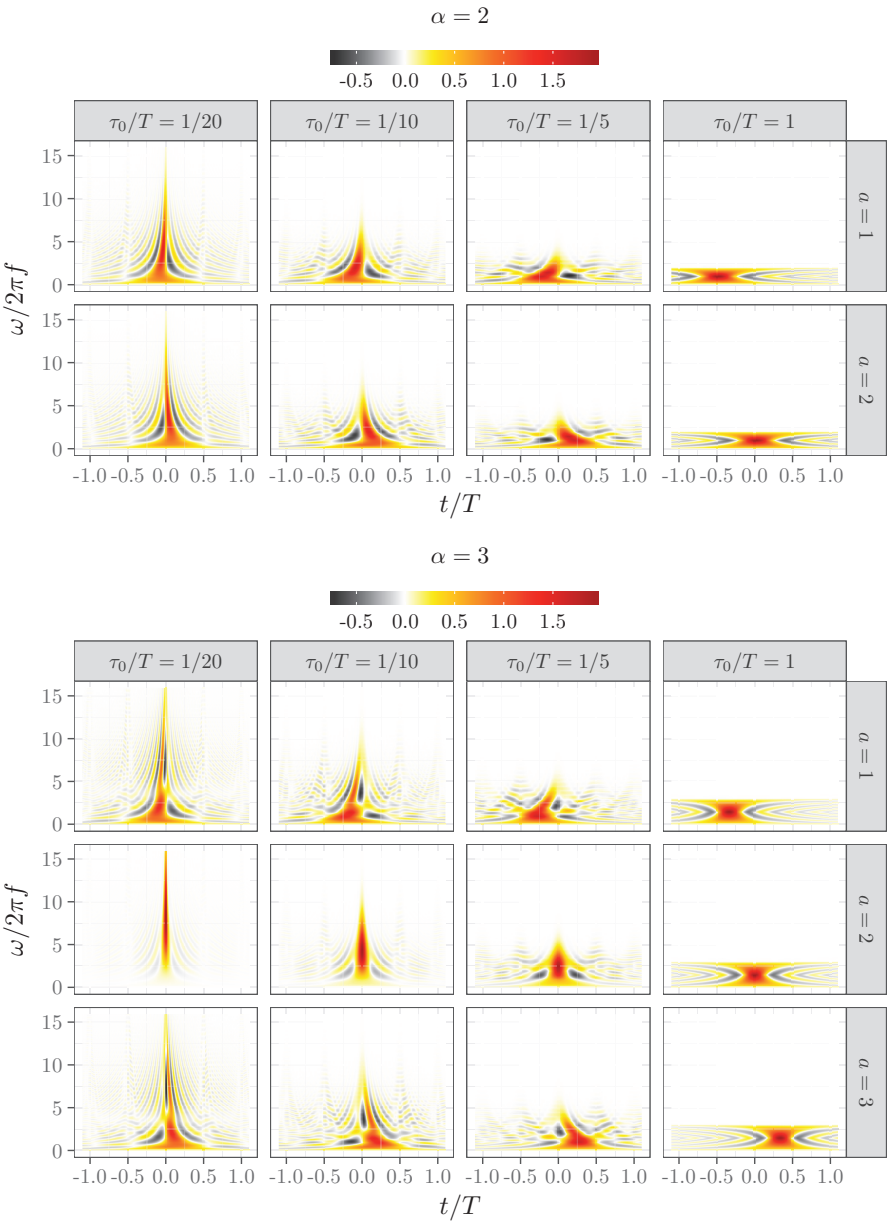

Figure 2.23: The electronic atoms of signal of a train of charge α Lorentzian pulses for $\alpha = 2$ and $\alpha = 3$ for the same values of $f\tau_0$ is in fig. 2.22.

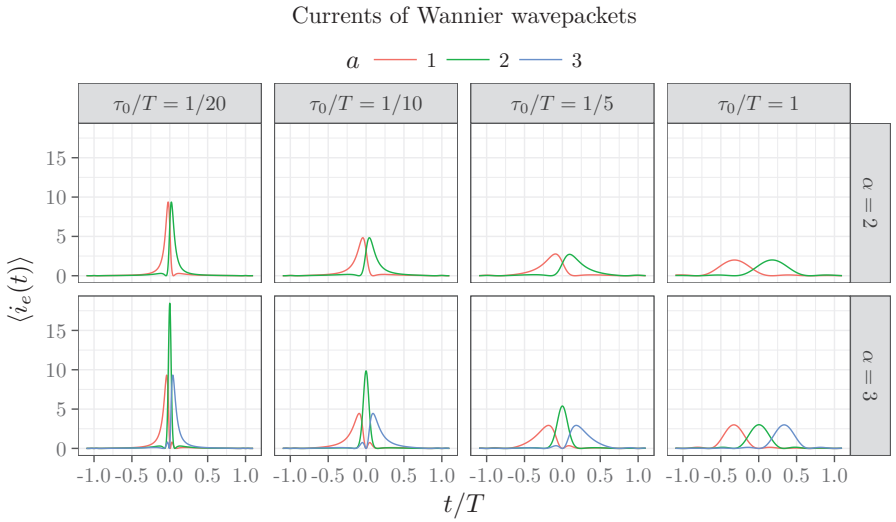

Figure 2.24: Currents of the atoms of signal pictured in fig. 2.23.

are different from Levitons of higher orders, even when $f\tau_0 \ll 1$. In fact, we are stumbling on the Wannier function ambiguity in the case of several degenerate bands. In the present case, when α is an integer, the Floquet–Bloch spectrum precisely consists of α degenerate bands with value 1. In this case, one expects the single-electron coherence to be of the form of the single-electron coherence of a Slater determinant containing exactly n electronic excitations on top of the Fermi sea. But such a Slater determinant can be represented in terms of diverse sets of wavefunctions: applying an element of $\mathcal{SU}(n)$ to the original family of n electronic wavefunctions building this Slater determinant gives another orthonormal family of electronic excitation describing exactly the same n-electron excitation.

Once again, when $f\tau_0 \simeq 1$, we find that the suitable wavepackets are Martin–Landauer wavepackets. It is expected, since in this case, the drive induces almost a stationary situation. To optimize the spreading, the Martin–Landauer must be as large as they can be in frequency. What we see is that there are α Martin–Landauer wavepackets that are separated in time by a duration T/n, and whose energy widths are $\gamma_e = 2\pi\alpha f$. This description would be the one for a T/n-periodic system, which would have a d.c. bias corresponding to a single electron added per period.

The structure of the spreading functional is not as well behaved as it is in the commutative case. In particular, it is quite flat around the minima, and possesses some non-global local minima. One must thus take care when carrying out the numerical minimization procedure in this case, that the minimum found is the good one.

Perspectives

In order to complete the program sketched at the beginning of the present section, an exploration of the deformation of the Floquet–Bloch spectrum when α increases continuously is necessary. However this requires a careful numerical exploration since when α is not an integer, we expect electron/hole excitations to appear and their number to diverge when $f\tau_0 \to 0$ [Dubois et al., 2013a].

An interesting perspective would then be to study electron fractionalization [Grenier et al., 2013] using our signal processing technique and, in particular, look for the behavior of the Floquet–Bloch spectrum when a Leviton train experiences fractionalization under the effect of Coulomb interactions as will be discussed in the next chapter.

2.7 A quantum electrical current analyzer

In this section, I will present the application of our signal-processing algorithm to real experimental data. This constitutes the experimental demonstration of the analysis of quantum electrical currents discussed in the present chapter. More specifically, we perform the analysis of a quantum electrical current arising from the application of a sinusoidal drive $V_S(t) = V_S \cos(2\pi f t)$ to a quantum Hall edge channel when the frequency of the drive and the drive's amplitude are such that ev_S and hf are slightly above $k_B T_{\mathrm{el}}$ (quantum regime). Electronic tomography has also been performed on a quantum current in the quasi-classical regime in order to compare both situations and show clear evidences of non classicality such as negativities of the electronic Wigner function.

2.7.1 Quantum tomography

The first step is the reconstruction of single-electron particle using the tomography protocol described in section 1.6. This is a central part of the PhD work of A. Marguerite in G. Fève's group in Paris. I refer the

reader to his PhD thesis [Marguerite, 2017] for details on the experimental setup. Here, I will mainly describe the main results.

The point is to reconstruct an unknown single-electron coherence by probing its overlap with a suitable family of single-electron coherences emitted by probes P_n. As discussed in section 1.6, the generic protocol proceeds by reconstructing the time dependance of the unknown T-periodic Wigner function $\Delta W_S^{(e)}(t,\omega)$ through its Fourier series, that is harmonic by hamonic.

Let us first focus on the $n=0$ harmonic, $\Delta W_{S,0}^{(e)}(\omega)$, which represents the excess source electronic distribution function. This time averaged quantity can be extracted from eq. (1.100) by using a d.c. bias $V_{\rm DC}$ as the probe P_0 so that $\Delta W_{P_0}^{(e)}(t,\omega) = f_{\rm eq}(\omega-\omega_{\rm DC}) - f_{\rm eq}(\omega)$ (with $\omega_{\rm DC} = -eV_{\rm DC}/\hbar$) is very close to 1 for $0 \leq \omega \leq \omega_{\rm DC}$ and to 0 elsewhere. Figure 2.25 (upper left panel) represents the excess noise ΔS as a function of $V_{\rm DC}$ for various sinusoidal source drives of increasing frequency (1.75 GHz, 9 GHz and 20 GHz) with drive amplitudes ($V_{\rm s} = 28\,\mu$V at $f = 1.75$ GHz, 31 µV at 9 GHz and 38 µV at 20 GHz) chosen to produce similar partition noise (around $2\times10^{-29}\,{\rm A^2\,Hz^{-1}}$) at $V_{\rm DC}=0$ (P_0 switched off). The partition noise is suppressed to zero when the d.c. bias is increased but in different ways for different frequencies. $\Delta W_{S,0}^{(e)}(\omega)$ can then be obtained via the derivative of ΔS with respect to $\omega_{\rm DC}$ [Grenier et al., 2011a; Gabelli and Reulet, 2012]. The obtained values of $\Delta W_{S,0}^{(e)}(\omega)$ are plotted on the upper right panel of fig. 2.25. The three curves show that as the drive frequency increases, the spectral weight is shifted towards higher frequencies.

In the quasi-classical case ($f = 1.75$ GHz), the typical energy at which electrons (respectively holes) are promoted above (respectively below) the Fermi energy is given by the amplitude $eV_S = 28\,\mu$eV of the chemical potential variations. On the contrary, in the quantum regime ($f = 20$ GHz so that $hf > k_B T_{\rm el}$), electron/hole pair creation results from the absorption of photons at energy hf [Tien and Gordon, 1963; Rychkov et al., 2005]. The excess electron distribution function presents square steps of width $hf = 83\,\mu$eV and amplitude $(eV_S/hf)^2/4$, which is the probability to absorb one photon from the drive [Tien and Gordon, 1963]. The experimental results compare very well with photo-assisted noise calculations [Rychkov et al., 2005] (plain lines) without any adjustable parameters, thus confirming the robustness of the measurement of $\Delta W_{S,0}^{(e)}(\omega)$.

As explained in section 1.6, accessing the time dependence of $W^{(e)}$

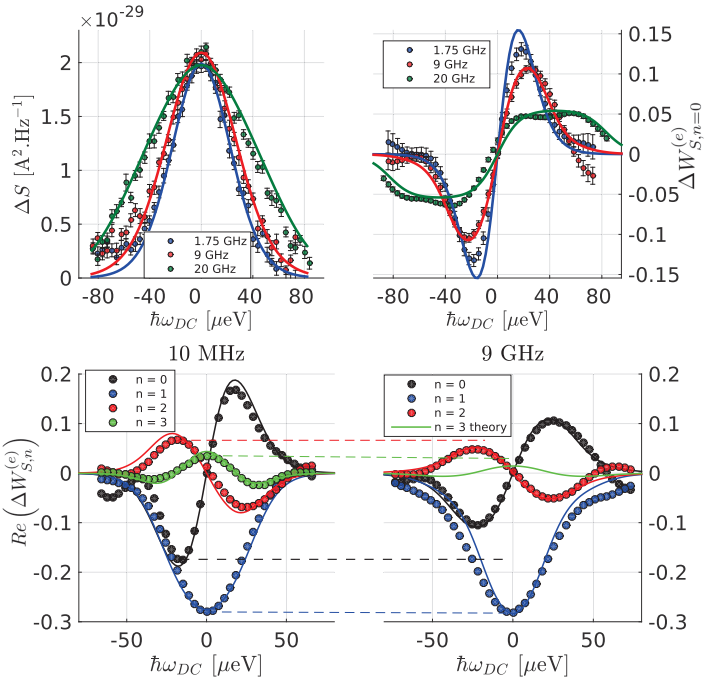

Figure 2.25: Upper left panel: Excess noise ΔS as a function of d.c bias $\omega_{\rm DC}$. The plain lines represent numerical calculations for $V_S = 28\,\mu$V, $f = 1.75\,$GHz, $V_S = 31\,\mu$V, $f = 9\,$GHz, and $V_S = 38\,\mu$V, $f = 20\,$GHz and $T_{\rm el} = 100\,$mK. Upper right panel: electronic distribution function $\Delta W^{(e)}_{S,0}(\omega)$. Plain lines represent numerical calculations (same parameter as the left panel). Lower panel: $\Delta W^{(e)}_{S,n}(\omega)$ for $f = 10\,$MHz (left) and $f = 9\,$GHz (right). The plain lines represent numerical calculations with $T_{\rm el} = 100\,$mK, $V_S = 33\,\mu$V ($f = 10\,$MHz) and $V_S = 31\,\mu$V ($f = 9\,$GHz).

requires measuring non-zero harmonics $\Delta W^{(e)}_{S,n\neq 0}$. Fortunately, due to the smoothing introduced by the non-zero electronic temperature, an accurate reconstruction is usually achieved with $|n| \leq 3$. As explained before, accessing the nth harmonic requires a probe P_n whose Wigner distribution evolves periodically in time at frequency nf and, as explained before, the point is to look at the linear response of the excess current noise to a probe P_n of the form $V_{P_n}(t) = V_{P_n}\cos(2\pi nft + \phi)$. Changing the phase ϕ of the probe allows us to scan the temporal axis, whereas the width of $\Delta W^{(e)}_{P_n}$ along the energy axis is fixed by the width of g_n, given by the maximum of k_BT and nhf. As in the $n = 0$ case, varying a d.c. bias $V_{\rm DC}$ on top of the a.c. probe excitation enables scanning the energy axis. As explained in section 1.6, the real and imaginary parts of $\Delta W^{(e)}_{S,n}$ can be directly related to the variations of ΔS as a function of the phase ϕ and d.c. bias $V_{\rm DC}$ of the probe P_n.

Figure 2.25 presents $\Re(\Delta W^{(e)}_{S,n}(\omega))$ ($\Im(\Delta W^{(e)}_{S,n}(\omega)) = 0$) for $n = 0, 1, 2, 3$ for a quasi-classical drive $f = 10\,\text{MHz}$ (lower left panel), and $n = 0, 1, 2$ ($n = 3$ falls below the experimental resolution) for a quantum drive $f = 9\,\text{GHz}$ (lower right panel). While the $n = 1$ harmonics take very close values as explained by the similar amplitudes of the drives ($V_S = 33\,\mu\text{V}$ for $f = 10\,\text{MHz}$ and $V_S = 31\,\mu\text{V}$ for $f = 9\,\text{GHz}$), the $n = 0$, 2 and 3 harmonics are lower in the high frequency case compared to the low-frequency one. Indeed, these terms are related to multiphoton absorption/emission processes, whose strength increases with the ratio $\alpha = eV_S/hf$. This ratio is very high in the quasi-classical case ($\alpha \approx 800$) and smaller than one in the quantum one ($\alpha \approx 0.8$) thus explaining the smaller amplitude of the harmonics $n \neq 1$. After extracting all relevant $\Delta W^{(e)}_{S,n}(\omega)$, we can combine them to reconstruct the full Wigner distribution:

$$W^{(e)}_S(t,\omega) = f_{\rm eq}(\omega) + \Delta W^{(e)}_{S,0}(\omega) + 2\sum_{n=1}^{N} \Re(\Delta W^{(e)}_{S,n}(\omega))\cos(2\pi nft), \tag{2.87}$$

where the sum extends to $N = 3$ at $f = 10\,\text{MHz}$ and $N = 2$ at $f = 9\,\text{GHz}$ and where $\Im(\Delta W^{(e)}_{S,n}(\omega)) = 0$ has been used. The two reconstructed Wigner distributions are represented on fig. 2.26 (upper panel).

Apart for small discrepancies related to the deconvolution process, the quasi-classical case is very close to the expected equilibrium distribution function with a time varying chemical potential $\mu(t) = -eV_S\cos(2\pi ft)$

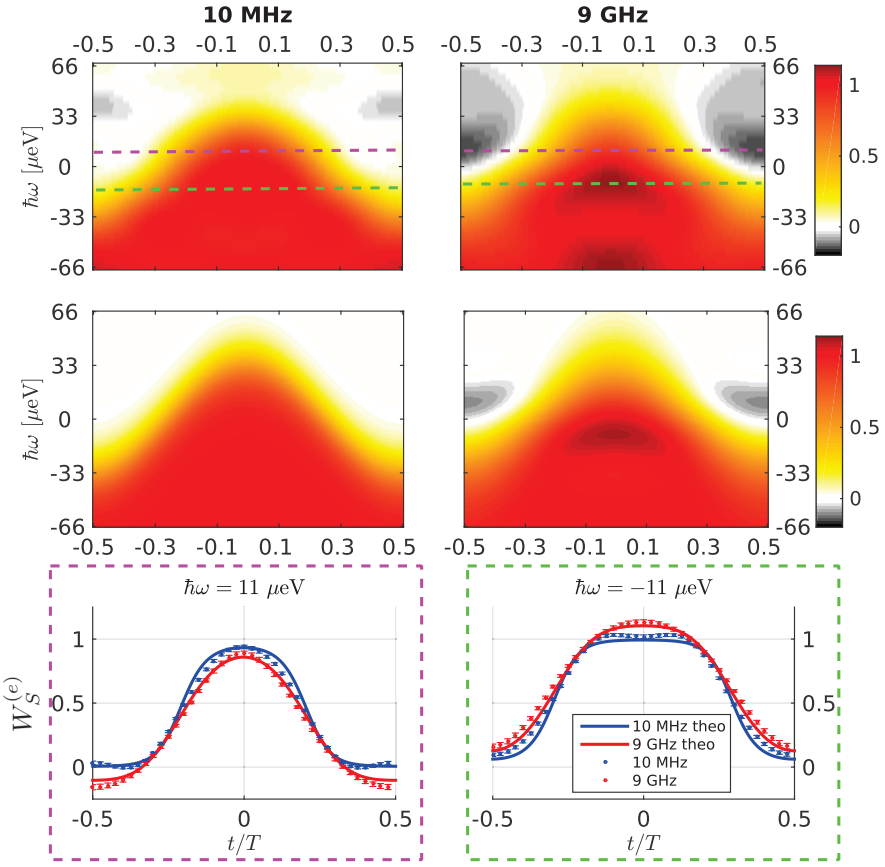

Figure 2.26: Upper panels: experimental data of $W_S^{(e)}(t,\omega)$ in the quasi-classical ($f = 10\,\mathrm{MHz}$, left panel) and quantum ($f = 9\,\mathrm{GHz}$, right panel) cases. Middle panels: theoretical calculations of $W_S^{(e)}(t,\omega)$ in the quasi-classical case $f = 10\,\mathrm{MHz}$ (left panel) and in the quantum case $f = 9\,\mathrm{GHz}$ (right panel). Lower panels: cuts of $W_S^{(e)}(t,\omega)$ at constant energy $\hbar\omega = 11\,\mu\mathrm{V}$ (left panel) and $\hbar\omega = -11\,\mu\mathrm{eV}$ (right panel). Blue points are for $f = 10\,\mathrm{MHz}$, red points for $f = 9\,\mathrm{GHz}$, the plain lines (cyan for $f = 10\,\mathrm{MHz}$, brown for $f = 9\,\mathrm{GHz}$) represent cuts of the Wigner functions calculated numerically (middle panel).

(see middle left panel). In particular, it is basically constrained to values between 0 and 1. In contrast, in the quantum case, the Wigner distribution can take values that are strongly negative or that are well above one. Consequently, single-particle properties are no longer described in terms of a time varying electronic distribution function, in good agreement with theoretical predictions from a Floquet calculation (middle right panel).

The difference between the classical and quantum regimes can be understood by plotting cuts of the Wigner distribution at constant energy $\hbar\omega = \pm 11\,\mu\text{eV}$ (lower panels of fig. 2.26). In the classical case the sizeable values of the high harmonics of the Wigner distribution are necessary to reconstruct an equilibrium Fermi distribution which varies sharply from 0 to 1. On the contrary, high harmonics are suppressed in the quantum case such that $W_S^{(e)}(t,\omega)$ varies in a much smoother way. This explains the overshoots (undershoots) above 1 (below 0) which agree well with theoretical expectations (plain lines).

2.7.2 Signal processing of the experimental $\Delta\mathcal{G}_S^{(e)}$

The second step of quantum current analyzis is the main topic of the present chapter: the extraction of individual electronic wavepackets from the reconstructed Wigner distribution.

In order to capture all excitations present with the quantum electrical current, the first step is to compute the excess Wigner distribution $\Delta_0 W_S^{(e)}(t,\omega) = W^{(e)}(t,\omega) - \mathrm{H}(-\omega)$, defined with respect to the zero temperature Fermi sea described by the electronic distribution function $\mathrm{H}(-\omega)$. As explained before, this reference choice ensures that all excitations, including the thermal ones, are extracted by our algorithm.

Figure 2.27 presents the result of this analysis on the experimental data obtained for the quantum sinusoidal drive at $f = 9\,\text{GHz}$. As expected, the excess coherence is strongly dominated by one electron and one hole wavepacket which, here, we respectively denote by $\varphi^{(e)}$ and $\varphi^{(h)}$. Their Wigner representations are plotted on the upper and middle panels. The hole is shifted by half a period with respect to the electron and its energy dependence is almost the same as that of the electron's at positive energy, as can be seen from their electronic distribution functions $f|\varphi^{(e/h)}(\omega)|^2$. Note that these functions present almost flat plateaus of width hf: deviations from flatness express that atoms of signal at finite temperature are indeed contaminated by thermal excitations compared

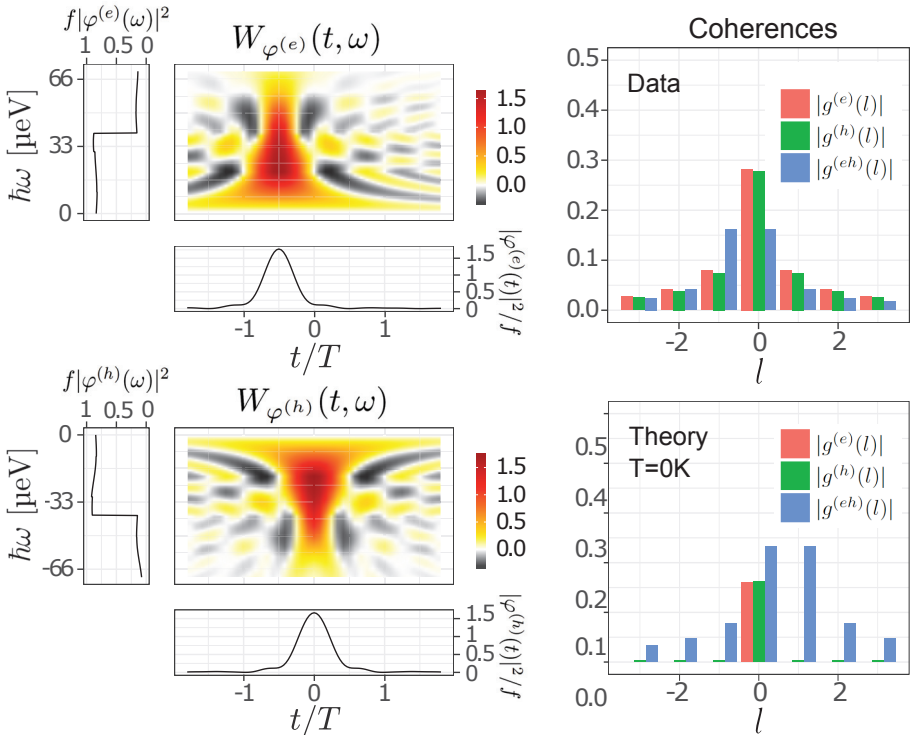

Figure 2.27: Left panel: Wigner distribution functions $W_{\varphi^{(e/h)}}(t,\omega) = \int \varphi^{(e/h)}(t+\frac{\tau}{2})\varphi^{(e/h)*}(t-\frac{\tau}{2})\mathrm{e}^{\mathrm{i}\omega\tau}\,\mathrm{d}\tau$ for the dominant electronic $\varphi^{(e)}$ and hole $\varphi^{(h)}$ atoms of signal in the $f = 9\,\mathrm{GHz}$ case. The panels in the margins of the colour plots represent the time $|\varphi^{(e/h)}(t)|^2/f$ and energy $f|\varphi^{(e/h)}(\omega)|^2$ distributions obtained by integration of $W_{\varphi^{(e/h)}}(t,\omega)$ over ω and t. Right panel: moduli of the inter-period coherence $|g^{(e)}(l)|$ between electronic atoms of signal and $|g^{(h)}(l)|$ for the holes and electron/hole inter-period coherence $|g^{(eh)}(l)|$ (upper right panel: experimental data at $T_{\mathrm{el}} = 100\,\mathrm{mK}$; lower right panel: numerical simulation at $T_{\mathrm{el}} = 0\,\mathrm{mK}$).

to the zero temperature case.

The moduli of the corresponding inter-period coherences are depicted on the right panel: they extend beyond one period as expected since the thermal coherence time of electron $h/k_B T_{\rm el} \simeq 0.5\,{\rm ns}$ is roughly 4 times larger than the period. Since $g^{(eh)}(l-l') \neq 0$ and both $g^{(e)}(0) \simeq g^{(h)}(0) \simeq 0.27 \neq 1$ we are not in the single-electron regime. The specific role of thermal fluctuations is illustrated by comparing the data with the numerical simulation of the inter-period coherences in the zero temperature case (see right column of fig. 2.27). The probabilities $g^{(e)}(0)$ and $g^{(h)}(0)$ that the electronic and hole atoms of signal are populated are increased when the temperature increases going from 0.16 ($T_{\rm el} = 0\,{\rm mK}$) to 0.27 ($T_{\rm el} = 100\,{\rm mK}$), reflecting the contamination by thermal excitations populating $\varphi^{(e/h)}$. Thermal fluctuations also decrease the electron/hole coherence $|g^{(eh)}(0)|$ with respect to electronic $g^{(e)}(0)$ and hole $g^{(h)}(0)$ excitation numbers, showing how the coherent superposition between the equilibrium state and the creation of an electron/hole pair is progressively destroyed by increasing the temperature.

2.8 Summary

To conclude, we have demonstrated a quantum electrical current analyzer which directly extracts the single electron and hole wavefunctions, as well as their emission probabilities and coherence from one emission period to the other. Assuming a minimal knowledge on the state of the electron fluid, it can be used to characterize any quantum electrical current (although sinusoidal drives have been used experimentally for demonstration).

It also explicitly takes into account the role of thermal excitations and their progressive contamination of the electron and hole wavefunctions. Although the chirality imposed by the high magnetic field used here enables the separation between the source and probe ports, the same principle could lead to quantum current analysers for any low-dimensional conductor that can be weakly tunnel-coupled to a probe port for noise measurements [Arakawa et al., 2015]. In this perspective, our analyzer appears as a crucial tool for quantum technologies based on the propagation of time-dependent electrical currents by enabling the control of the quantum state of the elementary excitations transferred across nanoscale conductors. It is the tool of choice for single-electron source characterization or for identifying single-particle wavefunctions

generated in interacting conductors [Marguerite et al., 2016b].

Finally, our quantum analyzer may also offer a way to access to the recently studied electron/hole entanglement [Dasenbrook and Flindt, 2015; Hofer et al., 2016] and, supplemented by other measurements [Thibierge et al., 2016; Thibierge, 2015], to quantify more precisely the importance of interaction-induced quantum correlations. Finally, it can establish a bridge between electron and microwave quantum optics [Grimsmo et al., 2015; Virally et al., 2016], by probing the electronic content of microwave photons injected from a transmission line into a quantum conductor. However, this requires establishing a bridge between the coherence properties of electrons and the coherence of the emitted radiation. Although this is not the main topic of the next chapter, we shall see that for quantum Hall edge channels, bosonization precisely provides an answer to this important question.

Chapter 3

Electrons, plasmons and photons

3.1 Introduction

The present chapter deals with the effects of interactions between the electron fluid and its environment, as well as with the effect of interactions between the electrons themselves (Coulomb interactions).

Two physical questions will be addressed: the first one is to understand the radiation emitted by quantum electrical currents within their electromagnetic environment. In particular, can we relate the coherences properties of the emitted radiations to the electronic coherences that have been discussed in chapter 1?

The second question is to determine the effect of interactions within the quantum Hall edge channel as well as with its environment on the properties of electronic coherence. This is the problem of electronic decoherence which is of crucial importance in condensed matter physics.

As we shall see, bosonization which is exact in chiral 1D channel enables us to discuss both of these problems in a single framework which relies on the use of quantum optics for bosonic modes corresponding to the quantized charge density waves propagating along the edge channel. Assuming that the environment of the edge channel is in a linear response regime with respect to the charge density modulation of the edge enables us to develop an approach in which interactions are described in terms of elastic scattering of bosonic modes.

3.2 Electrons and plasmons

We will now discuss how one can describe the state of the electronic fluid in terms of bosonic modes, called plasmons. For the sake of pedagogy, I will focus on the physical intuition rather than on a rigorous mathematical derivation. A reader interested by a more rigorous proof can read [Gogolin et al., 1998; Giamarchi, 2004; von Delft and Schoeller, 1998; Stone, 1994].

3.2.1 From electrons to plasmons

The bosonization formalism connects the electronic degrees of freedom to bosonic degrees of freedom representing charge density wave within the system. We will then first consider those charge density waves, also known as edge magnetoplasmons or plasmons, in terms of electrons. Then we will go the other way around and show how we can describe a single electron on top of the Fermi sea in terms of plasmonic degrees of freedom.

Let us consider the electronic particle current operator. Because of the linear dispersion relation of electrons, its finite-frequency components can be written as

$$i_e(\omega > 0) = \int c^\dagger(\omega' - \omega)c(\omega')\,\mathrm{d}\omega', \tag{3.1a}$$

$$i_e^\dagger(\omega > 0) = \int c^\dagger(\omega' + \omega)c(\omega')\,\mathrm{d}\omega'. \tag{3.1b}$$

Let us now focus on the non trivial commutator of the operators $i_e(\omega > 0)$ and $i_e^\dagger(\omega' > 0)$:

$$\left[i_e(\omega_1), i_e^\dagger(\omega_2)\right] = \int \Big(\delta(\omega_2 + \omega_2' - \omega_1')c^\dagger(\omega_1' - \omega_1)c(\omega_2') \tag{3.2a}$$

$$- \delta(\omega_1' - \omega_1 - \omega_2')c^\dagger(\omega_2 + \omega_2')c(\omega_1') \Big)\,\mathrm{d}\omega_1'\mathrm{d}\omega_2'. \tag{3.2b}$$

At this stage, one must be really cautious about how to treat this difference of infinite sums of operators. If we split the difference and integrate each term independently, we can end up with a trivial commutation relation, because it corresponds to a difference of two infinite quantities. The proper way to regularize this expression is to keep both terms together under the integral until we make the divergence explicit using normal

ordering:

$$\Big[i_e(\omega_1), i_e^\dagger(\omega_2)\Big] = \int \Big(:c^\dagger(\omega_2-\omega_1+\omega')c(\omega'): - :c^\dagger(\omega_2+\omega')c(\omega_1+\omega'): \Big)\,\mathrm{d}\omega' \tag{3.3a}$$

$$+ \int \Big(\Big\langle c^\dagger(\omega_2-\omega_1+\omega')c(\omega')\Big\rangle_F - \Big\langle c^\dagger(\omega_2+\omega')c(\omega_1+\omega')\Big\rangle_F \Big)\,\mathrm{d}\omega'. \tag{3.3b}$$

Each term of the difference (3.3a) being normal ordered possesses a finite integral, and thus the difference is zero. Only difference (3.3b) remains. We can replace correlator with its value and we obtain an integrand that is $\delta(\omega_2-\omega_1)g(\omega')$ where $g(\omega')$ is zero everywhere except in $[-\omega_1, 0]$, where it is one. Finally, we obtain

$$\Big[i_e(\omega_1), i_e^\dagger(\omega_2)\Big] = \delta(\omega_2-\omega_1)\omega_1. \tag{3.4}$$

Introducing the bosonic modes

$$b(\omega>0) = \frac{1}{\sqrt{\omega}} i_e(\omega) = \frac{1}{\sqrt{\omega}} \int c^\dagger(\omega'-\omega)c(\omega')\,\mathrm{d}\omega' \tag{3.5a}$$

$$b^\dagger(\omega>0) = \frac{1}{\sqrt{\omega}} i_e^\dagger(\omega) = \frac{1}{\sqrt{\omega}} \int c^\dagger(\omega'+\omega)c(\omega')\,\mathrm{d}\omega' \tag{3.5b}$$

it is trivial to show that they satisfy the canonical commutation relations:

$$\Big[b(\omega), b(\omega')^\dagger\Big] = \delta(\omega-\omega')\mathbf{1}. \tag{3.6}$$

3.2.2 From plasmons to electrons

Let us now express the fermionic operators in terms of the bosonic ones. But before doing this, we will focus on a particular class of bosonic states, the coherent plasmonic states which are defined as in optics, as eigenstates of the annihilation operators $b(\omega>0)$. Note that they are multimode coherent states and thus are parametrized by a function $\omega \mapsto \Lambda(\omega)$, where $\Lambda(\omega) = i_e(\omega)/\sqrt{\omega}$. These states are very important since they are generated by a classical driving.

Actually the idea behind the bosonized expression of a fermion is simple: if we inject a time-resolved electron at time t_0 on top of the Fermi sea, its average electrical current is a percussional pulse emitted

at time t_0. If we assume that it is a quasi-classical plasmon states, its creation should correspond to the action of a displacement operator for the bosonic modes. A first guess would be

$$\psi(t) \propto \mathcal{D}[\Lambda_t], \tag{3.7}$$

where $\Lambda_t(\omega) = \mathrm{e}^{\mathrm{i}\omega t}/\sqrt{\omega}$ to ensure that the average current is percussional. However, this expression has two flaws.

First, bosonic operators do not change the charge. In other words, the right-hand side of eq. (3.7) do not capture the d.c. part of the current. To cure this pathology, we introduce Klein operator U, whose effect is to remove one electron by shifting the chemical potential of the fluid, allowing to visit different charge sectors. This operator is unitary and the operator $U^\dagger$ raises the number of fermions by one. If there are several flavors of chiral fermions, as in presence of several edge channels, each flavor has its own Klein operator U_i. Two operators associated with different species must anticommute so that fermionic operators of different flavors also do. This cures the first pathology we have mentioned and also provides the fermionic operators with the proper anticommutation relations in case of several flavors[1].

The second flaw is that the right-hand side of eq. (3.7) is dimensionless whereas 1D chiral fermions have dimension $[\mathrm{L}]^{-1/2}$. To fix this, we introduce a length a, which as we will see will play the role of a UV cutoff, so that:

$$\psi^\dagger(t) = \frac{U^\dagger}{\sqrt{2\pi a}}\mathcal{D}[\Lambda_t] \qquad \Lambda_t(\omega) = \mathrm{e}^{\mathrm{i}\omega t}/\sqrt{\omega}. \tag{3.8}$$

To clarify the physical meaning of this length a, let us compute first-order coherence of the Fermi sea at zero temperature in the bosonization formalism

$$\left\langle \psi^\dagger(t')\psi(t) \right\rangle_F = \frac{1}{2\pi a} \left\langle -\Lambda_{t'} \,|\, -\Lambda_t \right\rangle. \tag{3.9}$$

The scalar product is a trivial generalization of the single-mode scalar product:

$$\left\langle -\Lambda_{t'} \,|\, -\Lambda_t \right\rangle = \exp\left(\int_0^\infty \left(\mathrm{e}^{\mathrm{i}\omega(t-t')} - 1 \right) \mathrm{d}\omega \right). \tag{3.10}$$

1. Since Klein operators are unitary, they do not enforce anticommutation relations for a given fermionic flavor. Actually, these relations come from the displacement operators themselves. We won't demonstrate this result, but the method for this should be clear from what follows.

Many of regularization problems in bosonization can be summarized by the previous equation. The integral has UV and IR divergences which we regularize using the fact that, for $\Re(\tau_1) > 0$ and $\Re(\tau_2) > 0$:

$$\exp\left(\int_0^\infty (\mathrm{e}^{-\omega\tau_1} - \mathrm{e}^{-\omega\tau_2})\,\frac{\mathrm{d}\omega}{\omega}\right) = \frac{\tau_2}{\tau_1}. \tag{3.11}$$

We can thus add a small real part $\tau = 0^+$ to eq. (3.10), which will play the role of a UV cutoff. Using $\tau_1 = \mathrm{i}(t - t') + \tau$ and $\tau_2 = \tau$, we obtain:

$$\frac{1}{2\pi a}\,\langle -\Lambda_{t'} \,|\, -\Lambda_t\rangle = \frac{\mathrm{i}}{2\pi a}\,\frac{\tau}{t - t' + \mathrm{i}\tau}, \tag{3.12}$$

which coincides with the expression of $\mathcal{G}_F^{(e)}(t, t')$ obtained chapter 1 if we identify $a = v_F\tau$, thus confirming its interpretation as a UV cutoff.

In bosonization, our basic block will thus be single-electron state $\psi^\dagger(0)\,|F\rangle$. Its Wigner function is depicted on the right part of fig. 3.1. Any single-electron excitation on top of the Fermi sea is obtained as a superposition of such states, injected at different times. The first iteration of this process is shown on the left part of fig. 3.1.

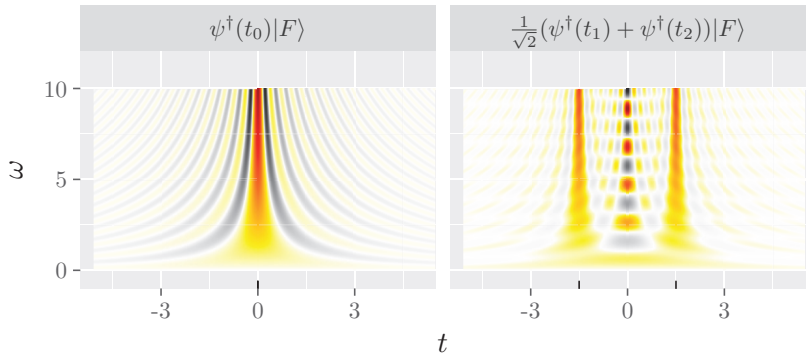

Figure 3.1: Wigner functions of simple bosonic states. On the left, we have the Wigner function of a time-localized single-electron state. Since there is no particular timescale here, the units are arbitrary (the only constraint is that ω must be consistent with t). This state is also a coherent plasmonic state. On the right, we have the Wigner function of an electron delocalized at t_1 and t_2. This is a simple superposition of plasmonic coherent states.

3.2.3 Single-electron states as Schrödinger cats

The general expression for the state involving an arbitrary single-electron excitation on top of the Fermi sea is

$$\psi[\varphi_e]\,|F\rangle = \int \varphi_e(t)\psi^\dagger(t)\,\mathrm{d}t\,|F\rangle = U^\dagger \int \varphi_e(t)\,|\Lambda_t\rangle\,\mathrm{d}t, \tag{3.13}$$

where each $|\Lambda_t\rangle$ describes a percussional current at time t. From the bosonization perspective, an electron emitted on top of the Fermi sea is just a continuous quantum superposition of elementary, single-electron, classical currents on top of $|F\rangle$. In the rest of this chapter, we will consider only zero-temperature equilibrium states. The bosonization description will act on different vacua depending on the channel we consider. For the channel in which the electron is injected, the vacuum will correspond to the superselection sector with one electron added on top of $|F\rangle$, namely $U^\dagger\,|F\rangle$. For the other channels, it will be the standard Fermi sea. We can do this distinction because of the absence of tunnel effect. Furthermore, in the quantities we will look at throughout this chapter, the Klein factors always come by self-cancelling pairs.

We might ask about the transcription of thermally excited Fermi sea in terms of bosonic states. This will notably be necessary in section 4.4. A major difficulty is that at non-zero temperature, fermionic state mixes several charge sectors, and cannot be described purely in terms of electron/hole pairs. However, in the thermodynamics limit, the chemical potential is not shifted by the addition of a single electron and this is why we can forget about Klein factors when describing thermally excited states, since in the quantities we will look at, the contribution arising from the mixing of different charge sectors will vanish. In finite-size systems, this abuse will have dramatic consequences since even adding a single electron changes the chemical potential.

An example of such a reconstruction in terms of elementary currents can be seen of fig. 3.2: it is the Landau quasi-particle introduced in section 1.4.4, page 55. The convergence towards this target state is clear, though not very quick, as we add up more and more contributions to the quantum superposition. A very interesting feature of this reconstruction process is that the Wigner function of each member of the quantum superposition has contributions close to the Fermi sea. However, the final result is localised around the Landau quasi particle's energy. This clearly shows how localization in energy space comes from destructive interferences between each contribution $\psi^\dagger(t)\,|F\rangle$ which, on the contrary,

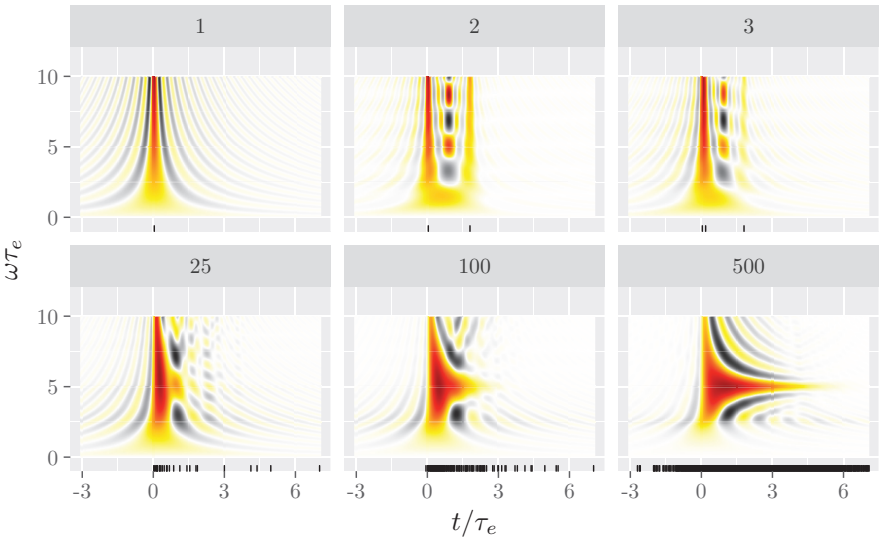

Figure 3.2: Reconstruction of the Landau quasi-particle. Each Wigner function shows a superposition with a finite number of terms (indicated on top of the graph). The time of each term is shown by a tick on the t-axis. As we increase the number of terms, we converge to the target state.

are delocalized in energy.

This picture of an electron as a Schrödinger cat of classical current a.c. pulses on top of $U^\dagger |F\rangle$ will be essential in our analysis of electronic decoherence.

3.3 Quantum optics of current noise

A complementary view on bosonization can be obtained by considering the radiation emitted by a quantum electrical current propagating along a quantum Hall edge channel. As is well known to experimentalists, the edge channels electronic or plasmonic modes are not directly accessed in experiments. The edge channel is coupled to a transmission line or coaxial cable in which an electrical signal propagates up to amplifiers and then, in the end, to the acquisition system. Within a coaxial cable, the electrical signal is propagated through hybrid light matter modes that are called "photon" since they usually correspond to the electromagnetic modes propagating along the coaxial cable seen as a waveguide.

In this section, we explore the properties of the emitted radiation by developing a quantum optics of current noise in quantum Hall edge channels that is the counterpart for quantum Hall edge channels of the recent work by Grimsmo et al. [2015]. As will be explained, the simplicity of quantum Hall edge channel enables us to directly understand the relation between the quantum optical properties of the emitted radiation and electron quantum optic coherence properties of the electrical current.

3.3.1 Plasmons and photons

We start by describing a simple model of antenna to collect the emitted radiation. We will discuss its coherence properties, showing that, under reasonable circumstances, probing the radiation is equivalent to probing the edge-magnetoplasmon modes that propagate along the chiral edge channel.

Plasmon-to-photon conversion

In chapter 1, we have introduced two devices through which this radiation can be collected: the first one is a top gate capacitively coupled to the edge channel and the second one is the Ohmic contact. Since we want to conserve quantum coherence of plasmonic excitations, we want to avoid dissipation and therefore, we shall focus on the direct capacitive coupling to the transmission line instead of the Ohmic contact.

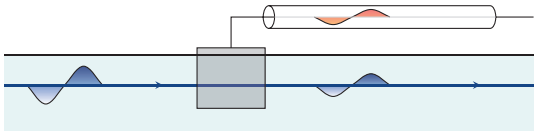

Figure 3.3: Plasmon-to-photon conversion. We can convert an incoming plasmonic state (white-blue ripple, on the left) into a photonic state (orange-red ripple on the right), by using a top gate that will act as a capacitive antenna which is connected to a transmission line. The efficiency of such a conversion is not one, so we expect that there are remaining outgoing plasmonic excitations (white-blue ripple on the right).

The capacitive coupling between an edge channel and a transmission line is depicted on fig. 3.3. Using an input/output formalism for describing the transmission line [Yurke, 1984] and the edge channel, it can be shown that the capacitive coupling region acts as an elastic scatterer of

plasmonic and photonic modes into outgoing plasmonic and photonic modes [Degiovanni et al., 2009]. Therefore, the end result is a linear relation between the incoming modes for plasmons $b_{\mathrm{pl}}^{\mathrm{in}}(\omega)$ and for photons $b_{\mathrm{ph}}^{\mathrm{in}}(\omega)$ and their outgoing counterparts:

$$\begin{pmatrix} b_{\mathrm{pl}}^{(\mathrm{out})}(\omega) \\ b_{\mathrm{ph}}^{(\mathrm{out})}(\omega) \end{pmatrix} = \begin{pmatrix} t(\omega) & r(\omega) \\ -r^*(\omega) & t(\omega) \end{pmatrix} \begin{pmatrix} b_{\mathrm{pl}}^{(\mathrm{in})}(\omega) \\ b_{\mathrm{ph}}^{(\mathrm{in})}(\omega) \end{pmatrix}, \tag{3.14}$$

where $t(\omega)$ and $r(\omega)$ are frequency-dependent transmission and reflexion amplitudes that depend on the details of the geometry of the capacitor [Grenier, 2011]. The converter described here is thus nothing more than a capacitive antenna. Of course, if one wants to convert bosonic excitations efficiently, a suitable sample design is required for ensuring the desired properties in the experimentally relevant bandwidth. When there is no leak towards others degrees of freedom, energy conservation implies that $|t(\omega)|^2 + |r(\omega)|^2 = 1$.

It is interesting to compare the present discussion to the one of Grimsmo et al. [2015]. In this paper, the authors consider the case of a two-port quantum conductor such as a tunnel junction connected to transmission lines. In order to study the properties of the radiation emitted by the conductor, they derive an input/output relation connecting the outgoing electromagnetic modes to the electrical current operator flowing through the conductor. The philosophy is extremely similar to the one developed here except that coupling is different: in the quantum Hall situation discussed in this thesis, the electronic degrees of freedom are capacitively coupled to the photonic ones whereas, in their case eq. (2) of their work expresses continuity of the electrical current when one goes from the conductor to the transmission lines. But in their case, because the quantum conductor is not chiral contrary to quantum Hall edge channel case, the current operator within the quantum conductor which appears as a source for the radiation in eq. (2), also depends on the incoming electromagnetic radiation. There are two ways to deal with this backaction effect: first, when there is a strong impedance mismatch between the conductor's impedance at the frequencies under consideration, the incoming vacuum fluctuations of the supposed not too-exotic drive cannot influcence the conductor. This is the case considered in [Beenakker and Schomerus, 2001] and we think that this approximation is also valid when considering the current captured by an Ohmic contact maintained at zero potential (but since it would require a better understanding of dissipative effects within an Ohmic contact, we do not

explore this more). In the case where the impedance mismatch is not as strong, which is the case in some experiments, one has to consider a regime in which the backaction is weak. This is the situation considered by Grimsmo et al. [2015]. We shall not further comment on this but the case considered here is, in some sense much simpler.

Photonic degrees of coherence

The simple linear relation 3.14 between the outgoing photonic modes and the incoming photonic and plasmonic ones enables us to relate outgoing photonic correlators to the edge-magnetoplasmonic ones. Assuming the incoming photonic modes are populated with the vacuum, the outgoing average electromagnetic amplitude is directly connected to the average edge-magnetoplasmon amplitude: $\langle b_{\mathrm{ph}}^{(\mathrm{out})}(\omega)\rangle = t(\omega)\langle b_{\mathrm{pl}}^{(\mathrm{in})}(\omega)\rangle$. If we now consider the coherences of the outgoing photonic modes (for simplicity, we will denote the incoming plasmonic ladder operators $b(\omega)$ and $b^\dagger(\omega)$), we see that

$$G^{(1)}_{\mathrm{ph,out}}(\omega,\omega') = t(\omega)t(\omega')^*\ \mathrm{tr}(b(\omega)\rho\, b^\dagger(\omega')) \tag{3.15}$$

because all photonic coherences of the vacuum are vanishing. This relation as well as the analogous ones for higher order photonic coherences imply that the photonic degrees of coherences defined by Mandel [Fox, 2006] are directly equal to the same quantity for the plasmonic modes:

$$g^{(n)}(\omega|\omega') = \frac{G^{(n)}_{\mathrm{ph,out}}(\boldsymbol{\omega},\boldsymbol{\omega'})}{\prod_{k=1}^n G^{(1)}(\omega_k,\omega_k)G^{(1)}(\omega'_k,\omega'_k)} \tag{3.16a}$$

$$= \frac{\mathrm{tr}\left(\prod_{k=1}^n b(\omega_k)\,\rho\,\prod_{k=1}^n b^\dagger(\omega'_k)\right)}{\prod_{k=1}^n \langle b^\dagger(\omega_k)b(\omega_k)\rangle_\rho \langle b^\dagger(\omega'_k)b(\omega'_k)\rangle_\rho}, \tag{3.16b}$$

thus showing that the coherence properties of the emitted radiation exactly reflect the ones of edge-magnetoplasmon modes. In the same way, the correlation functions that encode the anisotropy of the edge-magnetoplasmon modes are exactly the same as the ones encoding the outgoing mode fluctuations. In particular, an outgoing radiation mode of given frequency is squeezed if and only if the corresponding edge-magnetoplasmon mode is.

This shows that the non classical properties of the outgoing radiation such as squeezing or sub-Poissonian statistics reflect the non classical properties of the edge-magnetoplasmon modes. This explains why, in the remaining of the discussion, we shall focus on the properties of the edge-magnetoplasmon modes.

3.3.2 Plasmon fluctuations from current noise

The current correlation $S_i(t,t') = \langle i(t')i(t)\rangle_c$ represents the quantum fluctuations of the edge channel quantum electrical current operator $i(t) = -ev_F :(\psi^\dagger\psi)(t):$ where the fermionic normal ordering is defined with respect to a reference chemical potential $\mu_F = 0$. In the stationary case, $S_i(t,t')$ only depends on $\tau = t-t'$ but not on $\bar{t} = (t+t')/2$ whereas, in full generality, it depends on both times. The time-dependent power spectrum of this current is defined by eq. (1.91) which we recall here for clarity:

$$W_i(\bar{t},\omega) = \int_{-\infty}^{+\infty} S_i\left(\bar{t}+\frac{\tau}{2},\bar{t}-\frac{\tau}{2}\right) \mathrm{e}^{\mathrm{i}\omega\tau}\,\mathrm{d}\tau. \tag{3.17}$$

It gives the full power spectrum by averaging over $\bar{t}$. With our convention, the positive-frequency part contains the emission part of the spectrum which reflects the ability of the electronic fluid to absorb energy at frequency $\omega/2\pi$ whereas the negative-frequency part contains the absorption spectrum.

The frequency representation of the current noise is defined by

$$\tilde{S}_i(\omega,\Omega) = \int_{\mathbb{R}^2} \mathrm{e}^{\mathrm{i}(\omega\tau+\Omega\bar{t})} S_i\left(\bar{t}+\frac{\tau}{2},\bar{t}-\frac{\tau}{2}\right) \mathrm{d}t\,\mathrm{d}t', \tag{3.18}$$

which is the Fourier transform with respect to $\bar{t}$ of $W_i(\bar{t},\omega)$. The diagonal ($\Omega = 0$) contains the time-averaged power spectrum whereas the off-diagonal ($\Omega \neq 0$) part contains all the information on the non-stationarity properties of the current noise. Let us now discuss how $\tilde{S}_i(\omega,\Omega)$ relates to the fluctuations of the edge-magnetoplasmon operators. This follows from the relation $i(\omega>0) = -e\sqrt{\omega}\,b(\omega)$ expressing the current operator in term of edge-magnetoplasmon modes.

For $\omega < -|\Omega|/2$ (absorption quadrant), we have:

$$\tilde{S}_i\,(\omega,\Omega) = e^2\sqrt{\omega^2-\frac{\Omega^2}{4}}\,\langle b\,(\omega+\Omega/2)\;b^\dagger\,(\omega-\Omega/2)\rangle_{c,\rho}, \tag{3.19}$$

where $\langle AB\rangle_c = \langle AB\rangle - \langle A\rangle\langle B\rangle$ denotes the connected correlation function. For $\omega > |\Omega|/2$ (emission quadrant), we have:

$$\tilde{S}_i\,(\omega,\Omega) = e^2\sqrt{\omega^2-\frac{\Omega^2}{4}}\,\langle b^\dagger\,(-\omega+\Omega/2)\;b\,(-\omega-\Omega/2)\rangle_{c,\rho}, \tag{3.20}$$

which for $\omega > 0$ and $\Omega = 0$ gives the average number of quanta in the edge-magnetoplasmon mode at frequency $\omega/2\pi$. In particular, the energy

stored within $\mathrm{d}\omega$ around ω, $\mathrm{d}\mathcal{E}(\omega) = \hbar\omega\langle b^\dagger(\omega)\, b(\omega)\rangle\, \mathrm{d}\omega$, is given by:

$$\mathrm{d}\mathcal{E}(\omega) = \frac{h}{e^2}\left(|\langle i(\omega)\rangle|^2 + \tilde{S}_i(\omega, \Omega = 0)\right)\frac{\mathrm{d}\omega}{2\pi}. \tag{3.21}$$

This expression only involves the power spectrum of the noise as well as the finite-frequency average current. Remarkably, in many physically relevant situations, the power spectrum of the current noise is related to the finite-frequency admittance that governs the average current response to an external voltage drive. These relations are called fluctuation/dissipation relations. Their most general form has been obtained by Safi and Joyez [2011]. In particular, eq. (13) in Safi and Joyez [2011] relates the current correlators in the frequency domain to finite-frequency response functions in a general way.

One can go one step further by using a perturbative approach to describe the conductor. Here, the coupling constant in which the perturbative expansion is done describes how far we are from a situation in which we know the system is at equilibrium. When the corresponding fluctuation/dissipation relations are valid we can infer from a perturbative computation of the average current the finite-frequency properties of the current noise. In [Roussel et al., 2016], we have clarified the validity conditions of this approach in the case of a d.c.-biased quantum conductor such as a tunnel junction or a short conductor. Even in the presence of interactions or coupling to an external environment, the key requirement is the validity of the pertubative expansion. These theorems are expected to break down whenever non-equilibrum electronic transport through the conductor gives rise to fluctuations that are drastically different from equilibrium ones. An example being the tunnel junction coupled to its electromagnetic environment in the so-called good conductor regime when the temperature is small ($k_B T_{\mathrm{el}}$ being smaller than the intrinsic energy scale associated with the junction). In this case, low-frequency modes are no longer described by the UV fixed points and current fluctuations are not anymore given by these fluctuation/dissipation theorems. Last year, a violation of the FDR has been observed in a strongly-biased tunnel junction when probing the current noise at high frequencies in a regime where dynamical Coulomb blockade could be neglected [Février and Gabelli, 2017]. This violation came from the dependence of the transmission amplitude on the frequency and on the applied voltage. It is still unclear to us if this can be viewed as coming from a mechanism analogous to the one we have described, that is anomalous fluctuations of the phase.

Going back to the current noise, let's consider the off-diagonal quadrant of the (ω, Ω) plane defined by $\omega^2 < \Omega^2/4$. Then, for $\Omega > 2|\omega|$, we have:

$$\tilde{S}_i(\omega, \Omega) = e^2 \sqrt{\frac{\Omega^2}{4} - \omega^2}\, \langle b(\Omega/2 - \omega)\, b(\Omega/2 + \omega) \rangle_c. \tag{3.22}$$

Equations (3.21) and (3.22) show that the fluctuations properties of the edge-magnetoplasmon mode operator at frequency $f = \omega/2\pi$ are contained within the time-averaged noise power spectrum $S_i(2\pi f, \Omega = 0)$ and the off-diagonal part $S_i(\omega = 0, \Omega = 4\pi f)$. Note that being able to explore the whole dependence of $\tilde{S}_i(\omega, \Omega)$ would give access to all the intermode correlations characterizing the edge-magnetoplasmon fluctuations.

3.3.3 Accessing $W_{\Delta S_i}$ through homodyne measurements

In section 1.3.1, we discussed the fluctuations of the quantum electromagnetic field, introducing the notion of squeezing for a single mode. Since the edge-magnetoplasmon modes are also harmonic modes, the same notion can also be considered for these modes. Because, as explained just above, the edge-magnetoplasmon fluctuations are directly connected to electrical current fluctuations in the edge channel, it is important to look for practical criterion of squeezing expressed in terms of current noise correlator.

Accessing the time-dependent properties of current fluctuations requires homodyning the current at the desired frequency. Let us then consider the homodyned current at frequency f and phase φ defined by

$$i_{f,\varphi}(t) = \cos(2\pi f t + \varphi)\, i(t). \tag{3.23}$$

The auto-correlation of this homodyned current is then defined as

$$S^{(i)}_{f,\varphi}(t, t') = \langle i_{f,\varphi}(t')\, i_{f,\varphi}(t) \rangle - \langle i_{f,\varphi}(t') \rangle \langle i_{f,\varphi}(t) \rangle. \tag{3.24}$$

Its power spectrum at zero frequency is then related to the Wigner–Ville transform of the current correlation by:

$$S^{(\mathrm{exp})}_{f,\varphi} = \frac{1}{4} \left(\overline{W_i(t, 2\pi f) + W_i(t, -2\pi f)}^{t} \right) \tag{3.25a}$$

$$+ \frac{1}{2} \overline{\cos(4\pi f t + 2\varphi) W_i(t, 0)}^{t}. \tag{3.25b}$$

Subtracting the vacuum contribution gives the excess noise $\Delta S^{(\mathrm{exp})}_{f,\varphi}$:

$$\Delta S^{(\mathrm{exp})}_{f,\varphi} = \frac{1}{2}\left(\overline{\Delta W_i(t,2\pi f)}^{t} + \overline{\cos(4\pi f t + 2\varphi)\Delta W_i(t,0)}^{t}\right). \tag{3.26}$$

where we have used that the excess finite-frequency noise is an even function of ω in the present case [Safi and Joyez, 2011]. The squeezing criterion for the edge-magnetoplasmon mode at $\omega = 2\pi f$ is that for some φ, fluctuations are below the vacuum fluctuations which can be expressed as:

$$\Delta S^{(\mathrm{exp})}_{f,\varphi} < 0. \tag{3.27}$$

Note that for a T-periodic source, the time-dependent spectrum $W_i(t,\omega)$ is also T-periodic and can therefore be expanded as a Fourier series in time:

$$\Delta W_i(t,\omega) = \sum_{n\in\mathbb{Z}} \Delta W_i^{(n)}(\omega)\, \mathrm{e}^{-2\pi \mathrm{i} n f_d t}, \tag{3.28}$$

where $f_d = 1/T$ denotes the driving frequency. In order to have a non-zero anisotropic contribution, we must consider $f = n\, f_d/2$ ($n \in \mathbb{N}^*$) and the squeezing criterion becomes

$$\left|\Delta W_i^{(n)}(0)\right| > \Delta S_i(\pi n f_d). \tag{3.29}$$

The anisotropy defined by fig. 1.5 for the plasmon mode at $\omega = \pi n f$ is then obtained as

$$\chi = \frac{\left|W_{S_i}^{(n)}(\omega=0)\right|}{\left[\frac{e^2\omega}{4\pi} + W_{S_i}^{(0)}(-\omega)\right]_{\omega=\pi n f}}. \tag{3.30}$$

A numerical study During my PhD, I co-supervised the L3 internship of E. Chanrion who then precisely studied the full time-dependent current noise generated by the single-electron source of the LPA in all possible regimes. Using the Floquet code that evalues the excess single-electron coherence, he then computed the various quantities that are relevant for understanding the current noise emitted by the source: the Wigner–Ville transform of the excess current noise, the squeezing indicator (3.26) and the edge-magnetoplasmon mode anisotropy.

Figure 3.4 presents the results of these computations for a source driven by a square voltage drive of amplitude $\Delta/2$ and frequency $hf/\Delta = 0.01$, truncated at three harmonics and at temperature $k_B T_{\mathrm{el}} = 0.02$. By

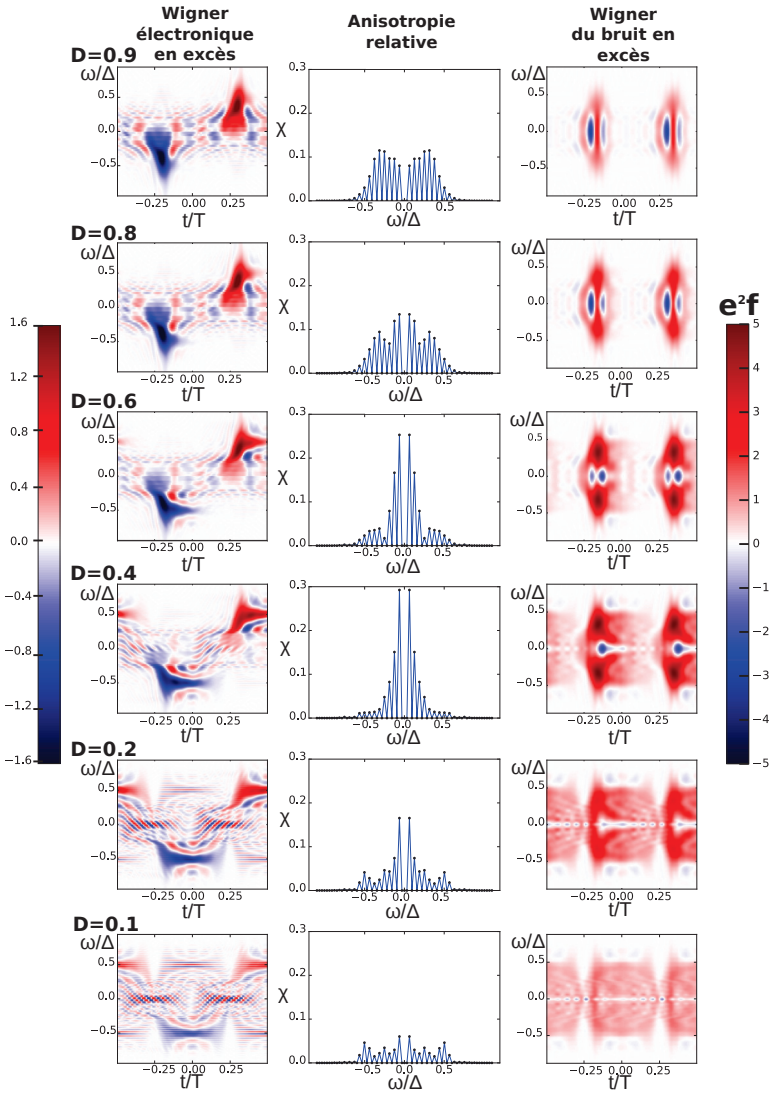

Figure 3.4: Study of the current noise for the LPA source driven by a square voltage drive truncated at three harmonics at frequency $hf/\delta = 0.01$, amplitude $\Delta/2$ and temperature $k_B T_{\rm el}/\Delta = 0.02$. Left column: excess electronic Wigner function. Middle column: noise anisotropy for $\omega = n\pi f$. Right column: Wigner–Ville transform of the excess current noise $W_{\Delta S_i}(t,\omega)$ in function of t/T and ω/Δ, scale in units of $e^2 f$. On this graph, D is varied from $D = 0.1$ (almost closed dot) to $D = 0.9$ (almost fully open dot).

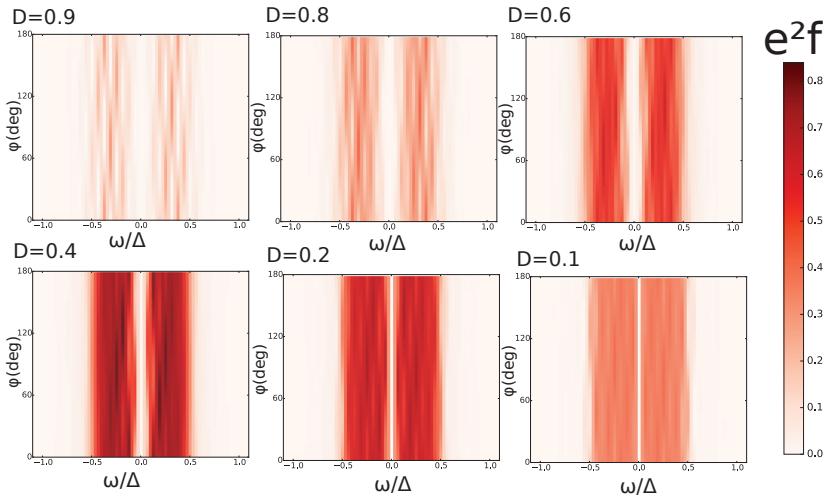

Figure 3.5: Density plots for $\Delta S^{(\mathrm{exp})}_{f,\varphi}$ as functions of φ and ω/Δ for the LPA sources with the same parameters as in fig. 3.4.

varying the dot transmission D, we span the various regimes of the LPA source as shown by the excess electronic Wigner distribution depicted in the left column.

The time-dependent power spectrum of the excess noise is shown on the right panel. It exhibits the expected features known from previous works [Parmentier et al., 2012]: at large D, the noise is mainly emitted close to the Fermi surface and vanishes in the limit $D \to 1$ since we recover a coherent edge-magnetoplasmon state. Around the optimal single-electron source operating point, we recover the familiar shape with noise emission up to slightly above $\Delta/2$ corresponding to the maximum energy carried by the emitted electron with a dip at low frequency whose width corresponds to γ_e (it decreases when D goes down). The noise power also goes down since the dot being more and more closed, less and less current is emitted. As expected, the time-dependent spectrum shows that burst of noise power are emitted synchronously with the emitted electronic and hole excitations. The relative anisotropy is depicted in the middle column. We see that it is maximal at the optimal operating point of the source. The maximum anisotropy is of the order of 30 %. In this case, as a function of φ, the excess noise varies from 0.5 to 0.8 in units of $e^2 f$ which is well above the noise measurement sensitivity available in the laboratory for the typical sources already studied.

However, as shown on fig. 3.5, $\Delta S^{(\mathrm{exp})}_{f,\varphi} \geq 0$ for all φ and all allowed frequencies. Thus, no squeezing can be observed within the current emitted by the LPA source.

Current noise and electronic coherences in the HBT geometry

In order to clarify further the relation between photonic (or equivalently plasmonic) coherences and electronic coherences, let us consider an Hanbury Brown–Twiss interferometer in which excitations emitted by a source (S) are sent onto an ideal electronic beam splitter. In this case, the time-dependent spectrum for the excess outgoing current noise in channel 1out is given by the Fourier transform of the current correlations obtained in [Grenier et al., 2011a]:

$$\begin{aligned}\Delta W^{(\mathrm{on/off})}_{i_{1\mathrm{out}}}(t,\omega) &= T^2\,\Delta W_{i_S}(t,\omega) \\ &\quad + e^2RT\int_{\mathbb{R}} g(\omega,\omega')\,\Delta W^{(e)}_S(t,\omega)\,\mathrm{d}\omega' \end{aligned} \tag{3.31a}$$

$$g(\omega,\omega') = 1 - f_\mu(\omega'+\omega) - f_\mu(\omega'-\omega), \tag{3.31b}$$

where f_μ denotes the electronic distribution function of the channel 2in (here $\mu = 0$). The first term comes from the current noise transmitted across the QPC wheras the second one arises from two-particle interferences between the excitations generated by the source and the particles present in the Fermi sea injected in the other incoming channel.

Given this expression, the excess outgoing low-frequency noise $\Delta S^{(\mathrm{out})}_{f,\varphi}$ at zero temperature can be obtained

$$\Delta S^{(\mathrm{out})}_{f,\varphi} = T^2\Delta S^{(S)}_{f,\varphi} + \frac{e^2RT}{4\pi} f_d\left(\bar{N}_e + \bar{N}_h\right)(\varepsilon \geq hf) \tag{3.32a}$$

$$+ \frac{e^2RT}{2\pi}\int_{\mathbb{R}} \mathrm{sign}(\omega')\overline{\cos(4\pi ft + 2\varphi)\,\Delta W^{(e)}_S(t,\omega')}^{t}\,\mathrm{d}\omega'. \tag{3.32b}$$

in which $(\bar{N}_e + \bar{N}_h)(\varepsilon \geq hf)$ denotes the average number of electronic and hole excitations emitted per period of energy greater than hf.

The first line does not depend on φ and therefore contributes to the isotropic part of the fluctuations. On the other hand, the second line depends on φ and corresponds to the anisotropic part of the fluctuations. As can be seen, this expression only depends on first-order coherences and, more precisely, on the part modulated at frequency $2f$. The $\mathrm{sign}(\omega')$ means that electronic and hole excitations contribute in the same way to this term.

If the source exhibits no squeezing, then the best is to choose one for which $\Delta S^{(S)}_{f,\varphi} = 0$ since it would only contribute to the isotropic part of fluctuations. A driven Ohmic contact is the best choice since it has vanishing excess noise. One has then to consider a source that tends to have most of its single-particle excitations at energies lower than hf but nevertheless has a strong modulation of its single-electron coherence at frequency $2f$. A study by Mendes and Mora [2015] shows that Levitons are indeed quite a good choice for generating squeezing at a tunnel junction in the type of systems considered by Grimsmo et al. [2015]. We now have a collaboration in progress with C. Mora and G. Fève on the quantum optics of noise in quantum Hall edge channels which I hope to resume after my PhD.

3.3.4 Single-particle states in electron and plasmon quantum optics

To make our exploration of the connection between electron and plasmon quantum optics more explicit, we shall now consider interesting examples of single- to few-excitation states either in electronic or plasmonic terms that can be obtained in a simple way. Such examples should be seen as a way to connect electron to photon quantum optics.

More precisely, we shall address the following questions:

- What are the single-electron excitations that can be generated by a classical voltage drive?
- How can we generate a single-plasmon excitation from a single electron/hole pair?

The answer to the first question will lead us to a very important class of elementary electronic excitations called Levitons. These are the Dr. Jekyll and Mr. Hyde excitations within quantum Hall edge channels in the sense that they are the only ones that are both purely electronic and generated by a classical voltage generator.

The answer to the second question is the opposite: it will give us a practical electronic way to generate a photonic or plasmonic state which is non-classical, being a Fock state of a given photonic or plasmonic mode.

Single-electron excitations and classical currents

Let us start by searching for single-electron excitations that can be generated by a classical current pulse. As we have seen, a classical

current is described by a coherent state of plasmons with functional parameter Λ_V. Since we consider a current that adds one electron, we have:

$$|\Psi\rangle = U^\dagger \mathcal{D}[\Lambda_V]\,|F\rangle = \mathcal{D}[\Lambda_V] U^\dagger\,|F\rangle\,. \tag{3.33}$$

where one should remember that each state $|F\rangle$ and $U^\dagger\,|F\rangle$ is a vacuum state with respect to the plasmonic mode operators.

But we can also describe the emission of a single electron on top of the Fermi sea by a superposition of plasmonic coherent state according to eq. (3.8). The principle is then to identify each contributions of the two expressions we obtained. To do this, we start by developing the displaced vacuum on a photon number basis:

$$\begin{aligned}\mathcal{D}[\Lambda]\,|0\rangle = \exp\left(-\frac{1}{2}\int_0^\infty |\Lambda(\omega)|^2\,\mathrm{d}\omega\right)\\ \times \sum_{n=0}^{\infty}\frac{1}{n!}\int_0^\infty \prod_{i=1}^{n}\frac{\Lambda(\omega_i)}{\sqrt{\omega_i}} b^\dagger(\omega_i)\,\mathrm{d}\omega_1\cdots\mathrm{d}\omega_n\,|0\rangle\,.\end{aligned} \tag{3.34}$$

Let us compare zero-, one- and two-plasmon contributions. We introduce the particle current $i_{e,V}(\omega) = \sqrt{\omega}\Lambda_V(\omega)$ generated by the classical voltage drive V. Each order in the number of plasmonic excitations gives a functional relation between the wavefunction and the current. At zero-plasmon order:

$$v_F\,\varphi_e(\omega=0) = \sqrt{2\pi a}\exp\left(\frac{1}{2}\int_0^\infty \left(1-|i_{e,V}(\omega)|^2\right)\,\frac{\mathrm{d}\omega}{\omega}\right), \tag{3.35}$$

and then, at the one-plasmon order:

$$\varphi_e(\omega) = \varphi_e(0) i_{e,V}(\omega), \tag{3.36}$$

and finally at the two-plasmon order:

$$\varphi_e(\omega_1+\omega_2)\varphi_e(0) = \varphi_e(\omega_1)\varphi_e(\omega_2). \tag{3.37}$$

The only continuous solutions of eq. (3.37) have the form $A\exp(-\omega\tau_e + \mathrm{i}\omega t_0)$. Wavefunctions being normalized, we thus have:

$$\varphi_e(\omega) = \sqrt{4\pi\tau_e v_F}\,\mathrm{H}(\omega)\exp(-\omega\tau_e)\exp(\mathrm{i}\omega t_0), \tag{3.38}$$

which is the Leviton of width τ_e emitted around time t_0. Having an expression for $i_{e,V}$, we can come back to eq. (3.35). Divergences within

the exponential will be regularized using the usual UV cutoff a. First, we have to compute:

$$\varphi_e(\omega=0) = \sqrt{2\pi a}\exp\left(\frac{1}{2}\int_0^\infty \left(1-|i_{e,V}(\omega)|^2\right)\,\frac{\mathrm{d}\omega}{\omega}\right), \tag{3.39}$$

which involves an integral of the form:

$$\exp\left(\int_0^\infty (\mathrm{e}^{-\omega\tau_1}-\mathrm{e}^{-\omega\tau_2})\,\frac{\mathrm{d}\omega}{\omega}\right) = \frac{\tau_2}{\tau_1}, \tag{3.40}$$

with $\tau_2 = 2\tau_e$ and $\tau_1 = 0$. Since $\tau_1 = 0$ would diverge, we regularize it using $\tau_1 = a/v_F = 0^+$ thus obtaining:

$$\sqrt{2\pi a}\exp\left(\frac{1}{2}\int_0^\infty \left(1-|i_{e,V}(\omega)|^2\right)\,\frac{\mathrm{d}\omega}{\omega}\right) = \sqrt{4\pi v_F\tau_e}, \tag{3.41}$$

showing that eqs. (3.35) to (3.37) are consistent. This shows that the only single-electron excitation that can be generated by a classical current is the Leviton of unit charge. In the same way, the only single-hole excitation that can be generated by a single voltage pulse is the anti-Leviton of charge e.

Single-plasmon state from electron/hole pair annihilation

Let us now determine if it is possible to generate a single photon from a single electron/hole pair. On one hand, if we create a single photon in wavefunction φ_b in the electronic fluid, the state of the fluid becomes:

$$\begin{aligned} b^\dagger[\varphi_b]\,|0\rangle &= \int_0^\infty \varphi_b(\omega) b^\dagger(\omega)\,\frac{\mathrm{d}\omega}{\sqrt{2\pi}}\,|0\rangle \\ &= \int \frac{\varphi_b(\omega)}{\sqrt{2\pi\omega}} c^\dagger(\omega+\omega')c(\omega')\,\mathrm{d}\omega\mathrm{d}\omega'\,|0\rangle\,. \end{aligned} \tag{3.42}$$

where we defined the bosonic creation operator using the normalization $\int |\varphi_b(\omega)|^2 \mathrm{d}\omega/2\pi = 1$. On the other hand, an electron/hole pair is described by the wavefunction of the electron φ_e and the wavefunction of the hole φ_h. The state of the fluid is:

$$c^\dagger[\varphi_e]c[\varphi_h]\,|0\rangle = \frac{1}{2\pi}v_F\int \varphi_e(\omega)\varphi_h^*(\omega')c^\dagger(\omega)c(\omega')\,\mathrm{d}\omega\mathrm{d}\omega'\,|0\rangle\,. \tag{3.43}$$

Identification between these two expressions impose the following functional relation, provided that $\omega' < 0$, $\omega > 0$ and $\omega+\omega' > 0$,

$$\frac{1}{\sqrt{2\pi}v_F}\varphi_e(\omega+\omega')\varphi_h^*(\omega') = \frac{\varphi_b(\omega)}{\sqrt{\omega}}. \tag{3.44}$$

This condititon is fulfilled by a synchronized Leviton/anti-Leviton pair emitted around time t_0 and of typical length τ_0:

$$\varphi_e(\omega) = \sqrt{4\pi\tau_e v_F}\,\mathrm{H}(\omega)\,\mathrm{e}^{-\omega\tau_e}\mathrm{e}^{\mathrm{i}\omega t_0} \tag{3.45a}$$

$$\varphi_h(\omega) = \sqrt{4\pi\tau_e v_F}\,\mathrm{H}(-\omega)\,\mathrm{e}^{-|\omega|\tau_e}\mathrm{e}^{\mathrm{i}|\omega|t_0}. \tag{3.45b}$$

At the same time, the photon is emitted in a broadband wavefunction centered around the same time t_0 and possessing the same typical timescale τ_0 as the Leviton/anti-Leviton pair. Its wavefunction φ_b is Lorentzian in time. Note that this single-plasmon state carries a vanishing average electrical current at all times! Its energy spectrum is

$$S(\omega) = |\varphi_b(\omega)|^2 = 8\pi\tau_e^2\omega\,\mathrm{e}^{-2\tau_e\omega}. \tag{3.46}$$

Is it possible to create such a pair in an actual device? Actually, it is, by using a quantum point contact. We can imagine someone sends synchronously a Leviton and an anti-Leviton on a QPC, like in fig. 3.6. In this case, we can have four processes, two being trivial (direct propagation or exchange) and two leading to the creation of a single photon in one branch of the interferometer. An alternative method has been suggested in [Dasenbrook and Flindt, 2015], which involves driving the gate voltage of a QPC in a suitable way.

3.4 Interactions and plasmon scattering

In this section, I will discuss single-electron decoherence. The problem is to compute the electronic coherence after an injected pure single-electron excitation has propagated within an interaction region of finite length.

I will describe my work on this subject, taking into account that the study of this very important problem has started long time ago, first when my advisor considered the many-body decoherence in a non-chiral Luttinger liquid [Degiovanni and Peysson, 2000] and when, with C. Grenier and G. Fève, they invented the method that forms the basis of all our subsequent work [Grenier, 2011] which they have applied to the problem of the relaxation of an energy-resolved electronic excitation of top of the Fermi sea $c^\dagger(\omega_\mathrm{e})\,|F\rangle$ [Degiovanni et al., 2009].

My contribution to this line of reaseach has been to solve, in collaboration with C. Cabart and D. Ferraro, the problem of decoherence of an arbitrary single-electron excitation [Ferraro et al., 2014a]. Let me stress once again that this step was essential for understanding the HOM experiments since, as explained in section 1.6.2, the HOM experimental signal

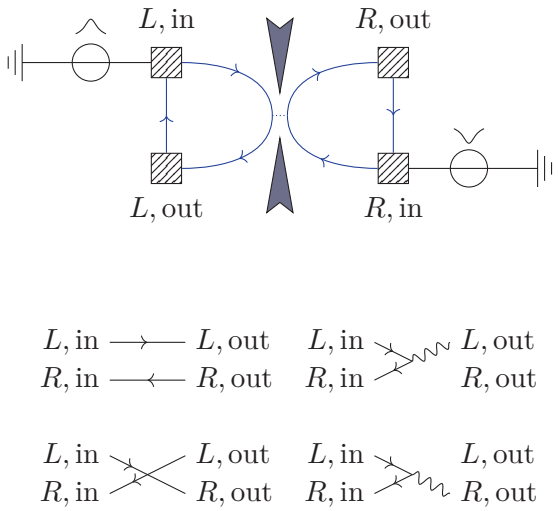

Figure 3.6: Creating a photon from a single electron/hole pair. On the left, we see a scheme of the device that could generate a single photon. We have two sources, one on the left that emits a single Leviton, the other one on the right that emits a single anti-Leviton. Both particles arrive synchronously at a balanced QPC. On the right, the four types of processes that can happen. Two of them (first column) are trivial ones, that are direct propagation and exchange. Two of them generate a single photon in one of the arm of the interferometer.

is the overlap of two time-shifted single-electron coherence. It turns out that the computation for an arbitrary single-electron excitation which have a coherent spreading in time and in energy is one order of magnitude more difficult than for the case of an energy-resolved single-electron excitation.

In the present section, I will present a review of this topic based on this reference and on a long paper in final stage of completion that will discuss the applications of the method to decoherence at filling fraction $\nu = 1$ and to the decoherence control by sample design. I will also review the comparison between our theoretical predictions, the predictions by Th. Martin's group [Wahl et al., 2014] and the experiment performed by G. Fève and his group in Paris [Marguerite et al., 2016b].

3.4.1 General method

During their propagation, electronic excitations will experience screened Coulomb interactions within the conductor and with charges located in nearby conductors. However in a regime of linear response for all conductors involved, interaction effects can be described within the edge-magnetoplasmon scattering formalism which describes how the bosonic edge-magnetoplasmon modes are altered within the interaction region. Therefore, the bosonization framework provides the key for describing electronic coherence propagation along chiral edge channels.

More precisely, we consider a length l region of a quantum Hall edge channel in which electrons experience intra-channel Coulomb interactions as well as Coulomb interactions with other edge channels (see fig. 3.7 (a)) or an external gate connected to an impedance (see fig. 3.7 (b)). To describe the dynamics, we will introduce the bosonic field $\phi(x,t)$, that can be written from the local charge density $n(x,t)$

$$\phi(x,t) = \frac{1}{\sqrt{\pi}} \int_x^\infty n(y,t)\,\mathrm{d}y. \tag{3.47}$$

Since the local density n and the particle current i_e are linearly related, this description is completely equivalent to the one we have considered in section 3.2. The bosonic field follows the following equation of motion:

$$(\partial_t + v_F \partial_x)\phi(x,t) = \frac{e\sqrt{\pi}}{h}\, U(x,t), \tag{3.48}$$

where $U(x,t)$ denotes the potential along the edge channel. Assuming we are in a linear screening regime within the edge channel and also for the external elements capacitively coupled to the edge channel, the potential $U(x,t)$ is linear in terms of the bosonic fields associated with the other edge channels as well as in terms of bosonic dynamical variables describing other circuit elements. In the case of a gate coupled to an external circuit, these are the bosonic modes associated with the transmission line representation of the circuit impedance (see section 3.3.1 as well as [Degiovanni et al., 2009]).

In the same way, the edge-magnetoplasmon modes of the current channel appear within source terms for the linear equations that describe bosonic modes for the other edge channels and circuit elements.

The interaction region being of finite length, solving the full set of equations of motion leads to an expression for the outgoing fields in terms of the incoming ones. Note that because the problem is time-translation

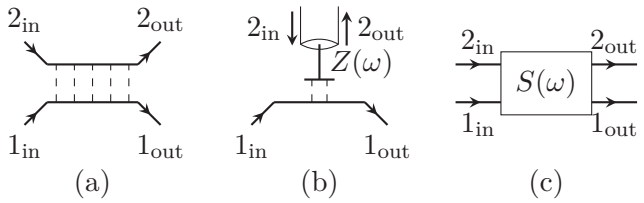

Figure 3.7: The edge-magnetoplasmon scattering approach describes (a) two copropagating edge channels capacitively coupled over a distance l, (b) a chiral edge channel capacitively coupled to a linear external circuit described by a frequency-dependent impedance $Z(\omega)$. Solving for the equation of motions leads to a frequency-dependent scattering matrix $S(\omega)$ between the channel's edge-magnetoplasmon modes and the bosonic modes of the other system (c).

invariant, the solution can be expressed in terms of an elastic scattering matrix $S(\omega)$ relating the incoming and outgoing bosonic modes (see fig. 3.7 (c)). In the present situation where all the incoming and outgoing channels correspond to non-interacting edge channels with the same Fermi velocity, this matrix is unitary which expresses energy conservation of edge-magnetoplasmon scattering.

The edge-magnetoplasmon scattering matrix is directly related to the dimensionless finite-frequency admittance $g_{\alpha,\beta}(\omega) = R_K G_{\alpha,\beta}(\omega)$ ($R_K = h/e^2$ being the quantum of resistance) defined as the ratio of the derivative of total current coming into the sample through the edge channel α with respect to the voltage applied to the reservoir feeding the edge channel β. Such a relation has been derived in the case of quantum wires [Safi and Schulz, 1995a,b; Safi, 1999] which are non-chiral Luttinger liquids. In the present case of chiral quantum Hall edge channel at integer filling fractions, this relation takes the following form [Degiovanni et al., 2010]:

$$g_{\alpha\beta}(\omega) = \delta_{\alpha,\beta} - S_{\alpha\beta}(\omega). \tag{3.49}$$

Relating edge-magnetoplasmon scattering to response functions also puts some constraints on scattering amplitudes.

First of all, let's consider the dimensionless finite-frequency admittance $g(\omega) = 1 - S_{11}(\omega)$ of the effective dipole formed by the interaction region of the edge channel 1. Its analytic continuation to negative frequencies obeys the reality condition: $g(\omega)^* = g(-\omega)$. Consequentely, $t(\omega) = S_{11}(\omega)$ can be analytically extended to negative frequencies by

$t(-\omega) = t(\omega)^*$.

Next, the finite-frequency admittance $g(\omega)$ is the one of a passive circuit. As such, it obeys the general property first proposed by Cauer [1926] and then proven by Brune [1931a,b] of being positive real. With our convention, this means that for $z = \sigma + i\omega$, $z \mapsto g(z)$ is analytic in the half plane $\Re(z) < 0$ and

$$\Re(Z(z)) > 0 \quad \text{when } \sigma < 0, \tag{3.50a}$$

$$\Im(Z(z)) = 0 \quad \text{when } z \in \mathbb{R}^-. \tag{3.50b}$$

These conditions put some constraints on the low-frequency expansion of $t(\omega)$ and consequentely on the effective interaction models that can be used. This raises the question of a discrete element circuit synthesis for modeling interaction regions in electron quantum optics, a mathematically entertaining topic which I will leave for future investigation.

Finally, since the edge-magnetoplasmon scattering matrix depends on the precise form of the electric potential within the wire $U(x,t)$, analytical models are often approximative descriptions of the real physics of the sample. Examples of effective model computations can be found in Ch. Grenier's thesis [Grenier, 2011]. Equation (3.49) also suggests that edge-magnetoplasmon scattering amplitudes can be measured using finite-frequency admittance measurements. This has indeed been done in the case of the $\nu = 2$ edge channel system [Bocquillon et al., 2013b] and this has led to a phenomenological model for edge-magnetoplasmon scattering that combines both the effect of long-range Coulomb interactions and of plasmon dissipation.

As will be discussed in section 3.5, the edge-magnetoplasmon scattering amplitudes are the key ingredients for computing electronic decoherence. Before turning to this problem, let us discuss several phenomenological edge channel models starting with the case of an ideal $\nu = 1$ edge channel with finite-range intra-channel interactions. We shall then consider the case of two interacting edge channels ($\nu = 2$) and discuss the case of specific geometries in which one of the edge channels is closed.

3.4.2 The $\nu = 1$ case

Let us first consider a single edge channel with Coulomb intra-channel interactions. In this case, the edge-magnetoplasmon scattering matrix reduces to a frequency-dependent transmission coefficient $t(\omega)$ which, in the absence of dissipation satisfies $|t(\omega)| = 1$.

Short-range effective screened Coulomb interactions correspond to a renormalization of the edge-magnetoplasmon velocity and therefore to a linear dependence of the phase of $t(\omega)$ in ω, $t(\omega) = \mathrm{e}^{\mathrm{i}\omega\tau(l)}$ where $\tau(l)$ is the renormalized time of flight. By contrast, finite-range interactions lead to a non-linear frequency dependence of the phase of $t(\omega)$. We shall write $t(\omega) = \mathrm{e}^{\mathrm{i}\omega\tau(l,\omega)}$ where the time of flight now depends on ω through a frequency dependent velocity $\tau(l,\omega) = l/v(\omega)$ for the edge magnetoplasmons. Since $t(\omega)^* = t(-\omega)$, $v(\omega)$ can be extended analytically to negative frequencies by $v(-\omega) = -v(\omega)$.

A simple model of a $\nu = 1$ edge channel with an interaction region of length l and capacitance C and bare Fermi velocity v_F is presented in appendix D. This model depends on a dimensionless coupling constant $\alpha = (e^2/C)/(\hbar v_F/l)$ representing the ratio of the Coulomb energy for the interaction region to the associated kinetic energy. As expected, it exhibits a non-linear dependence of the phase $t(\omega)$. The edge-magnetoplasmon velocity decreases from v_0 to an asymptotic value $v_\infty = v_F$ showing some mild oscillations as it approaches its asymptotic value v_∞ (see fig. 3.8). These oscillations arise from the sharp position dependence of the interaction potential at the boundary of the interaction region. Note that realistic estimates detailed in appendix D for the coupling constant α in AsGa/AsGaAl are of the order of $\alpha = 0.8$. The value of 0.8 leads to a ratio $v_0/v_F \simeq 4.2$.

In the end, we expect a realistic model of interactions to lead to a smoother behavior of $v(\omega)$ which nevertheless captures the essential physics of Coulomb interactions [Neuenhahn and Marquardt, 2009]. Key features are the two different asymptotic velocities v_0 and v_∞ in the limits $\omega \to 0$ and $\omega \to +\infty$. The infrared velocity v_0 is the velocity of low-energy edge-magnetoplasmon modes and should therefore be called the plasmon velocity. Due to Coulomb interactions, it is expected to be higher than the velocity of high-energy excitations who do not experience interactions for a long time. It is thus reasonable to consider a phenomenological model for $t(\omega) = \mathrm{e}^{\mathrm{i}\omega l/v(\omega)}$ in which $v(\omega)$ interpolates between v_0 and v_∞ with $v_0 > v_\infty$.

3.4.3 The $\nu = 2$ case

The $\nu = 2$ edge channel system is the simplest and experimentally most relevant case involving more than one channel. In this case, two copropagating edge channels separated by approximately 100 nm experience strong intra- and inter-channel screened Coulomb interactions. Several

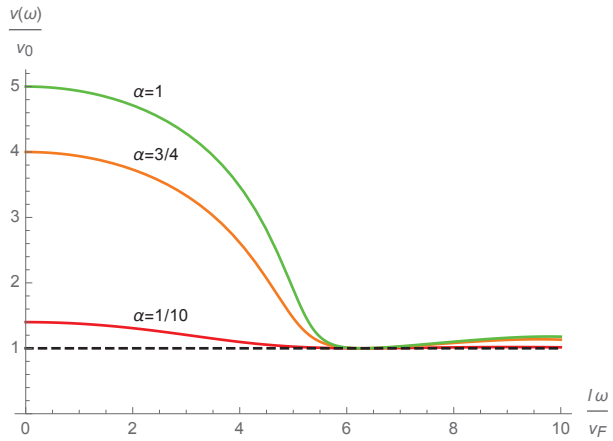

Figure 3.8: Velocity $v(\omega)/v_0$ corresponding to $\exp(\mathrm{i}\omega l/v(\omega))$ given by eq. (D.5) in terms of $\omega l/v_F$ for $\alpha = 1/10$, $\alpha = 3/4$ and $\alpha = 1$.

models have been developed to describe this situation and are briefly reviewed here.

Co-propagating channels with short-range interaction In the presence of metallic side gates, Coulomb interactions are screened and the charge density in one channel is capacitively coupled to the charge density at the same point in the other channel [Levkivskyi and Sukhorukov, 2008]. More precisely, charge density in channel i at position x and energy ω, $\rho_i(x,\omega)$, is coupled to the local electrostatic potential U through distributed capacitances: $\rho_i(x,\omega) = \mathcal{C}_{ij}U_j(x,\omega)$. This situation, schematically depicted on fig. 3.9, is known to give a good description of interactions in experimental systems at small energies, a fact that has been directly probed in the frequency [Bocquillon et al., 2013b] and time [Hashisaka et al., 2017] domains and indirectly confirmed in [Inoue et al., 2014]. Within the interaction region, edge-magnetoplasmon eigenmodes delocalized over the two channels propagate at different velocities. This leads to the following edge-magnetoplasmon scattering matrix [Degiovanni et al., 2010]:

$$S(\omega) = \begin{pmatrix} p_+ \mathrm{e}^{\mathrm{i}\omega\tau_+} + p_- \mathrm{e}^{\mathrm{i}\omega\tau_-} & q\left(\mathrm{e}^{\mathrm{i}\omega\tau_-} - \mathrm{e}^{\mathrm{i}\omega\tau_+}\right) \\ q\left(\mathrm{e}^{\mathrm{i}\omega\tau_-} - \mathrm{e}^{\mathrm{i}\omega\tau_+}\right) & p_+ \mathrm{e}^{\mathrm{i}\omega\tau_-} + p_- \mathrm{e}^{\mathrm{i}\omega\tau_+} \end{pmatrix}, \tag{3.51}$$

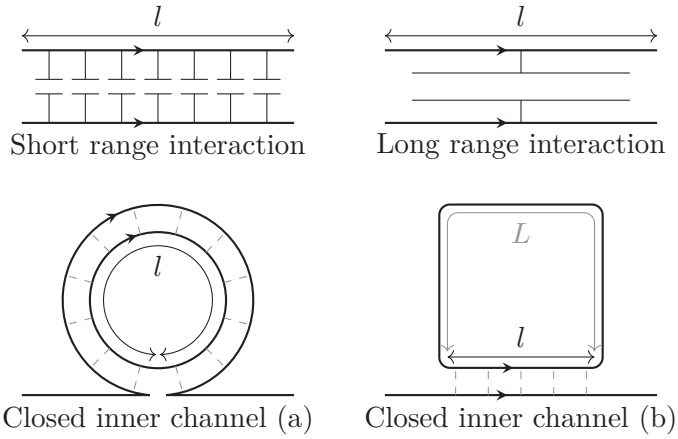

Figure 3.9: Schematic view of the main types of interaction discussed at $\nu = 2$. Short-range interaction corresponds to a capacitive coupling between charge densities at the same position in the two channels, and no coupling between different positions. Long-range interaction describes a situation where the system behaves as one big capacitor. We are also interested in situations where the inner channel is closed on itself and interacts with the outer channel either along its whole length (a), or only on a small portion of the closed loop (b). In either of these cases, interactions can be short-range or long-range.

where

$$p_\pm = \frac{1 \pm \cos(\theta)}{2}, \qquad q = \frac{\sin(\theta)}{2} \tag{3.52a}$$

$$\tau_+ = \frac{l}{v_+}, \qquad \tau_- = \frac{l}{v_-}. \tag{3.52b}$$

In these equations, θ is a mixing angle which corresponds to the coupling strength, v_+ to the velocity of the slowest mode and v_- to the one of the fastest mode. In the strong coupling regime, $\theta = \frac{\pi}{2}$, the corresponding modes are a fast charge mode symmetric over the two channels, and a slow neutral mode which is antisymmetric.

Co-propagating channels with long-range interaction The second model for interacting co-propagating channel assumes that local potentials U are uniform on the whole length of the interaction region. The system then behaves just as one big capacitor (see fig. 3.9) and can be discussed in the spirit of the discrete element circuit models introduced by Prêtre et al. [1996] for quantum conductors and then generalized for quantum Hall edge channels [Christen and Büttiker, 1996]. This approach leads to the following edge-magnetoplasmon scattering matrix [Grenier et al., 2013]:

$$S(\omega) = \begin{pmatrix} p_+\mathcal{T}_+(\omega) + p_-\mathcal{T}_-(\omega) & q\left(\mathcal{T}_-(\omega) - \mathcal{T}_+(\omega)\right) \\ q\left(\mathcal{T}_-(\omega) - \mathcal{T}_+(\omega)\right) & p_+\mathcal{T}_-(\omega) + p_-\mathcal{T}_+(\omega) \end{pmatrix}, \tag{3.53}$$

where $p_\pm$ and q are given by eq. (3.52) and other parameters are given in terms of the dimensionless parameter $x = \omega l / v_F$ by

$$\mathcal{T}_\pm(\omega) = \frac{\mathrm{e}^{\mathrm{i}x} - 1 + \mathrm{i}\alpha_\pm x \mathrm{e}^{\mathrm{i}x}}{\mathrm{e}^{\mathrm{i}x} - 1 + \mathrm{i}\alpha_\pm x}, \tag{3.54}$$

where $\alpha_\pm$ are linked to the eigenvalues of the capacitance matrix $C_\pm$ by $\alpha_\pm = R_K C_\pm v_F / l$.

3.4.4 The $\nu = 2$ case with a loop

Figure 3.9 (a) also depicts a different situation that can arise with two copropagating edge channels, where the inner one is closed on itself over the length l where interaction takes place [Altimiras et al., 2010b]. This imposes a periodicity condition on the bosonic field for channel 2:

$$\phi_2(l, \omega) = \phi_2(0, \omega). \tag{3.55}$$

The transmission coefficient for channel 1 is then given by

$$t(\omega) = \frac{S_{11}(\omega) - \det(S(\omega))}{1 - S_{22}(\omega)} \tag{3.56}$$

for any interaction type described in the open channel case by the scattering matrix S. As expected, this transmission coefficient has a modulus of 1 when S is unitary, which emphasizes the fact that no energy loss is present here. The presence of the closed channel leads to strong non-linearity in the phase of $t(\omega)$ and thus to electronic decoherence. For the specific case of short-range interaction between channels, this yields

$$t(\omega) = -\mathrm{e}^{\mathrm{i}\omega(\tau_+ + \tau_-)} \left(\frac{1 - p_+ \mathrm{e}^{-\mathrm{i}\omega\tau_+} - p_- \mathrm{e}^{-\mathrm{i}\omega\tau_-}}{1 - p_+ \mathrm{e}^{\mathrm{i}\omega\tau_+} - p_- \mathrm{e}^{\mathrm{i}\omega\tau_-}} \right). \tag{3.57}$$

The other type of interaction with a channel closed on itself, depicted on fig. 3.9 (b) appears when the length over which interaction takes place is not the full length of the closed loop, but rather only a part of that loop. Such a geometry has been used for mitigating decoherence in electronic Mach–Zehnder interferometers [Huynh et al., 2012]. In that second case, the periodicity condition on the field for the inner channel is slightly changed

$$\phi_2(0, \omega) = \phi_2(l, \omega) \mathrm{e}^{\mathrm{i}\omega\tau_L}, \tag{3.58}$$

where $\tau_L = \frac{L}{v_+}$ is the time it takes for an excitation to cover the non-interacting length L of the loop. For the short-range interaction model, this leads to

$$t(\omega) = -\mathrm{e}^{\mathrm{i}\omega(\tau_+ + \tau_- - \tau_L)} \left(\frac{\mathrm{e}^{\mathrm{i}\omega\tau_L} - p_+ \mathrm{e}^{-\mathrm{i}\omega\tau_+} - p_- \mathrm{e}^{-\mathrm{i}\omega\tau_-}}{\mathrm{e}^{-\mathrm{i}\omega\tau_L} - p_+ \mathrm{e}^{\mathrm{i}\omega\tau_+} - p_- \mathrm{e}^{\mathrm{i}\omega\tau_-}} \right). \tag{3.59}$$

As expected, case (a) is recovered when $\tau_L = 0$.

3.5 Electronic decoherence

Let us now explain how to obtain the outgoing electronic coherences when a single-electron excitation is injected into the interaction region. This section presents the main steps and the essentiel points of the general methods developed for comparing the electronic decoherence of Landau and Levitov quasi-particles [Ferraro et al., 2014a].

3.5.1 General results

In the bosonization framework, the interaction region is a frequency-dependent beam splitter for the edge-magnetoplasmon modes. An incoming coherent state for these modes is scattered exactly as a classical electromagnetic wave on an optical beam splitter [Grenier et al., 2013]. More precisely, an incoming coherent edge magnetoplasmon of the form $|\Lambda_1\rangle \otimes |\Lambda_2\rangle$ is transformed into an outgoing state $|\Lambda_1'\rangle \otimes |\Lambda_2'\rangle$ where for all $\omega > 0$, $\Lambda'_\alpha(\omega) = \sum_\beta S_{\alpha\beta}(\omega)\Lambda_\beta(\omega)$. Because single-electron states are described as quantum superposition of coherent edge-magnetoplasmon states, an exact description of the outgoing state after the interaction region can be obtained. A single-electron state injected in edge channel 1 corresponds to

$$|\varphi_e, F\rangle_1 \otimes |F\rangle_2 = \int_{-\infty}^{+\infty} \varphi_e(t) \frac{U_1^\dagger}{\sqrt{2\pi a}} \bigotimes_{\omega>0} (|\Lambda_\omega(t)\rangle_1 \otimes |0_\omega\rangle_2)\ \mathrm{d}t, \quad (3.60)$$

and comes out of the interaction region as:

$$\int \varphi_e(t) \frac{U_1^\dagger}{\sqrt{2\pi a}} \bigotimes_{\omega>0} (|t(\omega)\Lambda_\omega(t)\rangle_1 \otimes |r(\omega)\Lambda_\omega(t)\rangle_2)\ \mathrm{d}t. \quad (3.61)$$

In this equation, we adopt the convention used in the remaining of this text that $S_{11}(\omega) = t(\omega)$ and $S_{21}(\omega) = r(\omega)$, other coefficients of S being irrelevant as no injection is made in channel 2. Tracing on the second edge channel degrees of freedom leads to the reduced outgoing many-body density operator for the injection edge channel [Degiovanni et al., 2009]:

$$\rho_1 = \int \varphi_e(t)\varphi_e^*(t')\mathcal{D}_{\mathrm{ext}}(t-t')\psi^\dagger(t)|g(t)\rangle\langle g(t')|\psi(t')\mathrm{d}t\mathrm{d}t', \quad (3.62)$$

where $\mathcal{D}_{\mathrm{ext}}(t-t')$ is an extrinsic decoherence coefficient corresponding to the overlap of imprints left in the environment by localized electrons injected at times t and t'. It is given by [Degiovanni et al., 2009]:

$$\mathcal{D}_{\mathrm{ext}}(\tau) = \exp\left(\int_0^{+\infty} |r(\omega)|^2 (\mathrm{e}^{\mathrm{i}\omega\tau} - 1)\, \frac{\mathrm{d}\omega}{\omega}\right). \quad (3.63)$$

The coherent edge-magnetoplasmon state $|g(t)\rangle$ in eq. (3.62) corresponds to the cloud of electron/hole pairs generated by Coulomb interactions

when a localized electron $\psi^\dagger(t)|F\rangle$ goes through the interaction region:

$$|g(t)\rangle = \bigotimes_{\omega>0} |(1-t(\omega))\Lambda_\omega(t)\rangle. \tag{3.64}$$

In the same way, in the $\nu = 2$ case, the reduced density operator for the inner edge channel can be obtained by tracing out over the outer edge channel. This leads to

$$\rho_2 = \int \varphi_e(t)\varphi_e(t')\mathcal{D}_{\rm inj}(t-t')\,|\mathcal{E}_2(t)\rangle\langle\mathcal{E}_2(t')|\,{\rm d}t{\rm d}t'. \tag{3.65}$$

where

$$|\mathcal{E}_2(t)\rangle = \bigotimes_{\omega>0} |r(\omega)\Lambda_\omega(t)\rangle \tag{3.66}$$

and the decoherence coefficient

$$\mathcal{D}_{\rm inj}(\tau) = \exp\left(\int_0^{+\infty} |t(\omega)|^2(\mathrm{e}^{\mathrm{i}\omega\tau}-1)\,\frac{{\rm d}\omega}{\omega}\right) \tag{3.67}$$

is equal to the overlap of the outgoing states $|\mathcal{E}_1(t)\rangle$ of the injection edge channel corresponding to two different injection times:

$$|\mathcal{E}_1(t)\rangle = \bigotimes_{\omega>0} |t(\omega)\Lambda_\omega(t)\rangle. \tag{3.68}$$

This many-body description gives access to all electronic coherence functions after the interaction region.

3.5.2 Computing single-electron coherences

Going back to the general case, we turn to first-order coherences in the outer and inner channels after interaction, denoted respectively by $\mathcal{G}^{(e)}_{{\rm out},1}(t|t')$ and $\mathcal{G}^{(e)}_{{\rm out},2}(t|t')$.

Outer-channel coherence

When computing $\mathcal{G}^{(e)}_{{\rm out},1}(t,t')$, the final results appear as a sum of two terms. The first one corresponding to the modification of the Fermi sea which, under the right condition can be seen as the contribution of electron/hole pairs generated by Coulomb interaction vacuum state (namely the Fermi sea). This one is called the *modified vacuum*. The second contribution corresponds, also under the proper conditions, to

the incoming excitation elastically scattered or after interaction induced relaxation. This one is called the *wavepacket* contribution. These two contributions [Ferraro et al., 2014b] can be written as

$$\mathcal{G}^{(e)}_{\mathrm{MV},1}(t,t') = \int \varphi_e(t_+)\varphi_e^*(t_-)\mathcal{D}(t,t',t_+,t_-) \langle\psi^\dagger(t')\psi(t)\rangle_F \langle\psi(t_-)\psi^\dagger(t_+)\rangle_F \,\mathrm{d}t_+\mathrm{d}t_-, \tag{3.69a}$$

$$\mathcal{G}^{(e)}_{\mathrm{WP},1}(t,t') = \int \varphi_e(t_+)\varphi_e^*(t_-)\mathcal{D}(t,t',t_+,t_-) \langle\psi(t)\psi^\dagger(t_+)\rangle_F \langle\psi(t_-)\psi^\dagger(t')\rangle_F \,\mathrm{d}t_+\mathrm{d}t_-, \tag{3.69b}$$

where

$$\mathcal{D}(t,t',t_+,t_-) = \gamma_+(t_+ - t')\gamma_-(t_+ - t)\gamma_+^*(t_- - t)\gamma_-^*(t_- - t'), \tag{3.70}$$

is the effective single-particle decoherence coefficient which takes into account both the action of environmental degrees of freedom and of electron/hole pairs cloud created in the injection channel. It is determined by the two functions

$$\gamma_\pm(t) = \exp\left(\pm\int_0^\infty (1-t(\omega))(\mathrm{e}^{\mathrm{i}\omega t}-1)\frac{\mathrm{d}\omega}{\omega}\right). \tag{3.71}$$

Explicit expressions for the two contributions (3.69a) and (3.69b) are given in [Ferraro et al., 2014a, Supplementary Material] and form the starting point of the numerical evaluation of the outgoing electronic coherence in the frequency domain (see section 3.5.2).

Inner-channel coherence

Using the reduced density matrix ρ_2 for the inner channel, any coherence function we are interested in can be computed. The main result is strikingly simple: $\mathcal{G}^{(e)}_{\mathrm{out},2}(t,t')$ is of the same exact form as $\mathcal{G}^{(e)}_{\mathrm{MV},1}(t,t')$ if we replace the function $t(\omega)$ in the decoherence coefficient with $1 + r(\omega)$. The fact that there is no wavepacket term emphasizes that no electron has been injected into the inner channel, only electron/hole pairs are created.

Numerical method

As shown in [Ferraro et al., 2014a, Supplementary Material], the numerical evaluation consists in evaluating integral of factors. The implementation

is quite straightforward, even though the main difficulty comes from the number of nested integrals (four for each point of the electronic coherence). A naive implementation when there are n points in the input coherence in each direction ω and $\delta\omega$, would require an $\mathcal{O}(n^6)$ computation time. This is a lot, since doubling the number of points would require 64 more computation time. However, we lowered the overall complexity of the problem by using its internal structure.

First, it is possible to restate the problem analytically so that one of the integral takes a form

$$\int_{\omega}^{\infty} I(k; X)\,\mathrm{d}k, \tag{3.72}$$

lowering the complexity to $\mathcal{O}(n^5)$.

Second, the mathematical structure of the problem is the following. If we consider the coherence in energy, it is possible to show that the output coherence is obtained by a convolution of the input coherence with the propagator along each line parallel to the diagonal (see fig. 3.10). This implies that ω and $\delta\omega$ are completely uncoupled in this problem. Furthermore, $\delta\omega$ will encode temporal precision, which can usually be fixed once and for all, while ω will encode frequency precision as well as the precision of all our integrations. By using two different discretization, one along ω with n points, the other one along $\delta\omega$ with m points, we can obtain a complexity $\mathcal{O}(m \times n^4)$.

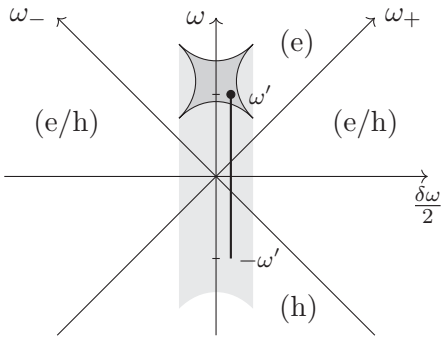

Figure 3.10: Propagation of the incoming wavepacket by the interactions. Each point of the post-interaction coherence comes from the propagation of the point of the incoming coherence along the same $\delta\omega$ line.

With these refinements and using OpenMP parallel framework, we are able to compute a post-interaction coherence in about five minutes

on a 64 cores computer.

We can use two indicators to check the errors. The obvious one is the trace which, as the total number of electrons, should not change. It turns out that it is a very sensitive indicator. If we have a doubt, we can also compare the outgoing average current from the coherence and from the convolution of transmission coefficient and incoming current (however, due to discontinuities in Landau quasi-particle wavepackets, there are unavoidable disparities between these two, due to Gibbs phenomenon).

3.5.3 Many-body decoherence

The decoherence and relaxation of a single electron propagating within a given edge channel is strongly influenced by the external degrees of freedom to which the edge channel can be coupled. Because such a dynamical environment can be excited by the incoming single-electron excitation, it leads to decoherence of the electronic fluid as a whole. The energy flow into the second edge channel has been shown to be the main source of energy relaxation of the inner channel in the $\nu = 2$ system [Le Sueur et al., 2010] although a quantitative description by bosonization [Degiovanni et al., 2010] showed that approximately 23 % of the energy in the inner edge channel does not flow into the outer one[2]. The experimental study also demontrated that, in the case of an out-of-equilibrium electronic distribution, the electronic lifetime was scaling as the inverse of the typical electronic energy, a result showing that the usual Fermi liquid picture is broken in this system. An important issue was then to understand the influence of the external environment on electronic decoherence in quantum Hall edge channels.

Inelastic scattering probability

To get a first hint at the underlying physics, let us consider the inelastic scattering probability across the interaction region: $\sigma_{\rm in}(\omega_e) = 1-|\mathcal{Z}(\omega_e)|^2$ where $\mathcal{Z}(\omega_e)$ denotes the elastic scattering amplitude for an electronic excitation introduced at the energy $\hbar\omega_e \geq 0$. This quantity is directly infered from the regular part of the Fourier transform of γ_- (see [Ferraro et al., 2014b]). Expanding the low-frequency dimensionless admittance

2. Together with high-frequency impedance measurements [Bocquillon et al., 2013b], this result shows that there is still a lot to understand in the physics of quantum Hall edge channels. New insights from experiments would certainly be useful.

$g(\omega)$ as

$$g(\omega) = -\mathrm{i}R_K C_\mu \omega + \frac{R_q}{R_K}(R_K C_\mu \omega)^2 + \mathcal{O}(R_K C_\mu \omega^3), \tag{3.73}$$

which defines the electrochemical capacitance C_μ and the relaxation resistance [Büttiker et al., 1993; Prêtre et al., 1996] R_q associated with the interaction region, the inelastic scattering probability behaves as [Grenier et al., 2011b]:

$$\sigma_{\mathrm{in}}(\omega_{\mathrm{e}}) = \left(\frac{R_q}{R_K} - \frac{1}{2}\right)(\omega_e R_K C_\mu)^2 \tag{3.74}$$

for $\omega_{\mathrm{e}} R_K C_\mu \ll 1$. In the presence of extrinsic degrees of freedom in which energy can be dissipated, $R_q > R_K/2$ and therefore the inelastic scattering probability grows quadratically with energy. On the contrary, when the edge channel is not coupled to external dynamical degrees of freedom, as in the $\nu = 1$ case (see section 3.4.2) as well as in the case of an edge channel coupled to a closed second edge channels (see section 3.4.4), this extrinsic decoherence is not present and single-electron decoherence only arises from the creation of electron/hole pairs within the electronic fluid. We then expect this process to be less efficient than excitation emission into the external environement due to phase-space limitations arising from the Pauli principle.

At higher energies, two different scenarios are possible and can be described by looking at the relaxation of a monochromatic electronic wave [Degiovanni et al., 2009]. This depends on the coupling between the system and its environment which is encoded in the functional dependence of $t(\omega)$:

- Provided the coupling is not too important and its bandwidth finite, the vicinity of the Fermi level can be seen as an effective environment for the incident electron. In this regime, which is similar to the usual approach to dynamical Coulomb blockade, the wavepacket contribution is of the form

$$\Delta\mathcal{G}^{(e)}_{\mathrm{MV}}(t,t') = \mathcal{D}_{\mathrm{tot}}(t-t')\varphi_{\mathrm{e}}(t)\varphi_{\mathrm{e}}(t'), \tag{3.75}$$

  where $\mathcal{D}_{\mathrm{tot}}(t-t')$ is an effective decoherence coefficient of the form

$$\mathcal{D}_{\mathrm{tot}}(t-t') = \mathcal{D}_{\mathrm{ext}}(t-t') \times \mathcal{D}_{\mathrm{int}}(t-t'), \tag{3.76}$$

in which we recognize the extrinsic decoherence coefficient given by (3.63) and an intrinsic one reflecting the imprits left under the form of an electron/hole pair cloud close to the Fermi sea: it is obtained by substituting $|r(\omega)|^2$ by $|1-t(\omega)|^2$ in the expression of $\mathcal{D}_{\rm ext}$.

In this regime, the relaxation tail of an electron injected at a given energy $\hbar\omega_{\rm e}$ is well separated from the wave of electron/hole pairs it generates close to the Fermi sea (see fig. 2 of [Degiovanni et al., 2009]).

- When the coupling is large and the bandwith infinite, the inelastic scattering amplitude saturates towards unity at large energies. The quasi-particle does not exist anymore at large energies. This is what happens at $\nu = 2$ within the short-range interaction model. In this example, the quasi-particle is swallowed by the wave of electron/hole pairs it generates in the Fermi sea as shown on fig. 3 of [Degiovanni et al., 2009].

Landau excitations vs Levitons

A more complete understanding of the role of many-body decoherence came by considering, within the same interaction model, the fate of two different single-electron excitations. In [Ferraro et al., 2014b], we have compared the fate of the Levitov and of the Landau quasi-particles in the $\nu = 2$ edge channel system with short-range interactions.

Figure 3.11 presents numerical evaluations of the outgoing Wigner function for an incoming Landau quasi-particle of energy $\hbar\omega_{\rm e}$ and duration $\tau_{\rm e} = \gamma_{\rm e}^{-1}$ for various propagation distances or, equivalently, times of flight. These results are obtained at zero temperature. They show that the decoherence scenario for the Landau quasi-particle involves two timescales. For an energy-resolved excitation ($\gamma_{\rm e} \ll \omega_{\rm e}$), the single-electron coherence relaxes close to the Fermi level after a time of flight proportional to $\omega_{\rm e}^{-1}$. Then, after a time of flight proportional to the wavepacket duration $\gamma_{\rm e}^{-1} \gg \omega_{\rm e}^{-1}$, $\Delta W^{(e)}_{\rm out}(t,\omega)$ splits into two parts progressing at the velocities of the two edge-magnetoplasmon eigenmodes, thus giving birth to collective excitations close to the Fermi sea. The first phenomenon is associated with energy relaxation discussed in the previous paragraph and probed by F. Pierre's group whereas the second one corresponds to the expected fractionalization arising from the

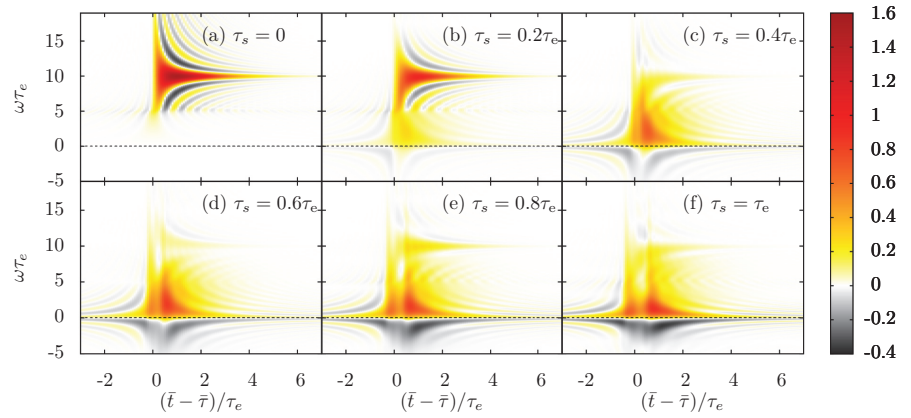

Figure 3.11: (Extracted from [Ferraro et al., 2014b]) Excess Wigner function $\Delta W^{(e)}_{\rm out}(t,\omega)$ at various propagation times for a Landau quasiparticle of lifetime $\tau_{\rm e}$ emitted at energy $\hbar\omega_e = 10\hbar\tau_{\rm e}^{-1}$. The horizontal dashed line at $\omega = 0$ is the Fermi level. Plots correspond to increasing propagating lengths expressed in terms of times of flight: τ_s for the slow mode and $\tau_c = \tau_s/20$ corresponds to the fast mode. The time shift $\bar{\tau} = (\tau_c + \tau_s)/2$ compensates for the global drift of the excitations. Panel (a) shows the initial excess Wigner function.

charged/neutral mode separation predicted by the short-range interaction model [Grenier et al., 2013].

This decoherence scenario must be compared to the Levitov quasiparticle one shown on fig. 3.12: the Leviton fractionalizes into two half-Levitons which are Lorentzian current pulses carrying a charge $-e/2$. The only timescale appearing is the time needed to fractionalize a Leviton.

The difference between these scenarios comes from the nature of the incoming many-body states: the Leviton is an edge-magnetoplasmon coherent state. Since the interaction region acts as a frequency-dependent beam splitter for the edge magnetoplasmons, the Leviton many-body state does not entangle with its environment: it is a pointer state [Zurek et al., 1993] which does not experience decoherence. In section 3.3.4, we have showed that these are the only single-electron excitations that are pointer states with respect to linear couplings to the edge channel's electromagnetic environment. The Wigner function changes shown on fig. 3.12 come from electron/hole pair generation in this pure many-body state.

On the other hand, as explained in section 3.2.3, the many-body state

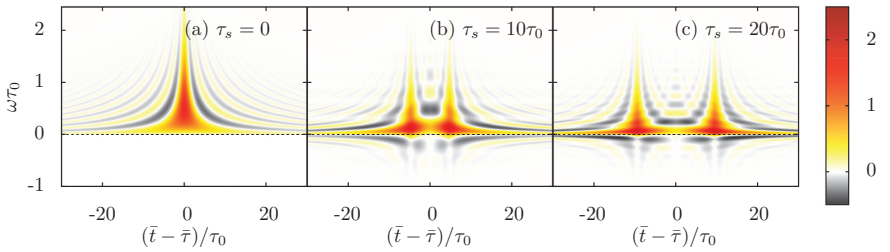

Figure 3.12: (Extracted from [Ferraro et al., 2014b]) Excess Wigner function $\Delta W^{(e)}_{\rm out}(t, \omega)$ of a single-electron Leviton of width τ_0 for various propagation times: τ_s (resp. τ_c) denotes the time of flight of the spin (resp. charged) mode within the interaction region and $\tau_c = \tau_s/20$ and $\bar{\tau} = (\tau_s + \tau_c)/2$.

corresponding to the Landau quasi-particle is a superposition of such pointer states. Entanglement with the second edge channel leads to its decoherence. Depending on the copropagation distance, the outgoing many-body state is a partly decohered mixture of coherent states, each of them corresponding to a localized electronic excitation dressed by a cloud of electron/hole pairs. This extrinsic decoherence is a many-body phenomenon which leads to the rapid decay of the Wigner function at the initial injection energy $\hbar\omega_{\rm e}$.

Therefore, the rapid electronic relaxation shown on fig. 3.11 appears as the electronic counterpart of the decay of interference fringes expected for the Wigner function of the superposition of two coherent states of an electromagnetic mode observed in cavity QED experiments [Deléglise et al., 2008]. Here, it arises from the decoherence of a mesoscopic superposition of edge-magnetoplasmon coherent states. This process takes place over a shorter time than the evolution of each of these quasi-classical states which corresponds to spin-charge separation.

Once extrinsic decoherence has taken place, the outgoing many-body state is an incoherent mixture of fractionalized localized electronic excitations. We confirm this scenario by computing both the current pulse and the electron distribution function corresponding to the Wigner functions of fig. 3.11: the decay of the quasi-particle peak takes place at short times (fig. 3.13 (c)) while the current pulses are almost unseparated (fig. 3.13 (a)) and no hole excitations created, thus confirming that it is a purely extrinsic decoherence effect. As the two half-charge current pulses split (fig. 3.13 (b)), hole excitations are created (fig. 3.13 (d)).

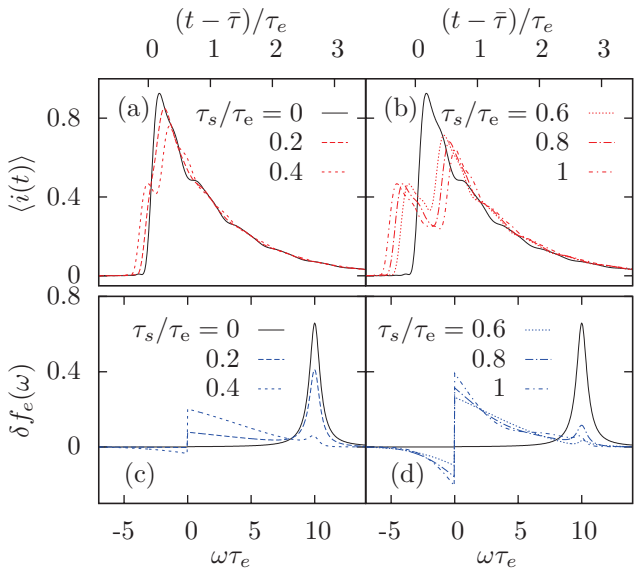

Figure 3.13: (Extracted from [Ferraro et al., 2014b]) The average current $\langle i(t)\rangle$ in units of $-e/\tau_e$ (top row) and the excess electron distribution function $\delta f_e(\omega)$ (bottom row) corresponding to the $\Delta W^{(e)}_{\rm out}(t,\omega)$ presented on fig. 3.11. The initial $\langle i(t)\rangle$ and $\delta f_e(\omega)$ appear as filled black curves. For short propagation times (panels (a) and (c)), the current peaks are not very well separated and no hole excitations are created but the quasi-particle peak in the electron distribution function strongly decays. For longer propagation times (panels (b) and (d)), hole excitations appear as the current pulse fractionalizes in two well separated peaks whereas the quasi-particle peak remains small.

The many-body decoherence manifests itself through a striking phenomenon: since it suppresses contributions arising from the initial coherence $\varphi_{\rm e}(t_+)\varphi_{\rm e}^*(t_-)$ at different times $t_+ \neq t_-$, $\Delta W_{\rm out}^{(e)}(t,\omega)$ only depends on $|\varphi_{\rm e}(t)|^2$. Consequently, it only depends on the shape of the incoming current pulse and not on its injection energy. This striking feature can be easily tested in a HOM experiment: at fixed $\gamma_{\rm e}$, the HOM curve should not depend on the injection energy of the electron when $\omega_{\rm e} \gtrsim \gamma_{\rm e}$. However, the precise shape of this curve depends on the effective interactions.

3.5.4 Experimental test

The decoherence scenario has been checked by the experimental group of G. Fève, thus leading to a joint paper with Th. Martin's group [Marguerite et al., 2016b]. This work presents a detailed comparison of theoretical predictions and experimental data for an HOM experiment involving two single-electron sources located at approximately 3 µm from the beam splitter (see fig. 3.14).

These two sources are driven by square voltage with repetition frequency $f = 0.9\,\mathrm{GHz}$ and a typical rise time of 30 ps. The peak-to-peak amplitude matches the dot level separation $\Delta/k_B = 1.4\,\mathrm{K}$ so that the electron and hole excitations are emitted at $\omega_{\rm e}/2\pi \simeq 14\,\mathrm{GHz}$ above or below the Fermi level. Two experimental parameters are available: the dot transmission wich controls the escape time $\tau_{\rm e}$ and a d.c. voltage applied to the dot's top gate which allows some detuning of the emission energies of one source with respect to the other. The values of $\tau_{\rm e}$ are obtained from the phase of the a.c. current (first harmonic) generated by the source so it is an indirect determination with significative error bars. These measurements can be checked against empirical fits performed on the HOM curves although, in this case, a broadening from interchannel Coulomb interaction is expected. Nevertheless, the two data sets are to some extent compatible and typical values of $\tau_{\rm e}$ range from 30 ps to 180 ps (first method of determination).

The evolution of a Landau excitation in the experiment, from its emission by the source to the beam splitter is depicted on fig. 3.15. When emitted, the electronic Wigner function exhibits some ripples of negative or above-unity values characteristic from the non-classical nature of the single-electron state. After a short propagation length, $\tau_s = 28\,\mathrm{ps}$, before the fractionalization has occurred, energy relaxes and the spectral weight at ω_e is transferred close to the Fermi energy. The non-classical ripples are also almost completely washed out. For the longest propagation length

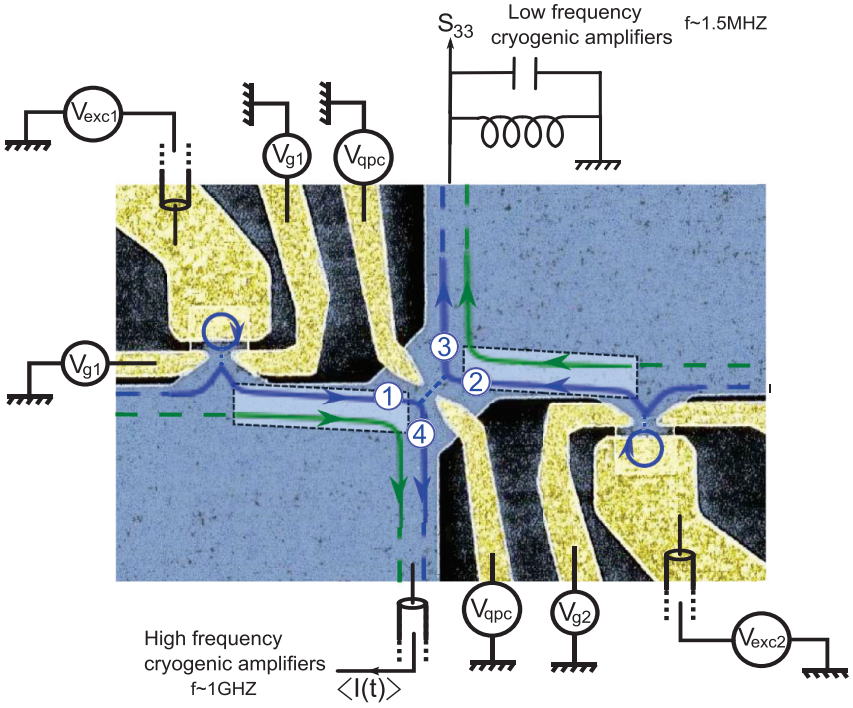

Figure 3.14: (Extracted from [Marguerite et al., 2016b]) Modified scanning electronic microscope picture of the sample. The electron gas is represented in blue, the edge channels by blue (outer channel) and green (inner channel) lines, and the metallic gates are in gold. The emitters are placed at inputs 1 and 2 of the QPC used as an electronic beam splitter. Single-electron emission by source i on the outer channel is triggered by the square voltage $V_{\mathrm{exc},i}$ of amplitude $eV_{\mathrm{exc},i}/k_B = 0.7\,\mathrm{K}$. The dot-to-edge transmission of source i is tuned by the gate voltage $V_{g,i}$. The central QPC is set to partition ($\mathcal{R} = 0.5$) the outer channel using the gate voltage V_{qpc}. Interaction regions of length $l \sim 3\,\mu\mathrm{m}$ are represented by light blue boxes. Average a.c. current measurements are performed on the splitter output 4 in order to characterize the source parameters (in particular e). Low-frequency noise measurements S_{33} are performed on output 3.

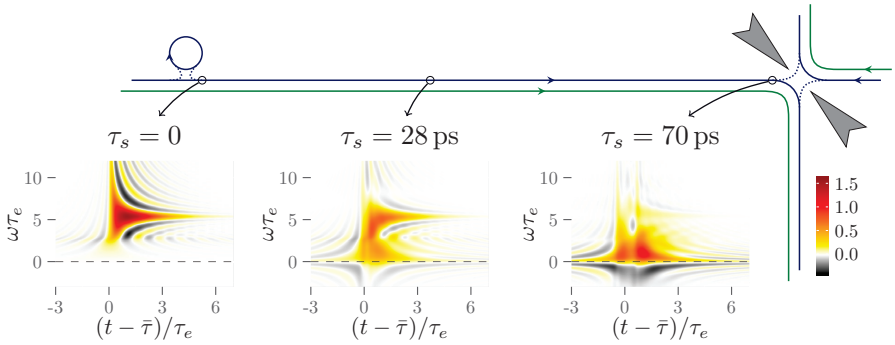

Figure 3.15: Density plots for the Wigner representation of the excess single-electron coherence at $T_{\mathrm{el}} = 0\,\mathrm{K}$ for different propagation lengths corresponding to the sample used in the experiment. The time axis are shifted by time $\tau_- = l/v_\rho$ to account for the propagation time on length l. For $\tau_s = 0$, we have the excess Wigner function of a Landau excitation emitted in the outer edge channel (blue line) with $\omega_{\mathrm{e}} = 0.7\,\mathrm{K}$ and $\tau_{\mathrm{e}} = 60\,\mathrm{ps}$. Then the effect Coulomb interactions between the outer and inner (green line) edge channels is taken into account and the right most excess distribution is the one arriving at the QPC and used to compute the HOM signal.

$\tau_s = 70\,\mathrm{ps}$, the fractionalization in two distinct pulses occurs and appears along the temporal axis. The value of $\tau_s = 70\,\mathrm{ps}$ is extracted from high-frequency admittance measurements [Bocquillon et al., 2013b] performed on a similar sample coming from the same batch and which confirmed the validity of the short-range interaction model up to frequencies $f = 6\,\mathrm{GHz}$. The same value has also been successfully used to describe the charge fractionalization [Freulon et al., 2015] using the same sample as in the present work (at the same value of the magnetic field). Since two pulses of charge $e/2$ cannot correspond to a single-quasiparticle excitation of the Fermi sea, collective neutral excitations are created. They appear on the excess Wigner function as negative values below the Fermi energy (corresponding to the creation of holes) compensated by an increase above the Fermi energy (corresponding to the creation of the same number of electrons).

Figures 3.16 and 3.17 present the comparison between theory and experiments: experimental points are depicted as data points with their error bars whereas full, dashed and dotted lines presents theoretical curves.

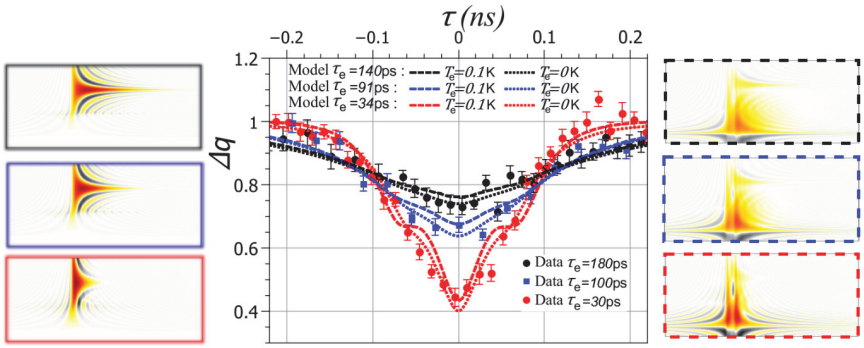

Figure 3.16: Comparison between theory and experiment when using the same injection energies for both single-electron sources and varying τ_e. Left panel: Wigner distribution function for the ideal single-electron excitations corresponding to ω_e and the three different values of τ_e (starting from the top: black 140 ps, blue 91 ps, red 34 ps). Middle panel: normalized HOM noise $\Delta q = \Delta S^{(S1\&S2)}/(\Delta S^{(S1)} + \Delta S^{(S2)})$ where ΔS is the excess current noise (see eq. (1.97)), as a function of the time shift between the two sources. This compares experimental data points and theoretical predictions using both our zero-temperature computations (dotted curves) and finite-temperature computations at $T_{el} = 100$ mK by Th. Martin's group (dashed curves). Right panel: theoretical predictions for the outgoing excess Wigner distribution corresponding to the three injected single-electron excitations of the left column. Their time-shifted self-overlaps give the dotted curves (same color code).

Figure 3.16 presents this comparison for various emission times τ_e at a fixed and identical energy injection for both sources. Experimental data are represented together with theoretical predictions at zero temperature and at $T_{el} = 0.1\,\mathrm{K}$, providing an evaluation of the effect of finite-temperature on single-electron decoherence. The red, blue, and black curves represent these theoretical predictions taking $\tau_e = 34,\ 91$ and $147\,\mathrm{ps}$. These values agree within experimental resolution with the values of e extracted from the measurements of the average current. In particular, for the short time $\tau_e = 34\,\mathrm{ps}$, theoretical predictions capture the broadening of the electronic wavepacket by the fractionalization process, which leads to an overestimate by a factor 2 of the emission time extracted from the exponential fit of the dip (although the experimental resolution is not good enough to observe the predicted side peaks for $\tau_e = 34\,\mathrm{ps}$ at $0.1\,\mathrm{K}$). The agreement between data and predictions is good: once the width of the dip has been chosen to match the data, the values of the contrast also agree. Note that the effect of temperature is very weak: this is explained by the fact that, the initial Landau excitation being emitted at high energy compared to $k_B T_{el}$ (7 times to be precise), and the coupling being broadband, most of the generated electron/hole pairs are not blocked by the thermally excited ones.

Figure 3.17 presents the data/model comparison when the emission energies of the two sources are detuned. This is where a striking distinctive prediction of the interaction model can be tested: the contrast and shape of the HOM trace is almost unchanged when the emission energy of one of the two sources is varied (from $0.7\,\mathrm{K}$ to $0.3\,\mathrm{K}$). This behavior is completely different from the non-interacting model predictions (black and red blurred lines), for which the contrast varies strongly from 1 to 0.25 when the energies are detuned by $0.4\,\mathrm{K}$ at $\tau_e = 40\,\mathrm{ps}$. Surprisingly, in the detuned case, interactions lead to enhancement of the contrast compared to the non-interacting prediction. This restoration of indistinguishability by decoherence is a consequence of electronic relaxation which erases the memory of the initial injection energy from the outgoing single-electron coherence after a long propagation. This erasure effect is a consequence of the entanglement of the electronic degrees of freedom of the outer edge channel where the single-electron excitation is injected with the inner one. Quantitatively confirming this effect is the most convincing signature of the single-electron decoherence scenario described within the bosonization framework.

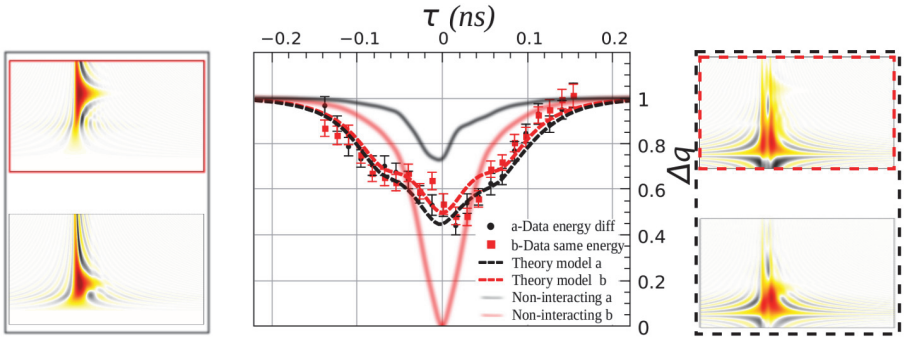

Figure 3.17: Comparison between theory and experiment when using different injection energies for both single-electron sources with the same τ_e. Left panel: Wigner distribution function for the ideal single-electron excitations corresponding to the two different injection energies (starting from the top: red $\hbar\omega_e/k_B = 0.7\,\mathrm{K}$, black $\hbar\omega_e/k_B = 0.3\,\mathrm{K}$). Middle panel: normalized HOM noise $\Delta q = \Delta S^{(S1\&S2)}/(\Delta S^{(S1)} + \Delta S^{(S2)})$ where ΔS is the excess current noise (see eq. (1.97)), as a function of the time shift between the two sources. This compares experimental data points and theoretical predictions using our zero temperature computations (same injection energy: red data points and dashed curves; different injection energies: black data points and dashed curves). The blurred lines correspond to the expected HOM signal in the absence of interactions (same color code as before). Right panel: theoretical predictions for the outgoing excess Wigner distribution corresponding to the injected single-electron excitations of the left column. The proper time-shifted overlaps give the dashed curves of the middle panel (same color code as before).

3.6 On-going works and perspectives

In this section, I will briefly describe our on-going works that are based on the ideals and methods we have developed to study single-electron decoherence. The versatility of our approach in which the form of the effective Coulomb interaction only appears through the functional dependence of the edge-magnetoplasmon transmission $t(\omega)$ makes it very easy to apply our technique to other physically relevant problems.

First of all, I would like to mention that ideally, it would be possible and interesting to perform a consistency check of our approach by measuring on the same sample the finite-frequency admittances that would determine $t(\omega)$ (see [Bocquillon et al., 2013b]) and then perform either a single-electron tomography as described in section 1.6.2 or an HOM experiment as described in the previous section to check for our theoretical predictions. Moreover, thanks to the signal processing technique presented in chapter 2, we are not anymore limited to toy model expressions for the single-electron wavepacket but we could extract them from a more precise modeling of the source.

Then, I will now present some of the problems we are going to address in our forthcoming publications. The study of electronic decoherence in ideal $\nu = 1$ edge channels and the analysis of decoherence control will appear in a forthcoming publication currently under completion [Cabart et al., 2017]. These problems are motivated by the present status of experiments which are now able to probe electronic decoherence with unprecedented accuracy.

We also plan to apply the technique to study the decoherence of an electron initially delocalized on two copropagating edge channels which are coupled to their environement and are possibly coupled together. This problem is relevant for quantum spintronics at the single-electron level and can also be viewed as a way to model propagation in a Mach–Zehnder interferometer.

3.6.1 The $\nu = 1$ case

Our approach can be applied to study the case of an ideal $\nu = 1$ edge channel system. By ideal, I mean without any dissipation: all the energy injected into the edge channel remains in the edge channel. Consequently, as explained before, there is no many-body decoherence. However, single-electron decoherence is present due to Coulomb interactions within the edge channel. An important question is to understand single-electron

decoherence within this particular context, that is, when it solely arises from intrinsic decoherence (no external environment).

In the model for edge-magnetoplasmon propagation along an interacting $\nu = 1$ edge channel presented in section 3.4.2, two velocities appear: the velocity of low-energy edge magnetoplasmons which is greater than the velocity of high-frequency edge magnetoplasmons. An important question concerns the velocity of electronic excitations: is it the low-energy velocity or the high-energy one? More generally, what is the propagation velocity of the disturbance of the electronic fluid when an electronic source is turned on?

Understanding electronic decoherence in the ideal $\nu = 1$ edge channel of single-electron excitations can shed some light on both problems. For this, we are studying both the realistic model discussed in section 3.4.2 as well as a simplified toy-model in which the frequency-dependent velocity is a Lorentzian that possesses two plateaus, corresponding to a fast low-energy velocity and a slow high-energy velocity. What we see for these two models is that when the electron excitation energy is localized below the energy threshold that governs the transition from fast to slow velocity, the initial wavepacket propagates without being much altered, at the fast velocity. In the other cases, i.e. when the energy of the excitation contains a non-negligeable part (if not all) above the frequency threshold, the initial electron experience intrinsic decoherence through the formation of electron/hole pairs. We observe on the current that the excitation is enlarged in time, due to the fact that it moves both at fast and slow speed. This is true even when the excitation is energy-localized fully in the high-energy zone (or equivalently in the slow-speed zone), because such an excitation will possess a non-vanishing plasmonic content even at low frequency[3].

3.6.2 Decoherence control

Another natural question is whether we can get rid off or, at least, mitigate the effect of decoherence. For this, we are studying the possibility to engineer the geometry of the inner channel, such as described in fig. 3.9 (lower pannel). This case can be seen as an effective single-channel interaction.

3. If we think about a plasmon at a given energy ω, it is a coherent superposition of all energy-resolved electron/hole pairs with energy ω. As such, it is not separated from Fermi surface, and the only way to achieve this is by constructing a destructing interference, thus populating low-energy plasmonic modes.

We will discuss here the simplest case, when the outer channel fully encloses the loop. In this case, the inner loop can be seen as a plasmonic cavity with a characteristic resonance frequency $\omega_c/2\pi$ and its harmonics. First, let us consider weak coupling between edge channels ($\theta \ll \pi/2$). If we consider a plasmonic mode slightly modulated around ω, it will propagate freely in the outer channel unless its energy is close to integer multiple of $\hbar\omega_c$. When its energy is around $\hbar\omega_c$, the speed of this mode drops suddenly, because of the time it spends inside the cavity. At weak coupling, we have thus an effective $\nu = 1$ system where the effective edge-magnetoplasmon velocity now exhibits strong variations around the resonances of the cavity. When injected below the first energy resonance, the single-electron excitation will be mostly unaltered. However, when the excitation passes above the first resonance of the cavity, there is a quantitative difference, since it will weakly excite electron/hole pairs. When increasing the coupling strength up to $\pi/2$, the scattering resonance become less defined as usual when coupling a set of discrete levels with a continuum. The effect of the cavity on an incident single-electron excitation is then drastic: although when sent the excitation below the lowest scattering energy resonance, it is almost preserved by this shaped environment, the decoherence effect when the excitation is sent above it is much stronger.

We are now using our approach to discuss experimentally relevant situations, in which the inner channel is not fully enclosed by the outer channel and using realistic parameters for the geometry. Results are in fact being generated as I complete the writing of this thesis and will therefore be detailed in [Cabart et al., 2017].

3.6.3 The delocalized electron

The creation of qubit from electronic modes is not as straightforward as with bosonic ones because of the superselection rules discussed in section 1.3.2. A way to avoid the difficulty is to use the so-called railroad qubits encoding it in the quantum delocalization between the two edge channels present at $\nu = 2$. Since the channels are spin polarized, we are indeed discussing a flying electronic spin quit.

In our case, the observable σ_z will correspond to the excess charge difference between the two channels. Since this system is safe from tunneling, the states corresponding to charge totally localized inside one channel will be pointer states. The coherences come from inter-channel charge coherences, which will be both affected by inter-channel interac-

tions and interactions of both channels with an external environment. Or course, the difficulty comes from the fact that it will not be possible to use the various energies to encode different spin qubits in parallel because of electronic decoherence.

Using our method, we can compute what happens for the effective qubit built from an arbitrary single-electron excitation when there are only two channels or in the presence of an external environment. The analytical expressions have been derived several years ago and some preliminary exploration had been done during my Master internship but the work has not been completed yet. We hope to complete it before the end of C. Cabart's PhD.

3.6.4 Perspectives

We have computed post-interaction single-electron coherence for a single-electron excitation. The single-electron wavepacket we have used comes from a toy model, which differs from the realistic wavepackets shown in chapter 2. A first, simple extension of this work would be to study the decoherence of a realistic wavepacket, making a bridge between our signal processing techniques and the decoherence technique.

Another extension, far less trivial, is to see what happens for higher-order, or with more electrons. Unfortunately, the number of terms increases incredibly fast, even for second-order coherence with one electron, or for first-order coherence with two electrons. This makes the general method we have developed more than tricky to implement in practice. This is even more regrettable since those two situations would be of great interest. The first one would allow to probe the two-particle entanglement generation from interactions. The second one would be a platform to test two-electron interactions, probing the Coulomb interaction in a metal in a rather elementary way. However, we hope that perturbative developments for weak interactions will give some insights about these cases. These issues will be more developed in C. Cabart's PhD.

To end on, at the beginning of my PhD, we started to work on out-of-equilibrium bosonization techniques. The hope was to compute the post-interaction single-electron coherence in the case of Floquet sources in full generality. This is indeed a much more complicated problem, since in this case, the number of excess particle is unbounded. We hope the work shown on the previous chapter will give us some hints to carry this further.

Chapter 4

Energy flows in quantum mesoscopic system

4.1 Motivation and scientific context

In the previous chapters, we have discussed probing a many-body quantum source using single- and two-particle quantities in the spirit of quantum optics. The study of electronic decoherence presented in the previous chapter demonstrated the importance of considering the many-body state of the whole system. In the case of chiral quantum Hall edge channels, the proper many-body states were edge-magnetoplasmon coherent states.

In the present chapter, we explore the possibility of accessing information on the many-body state using the statistical properties of global quantities that probe electronic coherences to all orders. As it is already clear from the discussion of current fluctuations in section 1.5, higher moments of the electrical current are sensitive to higher-order electronic coherences. In principle, the full counting statistics of charge transfer [Levitov et al., 1996] would naturally provide useful information but I was also motivated by conceptual issues related to quantum thermodynamics. This is why, in this chapter, I will discuss energy exchanges between mesoscopic systems and apply our approach to the study of heat dissipation in quantum conductors, a problem that we will call the quantum Joule effect.

As always with quantum systems, unperformed experiments have no results [Peres, 1978]. For this reason, quantizing energy exchanges between quantum systems requires an operatorial definition of the en-

ergy received by one of the systems. In practice, in quantum mesoscopic systems, this is not an easy problem as soon as one considers system that can transfer energy over a large range of frequencies. A lot of effort is devoted to building calorimeters that can measure an energy deposition down to the energy of a single quantum. The difficulty is to achieve broadband detection: a single artificial atom could detect a microwave photon but within a narrow band around its resonance frequency. Building a calorimeter able to measure a global energy deposition at this level of sensitivity is another story.

Recently, the group of J. Pekola in Aalto demonstrated a radiofrequency thermometry on a metallic island of micrometric size [Gasparinetti et al., 2015], operated at cryogenic temperatures ($\lesssim 100\,\mathrm{mK}$). The principle is based on the difference between the internal relaxation timescale of the island and the timescale associated with energy relaxation in its environment: absorption of energy leads to a temperature change that can be detected. The small capacity of the island ensures a high sensitivity of $90\,\mu\mathrm{K}/\sqrt{\mathrm{Hz}}$ with a 10 MHz bandwidth, meaning that it could detect energy depositions of the order of the energy of a single microwave photon. More recent devices are based on a superconducting weak link probed by sub-nanoseconds current pulse as a very sensitive thermometer with very short response time [Zgirski et al., 2017]. In the end, there is hope that some day, it will be possible to perform rapid and precise energy measurement over a timescale comparable to the experimentally relevant timescales and without being limited by the device bandwidth.

Foreseeing this future motivates to consider a measurement-based approach, called the two-time measurement protocol, pictured on fig. 4.1. The protocol goes as follows:

1. We start with the system of interest decoupled from every other systems. As part of the experiment initialization, an energy measurement is performed on the system. This initial energy E_i may of course fluctuate from one realisation to another because of classical fluctuations or because, right before the energy measurement, the system has quantum coherences in the energy basis.

2. We then couple this system to other ones during a finite time. This will generically give rise to an entangled state for all involved systems.

3. We decouple the system of interest and then measure its energy again. Denoting the resulting measurement value by E_f, we define

$Q = E_f - E_i$ as the energy (or heat when we are considering a thermal reservoir) received by the system of interest. Since E_f and E_i are fluctuating quantity, Q is also fluctuating in general. This means that if we perform the experiment another time, different values of E_f, E_i and thus of Q will be obtained.

4. Resetting and repeating the experiment enables us to collect statistics and infer the probability density $P(Q)$. In particular, we can access its average and all its fluctuations as well as its cumulants.

It is important to note that the initial measurement of the energy is essential. If the corresponding observable was not measured at the end of the initialization phase of the experiment, the quantity Q would make no sense: it would be contrafactual.

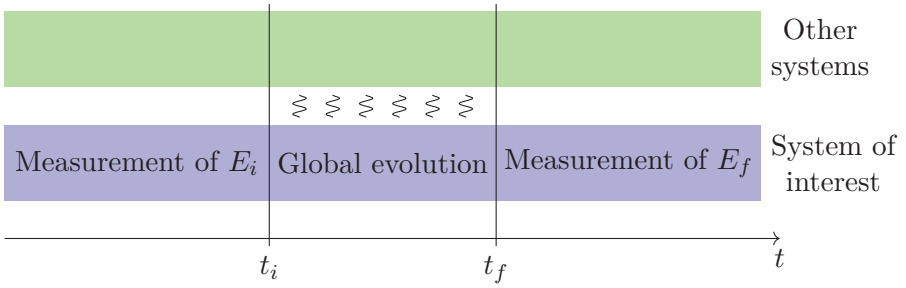

Figure 4.1: Two time measurement protocol: the system is prepared at the initial time t_i in one of its eigen-energy states (energy E_i), it is then coupled to its environment and at the final time t_f and an energy measurement is performed. The energy change is $Q = E_f - E_i$. The experiment is repeated to access the statistics of Q. Note that the measurement of E_i depletes all coherences between the eigen-energy states of the system.

Of course, this scheme can be used in various situations including the ones involving many subsystems. Here, we will focus on the case of single system that is connected to an environment which will be at equilibrium at a given temperature. Since we are interested in the heat dissipated in the environment, the system of interest on which we perform energy measurements will be the environment itself, as shown on figure fig. 4.2.

Before going into the detailed examples coming from photon and electron quantum optics, let us make an apparent detour through the

Figure 4.2: Typical mesoscopic physics lab experiment: a solid state quantum device is never accessed directly but through measurements performed in its electromagnetic environment part of which consists in coaxial cables extracting and bringing microwave radiation to the device.

dynamics of open quantum system within a path integral perspective. This will shed a new light on the dynamics of open system and will provide us the necessary tools to analyze the statistics of energy transfers. Then, in section 4.3 we will consider energy flows in electronic systems and present our approach to the quantum Joule effect in section 4.4.

4.2 Path integral approach

Let us start our journey in the world of path integrals. We will present a general approach of the dynamics of open quantum systems based on Feynman path integral that will be relevant for discussing the statistics of energy exchange with the environment. More precisely, we will first briefly review Feynman path integral approach for closed and open systems, before we extend it into a path-integral based formalism for quantum trajectories. This will be our starting point for discussing energy exchanges within the two-time protocol and obtain exact expression of the heat flow for some systems.

As usual within the Feynman path integral approach, expressions take a lot of space and using them for actual calculations is often a nightmare, if not impossible in practice. Despite this slight inconvenience, the path integral formalism sheds a bright light on the physical meaning of what we are doing. We will thus spend some time on commenting each terms in rather abstract expressions to gain some physical insight.

4.2.1 Variations on Feynman path integrals

Before we dig deeper into Feynman path integrals and their variations, let us remind the terminology. Usually, paths in Feynman path integral are thought as real paths. Of course, these can be paths for any complete set

of observables[1]. Traditionally, one focuses on transition amplitudes that give the probability to go from one point to another one or correlation functions as in many quantum field theory textbooks. Here we will use a reformulation of this point of view by expressing the evolution of states as vectors in a Hilbert space as paths integrals themselves, thus mixing both the standard operatorial concepts with Feynman's path integral.

Closed systems

For a closed system, it is possible to compute transition amplitude to go from one point x_i at time t_i to another point x_f at time t_f, by summing over all paths γ that go from x_i to x_f the amplitude associated to this path. This is often noted:

$$A_{i\to f} = \langle x_f, t_f | x_i, t_i \rangle = \int_{\gamma(t_i)=x_i}^{\gamma(t_f)=x_f} \mathcal{A}[\gamma]\, \mathcal{D}[\gamma], \tag{4.1}$$

where $\mathcal{A}[\gamma] = \exp(\mathrm{i}S[\gamma]/\hbar)$ is the amplitude associated to the path γ. This amplitude is just a pure phase, proportional to classical action $S[\gamma]$ in the absence of any topological phase. Of course, the hard part comes from the summation over all path. A variety of techniques have been developed to compute this kind of integral and we will not get into the details: there are many textbooks on the subject [Feynman and Hibbs, 1965; MacKenzie, 2000]. The most intuitive and direct approach would be to discretize both time and the coordinate system (if it is not already discrete) as sketched on fig. 4.3. The key point of our approach is to insert the path integral expression of transition amplitudes into the expression of the evolution of states in terms of these amplitudes. This leads to an expression for the final quantum state of a system $|\psi(t_f)\rangle$, initally prepared in a pure state $|\psi(t_i)\rangle$:

$$|\psi(t_f)\rangle = \int \langle \gamma(t_i)|\psi(t_i)\rangle\, \mathcal{A}[\gamma]\ |\gamma(t_f)\rangle\ \mathcal{D}[\gamma]. \tag{4.2}$$

From left to right, we recognize three factors. First, the scalar product between $|\gamma(t_i)\rangle$ and $|\psi(t_i)\rangle$ is just the wavefunction of the initial state expressed in the basis chosen to describe the trajectories. Then appears the transition amplitude associated to the path, and finally the resulting state associated to the terminal point of path $|\gamma(t_f)\rangle$. This expression

1. In case of a 1/2-spin, we can consider the spin along one direction over time as a path.

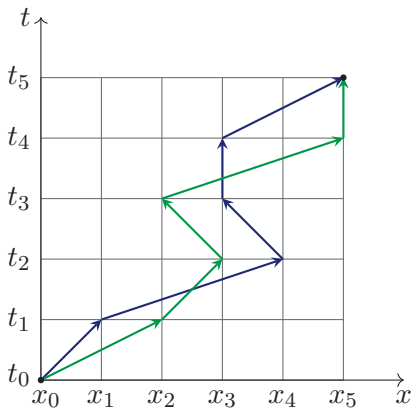

Figure 4.3: Paths in a discretized space. In order to obtain the transition amplitude between (x_0, t_0) and (x_5, t_5), we need to sum all the amplitudes of paths that connect them.

contains nothing new but as we shall see now, it leads to a surprisingly transparent derivation for the dynamics of an open quantum system!

Open systems

For open quantum systems, we use the usual approach and consider that the system comes along with an environment and that the composed system is closed. In order to avoid difficulties arising from the presence of pre-existing quantum correlations between the system and its environment, we shall always assume that the initial global state is factorized between the system and its environment.

Pure case When the environment is initially in a pure state, it is possible to associate a pure state $|\Psi(t)\rangle$ to the composed system. Furthermore, as the system follows a trajectory γ, the state of the environment is changed according to a corresponding forcing thus leading to a time-dependent imprint $t \mapsto |\mathcal{E}_t[\gamma]\rangle$. Apart from simple cases, it is not obvious how we can compute explicitly the state of the environment for a particular path followed by the system. However, this state always exists, as it is shown in appendix E.1.

If the environment is purely classical, its state is not affected by the evolution of the system and thus, up to a phase we have $|\mathcal{E}_t[\gamma]\rangle = |\mathcal{E}_0\rangle$. The only effect of the environment on the system is a modification of

its action – as if the environment introduced a kind of refraction index – but the quantumness of its evolution remains. Things become more interesting when the state of the environment is altered depending on the trajectory of the system.

The evolution of the composed system can then be easily described using Feynman amplitude associated to the proper dynamics of the system $\mathcal{A}[\gamma]$ and the state of the environment for a given trajectory:

$$|\Psi(t_f)\rangle = \int \mathcal{A}[\gamma]\langle\gamma(t_i)|\psi(t_i)\rangle\,|\gamma(t_f)\rangle \otimes |\mathcal{E}[\gamma]\rangle\ \mathcal{D}[\gamma], \tag{4.3}$$

where $|\psi(t_i)\rangle$ is the state associated to the system at initial time. This expression is very similar to eq. (4.2) except that it takes into account the drive induced by the system on its environment.

Let us now focus on the dynamics of the open system under consideration, forgetting whatever happens to the environment. To this end, we trace out the degrees of freedom of the environment and obtain the reduced density operator for the system:

$$\rho_{\mathcal{S}}(t_f) = \int \langle\gamma_+(t_i)|\rho_{\mathcal{S}}(t_i)|\gamma_-(t_i)\rangle \times \mathcal{A}[\gamma_+]\mathcal{A}^*[\gamma_-] \tag{4.4a}$$

$$\times \langle\mathcal{E}[\gamma_-]|\mathcal{E}[\gamma_+]\rangle\ |\gamma_+(t_f)\rangle\,\langle\gamma_-(t_f)|\ \mathcal{D}[\gamma_+]\mathcal{D}[\gamma_-]. \tag{4.4b}$$

Again, let us comment this expression factor by factor. The first two factors are not different from what we have encountered for the closed system case. The first one is the initial condition, and the second one comes from the dynamics of the system alone. The last factor of the full expression spans the density matrix in the coordinate space we have chosen. The novelty in this expression comes from the third factor which we will denote $\mathcal{F}_{FV}[\gamma_+,\gamma_-] = \langle\mathcal{E}[\gamma_-]|\mathcal{E}[\gamma_+]\rangle$. It is usually called the Feynman–Vernon influence functional and contains all we want to know about the influence of the environment [Feynman and Vernon, 1963]. Being a scalar product, it is a complex number whose modulus is less or equal to unity. As mentioned above, we can interpret the phase as an alteration of the self-dynamics of the system due to its environment. The module ponderates the weight of the various couples of trajectories (γ_+,γ_-). If, for example, the scalar product between two environment states tends to be negligible for couple of trajectories being just slightly different, interference effects will be killed and we recover a classical dynamics in a path integral framework. The Feynman–Vernon influence functional is a contrast factor governing the interference of paths in the path integral.

General case The case of an initial mixed state for the environment can easily be obtained from previous discussion. We will suppose that we will start from a factorized state $\rho(t_i) = \rho_{\mathcal{S}}(t_i) \otimes \rho_{\mathcal{E}}(t_i)$. In this case, we can proceed with the same method and we obtain

$$\rho_{\mathcal{S}}(t_f) = \int \langle \gamma_+(t_i)|\rho_{\mathcal{S}}(t_i)|\gamma_-(t_i)\rangle \times \mathcal{A}[\gamma_+]\mathcal{A}^*[\gamma_-] \tag{4.5a}$$

$$\times \mathcal{F}_{FV}[\gamma_+, \gamma_-] \; |\gamma_+(t_f)\rangle \langle \gamma_-(t_f)| \; \mathcal{D}[\gamma_+]\mathcal{D}[\gamma_-], \tag{4.5b}$$

where the Feynman–Vernom functional is modified to take into account the statistical nature of the initial condition

$$\mathcal{F}_{FV}[\gamma_+, \gamma_-] = \mathrm{tr}\left(U[\gamma_+]\, \rho_{\mathcal{E}}(t_i)\, U[\gamma_-]\right), \tag{4.6}$$

where $U[\gamma]$ denotes the evolution operator for the environment when the system follows the trajectory γ.

Quantum trajectories

Now that we have reviewed the traditional Feynman path integral for closed and open quantum systems, we will now show that quantum trajectories [Dalibard et al., 1992; Molmer et al., 1993] can also be formulated in terms of Feynman path integrals. The advantage of this generalization is that it defines the notion of a quantum trajectory in a very general way, not relying at all on any Markovian hypothesis.

In the usual approach to decoherence, the environment is traced out, and the information it contains about the system is completely forgotten. However, in the last decades, we have seen the existence of more and more controlled systems for which it is now possible to measure a significative part of the environment. In this case, it is possible to make deductions about the state of the system. In the ideal case where we can perfectly measure the whole environment, it is even possible to associate and compute a pure quantum state of the system along its evolution, given the measurement results. This state, conditioned or relative to a measurement result is what is called a quantum trajectory. In this section, we will consider only this ideal case, where the measurement gives a complete knowledge of the environment. The general case, with incomplete measurement is more tedious. However, for our two-time measurement protocol as we will see in section 4.2.2, we can use a fine-grained measurement, which is complete, and then average over the unobserved degrees of freedom.

An example of an ideal measurement record for an quantum electronic system would be, for example, a record of a voltage at one end of a transmission line as a function of time. But it could also be some information in the time/frequency domain... or maybe in the frequency domain when using a spectral analyzer. With this in mind, we will consider that a measurement record is a function. Usually, it is a measurement in the time domain but this is not necessarily the case.

Of course, each possible measurement record corresponds to a state for the environment. All possible records $\alpha \mapsto x(\alpha)$, correspond to an orthogonal basis for the environment since they are perfectly distinguished by the measurement apparatus! We denote this orthonormal basis by $(|[x]\rangle)_{[x]}$. Given a pure state $|\Psi(t_f)\rangle$ for the composed system, it is possible to decompose the environmental part onto the basis given by our measurement apparatus:

$$|\Psi(t_f)\rangle = \int \sqrt{p[x]}\, |\psi(t_f|[x])\rangle \otimes |[x]\rangle\, \mathcal{D}[x], \tag{4.7}$$

in which the normalized state $|\psi(t_f|[x])\rangle$ is called the conditioned or relative state [Everett, 1957a] of the system with respect to the measurement record $[x]$ and $p[x]$ denotes the probability of the corresponding record. Of course, in general, those states are not orthogonal for different measurement record.

In the following, it will be more convenient to keep trace of the probability of a given record in the norm of the state. We will thus introduce the non-normalized state

$$|\psi(t_f;[x])\rangle = \sqrt{p[x]}\, |\psi(t_f|[x])\rangle\,. \tag{4.8}$$

We will call it a state *joint* to the measurement $[x]$, by analogy with joint probabilities. One advantage is that it is then more compact to use expressions based on joint states. The other advantage will appear clearly in the following.

A natural question is to relate the trajectory vision to the reduced density matrix of the system. To do this, we simply forget the measurement record by averaging over the probability distributions of all the measurements results:

$$\begin{aligned} \rho_{\mathcal{S}}(t_f) &= \int p[x]\, |\psi(t_f|[x])\rangle\, \langle\psi(t_f|[x])|\, \mathcal{D}[x] \\ &= \int |\psi(t_f;[x])\rangle\, \langle\psi(t_f;[x])|\, \mathcal{D}[x]. \end{aligned} \tag{4.9}$$

Since the quantum trajectory method associates with each measurement record a pure quantum state for the system, it is natural to ask whether a Feynman path integral formulation exists for this state.

This question makes sense when the environment is initially prepared in a pure state. Then using the path integral expression for the full quantum state of the system and its environment, and decomposing the environmental states $|\mathcal{E}[\gamma]\rangle$ onto the measurement results basis, we obtain a path integral expression for the joint state of the system $|\psi(t_f;[x])\rangle$:

$$|\psi(t_f;[x])\rangle = \int \langle\gamma(t_i)|\psi(t_i)\rangle\ \mathcal{A}[\gamma]\ \langle[x]|\mathcal{E}[\gamma]\rangle\ |\gamma(t_f)\rangle\ \mathcal{D}[\gamma]. \tag{4.10}$$

Once again, this expression is a minimal modification of eq. (4.2), obtained for closed system. The only novelty is the factor $\langle[x]|\mathcal{E}[\gamma]\rangle$, which encodes alterations made to the dynamics of the system from measurement. The only effect of measuring on the environment is to introduce a linear filter within the path integral!

The scalar product $\langle[x]|\mathcal{E}[\gamma]\rangle$ has a modulus and a phase. The modulus part will select some classes of trajectories, potentially suppressing some paths. The phase will add up to the action, giving an new effective action for the system. This corresponds to the quantum backaction of the measurement in the system: its dynamics is modified depending on the measurement performed in the environment.

We can also derive expressions when the initial state is not pure, either for the environment or the system. In this case, it is possible to write down a path integral expression similar from eq. (4.5b), for what we call the joint density operator of the system:

$$\rho_{\mathcal{S}}(t_f;[x]) = \int \langle\gamma_+(t_i)|\rho_{\mathcal{S}}(t_i)|\gamma_-(t_i)\rangle \times \mathcal{A}[\gamma_+]\mathcal{A}^*[\gamma_-] \tag{4.11a}$$

$$\times\, \mathcal{F}[\gamma_+,\gamma_-;x]\ |\gamma_+(t_f)\rangle\langle\gamma_-(t_f)|\ \mathcal{D}[\gamma_+]\mathcal{D}[\gamma_-], \tag{4.11b}$$

where we have introduced $\mathcal{F}[\gamma_+,\gamma_-;x]$ the influence functional conditioned to measurement x, defined by

$$\mathcal{F}[\gamma_+,\gamma_-;x] = \langle[x]|U[\gamma_+]\rho_{\mathcal{E}}(t_i)U^\dagger[\gamma_-]|[x]\rangle\,. \tag{4.12}$$

As expected, summing up these functionals over all possible measurement records gives back the Feynman–Vernon influence functional.

Once again, the operator $\rho_{\mathcal{S}}(t_f;[x])$ is not trace-normalized. Its trace is nothing but the probability of the measurement record $[x]$. Of course,

it is possible to renormalize it and this leads to the reduced density operator for the system, conditioned or relative to the measurement $\rho_{\mathcal{S}}(t_f;[x]) = p[x]\rho_{\mathcal{S}}(t_f|[x])$.

4.2.2 Energy flows and Feynman path integral

Let us now introduce the two-time measurement protocol in the light of the path integral approach. The basic idea is to define quantum trajectories associated with a given heat exchanged Q. Namely, we ultimately want to access $p(Q) = \mathrm{tr}(\rho(t_f;Q))$. To this end, we need to compute the associated influence functional $\mathcal{F}[\gamma_+,\gamma_-;Q]$, since we can express the probability of a given heat as a trace, which is a double path integral

$$p(Q) = \int_{\gamma_+(t_f)=\gamma_-(t_f)} \langle\gamma_+(t_i)|\rho_{\mathcal{S}}|\gamma_-(t_i)\rangle \times \mathcal{A}[\gamma_+]\mathcal{A}^*[\gamma_-]\mathcal{F}[\gamma_+,\gamma_-;Q]\,\mathcal{D}[\gamma_+]\mathcal{D}[\gamma_-]. \tag{4.13}$$

A first remark is that there are many possible microscopic states for each Q. They arise from three different reasons. First, energy levels in the environment are generically degenerate, allowing to have two microscopic states with the same energy. Second, it is possible that two different microscopic configurations of the environment lead to the same energy by different arrangement of populations in the various energy levels. Finally, since the initial state is not pure in general (it would be a thermal state), it is possible to start from two different microscopic configurations that possess different energies, but that the exchanged energy with the system is the same in the end. In order to treat all those possibilities, we will first make them explicit and then average over them. This is made possible because we consider that the initial state for the environment is a thermal state, which is diagonal in the energy basis. This is an important assumption here, which justifies to call the energy exchanged "heat".

We will thus assume that the apparatus is able to measure the population in each non-degenerate energy level, effectively measuring the environment in its full energy eigenstate basis. For example, if we suppose that we have a continuum of bosonic modes, it would correspond to access to the number of bosons in each frequency mode (Fock basis). If we denote $\mathcal{N}_i$ the result of the first measure in the two-time measurement protocol, and $\mathcal{N}_f$ the second one, we can then compute the influence

functionals associated to the transition from $\mathcal{N}_i$ to $\mathcal{N}_f$:

$$\mathcal{F}[\gamma_+, \gamma_-; \mathcal{N}_i \to \mathcal{N}_f] = \langle \mathcal{N}_i | U^\dagger[\gamma_-] | \mathcal{N}_f \rangle \langle \mathcal{N}_f | U[\gamma_+] | \mathcal{N}_i \rangle , \tag{4.14}$$

where we suppose that the environment starts in $\mathcal{N}_i$. From this, we can compute the influence functional of a given energy exchange by summing the influence functional corresponding to all possibilities associated with this exchange. Starting from a situation in which energy levels are populated with probabilities $p_i[\mathcal{N}]$, the influence functional $\mathcal{F}[\gamma_+, \gamma_-; Q]$ is

$$\begin{aligned} \mathcal{F}[\gamma_+, \gamma_-; Q] = \int & p_i[\mathcal{N}_i] \mathcal{F}[\gamma_+, \gamma_-; \mathcal{N}_i \to \mathcal{N}_f] \\ & \times \delta(Q - (E[\mathcal{N}_f] - E[\mathcal{N}_i])) \, \mathcal{D}[\mathcal{N}_i] \mathcal{D}[\mathcal{N}_f], \end{aligned} \tag{4.15}$$

where $E[\mathcal{N}]$ is the energy associated to configuration $\mathcal{N}$.

Unfortunately, directly computing $\mathcal{F}[\gamma_+, \gamma_-; Q]$ is really hard. Instead, we will compute its Fourier transform along Q which would give us access to the generating function for the probability density function. This is why we will call the Fourier transform the generating functional of heat. Its expression is quite compact if the environment is in an equilibrium state at temperature $k_B T = 1/\beta$, at the initial time[2]:

$$\hat{\mathcal{F}}_{\text{eq}}(\gamma_+, \gamma_-; \lambda) = \int \mathrm{e}^{\mathrm{i}\lambda Q} \mathcal{F}_{\text{eq}}[\gamma_+, \gamma_-; Q] \, \mathrm{d}Q \tag{4.16a}$$

$$= \frac{1}{Z_\beta} \operatorname{tr} \left(\mathrm{e}^{\mathrm{i}\lambda H_\mathcal{E}} U[\gamma_+] \mathrm{e}^{-(\beta + \mathrm{i}\lambda) H_\mathcal{E}} U^\dagger[\gamma_-] \right) , \tag{4.16b}$$

where $H_\mathcal{E}$ is the Hamiltonian of the environment alone and Z_β denotes its equlibrium partition function at inverse temperature β.

Equation (4.16) is the best expression we can have in the general case with an environment initially prepared in a thermal state. Going beyond it requires using a specific model for the environment.

Harmonic bath linearly coupled to the system

Starting from now, we shall consider an environment built from uncoupled harmonic oscillators as in [Caldeira and Leggett, 1985] and [Feynman and Vernon, 1963]. Natural examples include phonon and photon baths

2. This is what we expect from a thermostat or energy reservoir. A key point is that to quantify heat, we need a reservoir prepared in a state that has no coherences in the energy basis.

but artificial systems can be designed to enforce a certain texture of the oscillator bath. For example, nanofabricated circuits can be manufactured so that it is possible to go from situations with a continuum of modes (that is the case in a transmission line) to situations where a single mode with quality factor up to 10^6 can be addressed [Frunzio et al., 2005]. As a matter of fact, most natural environments behave as harmonic baths [Weiss, 1999] except for nuclear spins in materials [Prokofev and Stamp, 2000] and specially manufactured mesoscopic systems such as non-linear transmission lines built from Josephson junctions which can exhibit strong non linearities [Bourassa et al., 2012; Weißl et al., 2015].

As such, we will consider a set of oscillators, that can be either finite or infinite, discrete or continuous. For simplicity, we shall use discrete notations, but there are no difficulties to take the continuum limit. We will thus consider that each oscillator is labelled by α, and possesses a frequency ω_α. A Fock state described by a record $\mathcal{N} = (n_\alpha)$, where n_α indicates the number of excitations in the oscillator α, would possess an energy

$$E[\mathcal{N}] = \hbar \sum_\alpha n_\alpha \omega_\alpha. \tag{4.17}$$

In order to define completely the environment we also need to choose the coupling between the system and each oscillator. In this section, we will consider the simplest form of coupling, which is the linear coupling between the system and the position of each oscillator. If we consider $x_\mathcal{S}$ as the operator associated to the observable we used to describe the trajectory γ of the system, and $a_\alpha, a_\alpha^\dagger$ the ladder operators for oscillator α, the interaction can be written as

$$H_{\text{int}} = \hbar \sum_\alpha g_\alpha x_\mathcal{S} (a_\alpha + a_\alpha^\dagger), \tag{4.18}$$

where $g_\alpha \in \mathbb{R}$ is the coupling constant between the system and oscillator α.

The fact that, system-wise, interaction only concerns $x_\mathcal{S}$, which is the observable on which the path is described, makes it easy to compute the evolution of oscillators associated to a particular path: we just have to replace $x_\mathcal{S}$ by its classical value $\gamma(t)$, to find the forced evolution operator. Furthermore, since we are looking for linear coupling between the system and oscillators, the evolution of oscillators is just a linearly-forced evolution. It is well known that this kind of evolution is just a displacement operator and a phase, that depends on the frequency of each oscillator and on the form of the forcing.

Since it is a very standard problem in quantum mechanics, we won't derive fully the expressions for the operator $U[\gamma]$ here. The reader can refer to [Le Bellac, 2003]. In the end, the evolution operator is given by:

$$U[\gamma] = \mathrm{e}^{\mathrm{i}\theta[\gamma]}\mathcal{D}(\Lambda[\gamma]), \tag{4.19}$$

where θ is a phase that depends on the path, and $\mathcal{D}(\Lambda[\gamma])$ is a multimode displacement operator. If we compute everything, and introduce the operator that displaces oscillator α by Λ_α, $D_\alpha(\Lambda_\alpha)$, we get:

$$\theta[\gamma] = \int_{t_i}^{t_f}\int_{t}^{t_f} \frac{\gamma(t)\gamma(t')}{2}\sum_\alpha g_\alpha^2 \sin\left(\omega_\alpha(t-t')\right)\,\mathrm{d}t'\mathrm{d}t, \tag{4.20a}$$

$$\mathcal{D}(\Lambda[\gamma]) = \bigotimes_\alpha D_\alpha(\Lambda_\alpha[\gamma]) \qquad \Lambda_\alpha[\gamma] = -\frac{\mathrm{i}}{\sqrt{2}}\int_{t_i}^{t_f} \mathrm{e}^{\mathrm{i}\omega_\alpha t}\gamma(t)\,\mathrm{d}t. \tag{4.20b}$$

From this, we can derive an expression for $\mathcal{F}_{\mathrm{eq}}$. Since this is a bit technical, we will skip the detail here, the interested reader can find them in appendix E.2. If we introduce $\bar{n}_\alpha$ the average number of bosons at the initial temperature T in the oscillator α, we have

$$\begin{aligned}
\hat{\mathcal{F}}_{\mathrm{eq}}[\gamma_+,\gamma_-;\lambda] &= \mathcal{F}_{FV,T}[\gamma_+,\gamma_-] && \text{(4.21a)}\\
&\times \prod_\alpha \exp\left((1+\bar{n}_\alpha)(\mathrm{e}^{\mathrm{i}\hbar\lambda\omega_\alpha}-1)\Lambda_\alpha[\gamma_+]\Lambda_\alpha^*[\gamma_-]\right) && \text{(4.21b)}\\
&\times \prod_\alpha \exp\left(\bar{n}_\alpha(\mathrm{e}^{-\mathrm{i}\hbar\lambda\omega_\alpha}-1)\Lambda_\alpha^*[\gamma_+]\Lambda_\alpha[\gamma_-]\right), && \text{(4.21c)}
\end{aligned}$$

where $\mathcal{F}_{FV,T}$ is the Feynman–Vernom functional at temperature T. Since it is what we find when no measurement record is kept, we recover it when $\lambda = 0$, which corresponds to averaging over all possible values of Q. It is "solely" a constant with respect to Q. However, it will play its usual role on the dynamics, influencing the probability density by affecting trajectories. Its expression is

$$\begin{aligned}
\mathcal{F}_{FV,T}[\gamma_+,\gamma_-] &= \mathrm{e}^{\mathrm{i}(\theta[\gamma_+]-\theta[\gamma_-])}\\
&\times \prod_\alpha \exp\left(-(1+2\bar{n}_\alpha)\left(|\Lambda_\alpha[\gamma_+]|^2+|\Lambda_\alpha[\gamma_-]|^2\right)/2\right)\\
&\times \exp\left((1+\bar{n}_\alpha)\Lambda_\alpha[\gamma_+]\Lambda_\alpha^*[\gamma_-]\right)\\
&\times \exp\left(\bar{n}_\alpha\Lambda_\alpha^*[\gamma_+]\Lambda_\alpha[\gamma_-]\right).
\end{aligned} \tag{4.22}$$

Of course, we have $\mathcal{F}_{FV,T}[\gamma,\gamma] = 1$.

Even though eq. (4.21) may seem complicated, it is still possible to understand the meaning of each of its factors. First, for each oscillator α, it is only possible to have energy exchange by integer multiples of $\hbar\omega_\alpha$. Thus, if we have a discrete number of modes, heat can take values only on a discrete set. Furthermore, contribution (4.21c) vanishes when $T = 0\,\mathrm{K}$, and can thus be attributed to absorption processes. Conversely, contribution (4.21b) can be attributed to emission processes. Quite interestingly, those contributions arise with factors $\bar{n}_\alpha$, reminding of absorption processes, and $\bar{n}_\alpha + 1$ reminding of the combination of stimulated and spontaneous emission processes.

Quantum Bremstrahlung within a cavity

Even though the result given in eq. (4.21) is, for itself, quite satisfactory, it seems that we are still a bit far from the probability distribution. As usual, we will specialize the model. But before we concentrate on the environment, let's simplify the dynamics of the system.

Here, we will consider a system that is constrained onto two quasiclassical paths, that arrive at the same spot. That is typical of a Mach–Zehnder interferometer or a two-slit experiment. Of course, due to Heisenberg principle, it is not possible to constrain the particle on an infinitely thin path. What we are doing is rather an effective description where there can be quantum fluctuations around a classical path, as pictured on fig. 4.4. What we suppose is that if the particle travels on one path, it will affect the environment in the same way, whatever the fluctuation nearby this path. Similarly, since we are nearby quasiclassical trajectories, we will suppose that the classical action is identical for each trajectory around the quasiclassical one.

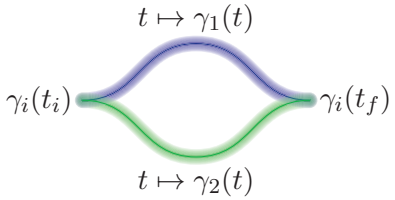

Figure 4.4: Clustering of trajectories γ in a gedanken two-path interferometry experiment: the source emits particles from the initial position $S = \gamma_{1,2}(t_i)$ which are detected at position $D = \gamma_{1,2}(t_f)$. Paths are clustered in two families $\gamma_{1,2}$.

We can then compute an effective amplitude, associated to all trajectories nearby γ_1 and γ_2. This amplitude $\mathcal{A}_{\text{eff}}[\gamma]$ will be proportional to the action, up to a non-zero complex number. We will decompose it as a modulus part, which will dictate the relative weight of each trajectory and a phase that will be an effective action. As such, we will have

$$\mathcal{A}_{\text{eff}}[\gamma_i] = \sqrt{\frac{p_i}{\mathfrak{N}}} \mathrm{e}^{\mathrm{i}S_{\text{eff},i}/\hbar} \qquad i \in \{1,2\}, \tag{4.23}$$

with $p_1 + p_2 = 1$, the normalized weights for each trajectory, $\mathfrak{N}$ being a normalization factor ensuring that the resulting state is normalized. Its expression is

$$\mathfrak{N} = 1 + 2\sqrt{p_1 p_2}\, \Re\left(\mathrm{e}^{\mathrm{i}\Delta S_{\text{eff}}/\hbar} \mathcal{F}_{FV,T}[\gamma_1, \gamma_2]\right), \tag{4.24}$$

where we introduced the difference of action between the two quasiclassical trajectories

$$\Delta S_{\text{eff}} = S_{\text{eff},1} - S_{\text{eff},2}. \tag{4.25}$$

Now that we have simplified the dynamics for the system, let's take some care about the environment. We will consider here the simplest possible environment, which is a single harmonic oscillator, at frequency ω. This implies that energy exchange will happen at integer multiple of $\hbar\omega$. It is also simpler to express the amplitude of the displacement induced by the system when it follows a given trajectory, by splitting the energy of the displacement and its phase. Thus, we will introduce for each trajectory $i \in \{1,2\}$:

$$\Lambda[\gamma_i] = \sqrt{N_i} \mathrm{e}^{\mathrm{i}\phi_i}, \tag{4.26}$$

where N_i would be the average photon number after the system has followed path γ_i if we started with the environment in the vacuum, and ϕ_i would be the average phase. Since there are no absolute phase reference, we will look at relative phase between one path and one another. To this end, we introduce the following notations

$$\Delta\theta = \theta[\gamma_1] - \theta[\gamma_2] \qquad \Delta\phi = \phi_1 - \phi_2. \tag{4.27}$$

We refer the reader to appendix E.3 for the computation giving the result. What we will do here is to decompose the probability of a given heat into two contributions: a first that comes from classical paths, $\gamma_+ = \gamma_-$, and another that comes from interfering quantum paths, $\gamma_+ \neq \gamma_-$. Of

course, the total probability will be the sum $p(Q) = p_{\rm cl}(Q) + p_{\rm qu}(Q)$. The classical contribution reads

$$p_{\rm cl}(Q) = \frac{1}{\mathfrak{N}} \sum_{i\in\{1,2\}} p_i f\left(\frac{Q}{\hbar\omega}; N_i(1+\bar{n}), N_i\bar{n}\right), \tag{4.28}$$

where $f(n; x, y)$ is the Skellam law of parameters (x, y) (see appendix E.3). It corresponds to the probability distribution associated to a random variable $Z = X - Y$, where X and Y follow Poisson laws of average x and y respectively. It is thus possible to understand it, for a given trajectory γ_i, as the convolution of emission events with an average $N_i(1+\bar{n})$ and of absorption events, with an average $N_i\bar{n}$. If we start at zero temperature, we recover a Poisson distribution of parameter N_i, for each trajectory, which accounts for the statistics of a coherent state. Since here we consider classical couples of trajectories, we just have to sum up each distribution, weighted by its probability.

We can also look at the part of the probability distribution arising from non-classical couples of trajectories:

$$\begin{aligned} p_{\rm qu}(Q) = {} & 2\frac{\sqrt{p_1 p_2}}{\mathfrak{N}} \mathrm{e}^{-(1+2\bar{n})(\sqrt{N_1}-\sqrt{N_2})^2/2} \\ & \times \cos\left(\frac{\Delta S_{\rm eff}}{\hbar} + \Delta\theta + \frac{Q}{\hbar\omega}\Delta\phi\right) \\ & \times f\left(\frac{Q}{\hbar\omega}; \sqrt{N_1 N_2}(1+\bar{n}), \sqrt{N_1 N_2}\bar{n}\right). \end{aligned} \tag{4.29}$$

We again find a Skellam law, whose parameters are the geometric means of the parameters for each classical trajectory. More than that, there are two interesting factors. First, there is a cosine oscillation. This oscillation is of course, a trace of quantum interference between two paths. That is the trace we want to look at to prove coherent behavior between the two paths. There is also an attenuation factor, that is exponential in the number of thermal excitations as well as in the difference of energy in the driving. It means that if the driving gives different average energy for two trajectories, there will be an exponential suppression of the interference contrast as the average number of thermal excitation increases.

However, we can completely cancel this factor if the driving gives the same average energy for two trajectories. Physically, it is expected, since we are measuring everything in the energy basis. Information about the trajectory of the system would be, in this case, completely encoded into the phase of the oscillator, which is inaccessible from energy

measurement. In other words, it would be completely impossible to say which trajectory was chosen by the system from an energy measurement in this case, conserving completely the coherences. Obviously, this situation would correspond to $N = N_1 = N_2$. We can further simplify and imagine that each path is followed with the same statistical weight, giving $p_1 = p_2 = 1/2$. That would be the case, for example, with a perfectly balanced beam splitter. In this case, the probability to obtain a given heat would be

$$\begin{aligned} p(Q) = \frac{1}{\mathfrak{N}} f\left(\frac{Q}{\hbar\omega}; N(1+\bar{n}), N\bar{n}\right) \\ \times \left(1 + \cos\left(\frac{\Delta S_{\text{eff}}}{\hbar} + \Delta\theta + \frac{Q}{\hbar\omega}\Delta\phi\right)\right). \end{aligned} \tag{4.30}$$

This is a Skellam law modulated by a cosine, as can be seen on fig. 4.5. The Skellam law parameters are fully determined by initial temperature and the energy of the driving. By contrast, the speed of the modulation is determined by the phase difference of the coherent states. Two extreme cases would be $\Delta\phi = 0$, in which the two states in the environment would be completely indistinguishable. In this case, the modulation completely disappears, since $Q/\hbar\omega$ must be an integer. On the other hand, if the phase between two coherent states is $\Delta\phi = \pi$, as depicted on fig. 4.5, it is possible to have a completely different situation for different dephasing $\Delta S/\hbar + \Delta\theta$. If this phase is 0 or π, there will be a blocking of half of the possible emission, leading to $Q/\hbar\omega$ being either even or odd. By contrast, if the phase determined by $\Delta S/\hbar + \Delta\theta$ is $\pm\pi/2$, there are no modulation, despite the fact that the quantum coherence is fully preserved in the environment for different trajectories.

4.3 Energy flows in electronic systems

In this section, we just derive expression for the energy flow in one dimensional ballistic conductors. Such results are not really new but the visit of M. Moskalets has incited us to clarify these notions for our future work. Previous studies on these questions may be found in [Battista et al., 2013; Ludovico et al., 2014; Battista et al., 2014; Moskalets, 2014a; Ludovico et al., 2016].

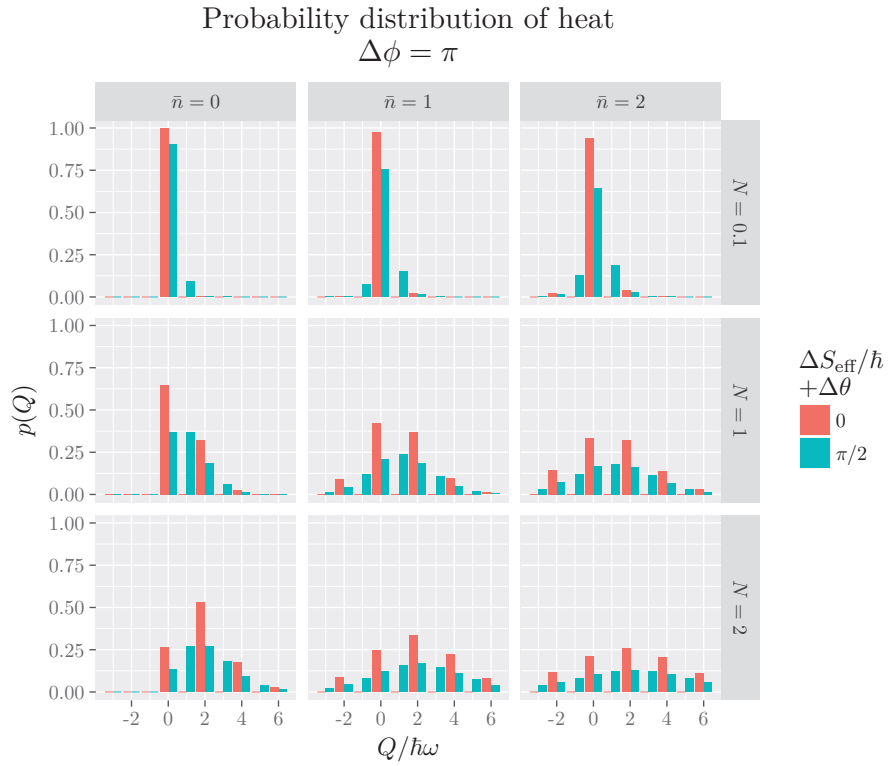

Figure 4.5: Probability distributions for the number of quanta emitted in as a function of the thermal photon number $\bar{n}$ and of the number N of photons emitted along a single trajectory of fig. 4.4.

4.3.1 One-dimensional non-relativistic free fermions

Let us consider a Fermi gas of non-relativistic fermions in an external time-dependent potential $U(x,t)$ whose Hamiltonian is expressed in terms of fermionic creation and annihilation operators $\psi(x,t)$ and $\psi^\dagger(x,t)$:

$$H_{\rm kin} = \frac{\hbar^2}{2m}\int (\partial_x\psi^\dagger)(x)\,(\partial_x\psi)(x)\,\mathrm{d}x, \tag{4.31a}$$

$$H_{\rm pot} = \int U(x,t)\,(\psi^\dagger\psi)(x)\,\mathrm{d}x. \tag{4.31b}$$

The operator $\mathcal{E}_{x_1,x_2}$ representing the energy of the system between two positions $x_1 < x_2$ is given by the same expressions as above with integrals limited to the $[x_1,x_2]$ interval. Using Heisenberg equations of motion for ψ and $\psi^\dagger$, the derivative of this operator can be written as:

$$\frac{\mathrm{d}\mathcal{E}_{x_1,x_2}(t)}{\mathrm{d}t} = \int_{x_1}^{x_2} (\partial_t U)(x,t)(\psi^\dagger\psi)(x,t)\,\mathrm{d}t \tag{4.32a}$$

$$- \int_{x_1}^{x_2} \frac{\mathrm{i}\hbar}{2m}\,\partial_x\Big((\partial_x\psi^\dagger)\psi - \psi^\dagger(\partial_x\psi)\Big)(x,t)\,U(x,t)\,\mathrm{d}x \tag{4.32b}$$

$$- \int_{x_1}^{x_2} \partial_x\left(J_{\rm kin}(x,t)\right)\,\mathrm{d}x, \tag{4.32c}$$

where the kinetic energy current is given by

$$J_{\rm kin}(x,t) = \frac{\mathrm{i}\hbar^3}{4m^2}\Big((\partial_x^2\psi^\dagger)(\partial_x\psi) - (\partial_x\psi^\dagger)(\partial_x^2\psi)\Big)(x,t). \tag{4.33}$$

The right-hand side of eq. (4.32a) is associated with varying the external potential, which justifies calling it an external work contribution, whereas the remaining terms represent the variation associated with the kinetic and potential energy flows. One recognizes eq. (4.32b) as $U(x,t)j_P(x,t)$ where

$$j_P(x,t) = \frac{\mathrm{i}\hbar}{2m}\Big((\partial_x\psi^\dagger)\psi - \psi^\dagger(\partial_x\psi)\Big)(x,t) \tag{4.34}$$

denotes the particule current. Finally, the kinetic energy contribution to the variation of $\mathcal{E}_{x_1,x_2}$ is expressed as the divergence of the kinetic energy current given by eq. (4.33). When the external potential is uniform but time dependent, then the energy variation decomposes into the work contribution (right-hand side of eq. (4.32a)) and a total energy current flow

$$J_E(x,t) = J_{\rm kin}(x,t) + U(t)\,j_P(x,t). \tag{4.35}$$

4.3.2 Chiral fermions: expansion near k_F

Let us now consider a 1D fermion system whose ground state is a filled Fermi sea up to momentum k_F. We want to consider how excitations with momentum $k = k_F + q$ where $|q| \ll k_F$, that is excitations close to one of the Fermi points, contribute to the energy flow. They are the right-moving slow fermionic modes described the operator $\psi_R(x)$ such that

$$\psi(x) = \mathrm{e}^{\mathrm{i}k_F x}\psi_R(x). \tag{4.36}$$

The Fermi energy is then given by $E_K = \hbar^2 k_F^2/2m$ and the Fermi velocity is $v_F = \hbar k_F/m$. For fermionic excitations of momentum close to $\hbar k_F$, the single-particle energy is $E(k_F + q) = E_F + \hbar v_F q + \mathcal{O}((q/k_F)^2$ showing that $(q/k_F)^2$ is the small parameter measuring deviation to the linear dispersion relation $E(k_F+q) = E_F+\hbar v_F q$. We shall now compute the main contributions to particle and energy currents associated with electronic excitations close to the Fermi level.

Let us start with the particle current given by eq. (4.34) which then becomes

$$j_P(x,t) = v_F(\psi_R^\dagger\psi_R)(x,t) \tag{4.37a}$$

$$+ \frac{\mathrm{i}v_F}{2k_F}\left((\partial_x\psi_R^\dagger)\psi_R - \psi_R^\dagger(\partial_x\psi_R)\right)(x). \tag{4.37b}$$

Note that the second term is subdominant with respect to the first one, being scaled down by a factor $|q|/k_F \ll 1$.

We now turn to the kinetic energy current $J_{\mathrm{kin}}(x)$ defined by eq. (4.33). We find that:

$$J_{\mathrm{kin}}(x) = v_F E_F\,(\psi_R^\dagger\psi_R)(x) \tag{4.38a}$$

$$+ v_F\,\frac{\mathrm{i}\hbar v_F}{2}\left((\partial_x\psi_R^\dagger)\psi_R - \psi_R^\dagger(\partial_x\psi_R)\right)(x) \tag{4.38b}$$

$$+ v_F\frac{E_F}{2k_F^2}\left((\partial_x^2\psi_R^\dagger)\psi_R + \psi_R^\dagger(\partial_x^2\psi_R) - 4(\partial_x\psi_R^\dagger)(\partial_x\psi_R)\right)(x) \tag{4.38c}$$

$$+ v_F\frac{\mathrm{i}E_F}{2k_F^3}\left((\partial_x^2\psi_R^\dagger)(\partial_x\psi_R) - (\partial_x\psi_E^\dagger)(\partial_x^2\psi_R)\right)(x). \tag{4.38d}$$

The first term corresponds to the Fermi energy carried by each particle and, not surprisingly, this is the main contribution to the kinetic energy current. The second term arises from the linear dispersion relation:

although a particle with momentum $k = k_F + q$ has, in this linear dispersion approximation, a constant velocity v_F, its energy differs from E_F by $\varepsilon(q) = \hbar v_F q$. The third and fourth terms are subdominant with respect to the second one and arise from deviations to the linear dispersion relation.

In the following, we will consider a reference situation where a Fermi sea is present. The confinement potential of the electrons should then be taken into account but within the bulk of the material, it would only contribute to the change of $\mathcal{E}_{x_1,x_2}$ through the term $-U(t)\,\partial_x(j_P(x,t))$. In a stationary situation, the total energy current given by the sum of this contribution and of the kinetic energy current (see eq. (4.35)). Using the expansion of the particle current eq. (4.37), the part due to the potential energy thus adds to the first two terms given by eqs. (4.38a) and (4.38b). It will thus contribute to a redefinition of the Fermi energy that takes into account the confinement potential which defined the bottom of the electron band and to a redefinition of the Fermi velocity. The modification of the Fermi velocity is of order $U/\hbar v_F k_F$ which is a small correction and thus will be neglected.

In the end, keeping only terms of the first order in q/k_F, we find that the energy current in the 1D chiral edge channel is of the form

$$J_E(x) = v_F \frac{\mathrm{i}\hbar v_F}{2}\left((\partial_x\psi_R^\dagger)\psi_R - \psi_R^\dagger(\partial_x\psi_R)\right)(x) \tag{4.39a}$$

$$+ v_F(E_F + U(t))(\psi_R^\dagger\psi_R)(x). \tag{4.39b}$$

Note that this contains the contribution of the whole Fermi level. In the following, we will redefine origins of energies so that E_F is taken to zero. The potential being present in eq. (4.39), the effect of a change of the electric potential of the 1D chiral channel is still taken into account.

4.3.3 Energy current, electronic coherences and edge magnetoplasmons

Let us now focus on the average of the total energy current (4.39) for $E_F = 0$, in the absence of an electric potential applied to the conductor ($U(t) = 0$) and relate it to single-electron coherence. By doing so, we will connect the electronic coherence properties to the heat transport. Moreover, we will derive the corresponding expression in the bosonization formalism.

Average energy current from electronic coherence

The average of the energy current $J_E(t)$ is then nothing but

$$\langle J_E(x,t)\rangle_\rho = \mathrm{i}\hbar v_F \partial_\tau \left(\mathcal{G}^{(e)}_{\rho,x}\left(t+\frac{\tau}{2}, t-\frac{\tau}{2}\right)\right)_{\tau=0}. \tag{4.40}$$

Of course, this already contains the infinite contribution of the Fermi sea. As usual, the expression is regularized by taking the normal ordering with respect of the chemical potential $\mu = 0$ within the edge channel and expressing the single-electron coherence in terms of the electronic Wigner function $W^{(e)}(t,\omega)$, we find the average excess energy current:

$$\langle j_{\mathrm{H}}(x,t)\rangle_\rho = \int_{-\infty}^{+\infty} \hbar\omega\, \Delta_0 W^{(e)}_{\rho,x}(t,\omega)\, \frac{d\omega}{2\pi}, \tag{4.41}$$

in which Δ_0 denotes the excess contribution with respect to the reference state $|F_{\mu=0}\rangle$. The average excess energy current thus appears as the "average" single-particle energy over the quasi-probability distribution given by the excess Wigner function at time t.

Electrochemical energy versus heat

Let us now consider a 1D chiral edge channel at zero temperature connected to an electron reservoir at a possibly non-zero chemical potential μ. According to eq. (4.41) there is a non-zero energy current compared to $\mu = 0$. It is given by

$$j_E^{(\mathrm{ech})}(\mu) = \frac{\mu^2}{2h}. \tag{4.42}$$

This is called the electrochemical energy current since it is due to the shift of the electrochemical potential. Note that it does not correspond to heat: no thermal excitations have been generated, since the many-body state $|F_\mu\rangle$ is pure.

When dealing with a general many-body state ρ of the electron fluid, the energy current at position x can thus be decomposed in two distinct contributions. The first one, $j_E^{(\mathrm{ech})}(\mu(x))$ is the electrochemical energy current associated with the local chemical potential $\mu(x)$ at position x. The second one corresponds to the average energy of all the excitations present in the fluid:

$$\langle j_E(x,t)\rangle_\rho = j^{(\mathrm{ech})}(\mu(x)) + j_H(x,t). \tag{4.43}$$

Since the states ρ viewed at position x and $|F\rangle_{\mu(x)}$ correspond to the same superselection sector in terms of total fermion number, the heat current is only due to electron/hole pairs with respect to the chemical potential $\mu(x)$.

Edge magnetoplasmons and heat flow

In the bosonization technique, the edge-magnetoplasmon operators $b(\omega)$ and $b^\dagger(\omega)$ are precisely the ones that generate all the excitations over each superselected vacuum. It is thus natural to discuss the heat current in term of these operators. Although expression eq. (4.40) is true on average, it suggests to consider the operator product[3]

$$O(t,\tau) = \psi^\dagger\left(t - \frac{\tau}{2}\right)\psi\left(t + \frac{\tau}{2}\right), \tag{4.44}$$

whose expansion, at first order in τ is

$$O(t,\tau) = \psi^\dagger(t)\psi(t) + \frac{1}{2}\left(\psi^\dagger(\partial_t\psi) - (\partial_t\psi^\dagger)\psi)\right)(t) + \mathcal{O}(\tau^2). \tag{4.45}$$

We can then consider the operator product $O(t,\tau)$ and use the expression of fermionic fields in terms of the bosonic field defined by eq. (3.47). This leads to the following expression for the heat current operator in terms of the electrical current:

$$j_h(x,t) = \frac{h}{2e^2}\ \ddagger i(x,t)^2\ddagger, \tag{4.46}$$

where $\ddagger A\ddagger$ denotes bosonic normal ordering of operator A. Interestingly, we recover the relaxation resistance of a single coherent electronic channel $R_q = h/2e^2$. Since edge magnetoplasmons describe the excitations that carry the heat flow, I conjecture that there is an interesting relation between quantum optics of noise discussed in section 3.3 and statistical properties of heat flow. Since its exploration is still underway, I will not elaborate further on this topic but instead describe my work on the determination of the statistics of dissipated heat in quantum conductors.

4.4 Joule heating in quantum conductors

In a classical macroscopic conductor, Joule heating arises from the inelastic processes within the conductor: electrons injected through the

3. Here we drop the x coordinate for simplicity.

lead experience inelastic collisions which lead to an energy cascade from the electronic degrees of freedom to the acoustic phonon and the resulting heating generates photons as in incandescence bulbs. Any description of Joule heating must include a coupling of the electronic degrees of freedom to environmental degrees of freedom within the conductor.

On the other hand, in a quantum conductor, electron delocalization implies that the electronic transport properties of a quantum conductor cannot easily be decomposed into contact and bulk properties. For example, the d.c. conductance of a clean ballistic single channel quantum wire is e^2/h regardless of interactions because of contact resistances [Safi and Schulz, 1995a]. One should thus expect that, in the absence of couplings to external dynamical degrees of freedom, dissipation in quantum conductors occurs within the electronic reservoir, i.e. at the contacts. This explains why dissipation in an ideal 1D quantum wire is given by the quantum of resistance $R_K = h/e^2$ even in the presence of interactions [Safi and Schulz, 1995a; Safi, 1997]. This corresponds to the series addition of two contact resistances $h/2e^2$ for a single coherent channel. In quantum Hall experiments, the fact that dissipation occurs at the contacts has been beautifully confirmed by direct imaging [Klass et al., 1990].

Nevertheless, ballistic quantum conductors may not be totally isolated from external degrees of freedom: energy may be dissipated through electron/phonon coupling and moreover, at finite frequency, through capacitive couplings to nearby conductors which may provide dissipation channels. We could thus expect a remote Joule heating effect: the quantum conductor itself would not heat because there would be no local dissipation within it but energy would be dissipated within a nearby part of the device capacitively coupled to it. This effect has been evidenced in carbon nanotubes in the ballistic regime [Baloch et al., 2012].

Modeling Joule heating in quantum conductors therefore requires to take into account both mechanisms. This section is organized as follows: a simple model for Joule heating that encapsulates both aspects is introduced in section 4.4.1. The probability density function (p.d.f.) for dissipated heat is obtained in full generality. We shall also present the $\nu = 2$ edge channel system as a simple illustration of our general model used to discuss our results. The case of time-dependent current pulses generated by a classical drive will be discussed in section 4.4.2, starting first by a simple a.c. drive and moving forward to Lorentzian current pulses which in particular, involve the Leviton excitation. Section 4.4.3

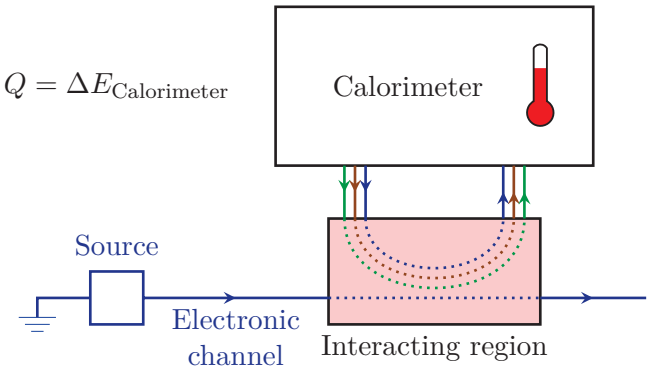

Figure 4.6: An electronic source emits electronic excitations into an edge channel coupled to environmental degrees of freedom with an interaction region. One measures the energy change of the environmental degrees of freedom through single-shot calorimetry. The interaction region is described by an elastic scattering matrix between edge magnetoplasmons and environmental modes. Electrons cannot tunnel from the edge channel to the environment.

then discusses the p.d.f. of the heat generated by an arbitrary single-electron excitation.

4.4.1 Scattering theory approach to the Joule heating

We consider a simple model for Joule heating involving one chiral electronic 1D edge channel coupled to environmental modes represented as incoming and outgoing harmonic channels (see fig. 4.6). The edge channel interacts with the environmental modes within and interaction region of finite size l and a linear coupling is assumed between the environmental modes and the edge-channel edge magnetoplasmons as in chapter 3.

Part of the energy injected by the electronic source will then be transfered to these environmental modes which could be acoustic phonon modes but also other linear modes corresponding to the electromagnetic environment of the edge channels or, in the $\nu = 2$ quantum Hall edge channel system, edge-magnetoplasmon modes of the second edge channel. As discussed in the previous chapter, the bosonization formalism provides the proper framework for discussing the dynamics of such a system.

As stressed before, understanding Joule heating for a quantum conductor also requires to understand the energy dissipated into the contact

when the electronic flow reenters it. Dealing with quantum Hall edge channels, the situation is different depending whether we are dealing with a two-terminal or four-terminal geometry (see figs. 4.7 and 4.8).

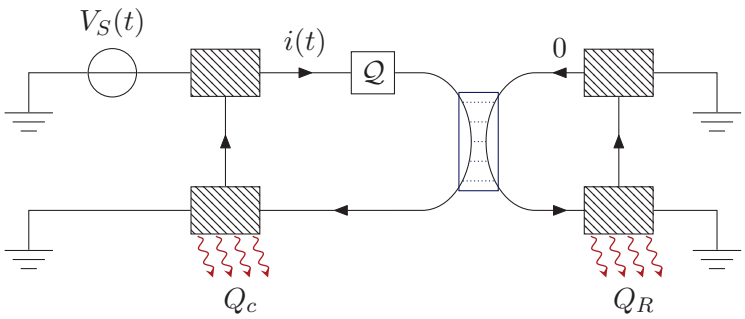

Figure 4.7: Four-terminal geometry. The quantum electronic source is decomposed into a driven Ohmic contact generating the average time-dependent current $\langle i(t)\rangle_{\rho_S}$ and a quantum device $\mathcal{Q}$ generating the non-trivial quantum fluctuations of the current at all order that characterize the edge-magnetoplasmon state ρ_S. The finite-frequency average current $\langle i(\omega)\rangle_{\rho_S}$ entering the interaction region is linearly related to the drive $V_S(t)$ by $\langle i(\omega)\rangle_{\rho_S} = (e^2/h)\, V_S(\omega)$. When considering classical sources, the quantum device $\mathcal{Q}$ is not present. Each outgoing modes reenter a contact at equilibrium at the same temperature and chemical potential.

The simplest case is the one of the four-terminal geometry: the electronic source sends excitations onto an elastic frequency-dependent beam splitter which partitions the incoming flow of edge magnetoplasmons into an outgoing channel and environmental channels. The energy of these outgoing edge magnetoplasmons is then dissipated into the contact.

The case of the two-terminal geometry (see fig. 4.8) is more subtle since, in the a.c. Joule heating, the contact is itself driven by a time-dependent potential $V_S(t)$. Therefore, the electrons entering the Ohmic contact see a time-dependent electric field. Thinking in classical terms, this electric field will perform work on the incoming current flow and that makes the energy balance at the contact more subtle: due to the time-dependent electric field, only part of the incoming energy will be transfered to the phonon modes into the contact.

Describing the dissipation within a driven Ohmic contact seems to be a highly non-trivial problem. However, in this case, gauge invariance provides us a way to bypass a microscopic modeling of dissipation within

the driven contact. Dissipation within the contact being local, a gauge transformation can be applied to neutralize the time-dependent potential of the contact locally. Such a gauge transformation acts on the many-body state entering the contact as a many-body unitary transformation[4]. Since the physics is locally gauge invariant, we just have to study energy dissipation for the corresponding gauge-transformed many-body state into an undriven contact which, in principle, could be done.

The natural and crucial question is now to extend this line of reasoning beyond the case of a simple a.c. drive, for example, to the case of a quantum electron flow generated by the mesoscopic capacitor in the ideal single-electron source regime [Fève et al., 2007]. It requires a careful understanding of a quantum electronic source in terms of edge magnetoplasmons. For simplicity, we shall assume that the source does not change the chemical potential (no d.c. bias) so that it really emits edge magnetoplasmons on top of the reference Fermi sea $|F_{\mu=0}\rangle$. Such a source generates a time-dependent current $\langle i(t)\rangle_S$ whose time average is zero. A time-dependent voltage drive $V_S(t) = R_K\langle i(t)\rangle_S$ reproduces the same average current but not its higher moments. This is the main difficulty and, it seems difficult to imagine that the Ohmic contact is driven in a quantum way.

This is where our theorist ansatz comes into play. It is conceptually natural to represent an arbitrary electronic source as a two-stage device composed, first, of a time-dependent voltage drive $V_S(t)$ which generates a classical edge-magnetoplasmon state carrying the average current $\langle i(t)\rangle_S$ and second of a quantum device generating all the non trivial higher order momenta while keeping the same average current. This fictitious arrangement depicted on fig. 4.8 enables us to discuss the heat dissipated within the contact in the presence of an arbitrary quantum electronic source such as the mesoscopic capacitor while keeping the dipole arrangement by giving a clear prescription on the partitioning of the reentering energy flow between work and heat.

Note that, even for a classical current, the work is brought through the transmission line driving the contact. It makes no sense to study its probability since a classical drive $V_S(t)$ generates a coherent state which is a quantum state with coherences between eigen-energy states of the electromagnetic field.

4. In the edge-magnetoplasmon language, it is nothing but a displacement operator for all the edge-magnetoplasmon modes corresponding to the time-dependent potential $-eV(t)$.

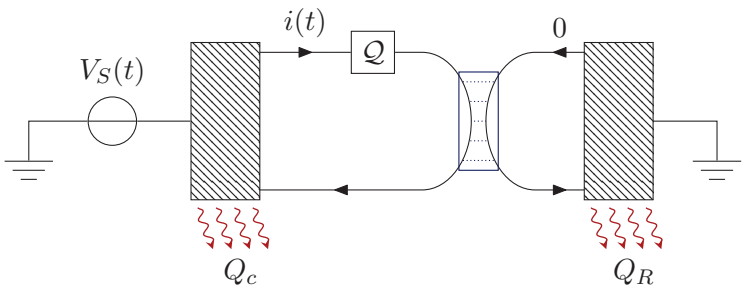

Figure 4.8: Two-terminal geometry: The effective RC circuit obtained from the setup depicted in fig. 4.6. The quantum electronic source is decomposed into a driven Ohmic contact generating the average time-dependent current $\langle i(t)\rangle_{\rho_S}$ and a quantum device $\mathcal{Q}$ generating the non-trivial quantum fluctuations of the current at all order that characterize the edge-magnetoplasmon state ρ_S. The finite-frequency average current $\langle i(\omega)\rangle_{\rho_S}$ entering the interaction region is linearly related to the drive $V_S(t)$ by $\langle i(\omega)\rangle_{\rho_S} = (e^2/h)\, V_S(\omega)$. When considering classical sources, the quantum device $\mathcal{Q}$ is not present.

The quantum device $\mathcal{Q}$ depicted on fig. 4.8 plays a crucial role in generating the single-electron excitation. It is an active device which is also driven in a coherent way. Note that for the LPA source, what would play the role of $\mathcal{Q}$ would be the mesoscopic capacitor preceded by a capacitive coupling to another transmission line whose purpose is to displace back the edge-magnetoplasmon coherent state with average current $\langle i(t)\rangle_S$ onto the edge-magnetoplasmon vacuum state.

Dissipated heat

Let us now obtain general expressions for the generating functions for the p.d.f. of the heat dissipated in the external environment (extrinsic dissipation) and for the heat dissipated into the contact (contact dissipation). We shall first start with the heat dissipated into the environment since it could be accessed experimentally by a calorimetric measurement of the environmental channels and we will then discuss the generating function for both the dissipated heat into the environment and into the contact.

Extrinsic dissipation Heat dissipated into the environment corresponds to the energy change of the environmental modes: the incoming modes are prepared in a thermal state at temperature T_R which is a statistical mixture of the reservoir eigenstates $|N_i\rangle$ indexed by their occupation numbers $N_i = (N_i(\mu,\omega))_{\mu,\omega}$ where μ labels the environmental channels at frequency ω. The extrinsic heat Q_R is thus defined as the energy change of the environmental modes, in a scattering theory version of the two-time measurement [Esposito et al., 2009]: it is the difference of the incoming and outgoing energies of the environmental modes $\Delta E_R = E[N_f] - E[N_f]$ where $E[N] = \sum_{\mu,\omega} \hbar\omega N(\mu,\omega)$. In the following, we shall denote by H_R the Hamiltonian for the environmental modes which is expressed in term of the creation and destruction operators as:

$$H_R = \sum_{\mu,\omega} \hbar\omega \, a_\mu(\omega)^\dagger a_\mu(\omega). \tag{4.47}$$

Contact dissipation Let us now turn to the energy dissipated within the contact. In the dipole representation of the system depicted on fig. 4.8, the outgoing excitations of the edge channel are sent back into the contact driven by the time-dependent voltage $V_S(t)$ which depends on the characteristics of the source. As explained before, heat dissipation within a driven contact is identical to heat dissipation within an undriven contact from a many-body state $\rho'_{\rm back}$ obtained by applying the gauge transformation neutralizing the applied potential $V_S(t)$. This gauge transformation is described by a displacement operator of parameter $\Lambda_S(\omega) = \langle i(\omega)\rangle_S / e\sqrt{\omega}$ $(\omega > 0)$ where $\langle i(\omega)\rangle_S$ denotes the finite-frequency average current emitted by the source S.

For an edge channel at zero temperature, the dissipated heat Q_c corresponds to the result of an energy measurement on the plasmonic many-body state $\rho'_{\rm back}$. This edge-magnetoplasmon energy operator is $H_0 = \sum_\omega \hbar\omega b^\dagger_{\rm out}(\omega) b_{\rm out}(\omega)$ where the $b_{\rm out}$ operators correspond to the outgoing edge-magnetoplasmon modes with respect to the interaction region.

Dissipated heat characteristic function

We can now compute the generating function for the p.d.f. for the extrinsic heat Q_R and the heat Q_c dissipated within the contact as defined in the previous paragraphs. Because of their definitions from two-point measurements of the H_R and H_0 operators, the generating function is

expressed in terms of the incoming state ρ_S of the edge channel and of $\mathbb{S}$ the scattering operator acting on the full Hilbert space of all many-body states of the system:

$$P(\lambda_c, \lambda_R|\rho_S, T_R) = \mathrm{tr}\left(\mathrm{e}^{\mathrm{i}(\lambda_R H_R + \lambda_c H_e)/2} D_b[\Lambda_S]\, \mathbb{S} \left[\rho_S \otimes \frac{e^{-H_R(\beta_R - \mathrm{i}\lambda_R)}}{Z_{\beta_R}} \right] \mathbb{S}^\dagger\, D_b[-\Lambda_S]\, \mathrm{e}^{\mathrm{i}(\lambda_R H_R + \lambda_c H_e)/2} \right), \tag{4.48}$$

where, in this expression Z_{β_R} denotes the partition function of the reservoir at temperature $k_B T_R = 1/\beta_R$. Note that the incoming many-body state in the edge channel also appears via Λ_S which is related to the average current generated by the electronic source.

Ignoring what happens within the contact corresponds to $\lambda_c = 0$ and gives the generating function for the p.d.f. of the heat Q_R exchanged from the edge channel to the environment.

The next step is to rewrite the expression in a suitable way allowing the evaluation of $\hat{P}(\lambda_c, \lambda_R|\rho_S, T_R)$ and the corresponding p.d.f. $P(Q_c, Q_R|\rho_S, T_R)$ for physically relevant states in the context of quantum coherent nanoelectronics. A first class of states is obtained by considering that the edge channel is driven by a classical voltage drive, in which case, ρ_S is a displaced state of the edge-magnetoplasmon modes. This corresponds to the usual a.c. Joule heating.

Another important class of states are the ones generated by an ideal single-electron source. As explained in chapter 3, they are described as quantum superpositions of coherent states of edge magnetoplasmons. More generally, eq. (4.48) could be used to discuss any superposition of coherent edge-magnetoplasmon states and thereby an arbitrary n-electron state (Slater determinant) of electronic excitations on top of the Fermi sea. These considerations strongly suggest to use a coherent state representation for both the edge magnetoplasmons and the environmental modes in order to rewrite $\hat{P}(\lambda_c, \lambda_R|\rho_S, T_R)$ under a suitable form for explicit computations as well as physical discussion.

Zero temperature expressions

When both the edge channel and the environment are at zero temperature, eq. (4.48) can be simplified using the unitarity of the scattering matrix S as well as the commutation relations of the many-body scattering matrix with the displacement operators. This leads to a more compact expression for the characteristic function of the p.d.f. of Q_c and Q_R:

$$\begin{aligned}\hat{P}(\lambda_c,\lambda_R|\rho_S) = \int \mathrm{d}y_+\,\mathrm{d}y_-\,\rho_S(y_+,y_-)\langle\Lambda(y_-)|\Lambda(y_+)\rangle \\ \times \exp\Big((r\cdot\Lambda(y_-))^\dagger(\mathrm{e}^{\mathrm{i}\hbar\omega\lambda_R}-1)\,(r\cdot\Lambda(y_+))\Big) \\ \times \exp\Big((t\cdot\Lambda(y_-)-\Lambda_S)^*(\mathrm{e}^{\mathrm{i}\hbar\omega\lambda_c}-1)(t\cdot\Lambda(y_+)-\Lambda_S)\Big)\,.\end{aligned} \tag{4.49}$$

This expression shows that, at zero temperature, energy can only flow into the environment and into the contact since only positive powers of $\mathrm{e}^{\mathrm{i}\hbar\omega\lambda_c}$ and $\mathrm{e}^{\mathrm{i}\hbar\omega\lambda_R}$ appear. Note that, the generating functional for the p.d.f. of the total dissipated heat is found by considering $\lambda_R = \lambda_c = \lambda$.

Expression (4.49) contains all the information on the p.d.f. of Q_c and Q_R under a form that makes it quite simple to understand separately the role of the average current, of current fluctuations and of higher moments. To explore these issues, we shall first consider Joule heating from current voltage pulses generated by a classical drive (the usual a.c. Joule heating) before moving to the case of single-electron states.

4.4.2 Joule heating from current pulses

Let us now discuss the Joule heating in the case of current pulses generated by a voltage pulse. At zero temperature, these correspond to the edge-magnetoplasmon coherent states. We first obtain in full generality the joint p.d.f. for the heat dissipated into the environment and into the contact and show that it factorises due to the absence of correlations generated by the interaction region in the case of current pulses. We show that the average dissipated energy is given by the standard a.c. Joule heating expression. We then discuss more specifically the case of an a.c. drive at a given frequency and also the case of a Lorentzian pulse of given duration τ_0 and charge q. Discussing the case of the $\nu = 2$ edge channel system, we show how fractionalization of Levitov pulses leads to striking signature on the p.d.f. of Q_R and Q_c.

General current pulses

A time-dependent voltage $V_d(t)$ generates a coherent state $|\Lambda_{V_d}\rangle$ where the functionnal parameter is given by $\Lambda_{V_d}(\omega) = -e\tilde{V}_d(\omega)/h\sqrt{\omega}$. In this case, the interaction region does not lead to any entanglement between the edge channel and the environmental degrees of freedom. Therefore, there are no correlations between the heat dissipated in the environment and the heat dissipated in the electronic reservoir. More specifically, the generating function $\hat{P}(\lambda_c, \lambda_R)$ factorises as:

$$\hat{P}(\lambda_c, \lambda_R) = \hat{P}_{r\cdot\Lambda_{V_d}}(\lambda_R) \times \hat{P}_{(t-1)\cdot\Lambda_{V_d}}(\lambda_c), \tag{4.50}$$

where $\hat{P}_\Lambda(\lambda)$ denotes the generating function for the energy p.d.f. of a coherent state $|\Lambda\rangle$

$$\hat{P}_\Lambda(\lambda) = \exp\left(\int_0^{+\infty} |\Lambda_\omega|^2 (\mathrm{e}^{\mathrm{i}\hbar\omega\lambda} - 1)\,\mathrm{d}\omega\right). \tag{4.51}$$

The generating function given by eq. (4.51) being an exponential of a sum, it can be understood as the generating function of an infinite convolution of all the p.d.f. associated with each mode. Since we have a tensor product of coherent states in each frequency mode, we obtain an infinite convolution of Poisson laws corresponding to all the coherent states at all possible frequencies.

Here, the two terms in eq. (4.50) correspond to the many-body state of the environmental degrees of freedom: $r \cdot \Lambda$ and of the state of the electron/hole pairs carrying the heat to be dissipated in the contact $|(t-1)\cdot\Lambda\rangle$. We then have to use eq. (4.51) with $|r \cdot V_d|^2_\omega = (e/h)^2\, R(\omega)|\widetilde{V}_d(\omega)|^2/\omega$ and $|(1-t)\cdot V_d|^2_\omega = (e/h)^2\,|(1-t(\omega))\widetilde{V}_d(\omega)|^2/\omega$.

Average dissipated heat Let us first show that the classical Joule heating expression is recovered. From the effective circuit perspective, the average energy dissipated is $\bar{E}_{\mathrm{Joule}} = \int \langle I(t)\rangle V_d(t)\,\mathrm{d}\omega$. Going to the frequency domain, the heat dissipated by Joule heating is:

$$\bar{E}_{\mathrm{Joule}} = \int_{-\infty}^{+\infty} \Re(G(\omega))\,|\tilde{V}_d(\omega)|^2\,\frac{\mathrm{d}\omega}{2\pi}, \tag{4.52}$$

where $G(\omega)$ denotes the finite-frequency admittance of the circuit. In our model, the average heat dissipated in the environment is given by:

$$\bar{Q}_R = \frac{e^2}{h}\int_0^{+\infty} R(\omega)\,|\tilde{V}_d(\omega)|^2\,\frac{\mathrm{d}\omega}{2\pi}, \tag{4.53}$$

but we also have to account for the heat dissipated in the contact when an incoming edge-magnetoplasmon coherent state of parameter $\Lambda_{0,\mathrm{out}}(\omega) = t(\omega)\Lambda_{V_d}(\omega)$ is sent into an electronic reservoir driven by the voltage $V_d(t)$. Using a gauge transformation, this is equivalent to the heat dissipated when a coherent edge-magnetoplasmon state of parameter $(t(\omega)-1)\Lambda_{V_d}(\omega)$ is dissipated in an electronic reservoir at fixed chemical potential $\mu = 0$. The average dissipated heat is then given by:

$$\bar{Q}_e = \frac{e^2}{h}\int_0^{+\infty} |t(\omega)-1|^2\,|\tilde{V}_d(\omega)|^2\,\frac{\mathrm{d}\omega}{2\pi}. \tag{4.54}$$

Summing eqs. (4.53) and (4.54), and defining $t(-\omega) = t(\omega)^*$ for $\omega > 0$ gives the total average dissipated heat

$$\bar{Q}_{\mathrm{tot}} = \frac{e^2}{h}\int_{-\infty}^{+\infty} \Re(1-t(\omega))\,|\tilde{V}_d(\omega)|^2\,\frac{\mathrm{d}\omega}{2\pi}, \tag{4.55}$$

which, using the relation $R_K G(\omega) = 1 - t(\omega)$ coincides with the Joule expression given by eq. (4.52).

Example of a.c. Joule heating

To illustrate the above analysis in a more familiar case, let us consider the case of a monochromatic a.c. drive at frequency $f = \omega_0/2\pi$: $V_S(t) = V_0\cos(\omega_0 t + \varphi)$ and let us assume that it is applied during the time interval $[-T/2, T/2]$. Then, for $\omega > 0$, the Fourier transform $\widetilde{V}_S(\omega)$ is given by:

$$\widetilde{V}_S(\omega) = \frac{V_0 T}{2}\,\mathrm{e}^{\mathrm{i}\varphi}\,\mathrm{sinc}\left(\frac{(\omega-\omega_0)T}{2}\right). \tag{4.56}$$

Using this expression to compute $\hat{P}(\lambda)$ shows that

$$\hat{P}(\lambda_c,\lambda_R) = \mathrm{e}^{\bar{n}_{\mathrm{ac}}\left(R(\omega_0)\,(\mathrm{e}^{\mathrm{i}\lambda_R\hbar\omega_0}-1)+|1-t(\omega_0)|^2(\mathrm{e}^{\mathrm{i}\lambda_c\hbar\omega_0}-1)\right)}, \tag{4.57}$$

where we denote

$$\bar{n}_{\mathrm{ac}} = \frac{T}{4}\frac{e^2}{h}V_0^2 \times (\hbar\omega_0)^{-1}. \tag{4.58}$$

Equation (4.57) is the characteristic function of the product of two Poisson distributions for the variables $Q_c/\hbar\omega_0$ and $Q_R/\hbar\omega_0$ with respective average values $\bar{n}_{\mathrm{ac},c}$ and $\bar{n}_{\mathrm{ac},R}$ given by:

$$\bar{n}_{\mathrm{ac},R} = R(\omega_0)\,\bar{n}_{\mathrm{ac}} \tag{4.59a}$$

$$\bar{n}_{\mathrm{ac},c} = |1-t(\omega_0)|^2\,\bar{n}_{\mathrm{ac}}. \tag{4.59b}$$

The energy is dissipated under the form of individual quantum of energy $\hbar\omega_0$ as expected from the photo-assisted noise theory. The statistics for the number of emitted quanta are Poissonian with averages given by eq. (4.59). The p.d.f. for the total dissipated heat $Q = Q_c + Q_R$ is also Poissonnian for the discrete variable $Q/\hbar\omega_0$ and the average dissipated energy is given by

$$\bar{Q} = \frac{T}{2}\,\frac{e^2}{h}\,V_0^2\,\Re(1 - t(\omega_0)), \tag{4.60}$$

and therefore grows linearly with time. The corresponding average power coincides with the classical a.c. Joule heating expression.

Lorentzian pulses

Applying a Lorentzian voltage pulse to an Ohmic contact generates a Lorentzian current pulse characterized by its duration τ_0 and its charge q. When q is a positive integer mutiple of the electronic charge $-e$ corresponds to an electronic many-body state built from the Fermi sea by adding on top of it a Slater determinant of n mutually orthogonal single-electron states, as previously discussed in sections 1.2.3, 1.4.4 and 3.3.4. For non-integer values of q/e, the many-body state involves both electronic and hole excitations. These states are therefore very convenient to explore Joule heating for quasi-classical currents involving an increasing number of electronic excitations and, at the same time, admitting a clean single-electron limit (the Leviton).

Besides their charge, Lorentzian pulses are characterized by their duration τ_0. In the $\nu = 2$ edge channel system with short-range interactions discussed in section 3.4.3, the fate of a Lorentzian pulse depends on the ratio of τ_0 to the characteristic time of flight $\tau_s(l) = l/v_s$ within the interaction region. Two distinct regimes can be probed: when $\tau_0 \gg \tau_s(l)$, the current pulse is much wider than the interaction region which then sees a slowly varying homogeneous charge. Charge/neutral mode separation discussed in section 3.4.3 then appears as a small perturbation compared to the very broad shape of the pulse and, as we shall see, interactions can be considered as a weak disturbance acting on the pulse.

On the other hand, in the opposite limit where $\tau_0 \ll \tau_s(l)$, this approximation breaks down and the Lorentzian pulse comes out fully fractionalized from the interaction region. As we shall see, fractionalization which is specific to the interaction model considered in section 3.4.3 has

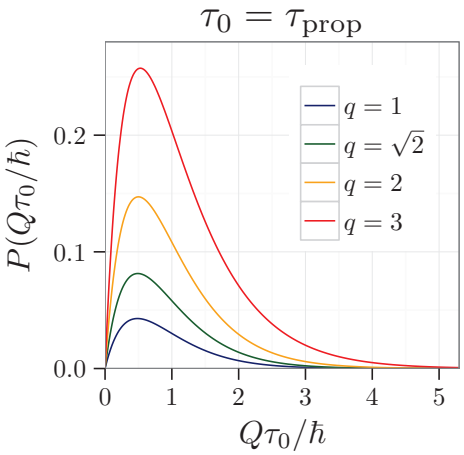

Figure 4.9: Regular part of the p.d.f. $P_l(Q|q,\theta)$ when fractionalization is not completed ($\tau_0 \sim \tau_s(l)$) for $\theta = \pi/2$ and various values of the charge ($q/(-e) = 1, \sqrt{2}, 2, 3$). The shape of the curve is qualitatively the same for different charges. Increasing the charge also increases the probability of heat emissions, scaling the curves towards higher probabilities. Furthermore, we observe a slight shift of the most probable heat value towards higher energies as we increase the charge, for this regular contribution.

drastic consequences on the heat p.d.f. which indeed is deeply related to the energy content of Lorentzian pulses.

Small impedance regime This regime is characterized by $\tau_s(l) \ll \tau_0$ which implies that the incoming pulse is weakly distorted by its passing across the interaction region. In this regime, the frequencies involved in the Lorentzian pulse are such that the coupling to the environment is weak: $R(\omega) = \sin^2(\omega l/2v_s(l)) \ll 1$ at $\theta = \pi/2$. At a given frequency, we are thus probing the energy content of the Lorentzian pulse. This explains why all the curves on fig. 4.9 have the same shape and moreover, a scaling in the square of the amplitude of the pulse is expected.

Fully-fractionalized regime Let us now turn to the $\tau_s(l) \gg \tau_0$. As noticed, the electronic pulse is fully fractionalized when it comes out of the interaction region. In the energy domain, the edge magnetoplasmon reflexion probability amplitude $R(\omega, l)$ oscillates rapidly over the typical

energy scale associated with the Leviton ($\hbar/2\tau_0$). Going deeper into the $\tau_s(l) \ll \tau_0$ regime thus leads to an equipartition of the energy of edge-magnetoplasmon eigenmodes between the two edges, as observed in relaxation experiments in quantum Hall edge channels [Grenier et al., 2011a; Le Sueur et al., 2010].

We thus expect that the p.d.f. of the dissipated heat into the environmental channel slowly reaches a limiting regime, at least for $|Q| \ll \hbar v_S/l$. Numerical computations presented on fig. 4.10 precisely show that, in the limit $l \to +\infty$, the p.d.f. converges towards a limiting distribution. Replacing $R(\omega, l)$ by its coarse grained value $R_\infty(\theta) = \sin^2(\theta)/2$ shows that this limiting prediction is given by ($\gamma_{q,\theta} = q^2 \sin^2(\theta)/2$):

$$P_\infty(Q\,|q, \tau_0) = \frac{1}{\hbar/2\tau_0}\, P_{\gamma_{q,\theta}}\left(\frac{Q}{(\hbar/2\tau_0)}\right), \tag{4.61}$$

where $P_\gamma(x)$ is the Gamma law defined by:

$$P_\gamma(x) = \frac{\mathrm{H}(x)}{\Gamma(\gamma)}\, x^{\gamma-1}\, \mathrm{e}^{-x}. \tag{4.62}$$

First of all, the $Q = 0$ elastic peak has disappeared meaning that energy has been released into the environment. Next, eqs. (4.61) and (4.62) show that $P_\infty(Q\,|q, \tau_0)$ exhibits infrared divergences when $Q \to 0$ for $q^2 \sin^2(\theta)/2 < 1$. This qualitative change in the p.d.f. can indeed be understood as a signature of the fractionalization of the pulse into two Lorentzian pulses, one of which having a charge smaller than the electronic charge. More precisely, the probability distribution function of the energy for Lorentzian current pulse carrying an electric charge $q > 0$ is also given by a Gamma law P_γ with $\gamma = q^2$. Therefore, it exhibits infrared divergences, which reflects the fact that fractional Lorentzian pulses of sub-electronic charge ($|q| < e$) have an important low-energy electron/hole pair content compared to higher non-integer charge Lorentzian pulse which can be viewed as subelectronic pulses on top of a charge $n_q = \lfloor q/(-e) \rfloor$ Leviton. Coming back to our Joule heating setup, an incoming Lorentzian pulse of charge q comes out fractionalized from the interaction region. In the environmental edge channel, it comes out as two Lorentzian pulses of respective charges [Grenier et al., 2013] $-q \sin^2(\theta/2)$ and $q \cos^2(\theta/2)$ and the infrared divergence in the p.d.f. of Q appears when one of these two charges becomes smaller than one.

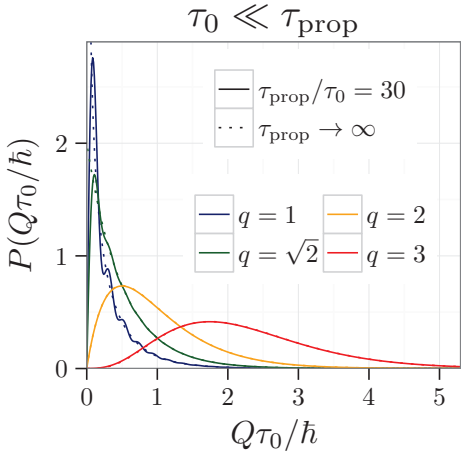

Figure 4.10: Case $\tau_0 \ll \tau_{\rm prop}(l)$: fractionalization completed; the p.d.f. $P_l(Q|q,\tau_O)$ converges towards a universal Gamma law with exponent $q^2\sin^2(\theta)/2$ in the limit $l \to +\infty$. Sub-electronic remnant pulses lead to IR divergences in $P_{l\to+\infty}(Q|q,\tau_0)$.

4.4.3 Joule heating from single-electron excitations

Here we shall consider the p.d.f. for the energy dissipated in the environment. At zero temperature, this is obtained by setting $\lambda_c = 0$ in eq. (4.49). Denoting $\lambda_R = \lambda$ here, the resulting expression can be recasted in terms of the extrinsic decoherence coefficient as:

$$\begin{aligned}\hat{P}(\lambda|\varphi_{\rm e}) = \int \varphi_{\rm e}(x_+)\varphi_{\rm e}^*(x_-)\left\langle\psi(x_-)\psi^\dagger(x_+)\right\rangle_F \\ \times \frac{\mathcal{D}_{\rm ext}(x_+ - x_- - v_F\lambda)}{\mathcal{D}_{\rm ext}(x_+ - x_-)}\,{\rm d}x_+\,{\rm d}x_-,\end{aligned} \tag{4.63}$$

where $\mathcal{D}_{\rm ext}(x_+ - x_-)$ denotes the extrinsic decoherence at zero temperature given by eq. (3.63). Going into Fourier space and using the well known behavior of $\mathcal{D}_{\rm ext}(z)$, the p.d.f. from dissipated heat can be recasted in an explicit form. The final result is of the form:

$$P(Q|\varphi_{\rm e}) = \int_0^{+\infty} P(Q|k_0)\,|\varphi_{\rm e}(k_0)|^2\,\frac{{\rm d}k_0}{2\pi}, \tag{4.64}$$

showing that it is an incoherent sum of probability distributions corresponding to single-electron excitations of initial energy $\varepsilon_0 = \hbar v_F k_0$.

First of all, as noticed before, energy can only flow from the edge channel into the environment and therefore $P(Q<0)=0$. We then find two contributions:

$$P(Q|\varepsilon_0) = \delta(Q)\, Z_{\rm ext}(\varepsilon_0) \tag{4.65a}$$

$$+\, d_+\left(\frac{-Q}{\hbar v_F}\right)\, Z_{\rm ext}(\varepsilon_0 - Q). \tag{4.65b}$$

The singular contribution given by eq. (4.65a) corresponds to trajectories in which no energy is dissipated into the environment. The corresponding probability $Z_{\rm ext}(\varepsilon_0)$ for an incoming electron of fixed energy ε_0 is given by:

$$Z_{\rm ext}(\varepsilon_0) = 1 + \int_{-Q/\hbar v_F}^{0} d_-(p)\,{\rm d}p. \tag{4.66}$$

where the $d_\pm(q)$ functions are defined from the following integral equations

$$\pm\, k d_\pm(k) = R(-kv_F) + \int d_\pm(k+q) R(qv_F)\,{\rm d}q \tag{4.67}$$

and thus obey the relation

$$d_+ + d_- + d_+ \star d_- = 0. \tag{4.68}$$

It should be noted that $Z_{\rm ext}(\varepsilon_0)$ does not coincide with the total elastic scattering probability function $Z(\varepsilon_0)$ appearing in the electronic decoherence of such a single-electron excitation [Degiovanni et al., 2009]. For example, if the edge channel was totally isolated from the outside, $Z_{\rm ext}(\varepsilon_0)=1$ ($R(\omega)=0$ for all $\omega>0$) whereas $Z(\varepsilon_0>0)<1$ as soon as $t(\omega)$ does not correspond to an energy-independent Wigner–Smith time delay $t(\omega)=\mathrm{e}^{-\mathrm{i}\omega\tau}$.

The regular contribution given by eq. (4.65b) corresponds to trajectories involving dissipation of an energy Q into the environment. Remarkably, their contribution to $P(Q|\varepsilon_0)$ comes as the product of a function of Q multiplied by the probability of not emitting energy from the energy $\varepsilon_0 - Q > 0$. The function $d_+(-Q/\hbar v_F)$ can then be interpreted as the emission probability of radiating energy Q into the environment but it should be kept in mind that its expression is given by the solution of the integral equation (4.67), and therefore all orders in $R(\omega)$ which represents the coupling to the environmental modes.

The average heat radiated by a single-electron excitation of energy $\hbar\omega_{\rm e}$ is then obtained as:

$$\langle Q\rangle_{\omega_{\rm e}} = \hbar\int_0^{\omega_{\rm e}} R(\omega)\,{\rm d}\omega, \tag{4.69}$$

which is consistent with the energy spectrum of the edge magnetoplasmons involved in such an excitation, since for such a single-electron excitation, a direct computation shows that the energy spectrum of the edge magnetoplasmons is given by ($\omega > 0$):

$$\hbar\omega\langle(b^\dagger b)(\omega)\rangle_{\omega_\mathrm{e}} = \mathrm{H}(\omega_\mathrm{e} - \omega). \tag{4.70}$$

In the same way, the fluctuation is obtained as:

$$\langle Q^2\rangle_{\omega_\mathrm{e}} = \hbar^2 \int_0^{\omega_\mathrm{e}} \omega\, R(\omega)\,\mathrm{d}\omega \tag{4.71a}$$

$$+ \hbar^2 \int_0^{\omega_\mathrm{e}} (R \star R)(\omega)\,\mathrm{d}\omega, \tag{4.71b}$$

where $(R \star R)$ denotes the self convolution of the reflexion probability. In the expression, the first term (4.71a) comes from the Poissonian shot noise associated with partitioning of the edge magnetoplasmons in the interaction region whereas the second term (4.71b) reflects their wave nature.

At low energy, dissipation is weak because

$$R(\omega) \simeq \frac{2R}{R_K}\,(R_K C_\mu \omega)^2 + \mathcal{O}((R_K C_\mu \omega)^4), \tag{4.72}$$

where $R = R_q - R_K/2$ denotes the environment contribution to the relaxation resistance R_q of the effective discrete-element circuit depicted on fig. 4.8 and C_μ denotes its electrochemical capacitance. It follows that

$$Z_\mathrm{ext}(\omega) \simeq 1 - \frac{2R}{R_K}\,(R_K C_\mu \omega)^2. \tag{4.73}$$

At this order, $Z_\mathrm{ext}(\omega)$ coincides with the total elastic scattering probability, as expected since in the low-energy limit, electron–hole pair creation is expected to be a subdominant process [Grenier et al., 2011b]. The regular part of the heat p.d.f. then follows, since in the perturbative limit, $d_+(-k) \simeq -\frac{\mathrm{d}Z_\mathrm{ext}(k)}{\mathrm{d}k}$. At lowest order, the regular part of the p.d.f. is thus linear and only depends on the universal parameters R and C_μ of the circuit:

$$P_\mathrm{reg}(Q) \simeq \frac{2R}{R_K}\,\frac{R_K C_\mu}{\hbar}\,(\hbar^{-1} R_K C_\mu Q). \tag{4.74}$$

Numerical results

We will now discuss the result for the short-range model at $\nu = 2$. Since the heat probability distribution for any incoming wavepacket is given by the convolution between the heat probability distribution for an electron at a given energy and the energy distribution of the electron, we will be interested by the heat dissipated in the undriven Ohmic contact, when we inject a single electron at a given energy ε_0 in the other contact.

First, let us present the results in the weak coupling case, when $\theta = \pi/10$ (see fig. 4.11). In this case, we see that Z_{ext} decreases slowly as we increase the energy of the incoming wavepacket. The regular part of the distribution $P_{\text{reg}}(Q)$, is non-zero when $Q \in [0; \varepsilon_0]$. This follows simply from the conservation of energy, because allowing heat emissions above ε_0 would amount to gain energy between initial and final situations. Furthermore, we can see that all the curves possess almost the same shape on their support. Actually, it turns out that first-order perturbation theory, in which only one plasmon is exchanged between the incoming single-electron excitation and the environment is an appropriate description in this case. In the weak coupling regime, increasing the energy of the incoming electron amounts to explore the same physics, over a greater energy range. Furthermore, we see that first-order perturbation theory leads to vanishing probabilities at $Q\tau_s(l)/h = 1$. This is due to destructive interferences in the spin-charge separation model.

The strong coupling ($\theta = \pi/2$) possesses very different features (see fig. 4.12). First, Z_{ext} decreases much faster as ε_0 increases. This is expected since a stronger coupling means higher dissipation. Furthermore, its behavior is far from monotonic, showing once again the resonances of the spin-charge separation model. Like in the weak coupling case, the regular part of the probability distribution has a support $[0, \varepsilon_0]$. However, in the strong coupling case, the curves are qualitatively different for two different energies ε_0. This amounts to multiplasmonic processes, which makes the physics richer in this case.

4.4.4 And next...

The next step would be to compute the p.d.f. of the total heat dissipated in the four-terminal geometry and in the two-terminal geometry.

Unfortunately, we have run into difficulties when considering the case of two-terminal geometry. For simplicity we have considered the zero-temperature case but even then, the situation proved to be quite

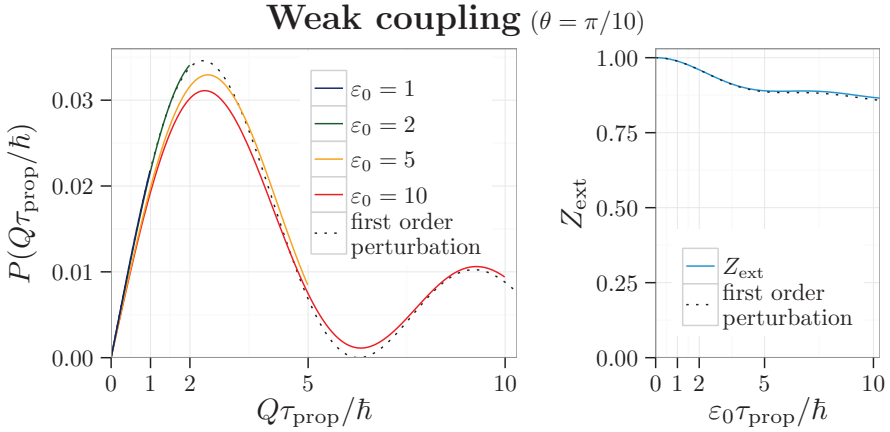

Figure 4.11: Probability of heat for a single-electron excitation at a given energy ε_0 in the weak coupling case ($\theta = \pi/10$). Right pannel: the regular part of the full probability distribution for different $\varepsilon_0\tau_s(l)/\hbar = 1, 2, 5, 10$. Each curve is appropriately described by the first-order perturbation theory, represented as a dashed line, up to $Q = \varepsilon_0$. For $Q > \varepsilon_0$ the probability of further emission is zero. We can also see strong resonances at $Q\tau_s(l)/\hbar = 2\pi$. Left pannel: probability of no heat emission in the environment, plotted as a function of the incoming wavepacket energy. This probability decreases slowly as ε_0 increases. This agrees extremely well with first-order perturbation theory (dashed line).

involved. The natural procedure would be to start from the explicit expression for $P(\lambda_c, \lambda_R|\rho_S, T_R = 0)$ and express it in terms of simpler blocks, in the same spirit as we did for the computation of single-electron decoherence (see chapter 3). Unfortunately we didn't succeed: the analytical expression that we have obtained proved to be numerically inappropriate. The main reason was, as far as we understood, a bad understanding of its singularities...

Because we were running out of time, we then decided to set the problem aside and elaborate on other topics which indeed gave birth to the quantum signal processing approach to electron quantum optics and thus the results presented in chapter 2. I hope to reconsider this problem in the future.

On the scientific side, the partial results presented here already point at the possibility of differentiating some characteristics of the many-body state by looking at the p.d.f. of dissipated heat in the environment.

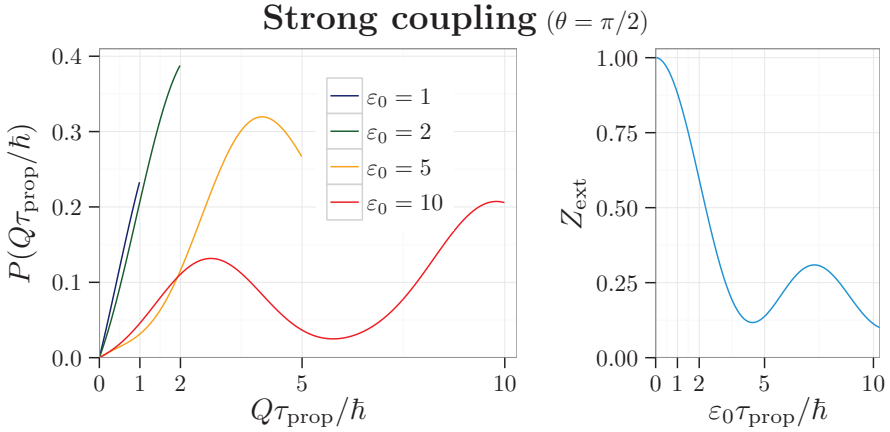

Figure 4.12: Probability of heat for a single-electron excitation at a given energy ε_0 in the strong coupling case ($\theta = \pi/2$). Right pannel: the regular part of the full probability distribution for different $\varepsilon_0\tau_s(l)/\hbar = 1, 2, 5, 10$. Each curve stops at $Q = \varepsilon_0$, probability being zero afterwards. Curves show very different behaviors, due to multiphotonic processes. Left pannel: probability of no heat emission in the environment, plotted as a function of the incoming wavepacket energy. Compared to the weak coupling case (fig. 4.11), the probability of having no emission decreases very quickly as ε_0 increases. We can also see resonances due to the spin-charge separation model.

The two extreme examples considered here which are the Leviton and the energy-resolved excitations already show spectacular difference. In the case of a single-electron excitation, we are probing the energy p.d.f. of the incoming electronic excitation. In the weak coupling regime, it might even be possible to reconstruct it from the p.d.f. It would be even more interesting to compare these results to the ones we could obtain for an already partially decohered superposition of edge-magnetoplasmon coherent state, which is what would appear if there was a second environment between the one in which the energy change is measured and the electronic source. This remains to be done but it will surely bring interesting insights.

Last but not least, even the four-terminal case is interesting since it is a quantum optics version of a problem considered in our lab by Ciliberto et al. [2013].

Chapter 5

Conclusion and perspectives

5.1 General conclusions

During my PhD, I have explored the concept of quantum signal processing in the context of electron quantum optics. As of now, I am not sure quantum signal processing can be described in its final form. Even its name is ambiguous since one can understand it as processing of quantum signals or as quantum processing of signals or maybe as signal processing of something quantum... The contributions of the present thesis are certainly not the end of the story but should rather be viewed as an empirical attempt at understanding what quantum signal processing could be in the spectific and concrete context of electron quantum optics.

By revisiting the interference experiments already performed in electron quantum optics, I have argued that the excess electronic coherences at first and second order (and indeed at all orders) should be considered as quantum signals characterizing the contents at a given order in the number of particles. This reinterpretation of the ideal MZI, HOM and Franson interferometery experiments showed that each of these interferometers could be interpreted as a quantum signal processor encoding the result of simple operations on the quantum signals fed in its input channels.

Having identified quantum signals such as the excess single-electron coherence $\Delta\mathcal{G}_S^{(e)}$ and given a way to reconstruct them experimentally, for example using HOM single-electron tomography, I have developed an algorithm that can extract from a time-perodic $\Delta\mathcal{G}_S^{(e)}$ a representation

in terms of electronic and hole atoms of signals. It contains a simple description of the single-particle states emitted within each period, their emission probabilities, as well as their interperiod coherences and also electron/hole coherences. The whole chain combining on-chip quantum signal processing (HOM tomography) and my classical algorithm can be viewed as a single-particle autopsy of a quantum electrical current.

I have also presented a concrete case of such an autopsy that demonstrates, for the first time, the extraction of individual wavefunctions propagating within a ballistic quantum conductor.

In the case of a pure state generated from the Fermi sea by the action of a T-periodic single-particle scattering, I have shown how the algorithm extracts an entanglement spectrum between the electron and hole excitations and can then be used to characterize the quality of a potential single-electron source.

This new tool could also be used to analyse and supplement the analysis of single-electron decoherence, a problem that I have contributed to solve for arbitrary incoming single-electron excitations and effective interactions, under the hypothesis of linear response to charge density perturbations.

In its globality, this corpus of works to which I have contributed demonstrates that the ideas and paradigm of quantum optics, when interpreted in terms of quantum signal processing are very effective to improve our understanding of electronic quantum transport and of the effects of Coulomb interactions within ballistic conductors.

An important question, which I have started to address in the last two chapters of this thesis is to try to characterize a quantum electrical current in a more global way, that probes the many-body state at all orders in the number of particles. For this, I have mainly explored the radiation emitted by the current, first by starting to unravel the relations beween photonic and electronic quantum coherences and then by considering the full statistics of the dissipated energy. These works are still in progress but my intuition is that this exploration will certainly be useful in extending the general message I have just delivered.

5.2 Perspectives

I feel that electron quantum optics arrives now at a turning point. Having entered the field five years ago, during my Master internship, I must say that the development of the subject has been really impressive since

then. Several milestones have been laid: the HBT and HOM experiment [Bocquillon et al., 2012, 2013a], the demonstration of the Leviton source Dubois et al. [2013a] and even the implementation of variants of the single-electron tomography protocol proposed by Grenier et al. [2011a] in specific cases Jullien et al. [2014].

These progresses make electron quantum optics an enabling platform to probe many-body physics, as was also proved by the recent studies of single-electron decoherence Marguerite et al. [2016b]. We are now to the point where we can analyze quantum electrical currents at an unprecedented level and I hope that the work presented here will contribute exposing the richness of the situations we can now explore in electron quantum optics.

Since important proofs of concept have been demonstrated, we are now entering a different time where applications of electron quantum optics can now be discussed, having in mind what is possible and what has still to be done. This is why, in this section, I will try to elaborate on the new possibilities for the field which are for a part, a natural extension of this thesis. I will first discuss the foreseen applications of electron quantum optics for the study of electronic correlations. Another promising topic teased in this thesis is the connection between electron and microwave quantum optics.

I believe that this thesis also opens perspectives beyond electron quantum optics. In particular, quantum signal processing is not the prerogative of electronic beams and the techniques we have described could be extended to other particle quantum beams. More generally it gives rise to the question of the many-body reconstruction from a set of partial indicators. Finally, our work on heat transfer might be a way to investigate some of the potential issues of quantum thermodynamics.

5.2.1 Applications of electron quantum optics

From the generation to the characterization of states at the single-particle level, electron quantum optics now embeds everything needed to use it as a powerful platform to probe electronic transport. A typical example of forthcoming achievement would be the experimental reconstruction of the Wigner function of a decohered single electron exactly as was done for a single electromagnetic mode [Guerlin et al., 2007]. This exciting example is, nonetheless, one of the many possible applications of electron quantum optics. I will review a few of them here.

First of all, when extending the realm of applications of electron quan-

tum optics, it might be necessary to mitigate or even control decoherence. This is why, as mentioned in section 3.6.2, we are now exploring various experimentally-relevant possibilities based on sample design. This will notably be a part of the hopefully forthcoming thesis of C. Cabart.

Electron quantum optics could be useful to probe strongly interacting systems, especially quantum impurity problems such as the Kondo problem. For example, one could imagine probing the Kondo cloud by sending single-electron excitations on it and measure the outgoing electron coherence. This would probably give new insight on the effect of strong interactions and may provide a new proof of the vicinity of the strong coupling point. This line of research would greatly benefit from the recent progresses on the analysis of the spin-boson model describing a simple two-level system coupled to a transmission line [Bera et al., 2014b,a] and more recently, application of this approach to the Kondo problem and quantum optics [Snyman and Florens, 2015; Bera et al., 2016; Blunden-Codd et al., 2017; Gheeraert et al., 2017].

Fine control of decoherence as well as the development of efficient quantum signal processing methods may also pave the way to the use of electron quantum optics for metrology. Strong Coulomb interaction effects may be used to probe local electrical or magnetic fields using electron quantum optics probes and analysis of electronic coherence. This is an idea currently discussed within electron quantum optics that is still at the level of exploration. By contrast, these questions have been dealt with great attention in the photon quantum optics community as reviewed in [Giovannetti et al., 2011], and bears interesting connections with quantum information [Pezzé and Smerzi, 2009].

Finally let me extend the list of potential applications by mentioning two rather natural generalizations of electron quantum optics. Of course some theory groups have already started to think about them [Ferraro et al., 2017] but it is useful to recast some relevant questions here.

A first one would be to incorporate superconductivity into the game. This would be a very important change, bringing non-zero pair correlations. Electron quantum optics in presence of superconductors is thus expected to be quite different from standard electron quantum optics. The main difficulty on the experimental point of view here, is to have both superconductivity and magnetic field. But there are recent hints that it may be possible [Lee et al., 2017].

A second natural extension is to use electron quantum optics concepts for probing the fractional quantum Hall regime. This might allow a

better understanding of the structure of conducting channels. In this case, the difficulty is twofold: on the experimental side, one would like to probe Laughlin quasi-particles and this require making an energy-independent Laughlin quasi-particle beam splitter, or at least a reasonable approximation of it. This might be possible but in a limited range of parameters, that is when a perturbative approach applies. On theory side, what are the relevant quantum coherence concepts for these objects and what are their properties?

5.2.2 Plasmon quantum optics

Plasmons are charge density wave of the electron fluid. The associated electrical current couples to the electromagnetic fluid and, in the case of 1D chiral (but also non chiral) systems, they are central to understanding the radiation emitted by a quantum electrical current. As explained in section 3.3 of this thesis, connecting electron quantum optics to microwave quantum optics goes through the study of "plasmon quantum optics". I have already sketched some relation between plasmon quantum coherences and electronic coherences and this is something we intend to pursue in the forthcoming months with a focus on relating the non-classical features of the emitted radiation such as squeezing to electronic coherences.

Besides this basic physics motivation, understanding the relation between photon and electron coherences may lead to interesting applications. Electronic systems can be very non-linear and could be used to generate or detect photon excitations. This was explored in section 3.3.4 of this thesis but there is surely more to explore. In particular, we can also imagine using electronic non-linearities to engineer interesting hybrid electron-plasmon states. This is another way to look at decoherence control by focusing on the interesting plasmonic properties which could be generated in a controlled way.

5.2.3 Signal processing in electron quantum optics

Let me now sketch some perspective for the development of quantum signal processing of quantum beams. Of course, the adaptation of the ideas discussed in this thesis to photonic cases is certainly the most promising, especially in the light of the developments of the manipulation of multimode beams of light. In the same way, claryfying the relation between the electronic atoms of signals present in a quantum electrical

current and the ones suitable to describe the emitted radiation is certainly worth spending some time. Here I will present a few perspectives that are more specific to electron quantum optics.

Machine-learning based tomography

We are just at the beginning of using the single-electron tomography protocol for applications such as probing decoherence effects for example. A first step would be to try to improve the method by looking for a suitable set of probes that minimizes the experimental work needed for performing single-electron tomography. Although the generic protocol is expected to be working, it may be more practical to use a different set of probes. Then, the idea would be to optimize for the reconstructed electron coherence by minimizing the distance between the expected HOM traces computed from the reconstructed single-electron coherence and the set of probes. One could do the minimization by adjusting the $\Delta W_n^{(e)}(\omega_k)$ for a discretization of the energy space, or one could use Floquet–Bloch decomposition and look for it using machine learning techniques.

It turns out that, during my PhD, several months before thinking of the algorithm presented in chapter 2 of this thesis, I have designed a machine-learning system able to look for the best single-electron wavefunction φ_e such that $\mathbf{G}_{++}^{(e)} = |\varphi_e\rangle\langle\varphi_e|$. This system minimized the distance between the given data $\mathbf{G}_{++}^{(e)}$ and the projector on $|\varphi_e\rangle$. One could imagine to extend such a system to reconstruct a single-electron coherence under the general form given by our algorithm starting from the HOM curves associated with a different set of probes than the one used in the generic algorithm.

Quantum signal processing for higher order coherences

A first question is the extension of the ideas of chapters 1 and 2 to higher-order coherences. This would enable us, for example, to find two-electron wavefunctions and the connection between these wavefunctions and their single-electron counterpart.

The first step would be to design another tomography protocol for the $\Delta\mathcal{G}^{(2e)}$ that would not rely on a Mach-Zenhder interferometer. We already have started to explore a possible idea but this will be pursued by C. Cabart and I will not elaborate more on this.

Concerning the signal-processing aspect, maybe the simplest thing to do would be to proceed step by step. We could, for example, first try

to use the Floquet–Bloch basis to express a Wick version of two-electron coherence and then, consider the deviation from Wick's expression for the excess two-electron coherence in this basis.

Then of course, given such a deviation, a natural question would be to guess some many-body ansatz that reproduces it on top of the many-body state discussed in section 2.5.1. It is not clear to me at present time how to implement this idea in practice.

5.2.4 Heat transport and quantum thermodynamics

Heat transport is, by far, the most exploratory topic discussed in this thesis. The objective is to capture information on the many-body state through the full statistics of an observable. Even if the observable is a single-particle quantity (such as the charge or the energy current), its fluctuations will involve two-particle correlations and the full statistics will involve all electronic coherences that is all the information available on the electronic many-body system.

We have first considered a general path-integral approach to heat current full statistics. It is very general and we have explored only one simple example that already shows its richness. Further exploration on more complicated models, and also in the semi-classical regime will be conducted to gain a more general, deeper understanding of the way the statistics of heat transfer gives us information on the coherence properties of the system.

We have then applied this approach to dissipation by a quantum electrical current in a ballistic conductor, which is nothing but a theory for Joule heating in the quantum regime. Our initial hope was to compute the full statistics of the total dissipated heat, including the one dissipated in the contacts but we have encountered technical difficulties in the two-terminal geometry. Nevertheless, I hope to come back to this problem since a preliminary study of the full statistics of heat dissipated within the environment already points out nice physical effects such as a qualitative change of the probability density function of the dissipated heat as a signature of fractionalisation of Leviton pulses.

Of course, this is just the beginning of an exploration here but it seems that electron quantum optics may lead to complementary and interesting insight compared to traditional approaches to these problems which are based on more usual quantum transport situations (d.c. regime) [Tauber, 2015].

Finally, this approach touches to the emerging field of quantum

thermodynamics. I haven't elaborated any further on this since it is not clear to me what quantum thermodynamics is. In the classical context, the energy flows can always be accounted for and the first principle expresses energy conservation. This nice image breaks down in the quantum domain since the measurement itself perturbs the system. The approach presented here is based on the availability of energy reservoirs whose dynamics involves a strong decoherence mechanism enduring that the reservoir is by definition incoherent in its eigenenergy basis. The definition of the heat flow is therefore not a problem. But in the case of an engine fed with a classical a.c. current, this no longer makes sense since a classical a.c. current is precisely classical because of coherences between Fock states of the quantum electromagnetic field (or equivalently of quantum plasmonic modes).

A possibility would be to build quantum thermodynamics as a quantum ressource theory as it has been done by Brandão et al. [2015] and there is certainly something to understand in terms of quantum trajectories here. Another one would be to try to generalize the connection between algorithmic complexity and thermodynamics first unraveled by Zurek and others [Zurek, 1989] to the quantum realm but this is far beyond the scope of the present thesis.

Appendix A

Conventions

A.1 Wavepacket

We will use those normalization conventions for the wavepacket:

$$\int |\varphi(x)|^2 \, \mathrm{d}x = 1 \tag{A.1}$$

$$v_F \int |\varphi(t)|^2 \, \mathrm{d}t = 1 \tag{A.2}$$

$$\frac{1}{v_F} \int |\varphi(\omega)|^2 \, \frac{\mathrm{d}\omega}{2\pi} = 1 \tag{A.3}$$

The change of basis is given by

$$\varphi(\omega) = v_F \int \varphi(t) \mathrm{e}^{\mathrm{i}\omega t} \, \mathrm{d}t \tag{A.4}$$

In the case where one wavepacket is emitted, those conventions ensure

$$\Delta\mathcal{G}^{(e)}(\omega_1, \omega_2) = \varphi^*(\omega_2)\varphi(\omega_1) \tag{A.5}$$

$$\Delta\mathcal{G}^{(e)}(t_1, t_2) = \varphi^*(t_2)\varphi(t_1) \tag{A.6}$$

A.2 Fermionic operators

We have the normalization conventions for the ladder operators

$$\{\psi(t), \psi^\dagger(t')\} = \delta(t - t')/v_F \tag{A.7}$$

$$\{c(\omega), c^\dagger(\omega')\} = \delta(\omega - \omega') \tag{A.8}$$

This implies the following definition

$$c(\omega) = \sqrt{\frac{v_F}{2\pi}} \int \psi(t) \mathrm{e}^{\mathrm{i}\omega t} \mathrm{d}t \tag{A.9}$$

$$c^\dagger[\varphi_e] = \sqrt{\frac{2\pi}{v_F}} \int \varphi_e(\omega) c^\dagger(\omega) \frac{\mathrm{d}\omega}{2\pi} = v_F \int \varphi_e(t)\psi(t)\,\mathrm{d}t \tag{A.10}$$

A.3 Single electron coherence operator

The single particle states $|t\rangle$ and $|\omega\rangle$, normalized as

$$\langle t|t'\rangle = v_F^{-1}\delta(t - t') \tag{A.11a}$$
$$\langle \omega|\omega'\rangle = 2\pi v_F \delta(\omega - \omega') \tag{A.11b}$$

are related by

$$|t\rangle = v_F \int \mathrm{e}^{\mathrm{i}\omega t}|\omega\rangle \frac{\mathrm{d}\omega}{2\pi} \tag{A.12a}$$
$$|\omega\rangle = \frac{1}{v_F} \int \mathrm{e}^{-\mathrm{i}\omega t}|t\rangle\,\mathrm{d}t \tag{A.12b}$$

Using eq. (2.13) and the expression of the fermion field operator

$$\psi(t) = \int_{\mathbb{R}} c(\omega)\,\mathrm{e}^{-\mathrm{i}\omega t} \frac{\mathrm{d}\omega}{\sqrt{2\pi v_F}} \tag{A.13}$$

in terms of fermionic ladder operators $c(\omega)$, $c^\dagger(\omega)$, which obey the canonical anticommutation relations $\{c(\omega), c^\dagger(\omega')\} = \delta(\omega - \omega')$, the $\mathbf{G}^{(e)}$ operator is expressed in these two bases as

$$\mathbf{G}^{(e)} = v_F^2 \int_{\mathbb{R}^2} |t_+\rangle\, \mathcal{G}^{(e)}(t_+|t_-)\langle t_-|\,\mathrm{d}t_+\,\mathrm{d}t_- \tag{A.14a}$$
$$= \int_{\mathbb{R}^2} |\omega_+\rangle\, \langle c^\dagger(\omega_-)\, c(\omega_+)\rangle_\rho \langle \omega_-|\,\mathrm{d}\omega_+\,\mathrm{d}\omega_-\,. \tag{A.14b}$$

Appendix B

Some remarks on Levitons

B.1 Classically driven two-electron excitations

In this section, we will show that the Leviton is the only plasmonic state that carries an excitation containing exactly two electrons. We will use here roughly the same technique used in chapter 3, with some refinements necessary to treat the two-particle case. For this, we will first establish expression for the general n-electron classical pulse that we will specialize to the $n = 2$ case.

A n-electron state above the Fermi sea is described by a n-electron wavefunction $\Phi_n(t_1, \ldots, t_n)$. This wavefunction is anti-symmetric and contains only positive frequencies. The state is given by

$$|\Psi\rangle = \Psi_n^\dagger[\Phi_n]\,|F\rangle = v_F^n \int \Phi_n(t_1, \ldots, t_n)\psi^\dagger(t_1)\cdots\psi^\dagger(t_n)\,\mathrm{d}t_1\cdots\mathrm{d}t_n\,|F\rangle\,. \tag{B.1}$$

We can now use bosonization formulae to express the bosonic state as a superposition of coherent states:

$$|\Psi\rangle = \left(U^\dagger\right)^n \left(\frac{v_F}{\sqrt{2\pi a}}\right)^n \int \Phi_n(t_1, \ldots, t_n)\mathcal{D}[\Lambda_{t_1}]\cdots\mathcal{D}[\Lambda_{t_n}]\,\mathrm{d}t_1\cdots\mathrm{d}t_n\,|0\rangle \tag{B.2}$$

We can reorganize terms according to normal bosonic ordering using

$$\begin{aligned}\mathcal{D}[\Lambda_1]\cdots\mathcal{D}[\Lambda_n] = \exp\left(-\frac{1}{2}\sum_{i=1}^{n}\int_0^\infty |\Lambda_i|^2\,\mathrm{d}\omega\right)\\ \times \exp\left(-\sum_{i<j}\Lambda_i^*\Lambda_j\right) :\mathcal{D}\left[\sum_{i=1}^{n}\Lambda_i\right]:\,.\end{aligned} \tag{B.3}$$

And we get

$$|\Psi\rangle = \left(U^\dagger\right)^n \left(\frac{v_F}{\sqrt{2\pi a}}\right)^n \exp\left(-\frac{n^2}{2}\int_0^\infty \frac{\mathrm{d}\omega}{\omega}\right) \tag{B.4a}$$

$$\times \int \exp\left(\sum_{i<j}\int_0^\infty \left(1-\mathrm{e}^{\mathrm{i}\omega(t_j-t_i)}\right)\frac{\mathrm{d}\omega}{\omega}\right)\Phi_n(t_1,\ldots,t_n) \tag{B.4b}$$

$$\exp\left(\int_0^\infty\left(\sum_{i=1}^n \frac{\mathrm{e}^{\mathrm{i}\omega t_i}}{\sqrt{\omega}}\right)b^\dagger(\omega)\,\mathrm{d}\omega\right)\,\mathrm{d}t_1\cdots\mathrm{d}t_n\,|0\rangle \tag{B.4c}$$

Using the UV regularization on the factor

$$\exp\left(\sum_{i<j}\int_0^\infty\left(1-\mathrm{e}^{\mathrm{i}\omega(t_j-t_i)}\right)\frac{\mathrm{d}\omega}{\omega}\right) = \mathrm{i}(t_j-t_i)/(a/v_F) \tag{B.5}$$

we obtain

$$|\Psi\rangle = \left(U^\dagger\right)^n \sqrt{\frac{v_F}{a}}^{n^2}\sqrt{\frac{v_F}{2\pi}}^n \exp\left(-\frac{n^2}{2}\int_0^\infty\frac{\mathrm{d}\omega}{\omega}\right) \tag{B.6a}$$

$$\times\int\prod_{i<j}(\mathrm{i}t_j-\mathrm{i}t_i)\Phi_n(t_1,\ldots,t_n) \tag{B.6b}$$

$$\exp\left(\int_0^\infty\left(\sum_{i=1}^n\frac{\mathrm{e}^{\mathrm{i}\omega t_i}}{\sqrt{\omega}}\right)b^\dagger(\omega)\,\mathrm{d}\omega\right)\,\mathrm{d}t_1\cdots\mathrm{d}t_n\,|0\rangle \tag{B.6c}$$

On the other hand, $|\Psi\rangle$ being issued from a classical current containing n electrons, we have

$$\begin{aligned}|\Psi\rangle = \left(U^\dagger\right)^n &\exp\left(-\frac{1}{2}\int_0^\infty |i_{e,V}(\omega)|^2\frac{\mathrm{d}\omega}{\omega}\right)\\ &\times\exp\left(\int_0^\infty\frac{i_{e,V}(\omega)}{\sqrt{\omega}}b^\dagger(\omega)\mathrm{d}\omega\right)|0\rangle\end{aligned} \tag{B.7}$$

In order to make things simpler, we will introduce the symmetric function κ

$$\kappa(t_1,\ldots,t_n) = \prod_{i<j}(\mathrm{i}t_j-\mathrm{i}t_i)\Phi_n(t_1,\ldots,t_n). \tag{B.8}$$

We will suppose that this function possesses a Fourier transform

$$\kappa(\omega_1,\ldots,\omega_n) = \int\kappa(t_1,\ldots,t_n)\prod_{i=1}^n\mathrm{e}^{\mathrm{i}\omega_i t_i}\,\mathrm{d}t_1\cdots\mathrm{d}t_n. \tag{B.9}$$

And now we can extract relations between $\kappa(\omega_1, \ldots, \omega_n)$ and current, through contributions at $i = 0, \ldots, n+1$ photons. The zero-photon contribution tells us that $\kappa(\omega_1 = \cdots = \omega_n = 0)$ exists, the right hand side of

$$\kappa(0, \ldots, 0) = \sqrt{\frac{v_F}{2\pi}}^n \sqrt{\frac{v_F}{a}}^{n^2} \exp\left(\frac{1}{2}\int_0^\infty \left(n^2 - |i_{e,V}(\omega)|^2\right) \frac{\mathrm{d}\omega}{\omega}\right) \quad \text{(B.10)}$$

being finite (this is because $i_{e,V}(0) = n$, and $i_{e,V}(\infty) = 0$).

Using the symmmetry of κ, we can show that single-photon contribution expresses $\kappa(\omega_1, 0, \ldots, 0)$ in terms of $i_{e,V}(\omega)$. We thus have

$$n\kappa(\omega, 0, \ldots, 0) = \kappa(0, \ldots, 0) i_{e,V}(\omega). \quad \text{(B.11)}$$

To simplify notations, we will introduce a sequence of functions of $i = 1, \ldots n$ variables, f_i such that

$$f_i(\omega_1, \ldots, \omega_i) = \kappa(\omega_1, \ldots \omega_i, 0, \ldots, 0)/\kappa(0, \ldots, 0) \quad \text{(B.12)}$$

We will also write $f_1(\omega) = f(\omega)$. This way, $f(0) = 1$.

The contribution with $i = 2, \ldots, n$ photons expresses f_i in terms of f_j with $j < i$, giving a recursive (though quite complicated) definition of f_i in terms of $f(\omega)$. Since the general case is quite complicated, we will illustrate the method for the simpler $n = 2$ case.

B.1.1 $n = 2$ case

In the $n = 2$ case, we still have to identify contributions containing two and three photons. As we said, the 2-photon contribution expresses f_2 in terms of f:

$$f_2(\omega_1, \omega_2) + f(\omega_1 + \omega_2) = 2f(\omega_1)f(\omega_2). \quad \text{(B.13)}$$

Now we can use 3-photon contribution to obtain the following equation:

$$(f_2(\omega_1 + \omega_2, \omega_3) + (\text{circ. perm.})) + f(\omega_1 + \omega_2 + \omega_3) = 4f(\omega_1)f(\omega_2)f(\omega_3), \quad \text{(B.14)}$$

which turns to be a functional equation for f once we reinject the equation from 2-photon contribution:

$$(f(\omega_1 + \omega_2)f(\omega_3) + (\text{circ. perm.})) - f(\omega_1 + \omega_2 + \omega_3) = 2f(\omega_1)f(\omega_2)f(\omega_3). \quad \text{(B.15)}$$

We now want to solve this equation from minimal assumption on f. It is reasonable to think that the current is continuous (or, at least, continuous by piece). We will use this equation to extract a recurrent sequence that we can solve, and use continuity to extend this solution to real field. We introduce a parameter $\alpha > 0$, that sole purpose is to allow us the extension to the real field. We then choose $n \in \mathbb{N}$ and set $\omega_1 = \alpha n$ and $\omega_2 = \omega_3 = \alpha$. Thus, we have a linear recurrence relation for each α, given by:

$$f(\alpha(n+2)) - 2f(\alpha)f(\alpha(n+1)) + \left(2f(\alpha)^2 - f(2\alpha)\right) f(\alpha n) = 0. \quad \text{(B.16)}$$

Such an equation has solutions of two possible forms. It can either be a sum of two exponentials with different parameters, or a first-order polynomial times an exponential. In the last case, the polynomial multiplying the exponential is necessarily a constant. This is because right-hand side of eq. (B.15) would be of order 3 otherwise, whereas left-hand side would be of order 2. We can thus write a general solution:

$$f(\alpha n) = a_\alpha \exp(\alpha k_\alpha n) + b_\alpha \exp(\alpha q_\alpha n). \quad \text{(B.17)}$$

with $a_\alpha, b_\alpha, k_\alpha$ and q_α complex parameters such that $a + b = 1$ (due to $n = 0$ behavior) and $k_\alpha \not\equiv q_\alpha[2\mathrm{i}\pi]$. We now have to find if there are any constraints on those parameters. To this, we will use eq. (B.15) and identify coefficients that possess identical exponential factors, setting $\omega_i = \alpha n_i$. If we look at the terms in $\exp(\alpha k_\alpha(n_1 + n_2 + n_3))$

$$3a_\alpha^2 - a_\alpha = 2a_\alpha^3. \quad \text{(B.18)}$$

whose solutions are $a_\alpha \in \{0, 1/2, 1\}$ are quantized. Since we impose continuity, the only possibility is that a_α and b_α does not depend on α. It is the same for k_α and q_α (in the case where $a = b = 1/2$, it is possible to have exchange between k and q, but it is unsignificant).

Finally, what we have demonstrated is that, for the Leviton $n = 2$, the current is a linear combination of two Leviton $n = 1$ pulses, emitted at t_1, t_2 and with widths τ_1, τ_2 (eventually equals):

$$i_{e,V}(\omega) = \exp(\mathrm{i}\omega t_1)\exp(-\omega\tau_1) + \exp(\mathrm{i}\omega t_2)\exp(-\omega\tau_2). \quad \text{(B.19)}$$

B.2 Wavefunction of a Leviton train

We will call a Levitonoid a normalized wavefunction $\psi(t)$ such that $\sum_{l\in\mathbb{Z}} \psi(t - lT)\psi^*(t' - lT)$ is the excess electronic first-order coherence generated by a train of Lorentzian pulses. As we will see, this wavefunction is not unique.

The Moskalets Levitonoids

In a recent work [Moskalets, 2015], Moskalets has identified one possible Levitonoid as:

$$\psi(t) = \sqrt{\frac{\tau_0}{\pi}} \frac{1}{t - \mathrm{i}\tau_0} \prod_{n=1}^{\infty} \frac{t + nT + \mathrm{i}\tau_0}{t + nT - \mathrm{i}\tau_0} \tag{B.20}$$

where $T = 1/f$ is the period and τ_0 is the typical time width of the excitation. This wavefunction has a spatial extention given by τ_0. Let us now discuss its energy content.

Using the identity

$$\Gamma(z) = \frac{1}{z} \prod_{n=1}^{\infty} \frac{\left(1 + \frac{1}{n}\right)^z}{1 + \frac{z}{n}} \tag{B.21}$$

we can rewrite the infinite product as a ratio of Γ functions, up to a global phase

$$\frac{\Gamma((t - \mathrm{i}\tau_0)/T)}{\Gamma((t + \mathrm{i}\tau_0)/T)} = \frac{t + \mathrm{i}\tau_0}{t - \mathrm{i}\tau_0} \prod_{n=1}^{\infty} \left(1 + \frac{1}{n}\right)^{-2\mathrm{i}\tau_0} \tag{B.22a}$$

$$\prod_{n=1}^{\infty} \frac{t + nT + \mathrm{i}\tau_0}{t + nT - \mathrm{i}\tau_0} \tag{B.22b}$$

Thus, up to a global phase factor, we can rewrite:

$$\psi(t) = \sqrt{\frac{\tau_0}{\pi}} \frac{1}{t + \mathrm{i}\tau_0} \frac{\Gamma((t - \mathrm{i}\tau_0)/T)}{\Gamma((t + \mathrm{i}\tau_0)/T)} \,. \tag{B.23}$$

We can compute the Fourier transform of this wavepacket, and we get (up to another global phase factor):

$$\psi(\omega) = \frac{1}{\sqrt{\mathcal{N}}} \mathrm{H}(\omega) \left(2 \sin \frac{\nu T}{2}\right)^{2\mathrm{i}\tau_0/T} \mathrm{e}^{-\omega_n \tau_0} \tag{B.24}$$

where $\omega = \omega_n + \nu$, with $\nu \in [0, 2\pi f[$ and thus $\omega_n = 2\pi f \lfloor \omega/2\pi f \rfloor$. $\mathcal{N} = f/v_F(1 - \mathrm{e}^{-4\pi\tau_0/T})$ is a normalization factor and H is the Heaviside step function. We can then rewrite the wavefunction as a real part and a periodic phase:

$$\psi(\omega) = \frac{1}{\sqrt{\mathcal{N}}} \mathrm{H}(\omega) \mathrm{e}^{\mathrm{i}\theta(\omega)} \mathrm{e}^{-\omega_n \tau_0} \tag{B.25}$$

with the phase satisfying the condition $\theta(\omega + 2\pi f) = \theta(\omega)$. This expression shows that the electronic distribution function of this Levitonoid is the staircase approximation of an exponential decay, with step widths given by $2\pi f$ as expected from T-periodicity. Note that it does not depend on the phase $\theta(\omega)$.

B.2.1 Other Wannier functions for a Leviton train

Moskalets Levitonoids having a spreading τ_0, they are naturally expected to be among the minimally spread atoms of signals when $f\tau_0 \ll 1$, that is when the Leviton spacing is large compared to their duration. But in the opposite limit $f\tau_0 \gtrsim 1$, this is certainly not the case. Let us discuss for other Levitonoids and clarify the relation between our algorithm and Moskalets work [Moskalets, 2015].

If a quantum electrical current has a time-reversal symmetry, which is the case for a Leviton train, then there must be a set of Wannier wavefunctions that possess this symmetry. This imposes that there is a set of real valued Wannier functions in the frequency domain: $\varphi(\omega) \in \mathbb{R}$. If we can furthermore suppose that $\varphi(\omega) \geq 0$, the time-spreading minimization problem becomes trivial and we find that, up to time-translation by T, the minimal wavefunctions are the ones that possess the time-reversal symmetry.

B.2.2 Minimally-spread Levitonoids

In the case of Levitonoids, we have seen in eq. (B.25) that the wavefunctions can be written as the product of a real part and a phase part, the phase part being periodic in time. Thus the minimization of eq. (2.40) is realized when the minimal wavefunction has a constant phase. We can set this global phase to zero, and thus we have the following wavefunction:

$$\varphi(\omega) = \frac{1}{\sqrt{\mathcal{N}}}\,\mathrm{H}(\omega)\mathrm{e}^{-\omega_n\tau_0} \tag{B.26}$$

This wavefunction is time-reversal invariant. In this case, the current of one pulse is different from the current of one Leviton of duration τ_0. The time-domain expression for this wavepacket is:

$$\varphi(t) = \frac{\mathrm{i}}{\sqrt{\mathcal{N}'}}\frac{1}{t}\frac{1-\mathrm{e}^{-2\mathrm{i}\pi ft}}{1-\mathrm{e}^{-2\pi f(\tau_0+\mathrm{i}t)}} \tag{B.27}$$

The corresponding average current is then

$$i(t) \propto \frac{\mathrm{sinc}^2(\pi f t)}{1 - \cos(2\pi f t)/\cosh(2\pi f \tau_0)} \tag{B.28}$$

The overlap between this wavepacket and a unique Leviton is given by

$$|\langle \varphi_{\text{train}} \,|\, \varphi_{\text{unique}} \rangle|^2 = \frac{1}{\pi f \tau_0} \frac{1 - \mathrm{e}^{-2\pi f \tau_0}}{1 + \mathrm{e}^{-2\pi f \tau_0}}. \tag{B.29}$$

The behavior when $f\tau_0 \ll 1$ is approached by

$$|\langle \varphi_{\text{train}} \,|\, \varphi_{\text{unique}} \rangle|^2 \simeq 1 - \frac{(\pi f \tau_0)^2}{6} \tag{B.30}$$

making the Leviton approximation a fairly good approximation in this case. When $f\tau_0 \gg 1$, we have, on the contrary

$$|\langle \varphi_{\text{train}} \,|\, \varphi_{\text{unique}} \rangle|^2 \simeq \frac{1}{\pi f \tau_0}, \tag{B.31}$$

the $1/\pi f \tau_0$ behavior implying a quite slow decays.

Appendix C

Splitting unitary matrices

In this appendix, we will introduce a decomposition for unitary matrices useful when we partition equally the Hilbert space in two. In what remains, we will consider a matrix $S \in \mathcal{U}_{2n}$, acting on a Hilbert space $\mathcal{H} = \mathcal{H}_+ \otimes \mathcal{H}_-$, where $\dim \mathcal{H}_+ = \dim \mathcal{H}_- = n$. The goal here is to show that there exists an orthogonal change of basis $P = P_- P_+$ that acts independently on $\mathcal{H}_+$ and $\mathcal{H}_-$ in which we can write

$$PSP^\dagger = \left(\begin{array}{c|c} u & v \\ \hline v & -u \end{array}\right) \mathrm{e}^{\mathrm{i}(\Theta_- + \Theta_+)} \tag{C.1}$$

where $u, v \in \mathcal{M}_n$ are positive real diagonal matrices, $\Theta_\pm$ are Hermitian matrices of size n. The first block-column corresponds to the Hilbert space $\mathcal{H}_-$ and the second one corresponds to $\mathcal{H}_+$.

Generically, one can write the S matrix as

$$S = \left(\begin{array}{c|c} S_{--} & S_{-+} \\ \hline S_{+-} & S_{++} \end{array}\right). \tag{C.2}$$

For the sake of simplicity, we will consider that each submatrix is invertible. Other cases would correspond to either fully scattered modes or fully reflected modes, which can be separated from the start without much problems.

We will first introduce the polar decomposition of $S_{--} = H_{--}\mathrm{e}^{\mathrm{i}\theta_-}$, where θ_- is Hermitian and H_{--} is a positive semi-definite Hermitian

matrix. This allows us to rewrite S as

$$S = \left(\begin{array}{c|c} H_{--} & S_{-+} \\ \hline S_{+-}\mathrm{e}^{-\mathrm{i}\theta_-} & S_{++} \end{array}\right) \mathrm{e}^{\mathrm{i}\theta_-}. \tag{C.3}$$

H_{--} being positive semi-definite, we can write it as $H_{--} = P_-^\dagger u P_-$, where u is a diagonal, real-valued, positive matrix. This leads us to

$$P_- S P_-^\dagger = \left(\begin{array}{c|c} u & S'_{-+} \\ \hline S'_{+-} & S_{++} \end{array}\right) \mathrm{e}^{\mathrm{i}\Theta_-}. \tag{C.4}$$

where $\Theta_- = P_- \theta_- P_-^\dagger$, $S'_{+-} = P_- S_{+-} \mathrm{e}^{-\mathrm{i}\theta_-}$ and $S'_{-+} = S_{-+} P_-^\dagger$. The first matrix of the rhs must be unitary. Since u is diagonal, it imposes that each column of S'_{+-} is orthogonal to each other. As such, we can rewrite this matrix as a product of a unitary matrix and a diagonal positive real matrix, $S'_{+-} = P_+^\dagger v$. Noting $P = P_- P_+$, we have shown

$$P S P^\dagger = \left(\begin{array}{c|c} u & S''_{-+} \\ \hline v & S'_{++} \end{array}\right) \mathrm{e}^{\mathrm{i}\Theta_-}. \tag{C.5}$$

where $S''_{-+} = S'_{-+} P_+^\dagger$, $S'_{++} = P_+ S_{++} P_+^\dagger$.

We can now use the hermitian properties of unitary matrices to build explicitly the constraints between u, v, S'_{++} and S''_{-+}. The orthogonality constraint gives us

$$S'_{++} = -(u/v) S''_{-+} \tag{C.6}$$

where u/v is the diagonal matrix formed by uv^{-1}. Conversely, the normalization conditions give us

$${S'_{++}}^\dagger (\mathbb{1}_n + (u/v)^2) S'_{++} = \mathbb{1} \tag{C.7}$$

Since $u^2 + v^2 = \mathbb{1}$, this shows that $v^{-1} S'_{++} = \mathrm{e}^{\mathrm{i}\Theta_+}$, where Θ_+ is an Hermitian matrix. Putting everything together, we have

$$P S P^\dagger = \left(\begin{array}{c|c} u & v \\ \hline v & -u \end{array}\right) \mathrm{e}^{\mathrm{i}(\Theta_- + \Theta_+)}. \tag{C.8}$$

This is the property we wanted to show.

This decomposition can also be useful to decompose a unitary transformation into circuit containing only 2-qubit gates, in the spirit of [Kitaev et al., 2002]. We produce a decomposition of a unitary matrix into smaller unitary matrices ($P_{\pm}, \mathrm{e}^{\mathrm{i}\Theta_{\pm}}$) and a simple unitary matrix constituted of matrices u and v. This last matrix can easily be expressed as a product of single-qubit gates controlled by all other qubits. Conversely, starting from a unitary matrix acting on n qubits, $P_{\pm}$ and $\mathrm{e}^{\mathrm{i}\Theta_{\pm}}$ can be written as a unitary matrix acting on $n-1$ qubits controlled by one qubit. Then it is easy to come back to a circuit containing only 2-qubit gates, using the arguments of [Kitaev et al., 2002, chapter 8].

Appendix D

An effective long range model for $\nu = 1$

In this section, we present an analytical expression for the edge-magnetoplasmon transmission coefficient in the $\nu = 1$ case using a simple model of Coulomb interaction based on discrete elements in the spirit of Büttiker's treatment of high-frequency quantum transport [Prêtre et al., 1996]. Similar computations can be found in [Grenier, 2011; Bocquillon et al., 2013b] and the present appendix, included here for completeness, is a contribution by C. Cabart to [Cabart et al., 2017].

The starting point is that electrons within the interaction region see the electrical potential $U(x,t)$ given by a capacitive coupling inside a finite-length region of size l thus making each electron see the potential created by all the ones present in the interacting region:

$$U(x,t) = \begin{cases} 0 & \text{if } x \notin \left[-\frac{l}{2}, \frac{l}{2}\right] \\ \frac{1}{C}\int_{-\frac{l}{2}}^{\frac{l}{2}} n(y,t)\mathrm{d}y & \text{else.} \end{cases} \tag{D.1}$$

where the excess density of charges n is itself linked to the bosonic field ϕ through eq. (3.47). Equation (3.48) can be recasted as a closed equation on ϕ expressed in the frequency domain as

$$\left(-\mathrm{i}\omega + v_F\partial_x\right)\phi(x,\omega) = \frac{e^2}{hC}\left(\phi\left(-\frac{l}{2},\omega\right) - \phi\left(\frac{l}{2},\omega\right)\right). \tag{D.2}$$

Expressing $\phi(x,\omega)$ as $\mathrm{e}^{\mathrm{i}\omega x/v_F}\varphi_\omega(x)$ leads to

$$\begin{aligned}\partial_x\varphi_\omega(x) = \frac{e^2}{v_F hC}\mathrm{e}^{-\mathrm{i}\omega x/v_F} \\ \times\left(\mathrm{e}^{-\mathrm{i}\omega l/(2v_F)}\varphi_\omega\left(-\frac{l}{2}\right) - \mathrm{e}^{\mathrm{i}\omega l/(2v_F)}\varphi_\omega\left(\frac{l}{2}\right)\right)\end{aligned} \tag{D.3}$$

which can be integrated over the whole interaction region to give us a relation between $\varphi_\omega\left(-\frac{l}{2}\right)$ and $\varphi_\omega\left(\frac{l}{2}\right)$. Finally, the solution reads

$$\phi\left(\frac{l}{2},\omega\right) = t(\omega)\phi\left(-\frac{l}{2},\omega\right) \tag{D.4}$$

where

$$t(\omega) = \mathrm{e}^{\mathrm{i}\omega l/v_F}\frac{1+A(\omega,l)\mathrm{e}^{-\mathrm{i}\omega l/(2v_F)}}{1+A(\omega,l)\mathrm{e}^{\mathrm{i}\omega l/(2v_F)}} \tag{D.5a}$$

$$A(\omega,l) = \frac{4e^2/C}{hv_F/l}\,\mathrm{sinc}\left(\frac{\omega l}{2v_F}\right) \tag{D.5b}$$

where we recognize the kinetic energy scale hv_F/l as well as the dimensionless ratio $\alpha = e^2 l/Chv_F$ of the electrostatic energy e^2/C to this kinetic energy scale, which quantifies the strength of Coulomb interactions in this system. Note that, at least for sufficiently long edge channels, this coupling constant does not depend on the length l since C also scales as l.

As expected, the transmission coefficient $t(\omega)$ is of modulus 1 because no energy can be lost in a $\nu = 1$ setup without any dynamical environment. The quantity of interest is therefore the phase of $t(\omega)$.

In the limit where Coulomb interaction effect can be neglected ($\alpha \to 0$), $t(\omega) = \mathrm{e}^{\mathrm{i}\omega l/v_F}$ showing that the bare Fermi velocity is recovered. The opposite limit of ultrastrong Coulomb interactions ($\alpha \to \infty$) leads to $t(\omega) = 1$, that is an infinite edge-magnetoplasmon velocity. However, at fixed coupling α, the edge-magnetoplasmon velocity tends to $v_\infty = v_F$ when $\omega l/v_F \gg 1$. At low frequency, we find that the time of flight of edge magnetoplasmons is renormalized thus leading to an increased renormalized plasmon velocity

$$\frac{v_0}{v_\infty} = 1 + \frac{4e^2/C}{hv_\infty/l}\,. \tag{D.6}$$

compared to the velocity at high frequency which is the bare Fermi velocity v_F. Let us remind that C being the capacitance of the interaction region that is roughly similar to a 1D wire, $C \simeq 4\pi\varepsilon_0\varepsilon_r l$ up to a

geometrical factor for large l, that is when boundary effects are small. Consequently, α does not depend on l but behaves as [Grenier et al., 2013]:

$$\alpha \simeq \frac{\alpha_{\text{qed}}}{\varepsilon_r} \times \frac{c}{v_F} \times (\text{Geometrical Factor}) \tag{D.7}$$

where α_{qed} denotes the fine-structure constant, ε_r the relative permittivity of the material and v_F the bare Fermi velocity. Using $v_F \simeq 3 \times 10^5\,\text{m/s}$ and $\varepsilon_r \simeq 10$ for AsGa, we find

$$\alpha \simeq 0.73 \times (\text{Geometrical Factor}) \tag{D.8}$$

Assuming a geometrical factor of order 1, this gives a velocity for the low-energy magnetoplasmons of the order of $v_0 \sim 1.2 \times 10^6\,\text{m/s}$ which is compatible to what is observed in $\nu = 2$ edge channel systems Kamata et al. [2010]. Let me remind that the edge-magnetoplasmon velocity depends on the details of the electrical potential seen by electrons near the edge of the 2DEG and therefore of the conception of the sample (electrostatic gating being a part of this). This is precisely used in the above reference to modulate it by polarising gates.

For intermediate values of the coupling, as shown on fig. 3.8, the edge-magnetoplasmon velocity deduced from $t(\omega)$ presents a decay from v_0 to a regime with small oscillations (for $a \lesssim 2$) above the asymptotic value of v_F.

Appendix E

Technical stuff for path integrals

Path integral is, at the same time, very beautiful, and yet, it usually ends up in quite nightmarish expression. That is why this appendix exists.

E.1 Path integral for open quantum system

In section 4.2.1, we introduce the notion of driven evolution for the environment conditioned to a trajectory $\gamma_{\mathcal{S}}$ followed by the system. It is actually possible to show it through path integral. For this, we will first need to write down a path integral for the composed system. For this, we introduce $\gamma = \gamma_{\mathcal{S}} \otimes \gamma_{\mathcal{E}}$, where $\gamma_{\mathcal{S}}$ is a path in a chosen observable for the system $\mathcal{S}$ and $\gamma_{\mathcal{E}}$ is a path in a chosen observable for the environment. Now, if we write down the combined evolution, we have

$$|\Psi(t_f)\rangle = \int \langle\gamma_{\mathcal{S}}(t_i)|\psi_{\mathcal{S}}(t_i)\rangle \langle\gamma_{\mathcal{E}}(t_i)|\psi_{\mathcal{E}}(t_i)\rangle \mathcal{A}_{\mathcal{S}\otimes\mathcal{E}}[\gamma_{\mathcal{S}}, \gamma_{\mathcal{E}}] \\ |\gamma_{\mathcal{S}}(t_f)\rangle \otimes |\gamma_{\mathcal{E}}(t_f)\rangle \mathcal{D}[\gamma_{\mathcal{E}}]\mathcal{D}[\gamma_{\mathcal{S}}], \tag{E.1}$$

where $\mathcal{A}_{\mathcal{S}\otimes\mathcal{E}}$ is the amplitude associated with the full dynamics.

Of course, it is possible to separate the action in three terms: one concerning the system alone, another concerning the environment alone, and a part corresponding to the interaction between the system and the environment. We can thus rewrite

$$\mathcal{A}_{\mathcal{S}\otimes\mathcal{E}}[\gamma_{\mathcal{S}}, \gamma_{\mathcal{E}}] = \mathcal{A}_{\mathcal{S}}[\gamma_{\mathcal{S}}]\mathcal{A}_{\mathcal{E}}[\gamma_{\mathcal{E}}]\mathcal{A}_{\text{int}}[\gamma_{\mathcal{S}}, \gamma_{\mathcal{E}}] \tag{E.2}$$

If we reorganize terms a little bit, we find

$$|\Psi(t_f)\rangle = \int \langle \gamma_{\mathcal{S}}(t_i)|\psi_{\mathcal{S}}(t_i)\rangle \, \mathcal{A}_{\mathcal{S}}[\gamma_{\mathcal{S}}] \; |\gamma_{\mathcal{S}}(t_f)\rangle \\ \left(\int \langle \gamma_{\mathcal{E}}(t_i)|\psi_{\mathcal{E}}(t_i)\rangle \, \mathcal{A}_{\text{int}}[\gamma_{\mathcal{S}}, \gamma_{\mathcal{E}}] \mathcal{A}_{\mathcal{E}}[\gamma_{\mathcal{E}}] \; |\gamma_{\mathcal{E}}(t_f)\rangle \; \mathcal{D}[\gamma_{\mathcal{E}}] \right) \mathcal{D}[\gamma_{\mathcal{S}}], \tag{E.3}$$

Now, we can introduce the state of the environment conditioned on trajectory $\gamma_{\mathcal{S}}$ followed by the system as

$$|\mathcal{E}[\gamma_{\mathcal{S}}]\rangle = \int \langle \gamma_{\mathcal{E}}(t_i)|\psi_{\mathcal{E}}(t_i)\rangle \, \mathcal{A}_{\text{int}}[\gamma_{\mathcal{S}}, \gamma_{\mathcal{E}}] \mathcal{A}_{\mathcal{E}}[\gamma_{\mathcal{E}}] \; |\gamma_{\mathcal{E}}(t_f)\rangle \; \mathcal{D}[\gamma_{\mathcal{E}}] \tag{E.4}$$

Of course, we need to be sure that this state is well normalized. But actually, we can see the factor $\mathcal{A}_{\text{int}}[\gamma_{\mathcal{S}}, \gamma_{\mathcal{E}}]\mathcal{A}_{\mathcal{E}}[\gamma_{\mathcal{E}}]$ as an action for the environment, forced classically by the trajectory $\gamma_{\mathcal{S}}$. So what we have is still a path integral and should then conserve the normalization of the state.

E.2 Harmonic bath linearly coupled to the system

In section 4.2.2, we derived the very general equation (4.16):

$$\hat{\mathcal{F}}_{\text{eq}}[\gamma_+, \gamma_-; \lambda] = \frac{1}{Z_i} \, \text{tr} \left(\mathrm{e}^{\mathrm{i}\lambda H_{\mathcal{E}}} U_{\mathcal{E}}[\gamma_+] \mathrm{e}^{-(\beta + \mathrm{i}\lambda) H_{\mathcal{E}}} U_{\mathcal{E}}^{\dagger}[\gamma_-] \right) \tag{E.5}$$

Here we will give the details that allow us to reach eq. (4.21). We will keep the same notation. The first thing we need to do is to express the influence functional with displacement operator

$$\hat{\mathcal{F}}_{\text{eq}}[\gamma_+, \gamma_-; \lambda] = \frac{\mathrm{e}^{\mathrm{i}(\theta[\gamma_+] - \theta[\gamma_-])}}{\text{tr}\left(\mathrm{e}^{-\beta H_{\mathcal{E}}}\right)} \\ \times \text{tr} \left(\mathrm{e}^{\mathrm{i}\lambda H_{\mathcal{E}}} \mathcal{D}(\Lambda[\gamma_+]) \mathrm{e}^{-(\beta + \mathrm{i}\lambda) H_{\mathcal{E}}} \mathcal{D}(-\Lambda[\gamma_-]) \right). \tag{E.6}$$

The objective here, is to express the trace through the formula [Cahill and Glauber, 1969]:

$$\text{tr}\left(z^N D\left(\xi, \bar{\xi}\right)\right) = \frac{\mathrm{e}^{-\frac{(z+1)\xi\bar{\xi}}{2(1-z)}}}{1-z} \tag{E.7}$$

where we introduced $D\left(\xi,\bar{\xi}\right)$, the generalized displacement operators:

$$D\left(\xi,\bar{\xi}\right)=\mathrm{e}^{\xi a^{\dagger}-\bar{\xi}a} \tag{E.8}$$

Lets first start with a single mode picture. We will need to commute operators in the form z^N with displacement operators, N being the number operator associated to the mode we are considering, here coming from the hamiltonian. We have the following relations:

$$z^N a^{\dagger} z^{-N}=z a^{\dagger} \qquad z^N a z^{-N}=z^{-1}a \tag{E.9}$$

It implies on displacement operators that

$$z^N D(\lambda)=D\left(z\lambda,z^{-1}\lambda^*\right)z^N \underset{|z|=1}{=} D\left(z\lambda\right)z^N \tag{E.10}$$

Using the traditional composition relation for displacement operators

$$D(\lambda_2)D(\lambda_1)=D(\lambda_1+\lambda_2)\mathrm{e}^{\mathrm{i}\Im(\lambda_2\lambda_1^*)} \tag{E.11}$$

We can find an expression for the generating functional

$$\begin{aligned}\hat{\mathcal{F}}_{\mathrm{eq}}[\gamma_+,\gamma_-;\lambda]=&\frac{\mathrm{e}^{\mathrm{i}(\theta[\gamma_+]-\theta[\gamma_-])}}{\mathrm{tr}\left(\mathrm{e}^{-\beta H\varepsilon}\right)}\\&\prod_{\alpha}\mathrm{tr}\left(\mathrm{e}^{-\beta H_{\mathcal{E}}^{\alpha}}D\left(\mathrm{e}^{\mathrm{i}\hbar\lambda\omega_\alpha}\Lambda_\alpha[\gamma_+]-\Lambda_\alpha[\gamma_-]\right)\right)\\&\times\exp\left(\mathrm{i}\Im\left(\Lambda_\alpha^*[\gamma_-]\Lambda_\alpha[\gamma_+]\mathrm{e}^{\mathrm{i}\hbar\lambda\omega_\alpha}\right)\right)\end{aligned} \tag{E.12}$$

that we can rewrite

$$\begin{aligned}\hat{\mathcal{F}}_{\mathrm{eq}}[\gamma_+,\gamma_-;\lambda]=&\mathrm{e}^{\mathrm{i}(\theta[\gamma_+]-\theta[\gamma_-])}\\&\prod_{\alpha}\exp\left(-(1+2\bar{n}_\alpha)\left|\mathrm{e}^{\mathrm{i}\hbar\lambda\omega_\alpha}\Lambda_\alpha[\gamma_+]-\Lambda_\alpha[\gamma_-]\right|^2/2\right)\\&\times\exp\left(\mathrm{i}\Im\left(\Lambda_\alpha^*[\gamma_-]\Lambda_\alpha[\gamma_+]\mathrm{e}^{\mathrm{i}\hbar\lambda\omega_\alpha}\right)\right)\end{aligned} \tag{E.13}$$

By setting $\lambda=0$, we find the Feynman–Vernom influence functional at

temperature T

$$\mathcal{F}_{FV,T}[\gamma_+,\gamma_-] = \hat{\mathcal{F}}_{\rm eq}[\gamma_+,\gamma_-;\lambda=0] \tag{E.14a}$$

$$\begin{aligned} &= \mathrm{e}^{\mathrm{i}(\theta[\gamma_+]-\theta[\gamma_-])} \\ &\quad \prod_\alpha \exp\left(-(1+2\bar{n}_\alpha)\left(|\Lambda_\alpha[\gamma_+]|^2+|\Lambda_\alpha[\gamma_-]|^2\right)/2\right) \\ &\quad \times \exp\left((1+\bar{n}_\alpha)\Lambda_\alpha[\gamma_+]\Lambda^*_\alpha[\gamma_-]\right) \\ &\quad \times \exp\left(\bar{n}_\alpha\Lambda^*_\alpha[\gamma_+]\Lambda_\alpha[\gamma_-]\right) \end{aligned} \tag{E.14b}$$

By factorizing Feynman–Vernom influence functional, we finally get eq. (4.21):

$$\begin{aligned} \hat{\mathcal{F}}_{\rm eq}[\gamma_+,\gamma_-;\lambda] &= \mathcal{F}_{FV,T}[\gamma_+,\gamma_-] \\ &\quad \times \prod_\alpha \exp\left((1+\bar{n}_\alpha)(\mathrm{e}^{\mathrm{i}\hbar\lambda\omega_\alpha}-1)\Lambda_\alpha[\gamma_+]\Lambda^*_\alpha[\gamma_-]\right) \\ &\quad \times \exp\left(\bar{n}_\alpha(\mathrm{e}^{-\mathrm{i}\hbar\lambda\omega_\alpha}-1)\Lambda^*_\alpha[\gamma_+]\Lambda_\alpha[\gamma_-]\right). \end{aligned} \tag{E.15}$$

E.3 Two trajectories, single-mode environment

Here you will find the technical details for the derivation of probability density eqs. (4.28) and (4.29) derived in section 4.2.2 in case of a single-mode environment, when the system is constrained to follow either one of two quasi-classical trajectories. We recall here that we splitted the heat probability density into two parts

$$p(Q) = p_{\rm cl}(Q) + p_{\rm qu}(Q) \tag{E.16}$$

where $p_{\rm cl}(Q)$ arises from classical couples of trajectories ($\gamma_+ = \gamma_-$), and $p_{\rm qu}(Q)$ arises from quantum couples of trajectories ($\gamma_+ \neq \gamma_-$).

E.3.1 Classical couple of trajectories

We will start with classical couple of trajectories. We have thus $\gamma_i = \gamma_+ = \gamma_-$.

$$\mathcal{F}_{\rm eq}[\gamma_i,\gamma_i;\lambda] = \exp\left(N_i(1+\bar{n})(\mathrm{e}^{\mathrm{i}\hbar\lambda\omega}-1)\right)\exp\left(N_i\bar{n}(\mathrm{e}^{-\mathrm{i}\hbar\lambda\omega}-1)\right) \tag{E.17}$$

This expression reminds us that the Fourier transform of Poisson law is:

$$p_x(n) = \mathrm{e}^{-x}\frac{x^n}{n!} \qquad \hat{p}_x(z) = \sum_{n\in\mathbb{N}} \mathrm{e}^{inz} p_x(n) = \exp\left(x(\mathrm{e}^{\mathrm{i}z} - 1)\right) \tag{E.18}$$

where $n \in \mathbb{N}$. We will also introduce a Poisson distribution for the negative values of n:

$$p'_x(n) = p_x(-n) \qquad \hat{p}'_x(z) = \hat{p}_x(-z) = \exp\left(x(\mathrm{e}^{-\mathrm{i}z} - 1)\right) \tag{E.19}$$

Generating functional is thus a product of Poisson distribution.

$$\hat{\mathcal{F}}_{\mathrm{eq}}[\gamma_i, \gamma_i; \lambda] = \hat{p}_{N_i(1+\bar{n})}(\hbar\lambda\omega)\hat{p}'_{N_i\bar{n}}(\hbar\lambda\omega) \tag{E.20}$$

This gives, in energy space:

$$\mathcal{F}_{\mathrm{eq}}[\gamma, \gamma; Q] = \left[p_{N(1+\bar{n})} * p'_{N\bar{n}}\right]\left(\frac{Q}{\hbar\omega}\right) \tag{E.21}$$

But this convolution product is what we would find if we consider a random variable $Z = X - Y$, where X and Z would be random variables following Poisson distribution with parameters x and z. In this case, Z would be described by a distribution $f(n; x, y)$ called the Skellam distribution.

$$f(n; x, y) = [p_x * p'_y](n) \tag{E.22}$$

It is also possible to give an explicit expression for Skellam distribution

$$f(n; x, y) = \mathrm{e}^{-(x+y)}\left(\frac{x}{y}\right)^{n/2} I_{|n|}(2\sqrt{xy}) \tag{E.23}$$

where I_n is a modified Bessel function of first kind

$$I_n(x) = \sum_k \frac{1}{k!(k+n)!}\left(\frac{x}{2}\right)^{2k+n}. \tag{E.24}$$

Finally, by summing on both trajectories, we get eq. (4.28).

E.3.2 Quantum trajectories

Now let us look at quantum trajectories. We will here consider $(\gamma_+, \gamma_-) = (\gamma_1, \gamma_2)$.

$$\hat{\mathcal{F}}_{\rm eq}[\gamma_1, \gamma_2; \lambda] = \mathrm{e}^{\mathrm{i}\Delta\theta} \exp\left(-(1+2\bar{n})\frac{N_1+N_2}{2}\right) \tag{E.25a}$$

$$\exp\left(\sqrt{N_1 N_2}\left((1+\bar{n})\mathrm{e}^{\mathrm{i}\Delta\phi} + \bar{n}\mathrm{e}^{-\mathrm{i}\Delta\phi}\right)\right) \tag{E.25b}$$

$$\hat{p}_{(1+\bar{n}_B)\sqrt{N_1N_2}\mathrm{e}^{\mathrm{i}\Delta\phi}}(\hbar\omega\lambda)\hat{p}'_{\bar{n}_B\sqrt{N_1N_2}\mathrm{e}^{-\mathrm{i}\Delta\phi}}(\hbar\omega\lambda) \tag{E.25c}$$

Once Fourier transformed, we get

$$\mathcal{F}_{\rm eq}[\gamma_1, \gamma_2; Q] = \mathrm{e}^{\mathrm{i}\Delta\theta} \exp\left(-(1+2\bar{n}_B)\frac{N_1+N_2}{2}\right) \tag{E.26a}$$

$$\exp\left(\sqrt{N_1 N_2}\left((1+\bar{n})\mathrm{e}^{\mathrm{i}\Delta\phi} + \bar{n}\mathrm{e}^{-\mathrm{i}\Delta\phi}\right)\right) \tag{E.26b}$$

$$f\left(\frac{Q}{\hbar\omega}; \sqrt{N_1N_2}(1+\bar{n})\mathrm{e}^{\mathrm{i}\Delta\phi}, \sqrt{N_1N_2}\bar{n}\mathrm{e}^{-\mathrm{i}\Delta\phi}\right) \tag{E.26c}$$

If we use the following property of Skellam distribution

$$f(n; r_1\mathrm{e}^{\mathrm{i}\theta}, r_2\mathrm{e}^{-\mathrm{i}\theta}) = \exp\left(r_1(1-\mathrm{e}^{\mathrm{i}\theta}) + r_2(1-\mathrm{e}^{-\mathrm{i}\theta})\right)\mathrm{e}^{\mathrm{i}n\theta} f(n; r_1, r_2). \tag{E.27}$$

we obtain

$$\begin{aligned}\mathcal{F}_{\rm eq}[\gamma_1, \gamma_2; Q] =& \mathrm{e}^{\mathrm{i}\Delta\theta}\mathrm{e}^{-(1+2\bar{n}_B)\frac{(\sqrt{N_1}-\sqrt{N_2})^2}{2}} \\ & \mathrm{e}^{\mathrm{i}Q\Delta\phi/\hbar\omega} f\left(\frac{Q}{\hbar\omega}; \sqrt{N_1N_2}(1+\bar{n}), \sqrt{N_1N_2}\bar{n}\right)\end{aligned} \tag{E.28}$$

To obtain eq. (4.29), we only need to take into account the phase due to the dynamics of the system. Then summing over all possible couples of trajectories comes down to take two times the real part of the obtained expression.

Bibliography

Aasi, J. et al. (2013). Enhanced sensitivity of the LIGO gravitational wave detector by using squeezed states of light. *Nature Photonics*, 7(8):613–619.

Abadie, J. et al. (2011). A gravitational wave observatory operating beyond the quantum shot-noise limit. *Nat Phys*, 7(12):962–965.

Abrikosov, A., Gorkov, L., and Dzyaloshinski, I. (1963). *Methods of quantum field theory in statistical physics*. Dover.

Altimiras, C., le Sueur, H., Gennser, U., Cavanna, A., Mailly, D., and Pierre, F. (2010a). Non-equilibrium edge channel spectroscopy in the integer quantum hall regime. *Nature Physics*, 6:34.

Altimiras, C., Le Sueur, H., Gennser, U., Cavanna, A., Mailly, D., and Pierre, F. (2010b). Tuning energy relaxation along quantum hall edge channels. *Phys. Rev. Lett.*, 105:226804.

Ando, T., Fowler, A., and Stern, F. (1982). Electronic properties of two-dimensional systems. *Review of Modern Physics*, 54:437.

Arakawa, T., Shiogai, J., Ciorga, M., Utz, M., Schuh, D., Kohda, M., Nitta, J., Bougeard, D., Weiss, D., Ono, T., and Kobayashi, K. (2015). Shot noise induced by nonequilibrium spin accumulation. *Phys. Rev. Lett.*, 114:016601.

Aspect, A., Boiron, D., and Westbrook, C. (2008). Quantum atom optics with bosons and fermions. *Europhysics News*, 39:25.

Auffèves, A. and Grangier, P. (2015). Contexts, systems and modalities: A new ontology for quantum mechanics. *Foundations of Physics*, 46(2):121–137.

Ballentine, L. (2000). *Quantum mechanics: a modern development*. World Scientific, Singapore River Edge, NJ.

Baloch, K. H., Voskanian, N., Bronsgeest, M., and Cumings, J. (2012). Remote joule heating by a carbon nanotube. 7:316 EP –.

Battista, F., Haupt, F., and Splettstoesser, J. (2014). Energy and power fluctuations in ac-driven coherent conductors. *Phys. Rev. B*, 90:085418.

Battista, F., Moskalets, M., Albert, M., and Samuelsson, P. (2013). Quantum heat fluctuations of single-particle sources. *Phys. Rev. Lett.*, 110:126602.

Baym, G. (1998). The physics of hanbury brown - twiss intensity interferometry: from stars to nuclear collisions. *Acta Physical Polonica B*, 29:1839.

Beenakker, C. and Schomerus, H. (2001). Counting statistics of photons produced by electronic shot noise. *Phys. Rev. Lett.*, 86:700.

Beenakker, C. and Schomerus, H. (2004). Antibunched photons emitted by a quantum point contact out of equilibrium. *Phys. Rev. Lett.*, 93:096801.

Bera, S., Baranger, H. U., and Florens, S. (2016). Dynamics of a qubit in a high-impedance transmission line from a bath perspective. *Phys. Rev. A*, 93:033847.

Bera, S., Florens, S., Baranger, H. U., Roch, N., Nazir, A., and Chin, A. W. (2014a). Stabilizing spin coherence through environmental entanglement in strongly dissipative quantum systems. *Phys. Rev. B*, 89:121108.

Bera, S., Nazir, A., Chin, A. W., Baranger, H. U., and Florens, S. (2014b). Generalized multipolaron expansion for the spin-boson model: Environmental entanglement and the biased two-state system. *Phys. Rev. B*, 90:075110.

Bertoni, A. (2007). Perspectives on solid-state flying qubits. *J. Comput. Electron.*, 6:67.

Bertoni, A., Bordone, P., Brunetti, R., Jacoboni, C., and Reggiani, S. (2000). Quantum logic gates based on coherent electron transport in quantum wires. *Phys. Rev. Lett.*, 84:5912–5915.

Beugnon, J., Jones, M., Dingjan, J., Darquié, B., Messin, G., Browaeys, A., and Grangier, P. (2006). Quantum interferences between two single photons emitted by independantly trapped atoms. *Nature*, 440:779.

Bianchetti, R., Filipp, S., Baur, M., Fink, J. M., Göppl, M., Leek, P. J., Steffen, L., Blais, A., and Wallraff, A. (2009). Dynamics of dispersive single-qubit readout in circuit quantum electrodynamics. *Phys. Rev. A*, 80:043840.

Blanter, Y. and Buttiker, M. (2000). Shot noise in mesoscopic conductors. *Physics Reports*, 336:1.

Blunden-Codd, Z., Bera, S., Bruognolo, B., Linden, N.-O., Chin, A. W., von Delft, J., Nazir, A., and Florens, S. (2017). Anatomy of quantum critical wave functions in dissipative impurity problems. *Phys. Rev. B*, 95:085104.

Bocquillon, E., Freulon, V., Berroir, J., Degiovanni, P., Plaçais, B., Cavanna, A., Jin, Y., and Fève, G. (2013a). Coherence and indistinguability of single electrons emitted by independent sources. *Science*, 339:1054.

Bocquillon, E., Freulon, V., Berroir, J., Degiovanni, P., Plaçais, B., Cavanna, A., Jin, Y., and Fève, G. (2013b). Separation between neutral and charge modes in one dimensional chiral edge channels. *Nature Communications*, 4:1839.

Bocquillon, E., Freulon, V., Parmentier, F., Berroir, J., Plaçais, B., Wahl, C., Rech, J., Jonckheere, T., Martin, T., Grenier, C., Ferraro, D., Degiovanni, P., and Fève, G. (2014). Electron quantum optics in ballistic chiral conductors. *Ann. Phys. (Berlin)*, 526:1–30.

Bocquillon, E., Parmentier, F., Grenier, C., Berroir, J.-M., Degiovanni, P., Glattli, D., Plaçais, B., Cavanna, A., Jin, Y., and Fève, G. (2012). Electron quantum optics: partitioning electrons one by one. *Phys. Rev. Lett.*, 108:196803.

Bourassa, J., Beaudoin, F., Gambetta, J. M., and Blais, A. (2012). Josephson-junction-embedded transmission-line resonators: From kerr medium to in-line transmon. *Phys. Rev. A*, 86:013814.

Bozyigit, D., Lang, C., Steffen, L., Fink, J. M., Eichler, C., Baur, M., Bianchetti, R., Leek, P. J., Filipp, S., da Silva, M. P., Blais, A., and

Wallraff, A. (2011). Antibunching of microwave-frequency photons observed in correlation measurements using linear detectors. *Nat Phys*, 7(2):154–158.

Brandão, F., Horodecki, M., Ng, N., Oppenheim, J., and Wehner, S. (2015). The second laws of quantum thermodynamics. *Proc. Natl. Acad. Sci. USA*, 112:3275.

Braunstein, S. L. and van Loock, P. (2005). Quantum information with continuous variables. *Rev. Mod. Phys.*, 77:513–577.

Brendel, J., Gisin, N., Tittel, W., and Zbinden, H. (1999). Pulsed energy-times entangled twin photon source for quantum communication. *Phys. Rev. Lett.*, 82:2594.

Breuer, H. and Petruccione, P. (2007). *The theory of quantum open systems*. OUP Oxford.

Brune, O. (1931a). *Synthesis of a finite two-terminal network whose driving-point impedance is a prescribed function of frequency*. PhD thesis, MIT.

Brune, O. (1931b). Synthesis of a finite two-terminal network whose driving-point impedance is a prescribed function of frequency. *J. Math. and Phys.*, 10:191–236.

Büttiker, M. (1986). Four terminal phase coherent conductance. *Phys. Rev. Lett.*, 57:1761.

Büttiker, M. (1988). Absence of backscattering in the quantum hall effect in multiprobe conductors. *Phys. Rev* **B**, 38:9375.

Büttiker, M. (1990). Scattering theory of thermal and excess noise in open conductors. *Phys. Rev. Lett.*, 65:2901–2904.

Büttiker, M., Imry, Y., Landauer, R., and Pinhas, S. (1985). Generalized many-channel conductance formula with application to small rings. *Phys. Rev.* **B**, 31:6207 – 6215.

Büttiker, M., Prêtre, A., and Thomas, H. (1993). Dynamic conductance and the scattering matrix of small conductors. *Phys. Rev. Lett.*, 70:4114.

Cabart, C., Roussel, B., Fève, G., and Degiovanni, P. (2017). Decoherence control in quantum hall edge channels. In preparation.

Cahill, K. E. and Glauber, R. J. (1969). Ordered expansions in boson amplitude operators. *Phys. Rev.*, 177:1857–1881.

Caldeira, A. and Leggett, A. (1985). Influence of damping on quantum interference: An exactly soluble model. *Phys. Rev.* **A**, 31:1059–1066.

Caroli, C., Combescot, R., Nozières, P., and Saint-James, D. (1971). Direct calculation of the tunneling current. *J. Phys. C: Solid St. Phys.*, 4:916–929.

Castellanos-Beltran, M. A., Irwin, K. D., Hilton, G. C., Vale, L. R., and Lehnert, K. W. (2008). Amplification and squeezing of quantum noise with a tunable josephson metamaterial. *Nat Phys*, 4:929–931.

Cauer, W. (1926). Die verwirklichung der wechselstromwiderst ände vorgeschriebener frequenzabh ängigkeit. *Archiv für Elektrotechnik*, 17:355–388.

Caves, C. M. (1981). Quantum-mechanical noise in an interferometer. *Phys. Rev. D*, 23:1693–1708.

Chalker, J., Gefen, Y., and Veillette, M. (2007). Decoherence and interactions in an electronic mach-zehnder interferometer. *Phys. Rev.* **B**, 76:085320.

Christen, T. and Büttiker, M. (1996). Low frequency admittance of quantized hall conductors. *Phys. Rev.* **B**, 53:2064.

Ciliberto, S., Imparato, A., Naert, A., and Tanase, M. (2013). Heat flux and entropy produced by thermal fluctuations. *Phys. Rev. Lett.*, 110:180601.

Cohen, L. (1986). *Positive and Negative Joint Quantum Distributions*, pages 97–117. Springer US, Boston, MA.

Cohen-Tannoudji, C. Lectures at collège de france.

da Silva, M. P., Bozyigit, D., Wallraff, A., and Blais, A. (2010). Schemes for the observation of photon correlation functions in circuit qed with linear detectors. *Phys. Rev. A*, 82:043804.

Dalibard, J., Castin, Y., and Molmer, K. (1992). Wave function approach to dissipative processes in quantum optics. *Phys. Rev. Lett.*, 68:580.

Dasenbrook, D. and Flindt, C. (2015). Dynamical generation and detection of entanglement in neutral leviton pairs. *Phys. Rev. B*, 92:161412.

Degiovanni, P., Grenier, C., and Fève, G. (2009). Decoherence and relaxation of single electron excitations in quantum hall edge channels. *Phys. Rev.* **B**, 80:241307(R).

Degiovanni, P., Grenier, C., Fève, G., Altimiras, C., le Sueur, H., and Pierre, F. (2010). Plasmon scattering approach to energy exchange and high-frequency noise in $\nu = 2$ quantum hall edge channels. *Phys. Rev. B*, 81:121302(R).

Degiovanni, P. and Peysson, S. (2000). Decoherence of Schrodinger cat states in a Luttinger liquid. *Phys. Rev.* **B**, 62:10706 – 10723.

Degiovanni, P., Portier, N., Cabart, C., Feller, A., and Roussel, B. (To Be Published). Physique, information et calcul.

Deléglise, S., Dotsenko, I., Sayrin, C., Bernu, J., Brune, M., Raimond, J.-M., and Haroche, S. (2008). Reconstruction of non-classical cavity field states with snapshot of their decoherence. *Nature*, 455:510.

Devoret, M. (2008). Quantum circuits and signals (part i). Lectures at Collège de France.

Devoret, M., Esteve, D., Grabert, H., Ingold, G.-L., Pothier, H., and Urbina, C. (1990). Effect of the electromagnetic environment on the coulomb blockade in ultrasmall tunnel junctions. *Phys. Rev. Lett.*, 64:1824.

Dowling, J. P. and Milburn, G. J. (2003). Quantum technology: the second quantum revolution. *Philosophical Transactions of the Royal Society of London A: Mathematical, Physical and Engineering Sciences*, 361(1809):1655–1674.

Dubois, J., Jullien, T., Grenier, C., Degiovanni, P., Roulleau, P., and Glattli, D. C. (2013a). Integer and fractional charge lorentzian voltage pulses analyzed in the framework of photon-assisted shot noise. *Phys. Rev. B*, 88:085301.

Dubois, J., Jullien, T., Portier, F., Roche, P., Cavanna, A., Jin, Y., Wegscheider, W., Roulleau, P., and Glattli, D. (2013b). Minimal excitation states for electron quantum optics using levitons. *Nature*, 502:659.

Eichler, C., Bozyigit, D., Lang, C., Steffen, L., Fink, J., and Wallraff, A. (2011). Experimental state tomography of itinerant single microwave photons. *Phys. Rev. Lett.*, 106:220503.

Einstein, A. (1925). Quantentheorie der einatomigen idealen gases. *Sitz. Ber. Preuss. Akad. Wiss.*, pages 18 – 25.

Esposito, M., Harbola, U., and Mukamel, S. (2009). Nonequilibrium fluctuations, fluctuation theorems, and counting statistics in quantum systems. *Rev. Mod. Phys.*, 81:1665–1702.

Everett, H. (1957a). *The many worlds interpretation of quantum mechanics*. PhD thesis, Princeton university.

Everett, H. (1957b). Relative state formulation of quantum mechanics. *Rev. Mod. Phys.*, 29:454.

Fano, U. (1961). Quantum theory of interference effects in the mixing of light from phase-independent sources. *Am. J. Phys.*, 29:539.

Ferraro, D., Feller, A., Ghibaudo, A., Thibierge, E., Bocquillon, E., Fève, G., Grenier, C., and Degiovanni, P. (2013). Wigner function approach to single electron coherence in quantum Hall edge channels. *Phys. Rev. B*, 88:205303.

Ferraro, D., Jonckheere, T., Rech, J., and Martin, T. (2017). Electronic quantum optics beyond the integer quantum hall effect. *Physica Status Solidi (b)*, 254(3):1600531–n/a. 1600531.

Ferraro, D., Roussel, B., Cabart, C., Thibierge, E., Fève, G., Grenier, C., and Degiovanni, P. (2014a). Real-time decoherence of landau and levitov quasiparticles in quantum hall edge channels. *Phys. Rev. Lett.*, 113:166403.

Ferraro, D., Wahl, C., Rech, J., Jonckheere, T., and Martin, T. (2014b). Electronic hong-ou-mandel interferometry in two-dimensional topological insulators. *Phys. Rev. B*, 89:075407.

Fève, G., Mahé, A., Berroir, J., Kontos, T., Plaçais, B., Glattli, D., Cavanna, A., Etienne, B., and Jin, Y. (2007). An on-demand single electron source. *Science*, 316:1169.

Février, P. and Gabelli, J. (2017). Violation of the fluctuation-dissipation relation in a tunnel junction at optical frequencies.

Feynman, R. and Hibbs, A. (1965). *Quantum Mechanics and Path Integrals*. McGraw-Hill.

Feynman, R. and Vernon, F. (1963). The theory of a general quantum system interacting with a linear dissipative system. *Annals of Physics*, 24:118 – 173.

Feynman, R. P. (1982). Simulating physics with computers. *International Journal of Theoretical Physics*, 21(6):467–488.

Fisher, D. and Lee, P. (1981). Relation between conductivity and transmission matrix. *Phys. Rev. B*, 23:6851.

Fletcher, R. and Reeves, C. M. (1964). Function minimization by conjugate gradients. *The Computer Journal*, 7(2):149–154.

Forgues, J., Lupien, C., and Reulet, B. (2014). Emission of microwave photon pairs by a tunnel junction. *Phys. Rev. Lett.*, 113:043603.

Fox, M. (2006). *Quantum optics: an introduction*. Oxford University Press.

Franson, J. D. (1989). Bell inequality for position and time. *Phys. Rev. Lett.*, 62:2205–2208.

Freulon, V. (2014). *Etude de la décohérence de paquets d'onde monoélectroniques dans les canaux de bord de l'effet Hall quantique entier*. PhD thesis, Ecole Normale Supérieure.

Freulon, V., Marguerite, A., Berroir, J., Plaçais, B., Cavanna, A., Jin, Y., and Fève, G. (2015). Hong-ou-mandel experiment for temporal investigation of single-electron fractionalization. *Nature Communications*, 6:6854.

Friis, N. (2016). Reasonable fermionic quantum information theories require relativity. *New Journal of Physics*, 18(3):033014.

Frunzio, L., Wallraff, A., Schuster, D., Majer, J., and Schoelkopf, R. (2005). Fabrication and characterization of superconducting circuit qed devices for quantum computation. *IEEE Transactions on Applied Superconductivity*, 15:860.

Gabelli, J., Fève, G., Berroir, J., Plaçais, B., Cavanna, A., Etienne, B., Jin, Y., and Glattli, D. (2006). Violation of kirchhoff's laws for a coherent rc circuit. *Science*, 313:499.

Gabelli, J. and Reulet, B. (2012). Shaping a time-dependent excitation to control the electron distribution function: noise minimization in a tunnel junction. *Phys. Rev.* **B**, 87(075403).

Gasparinetti, S., Viisanen, K. L., Saira, O.-P., Faivre, T., Arzeo, M., Meschke, M., and Pekola, J. P. (2015). Fast electron thermometry for ultrasensitive calorimetric detection. *Phys. Rev. Applied*, 3:014007.

Gasse, G., Lupien, C., and Reulet, B. (2013). Observation of squeezing in the electron quantum shot noise of a tunnel junction. *Phys. Rev. Lett.*, 111:136601.

Gheeraert, N., Bera, S., and Florens, S. (2017). Spontaneous emission of schrödinger cats in a waveguide at ultrastrong coupling. *New Journal of Physics*, 19:023036.

Giamarchi, T. (2004). *Quantum Physics in One Dimension (International Series of Monographs on Physics)*. Clarendon Press.

Giovannetti, V., Lloyd, S., and Maccone, L. (2011). Advances in quantum metrology. *Nat Photon*, 5(4):222–229.

Girvin, S., Glazman, L., Jonson, M., Penn, D., and Stiles, M. (1990). Quantum fluctuations and the single junction coulomb blockade. *Phys. Rev. Lett.*, 64:3183.

Glauber, R. (1962). Photon correlations. *Phys. Rev. Lett.*, 10:84.

Glauber, R. (1963a). Coherent and incoherent states of the radiation field coherent and incoherent states of the radiation field coherent and incoherent states of the radiation field. *Phys. Rev.*, 131:2766.

Glauber, R. (1963b). The quantum theory of optical coherence. *Phys. Rev.*, 130:2529.

Gogolin, A., Nersesyan, A., and Tsevlik, A. (1998). *Bosonization and strongly correlated systems*. Cambridge University Press.

Grenier, C. (2011). *Electron quantum optics*. PhD thesis, Ecole Normale Supérieure de Lyon.

Grenier, C., Dubois, J., Jullien, T., Roulleau, P., Glattli, D. C., and Degiovanni, P. (2013). Fractionalization of minimal excitations in integer quantum hall edge channels. *Phys. Rev. B*, 88:085302.

Grenier, C., Hervé, R., Bocquillon, E., Parmentier, F., Plaçais, B., Berroir, J., Fève, G., and Degiovanni, P. (2011a). Single electron quantum tomography in quantum hall edge channels. *New Journal of Physics*, 13:093007.

Grenier, C., Hervé, R., Fève, G., and Degiovanni, P. (2011b). Electron quantum optics in quantum hall edge channels. *Mod. Phys. Lett. B*, 25:1053 – 1073. Proceedings of the Statphys 24 satellite meeting "International Conference on Frustrated Spin Systems, Cold Atoms and Nanomaterials" (Hanoi, 14-16 July 2010).

Grimsmo, A., Qassemi, F., , Reulet, B., and Blais, A. (2015). Quantum optics theory of electronic noise in quantum conductors. *Phys. Rev. Lett.*, 116:043602. ArXiv:1507.00322.

Guerlin, C., Bernu, J., Deléglise, S., Sayrin, C., Gleyzes, S., Kuhr, S., Brune, M., Raimond, J.-M., and Haroche, S. (2007). Progressive field-state collapse and quantum non-demolition photon counting. *Nature*, 448:889.

Haack, G., Moskalets, M., and Büttiker, M. (2012). Glauber coherence of single electron sources. *Phys. Rev. B*, 87(201302(R)).

Haack, G., Moskalets, M., Splettstoesser, J., and Büttiker, M. (2011). Coherence of single-electron sources from mach-zehnder interferometry. *Phys. Rev. B*, 84:081303.

Halperin, B. (1982). Quantized Hall conductance, current carrying edge states, and the existence of extended states in a two dimensional disordered potential. *Phys. Rev.* **B**, 25:2185 – 2190.

Hanbury Brown, R. and Twiss, R. (1956a). Correlation between photons in two coherent beams of light. *Nature*, 177:27.

Hanbury Brown, R. and Twiss, R. (1956b). A test of a new type of stellar interferometer on sirius. *Nature*, 178:1046.

Hanbury Brown, R. and Twiss, R. (1957). Interferometry of the intensity fluctuations in light - i. basic theory: the correlation between photons in coherent beams of radiation. *Proc. Roy. Soc. A*, 242:300.

Hanbury Brown, R. and Twiss, R. (1958). Interferometry of the intensity fluctuations in light ii. an experimental test of the theory for partially coherent light. *Proc. Roy. Soc. A*, 243:291.

Haroche, S. and Raimond, J.-M. (2006). *Exploring the quantum*. Oxford University Press.

Hashisaka, M., Hiyama, N., Akiho, T., Muraki, K., and Fujisawa, T. (2017). Waveform measurement of charge- and spin-density wavepackets in a chiral tomonaga-luttinger liquid. *Nat Phys*, advance online publication:–.

Henny, M., Oberholzer, S., Strunk, C., Heinzel, T., Ensslin, K., Holland, M., and Schönenberger, C. (1999). The fermionic hanbury-brown and twiss experiment. *Science*, 284:296.

Hofer, P., Dasenbrook, D., and Flindt, C. (2016). On-demand entanglement generation using dynamic single electron sources. To appear in the present volume.

Hofheinz, M., Portier, F., Baudouin, Q., Joyez, P., Vion, D., Bertet, P., Roche, P., and Esteve, D. (2011). Bright side of the coulomb blockade. *Phys. Rev. Lett.*, 106:217005.

Hofheinz, M., Wang, H., Ansmann, M., Biazlczak, R., Lucero, E., Neeley, M., O'Connell, A., Sank, D., Wenner, J., Martinis, J., and Cleland, A. (2009). Synthetizing arbitrary quantum states in a superconducting resonator. *Nature*, 459:546.

Hong, C., Ou, Z., and Mandel, L. (1987). Measurement of subpicosecond time intervals between two photons by interference. *Phys. Rev. Lett.*, 59:2044.

Hudson, R. (1974). When is the wigner quasi-probability density non-negative? *Reports on Mathematical Physics*, 6(2):249 – 252.

Husimi, K. (1940). Some formal properties of the density matrix. *Proceedings of the Physico-Mathematical Society of Japan. 3rd Series*, 22(4):264–314.

Huynh, P.-A., Portier, F., le Sueur, H., Faini, G., Gennser, U., Mailly, D., Pierre, F., Wegschider, W., and Roche, P. (2012). Quantum coherence engineering in the integer quantum hall regime. *Phys. Rev. Lett.*, 108:256802.

Inoue, H., Grivnin, A., Ofek, N., Neder, I., Heiblum, M., Umansky, V., and Mahalu, D. (2014). Fractional charges in emergent neutral modes at the integer quantum hall effect. *Phys. Rev. Lett.*, 112:166801.

Ionicioiu, R. (2006). Spintronics devices as quantum networks. *Laser Physics*, 10:1444.

Ionicioiu, R., Amaratunga, G., and Udrea, F. (2001). Quantum computation with ballistic electrons. *Int. J. Mod. Phys. B*, 15:125.

Jeltes, T., McNamara, J., Hogervorst, W., Vassen, W., Krachmalnicoff, V., Schellekens, M., Perrin, A., Hong, C., Boiron, D., Aspect, A., and Westbrook, C. (2007). Comparison of the Hanbury Brown-Twiss effect for bosons and fermions. *Nature*, 445:402.

Johansson, M. (2016). Comment on 'reasonable fermionic quantum information theories require relativity'. ArXiv:1610.00539.

Jonckheere, T., Stoll, T., Rech, J., and Martin, T. (2012). Real-time simulation of finite-frequency noise from a single-electron emitter. *Phys. Rev. B*, 85:045321.

Jullien, T., Roulleau, P., Roche, B., Cavanna, A., Jin, Y., and Glattli, D. C. (2014). Quantum tomography of an electron. *Nature*, 514:603–607.

Kac, V. (1990). *Infinite dimensional Lie algebras*. Cambridge University Press.

Kamata, H., Ota, T., Muraki, K., and Fujisawa, T. (2010). Voltage-controlled group velocity of edge magnetoplasmon in the quantum hall regime. *Phys. Rev. B*, 81:085329.

Keeling, J., Klich, I., and Levitov, L. (2006). Minimal excitation states of electrons in one-dimensional wires. *Phys. Rev. Lett.*, 97:116403.

Kitaev, A. Y., Shen, A. H., and Vyalyi, M. N. (2002). *Classical and Quantum Computation (Graduate Studies in Mathematics)*. Amer Mathematical Society.

Klass, U., Dietsche, W., von Klitzing, K., and Ploog, K. (1990). Imaging of the dissipation in quantum hall effect experiments. *Z. Phys.* **B**, 82(351).

Klich, I. and Levitov, L. (2009). Quantum noise as an entanglement meter. *Phys. Rev. Lett.*, 102:100502.

Knill, E., Laflamme, R., and Milburn, G. J. (2001). A scheme for efficient quantum computation with linear optics. *Nature*, 409(6816):46–52.

Kovrizhin, D. L. and Chalker, J. T. (2009). Exactly solved model for an electronic mach-zehnder interferometer. *Phys. Rev. B*, 80:161306.

Kozhevnikov, A. (2001). PhD thesis, Yale University.

Kumada, N., Kamata, H., and Fujisawa, T. (2011). Edge magnetoplasmon transport in gated and ungated quantum hall systems. *Phys. Rev. B*, 84:045314.

Landauer, R. (1989). Johnson-Nyquist noise derived from quantum mechanical transmission. *Physica* **D**, 38:226 – 229.

Landauer, R. (1991). Information is physical. *Physics Today*, page 23.

Landauer, R. (1996). The physical nature of information. *Physics Letters A*, 217:188.

Landauer, R. (1998). The noise is the signal. *Nature*, 392:658.

Landauer, R. and Büttiker, M. (1985). Resistance of small metallic loops. *Phys. Rev. Lett.*, 54:2049–2053.

Lang, C., Eichler, C., Steffen, L., Fink, J., Woolley, M., Blais, A., and Wallraff, A. (2013). Probing correlations, indistinguishability and entanglement in microwave two-photon interference. *Nature Physics*, 9:345.

Laughlin, R. (1983). Anomalous quantum Hall effect: an incompressible quantum fluid with fractionally charged excitations. *Phys. Rev. Lett.*, 50:1395–1398.

Le Bellac, M. (2003). *Physique quantique*. EDP Sciences.

Le Hur, K., Henriet, L., Petrescu, A., Plekhanov, K., Roux, G., and Schiro, M. (2016). Many-body quantum electrodynamics networks: Non-equilibrium condensed matter physics with light. *C. R. Physique*, 17:808.

Le Sueur, H., Altimiras, C., Gennser, U., Cavanna, A., Mailly, D., and Pierre, F. (2010). Energy relaxation in the integer quantum hall regime. *Phys. Rev. Lett.*, 105:056803.

Lee, G.-H., Huang, K.-F., Efetov, D. K., Wei, D. S., Hart, S., Taniguchi, T., Watanabe, K., Yacoby, A., and Kim, P. (2017). Inducing superconducting correlation in quantum hall edge states. 13:693 EP –.

Levitov, L., Lee, H., and Lesovik, G. (1996). Electron counting statistics and coherent states of electric current. *J. Math. Phys.*, 37:4845.

Levkivskyi, I. and Sukhorukov, E. (2008). Dephasing in the electronic mach-zehnder interferometer at filling factor $\nu = 2$. *Phys. Rev.* **B**, 78:045322.

Lopes, R., Imanaliev, A., Aspect, A., Cheneau, M., Boiron, D., and Westbrook, C. I. (2015). Atomic hong-ou-mandel experiment. *Nature*, 520(7545):66–68.

Ludovico, M. F., Lim, J. S., Moskalets, M., Arrachea, L., and Sánchez, D. (2014). Dynamical energy transfer in ac-driven quantum systems. *Phys. Rev. B*, 89:161306.

Ludovico, M. F., Moskalets, M., Sánchez, D., and Arrachea, L. (2016). Dynamics of energy transport and entropy production in ac-driven quantum electron systems. *Phys. Rev. B*, 94:035436.

Lvovsky, A. I. and Raymer, M. G. (2009). Continuous-variable optical quantum-state tomography. *Rev. Mod. Phys.*, 81:299–332.

MacKenzie, R. (2000). Path integral methods and applications.

Mahé, A., Parmentier, F., Bocquillon, E., Berroir, J., Glattli, D., Kontos, T., Plaçais, B., Fève, G., Cavanna, A., and Jin, Y. (2010). Current correlations of an on-demand single electron source as an evidence of single particle emission. *Phys. Rev. B*, 82:201309. Arxiv:1004.1985.

Mahé, A., Parmentier, F., Fève, G., Berroir, J., Kontos, T., Cavanna, A., Etienne, B., Jin, Y., Glattli, D., and Plaçais, B. (2008). Subnanosecond single electron source in the time domain. *Journal of Low Temperature Physics*, 153:339.

Marcikic, I., de Riedmatter, H., Tittel, W., Scarini, V., Zbinden, H., and Gisin, N. (2002). Time-bin entangled qubits for quantum communication created by femtosecond pulses. *Phys. Rev. A*, 66:062308.

Marguerite, A. (2017). *Two particle interferometry for quantum signal processing*. PhD thesis, Université Pierre et Marie Curie.

Marguerite, A., Bocquillon, E., Berroir, J.-M., Plaçais, B., Degiovanni, P., and Fève, G. (2016a). Two-particle interferometry in quatum hall edge channels. To appear in Physica Status Solidi.

Marguerite, A., Cabart, C., Wahl, C., Roussel, B., Freulon, V., Ferraro, D., Grenier, C., Berroir, J.-M., Plaçais, N., Jonckheere, T., Rech, J., Martin, T., Degiovanni, P., Cavanna, A., Jin, Y., and Fève, G. (2016b). Decoherence and relaxation of a single electron in a one-dimensional conductor. *Phys. Rev. B*, 94:115311.

Marguerite, A., Roussel, B., Bisongnin, R., Cabart, C., Kumar, M., Berroir, J., Bocquillon, E., Plaçais, B., Cavanna, A., Gennser, U., Jin, Y., Degiovanni, ., and Fève, G. (2017). Extracting single electron wavefunctions from a quantum electrical current. Submitted to PRL.

Martin, T. and Landauer, R. (1992). Wave packet approach to noise in multichannel mesoscopic systems. *Phys. Rev.* **B**, 45:1742 – 1755.

Marzari, N., Mostofi, A. A., Yates, J. R., Souza, I., and Vanderbilt, D. (2012). Maximally localized wannier functions: Theory and applications. *Rev. Mod. Phys.*, 84:1419–1475.

Meir, Y. and Wingreen, N. (1992). Landauer formula for the current through an interacting electron region. *Phys. Rev. Lett.*, 68:2512 – 2515.

Mendes, U. and Mora, C. (2015). Cavity squeezing by a quantum conductor. *New Journal of Physics*, 17:11.

Misiorny, M., Fève, G., and Splettstoesser, J. (2017). Shaping charge excitations in chiral edge states with a time-dependent gate voltage. *ArXiv e-prints*.

Molmer, K., Castin, Y., and Dalibard, J. (1993). Monte carlo wave-function method in quantum optics. *J. Opt. Soc. Am. B*, 107:524.

Montambaux, G. et Akkermans, E. (2004). *Physique mésoscopique des électrons et des photons*. EDP Sciences.

Moskalets, M. (2011). *Scattering matrix approach to non-stationary quantum transport*. Imperial College Press, London.

Moskalets, M. (2014a). Floquet scattering matrix theory of heat fluctuations in dynamical quantum conductors. *Phys. Rev. Lett.*, 112:206801.

Moskalets, M. (2014b). Two-electron state from the floquet scattering matrix perspective. *Phys. Rev. B*, 89:045402.

Moskalets, M. (2015). First-order correlation function of a stream of single-electron wave packets. *Phys. Rev. B*, 91:195431.

Moskalets, M., Haack, G., and Büttiker, M. (2013). Single-electron source: Adiabatic versus nonadiabatic emission. *Phys. Rev. B*, 87:125429.

Moura, J. (2009). What is signal processing? *IEEE Signal Processing Magazine*, 26:6.

Neder, I., Marquardt, F., Heiblum, M., Mahalu, D., and Umansky, V. (2007). Controlled dephasing of electrons by non-gaussian shot noise. *Nature Physics*, 3:534.

Neuenhahn, C. and Marquardt, F. (2008). Dephasing by electron-electron interactions in a ballistic interferometer. *New Journal of Physics*, 10:115018.

Neuenhahn, C. and Marquardt, F. (2009). Universal dephasing in a chiral 1d interacting fermion system. *Phys. Rev. Lett.*, 102:046806.

Nigg, S. and Büttiker, M. (2008). Quantum to classical transition of the charge relaxation resistance of a mesoscopic capacitor. *Phys. Rev.* **B**, 77:085312.

Oliver, W., Kim, J., Liu, R., and Yamamoto, Y. (1999). Handbury brown and twiss experiment with electrons. *Science*, 284:299.

Ol'khovskaya, S., Splettstoesser, J., Moskalets, M., and Büttiker, M. (2008). Shot noise of a mesoscopic two-particle collider. *Phys. Rev. Lett.*, 101:166802.

Ourjoumtsev, A., Tualle-Brouri, R., and Grangier, P. (2006). Quantum homodyne tomography of a two-photon fock state. *Phys. Rev. Lett.*, 96:213601.

Parmentier, F., Mahé, A., Denis, A., Berroir, J.-M., Glattli, D., Plaçais, B., and Fève, G. (2011). A high sensitivity ultra-low temperature rf conductance and noise measurement setup. *Rev. Sci. Instrum.*, 82:013904.

Parmentier, F. D., Bocquillon, E., Berroir, J.-M., Glattli, D., Plaçais, B., Fève, G., Albert, M., Flindt, C., and Büttiker, M. (2012). Current noise spectrum of a single-particle emitter: Theory and experiment. *Phys. Rev. B*, 85:165438.

Pati, A. and Braunstein, S. (2000). Impossibility of deleting an unknown quantum state. *Nature*, 404:164.

Pauli, W. (1940). The connection between spin and statistics. *Phys. Rev.*, 58:716–722.

Peres, A. (1978). Unperformed experiments have no results. *Am. J. Phys.*, 46:746.

Pezzé, L. and Smerzi, A. (2009). Entanglement, nonlinear dynamics, and the heisenberg limit. *Phys. Rev. Lett.*, 102:100401.

Pines, D. and Nozières, P. (1966). *The theory of quantum liquids*. Perseus Book.

Prêtre, A., Thomas, H., and Büttiker, M. (1996). Dynamics admittance of mesoscopic conductors: discrete potential model. *Phys. Rev.* **B**, 54:8130.

Prokofev, N. and Stamp, P. (2000). Theory of the spin bath. *Rep. Prog. Phys.*, 63:669–726.

Reiserer, A. and Rempe, G. (2015). Cavity-based quantum networks with single atoms and optical photons. *Rev. Mod. Phys.*, 87:1379–1418.

Roussel, B., Cabart, C., Fève, G., and Degiovanni, P. Electronic atoms of signals and entanglement spectrum in electron quantum optics. In preparation.

Roussel, B., Cabart, C., Fève, G., Thibierge, E., and Degiovanni, P. (2017). Electron quantum optics as quantum signal processing. *Physica Status Solidi B*, 254:16000621.

Roussel, B., Degiovanni, P., and Safi, I. (2016). Perturbative fluctuation dissipation relation for nonequilibrium finite-frequency noise in quantum circuits. *Phys. Rev. B*, 93:045102.

Rovelli, C. (1996). Relational quantum mechanics. *Int. J. of Theor. Phys.*, 35:1637.

Rychkov, V. S., Polianski, M. L., and Büttiker, M. (2005). Photon-assisted electron-hole shot noise in multiterminal conductors. *Phys. Rev. B*, 72:155326.

Safi, I. (1997). Conductance of a quantum wire: Landauer's approach versus the kubo formula. *Phys. Rev. B*, 55:R7331–R7334.

Safi, I. (1999). A dynamic scattering approach for a gated interacting wire. *Eur. Phys. J.* **D**, 12:451.

Safi, I. and Joyez, P. (2011). Time-dependent theory of nonlinear response and current fluctuations. *Phys. Rev. B*, 84:205129.

Safi, I. and Schulz, H. (1995a). Transport in an inhomogeneous interacting one-dimensional system. *Phys. Rev. B*, 52:R1740.

Safi, I. and Schulz, H. (1995b). Transport through a single band wire connected to measuring leads. In Kramer, B., editor, *Quantum Transport in Semiconductor Submicron Structures*, page 159. Kluwer Academic Press, Dordrecht.

Scarani, V., Bechmann-Pasquinucci, H., Cerf, N. J., Dušek, M., Lütkenhaus, N., and Peev, M. (2009). The security of practical quantum key distribution. *Rev. Mod. Phys.*, 81:1301–1350.

Shannon, C. and Weaver, W. (1975). *Théorie mathématique de la communication*. Retz - CEPL.

Sharvin, D. and Sharvin, Y. (1981). Magnetic-glux quantization in a cylindrical film of a normal metal. *JETP Lett.*, 34:272.

Shytov, A. (2005). Structured energy distribution and coherent ac transport in mesoscopic wires. *Phys. Rev.* **B**, 71:085301.

Slobodeniuk, A. O., Idrisov, E. G., and Sukhorukov, E. V. (2016). Relaxation of an electron wave packet at the quantum hall edge at filling factor $\nu = 2$. *Phys. Rev. B*, 93:035421.

Smithey, D. T., Beck, M., Raymer, M. G., and Faridani, A. (1993). Measurement of the wigner distribution and the density matrix of a light mode using optical homodyne tomography: Application to squeezed states and the vacuum. *Phys. Rev. Lett.*, 70:1244.

Snyman, I. and Florens, S. (2015). Robust josephson-kondo screening cloud in circuit quantum electrodynamics. *Phys. Rev. B*, 92:085131.

Splettstoesser, J., Moskalets, M., and Büttiker, M. (2009). Two-particle nonlocal aharonov-bohm effect from two single-particle emitters. *Phys. Rev. Lett.*, 103:076804.

Srinivas, M. D. (1982). When is a hidden variable theory compatible with quantum mechanics? *Pramana*, 19(2):159–173.

Stone, M., editor (1994). *Bosonization*. World Scientific.

Stormer, H. L. (1999). Nobel lecture: The fractional quantum hall effect. *Rev. Mod. Phys.*, 71:875–889.

Tauber, C. (2015). *Trois applications d'une approche géométrique à la théorie conforme des champs*. PhD thesis, Ecole Normale Supérieure de Lyon.

Tewari, S., Roulleau, P., Grenier, C., Portier, F., Cavanna, A., Gennser, U., Mailly, D., and Roche, P. (2016). Robust quantum coherence above the fermi sea. *Phys. Rev. B*, 93:035420.

Thalineau, R., Weick, A., Bauerle, C., and Meunier, T. Using a two electron spin qubit to detect electrons flying above the fermi sea. Arxiv:1403.7770.

Thibaut, K., Gabelli, J., Lupien, C., and Reulet, B. (2015). Pauli-heisenberg blockade of electron quantum transport. *Phys. Rev. Lett.*, 114:236604.

Thibierge, E. (2015). *Cohérence à un et deux électrons en optique quantique électronique*. PhD thesis, Ecole Normale Supérieure de Lyon.

Thibierge, E., Ferraro, D., Roussel, B., Cabart, C., Marguerite, A., Fève, G., and Degiovanni, P. (2016). Two-electron coherence and its measurement in electron quantum optics. *Phys. Rev. B*, 113:081302(R).

Tien, P. K. and Gordon, J. P. (1963). Multiphoton process observed in the interaction of microwave fields with the tunneling between superconductor films. *Phys. Rev.*, 129:647–651.

Tsui, D., Stormer, H.L.rmer, A., and Gossard, A. (1982). Two-dimensional magnetotransport in the extreme quantum limit. *Phys. Rev. Lett.*, 48:1559.

Vallone, G., Bacco, D., Dequal, D., Gaiarin, S., Luceri, V., Bianco, G., and Villoresi, P. (2015). Experimental satellite quantum communications. *Phys. Rev. Lett.*, 115:040502.

van Houten, H., Beenakker, C., and van Wees, B. (1992). *Quantum Point Contacts*, volume 35 of *Semiconductors and semimetals*, chapter 2, page 9. Academic Press.

van Wees, B. J., Kouwenhoven, L. P., Willems, E. M. M., Harmans, C. J. P. M., Mooij, J. E., van Houten, H., Beenakker, C. W. J., Williamson, J. G., and Foxon, C. T. (1991). Quantum ballistic and adiabatic electron transport studied with quantum point contacts. *Phys. Rev. B*, 43:12431–12453.

van Wees, B. J., van Houten, H., Beenakker, C. W. J., Williamson, J. G., Kouwenhoven, L. P., van der Marel, D., and Foxon, C. T. (1988). Quantized conductance of point contacts in a two-dimensional electron gas. *Phys. Rev. Lett.*, 60:848–850.

Vanević, M., Gabelli, J., Belzig, W., and Reulet, B. (2016). Electron and electron-hole quasiparticle states in a driven quantum contact. *Phys. Rev. B*, 93:041416.

Vanević, M., Nazarov, Y. V., and Belzig, W. (2007). Elementary events of electron transfer in a voltage-driven quantum point contact. *Phys. Rev. Lett.*, 99:076601.

Vanević, M., Nazarov, Y. V., and Belzig, W. (2008). Elementary charge-transfer processes in mesoscopic conductors. *Phys. Rev. B*, 78:245308.

Vanević, M., Nazarov, Y. V., and Belzig, W. (2017). Electron and electron-hole excitations in a driven fermi sea. *Physica Status Solidi B*, 254:1600551.

Ville, J. (1948). Théorie et applications de la notion de signal analytique. *Câbles et Transmission*, 2:61–74.

Virally, S., Simoneau, J. O., Lupien, C., and Reulet, B. (2016). Discrete photon statistics from continuous microwave measurements. *Phys. Rev. A*, 93:043813.

von Delft, J. and Schoeller, H. (1998). Bosonization for beginners - refermionization for experts. *Annalen der Physik*, 7:225.

von Klitzing, K., Dorda, G., and Pepper, M. (1980). New method for high-accuracy determination of the fine-structure constant based on quantized hall resistance. *Phys. Rev. Lett.*, 45(6):494–497.

Wahl, C., Rech, J., Jonckheere, T., and Martin, T. (2014). Interactions and charge fractionalization in an electronic hong-ou-mandel interferometer. *Phys. Rev. Lett.*, 112:046802.

Wallraff, A., Schuster, D., Blais, A., Frunzio, L., Huang, R.-S., Majer, J., Kumar, S., Girvin, S., and Schoekopf, R. (2004). Strong coupling of a single photon to a superconducting qubit using circuit quantum electrodynamics. *Nature*, 431:162.

Walls, D. (1983). Squeezed states of light. *Nature*, 306:141.

Wannier, G. (1937). The structure of electronic excitation levels in insulating crystal. *Physical Review*, 52:191.

Washburn, S., Umbach, C. P., Laibowitz, R. B., and Webb, R. A. (1985). Temperature dependence of the normal-metal aharonov-bohm effect. *Phys. Rev. B*, 32:4789–4792.

Webb, R., Washburn, S., Umbach, C., and Laibowitz, R. (1985). Observation of h/eAharonov-Bohm oscillations in normal metal rings. *Phys. Rev. Lett.*, 54:2696 – 2699.

Weiss, U. (1999). *Quantum Dissipative Systems*. World Scientific.

Weißl, T., Küng, B., Dumur, E., Feofanov, A. K., Matei, I., Naud, C., Buisson, O., Hekking, F. W. J., and Guichard, W. (2015). Kerr

coefficients of plasma resonances in josephson junction chains. *Phys. Rev. B*, 92:104508.

Wick, G. C., Wightman, A. S., and Wigner, E. P. (1952). The intrinsic parity of elementary particles. *Phys. Rev.*, 88:101–105.

Wigner, E. (1932). On the quantum correction for thermodynamic equilibrium. *Phys. Rev.*, 40:749–759.

Wigner, E. (1997). Quantum-mechanical distribution functions revisited. In *Part I: Physical Chemistry. Part II: Solid State Physics*, pages 251–262. Springer.

Wiseman, H. (2014). *Quantum measurement and control*. Cambridge University Press.

Wootters, W. and Zurek, W. (1982). A single quantum cannot be cloned. *Nature*, 299:802.

Xiao, M., Wu, L.-A., and Kimble, H. J. (1987). Precision measurement beyond the shot-noise limit. *Phys. Rev. Lett.*, 59:278–281.

Yin, J., Cao, Y., Li, Y.-H., Liao, S.-K., Zhang, L., Ren, J.-G., Cai, W.-Q., Liu, W.-Y., Li, B., Dai, H., Li, G.-B., Lu, Q.-M., Gong, Y.-H., Xu, Y., Li, S.-L., Li, F.-Z., Yin, Y.-Y., Jiang, Z.-Q., Li, M., Jia, J.-J., Ren, G., He, D., Zhou, Y.-L., Zhang, X.-X., Wang, N., Chang, X., Zhu, Z.-C., Liu, N.-L., Chen, Y.-A., Lu, C.-Y., Shu, R., Peng, C.-Z., Wang, J.-Y., and Pan, J.-W. (2017). Satellite-based entanglement distribution over 1200 kilometers. *Science*, 356(6343):1140–1144.

Yurke, B. (1984). Quantum network theory. *Phys. Rev.* **A**, 29:1419.

Yurke, B. (1987). Squeezed-state generation using a Josephson parametric amplifier. *Journal of the Optical Society of America B Optical Physics*, 4:1551–1557.

Zakka-Bajjani, E., Dufouleur, J., Coulombel, N., Roche, P., Glattli, D. C., and Portier, F. (2010). Experimental determination of the statistics of photons emitted by a tunnel junction. *Phys. Rev. Lett.*, 104:206802.

Zakka-Bajjani, E., Ségala, J., Portier, F., Roche, P., Glattli, D., Cavanna, A., and Jin, Y. (2007). Experimental test of the high frequency quantum shot noise theory in a quantum point contact. *Phys. Rev. Lett.*, 99:236803.

Zernicke, F. (1938). The concept of degree of coherence and its application to optical problems. *Physica*, 5:785.

Zgirski, M., Foltyn, M., Savin, A., Meschke, M., and Pekola, J. (2017). Nanosecond thermometry with josephson junction. ArXiv::1704.04762.

Zibold, T. and Vogl, P. ans Bertoni, A. (2007). Theory of semiconductor quantum-wire-based single- and two-qubit gates. *Phys. Rev. B*, 76:195301.

Zurek, W. (1982). Environment-induced superselection rules. *Phys. Rev.* **D**, 26:1862–880.

Zurek, W. (1989). Algorithmic randomness and physical entropy. *Phys. Rev.* **A**, 40:4731.

Zurek, W., Habib, S., and Paz, J. (1993). Coherent states via decoherence. *Phys. Rev. Lett.*, 70:1187 – 1190.

Autopsy of a quantum electrical current

Quantum physics experiments have reached a level of precision and control that allows quantum state engineering for many systems. This has led to the birth of electron quantum optics, an emerging field which aims at generating, manipulating and characterizing quantum electrical currents built from few-electron excitations propagating within ballistic quantum conductors. This is challenging since it is generically impossible in practice to fully characterize the many-body state of a beam containing indistinguishable electrons. This thesis presents new quantum signal processing approaches for accessing, at least partially, to the quantum many-body state of quantum electrical currents.

A first approach is to access such a state at few-particle levels through electronic coherences. We will thus present a new representation of single-electron coherence in terms of electronic "atoms of signal". Combining this signal processing algorithm to HOM tomography enables us to present the first autopsy, wavefunction by wavefunction, of an experimental electrical quantum current.

Another method is to look for indicators giving information directly at the many-body level. We will investigate the radiation emitted by a quantum conductor and address the problem of decoherence of a general single-electron excitation. Finally, we will look at the heat deposited by a mesoscopic quantum system, leading to a quantum version of Joule heating and discuss how it gives an insight on the many-body state of the electron fluid.

Keywords: electron quantum optics, quantum signal processing, quantum coherence